Enhancing physical properties of low dimensional materials by engineering its environment in composite Van der Waals heterostructures

Goutham Nayak

Communauté
UNIVERSITÉ Grenoble Alpes

THÈSE

Pour obtenir le grade de

DOCTEUR DE LA

COMMUNAUTE UNIVERSITE GRENOBLE ALPES

Spécialité : **NANOPHYSIQUE**

Arrêté ministériel : 25 mai 2016

Présentée par

GOUTHAM NAYAK

Thèse dirigée par **Vincent Bouchiat**
codirigée par **Aveek Bid**
codirigée par **Julien Renard**

préparée au sein du **Laboratoire l'Institut Néel, CNRS**
dans **l'Ecole Doctorale Physique**

Amélioration des propriétés physiques de matériaux de basse-dimensionnalité par couplage dans des hétérostructures Van der Waals.

Enhancing physical properties of low dimensional materials by engineering its environment in composite Van der Waals heterostructures.

Thèse soutenue publiquement le **18 décembre 2018**,
devant le jury composé de :

Monsieur GUILLAUME CASSABOIS
PROFESSEUR, UNIVERSITE DE MONTPELLIER, Rapporteur
Monsieur BENOÎT JOUAULT
DIRECTEUR DE RECHERCHE, CNRS DELEGATION OCCITANIE EST, Rapporteur
Monsieur DAVID FERRAND
PROFESSEUR, UNIVERSITE GRENOBLE ALPES, Président
Monsieur CLEMENS WINKELMANN
MAITRE DE CONFERENCES, GRENOBLE INP, Examinateur
Monsieur VINCENT BOUCHIAT
Directeur de Recherche, Institut NEEL, CNRS, Directeur de thèse
Monsieur JULIEN RENARD
Chargé de Recherche, Institut NEEL, CNRS, Co-encadrant de thèse

Abstract

The extraordinary intrinsic properties of low dimensional materials depend highly on the environment they are subjected to. Hence they need to be prepared, processed and characterized without defects. In this thesis, I discuss about how to control the environment of low dimensional nanomaterials such as graphene, MoS_2 and carbon nanotubes to preserve their intrinsic physical properties. Novel solutions for property enhancements are discussed in depth. In the first part, we fabricate state-of-the-art, edge-contacted, graphene Van der Waals(VdW) heterostructure devices encapsulated in hexagonal-boron nitride(hBN), to obtain ballistic transport. We use a technique based on 1/f-noise measurements to probe bulk and edge transport during integer and fractional Quantum Hall regimes. In the second part, the same fabrication concept of VdW heterostructures has been extended to encapsulate monolayer MoS_2 in hBN to improve optical properties. In this regard we present an extensive study about the origin and characterization of intrinsic and extrinsic defects and their affect on optical properties. Further, we describe a technique to probe the interlayer coupling along with the generation of light with spatial resolution below the diffraction limit of light. Finally, we discuss a natural systemic process to enhance the mechanical properties of natural polymer silk using HipCO-made single walled carbon nanotubes as a food for silkworm.

Résumé

Les propriétés intrinsèques extraordinaires de ces matériaux de faible dimension dépendent fortement de l'environnement auquel ils sont soumis. Par conséquent, ils doivent être préparés, traités et caractérisés sans défauts. Dans cette thèse, je discute de la manière de contrôler l'environnement des nanomatériaux de faible dimension tels que le graphène, le MoS_2 et les nanotubes de carbone afin de préserver leurs propriétés physiques intrinsèques. De nouvelles solutions pour l'amélioration des propriétés sont discutées en profondeur. Dans la première partie, nous fabriquons des dispositifs d'hétérostructure à base de graphène de Van der Waals (VdW) de dernière génération, en contact avec les bords, encapsulés dans du nitrure de bore hexagonal (hBN), afin d'obtenir un transport balistique. Nous utilisons une technique basée sur des mesures de bruit 1 / f pour sonder le transport de masse et de bord lors de régimes Quantum Hall entiers et fractionnaires. Dans la deuxième partie, le même concept de fabrication des hétérostructures VdW a été étendu pour encapsuler la couche monocouche MoS $_2$ dans le hBN afin d'en modifier les propriétés optiques. À cet égard, nous présentons une étude approfondie sur l'origine et la caractérisation des défauts intrinsèques et extrinsèques et leur incidence sur les propriétés optiques. En outre, nous décrivons une technique pour sonder le couplage entre couches ainsi que la génération de lumière avec une résolution spatiale inférieure à la limite de diffraction de la lumière. Enfin, nous discutons d'un processus systémique naturel visant à améliorer les propriétés mécaniques de la soie polymérique naturelle à l'aide d'une nanotube de carbone à paroi unique fabriqués par HipCO comme aliment pour le ver à soie.

Contents

Preface **7**

Acknowledgements **8**

Outline of the thesis **10**

1 *Introduction: order/disorder in low dimensional materials* **12**
1.1 Motivation of the work . . . 13
1.1.1 The Questions addressed in this thesis . . . 15
1.2 Order in solids: crystals . . . 16
1.3 Defects and disorder in 2D materials . . . 17
1.3.1 Intrinsic defects . . . 17
1.3.2 Extrinsic defects . . . 17
1.4 Defect characterization techniques . . . 18
1.5 Solutions for protection and physical property enhancements . . . 19
1.5.1 Van der Waals (VdW) heterostructures . . . 20
1.5.1.1 Van der Waals (VdW) forces . . . 20
1.5.1.2 Hexagonal Boron Nitride (hBN), the work horse of 2D VdW heterostructures . . . 22
1.5.1.3 VdW heterostructures obtained by direct growth . . . 22
1.5.1.4 VdW heterostructures by exfoliation and polymer transfer . . . 24
1.5.2 Nanocomposites . . . 25
1.5.2.1 Nanocomposites by artificial processing methods . . . 26
1.5.2.2 Nanocomposites by natural systemic approach . . . 27

2 *Novel technique to probe defects of the bulk in quantum Hall regimes in hBN/graphene/hBN heterostructures* **28**
2.1 Brief Introduction to the chapter . . . 30
2.2 Electronic properties of Graphene . . . 31
2.2.1 Crystal structure . . . 31
2.2.2 Electronic band structure . . . 32
2.2.3 Field effect properties . . . 34
2.3 Sample fabrication . . . 36
2.3.1 Mechanical exfoliation and identification of graphene and hBN . . . 36
2.3.2 Stack preparation recipe using PPC Method . . . 39
2.3.2.1 Polypropylene Carbonate (PPC) Stamps . . . 39
2.3.2.2 Microtransfer setup . . . 40
2.3.2.3 Pick-up transfer technique Recipe using PPC . . . 41
2.3.2.3.1 First pick-up of top hBN . . . 42
2.3.2.3.2 Further pick-up steps for any 2D material . . . 42
2.3.2.3.3 Graphene encapsulation in pristine condition . . . 43

2.3.2.3.4 Drop-down of stack from PPC to desired substrate . . . 43
2.3.2.4 Improvements in the stacking process . . . 44
2.3.3 Nanofabrication of edge-contacted devices . . . 45
2.3.3.1 Markers using Laser Lithography . . . 46
2.3.3.2 E-Beam Lithography (EBL) for device area definition . . . 47
2.3.3.2.1 HSQ (hydrogen silesquioxane) process: 2-Layer Resist . . . 48
2.3.3.2.2 ARN 7700.18 process: 2-Layer Resist . . . 48
2.3.3.3 Reactive ion etch process . . . 49
2.3.3.4 Ebeam Lithography (EBL) for contacts electrode definition . . . 50
2.3.3.5 Metal deposition and lift-off process . . . 51
2.3.3.6 Top gate backend process . . . 52
2.4 Dilution fridge measurement technique . . . 53
2.5 Quantum electron transport in the quantum Hall regime . . . 54
2.5.1 Classical motion of electron in a magnetic field . . . 54
2.5.2 Shubnikov de Haas effect . . . 55
2.5.3 Landau quantization . . . 56
2.5.4 Integer Quantum Hall effect . . . 58
2.5.5 Relativistic iQHE in graphene . . . 61
2.5.6 Devices and iQHE measurements . . . 63
2.5.7 Ballistic transport and Landau-Buttiker formalism . . . 66
2.6 Fractional Quantum Hall effect . . . 67
2.6.1 Laughlin theory . . . 68
2.6.2 Composite fermions . . . 69
2.6.3 The curious case of 3/2 and 5/2 states . . . 70
2.6.4 Fractional states in graphene . . . 71
2.6.5 Fractional states in graphite backgated hBN encapsulated devices . . . 72
2.7 Noise in quantum devices . . . 73
2.7.1 Different types of noise in electron devices . . . 74
2.7.1.1 Thermal noise or Johnson-Nyquist noise . . . 74
2.7.1.2 Shot noise . . . 74
2.7.1.3 Flicker noise/ low frequency noise or 1/f noise . . . 75
2.7.2 Low frequency 1/f noise . . . 75
2.7.2.1 'du Pre' interpretation of 1/f noise . . . 75
2.7.2.2 McWhorter's model . . . 76
2.7.2.3 Dutta and Horn model . . . 77
2.7.2.4 Mobility fluctuations model . . . 77
2.7.2.5 Hooge's model . . . 77
2.7.3 1/f measurement technique . . . 78
2.7.4 1/f noise measurement in graphene . . . 80
2.7.5 1/f noise in iQHE and fQHE regime . . . 82
2.8 Conclusions and perspectives . . . 86
2.8.1 Conclusions . . . 86
2.8.2 Quantum point contacts for shot-noise measurements . . . 86
2.8.3 Fabry Perot interferometers . . . 87

3 *2D Synthetic MoS_2 versus Natural MoS_2 : Influence of defects on optical properties* **88**
3.1 Brief introduction to the chapter . . . 89
3.2 Electronic properties of monolayer MoS_2 . . . 92

3.2.1 Crystal structure . . . 92
3.2.2 Band diagram . . . 93
3.2.3 Excitonic properties in monolayer MoS_2 . . . 94
3.2.4 Vibrational properties in monolayer MoS_2 . . . 98
3.3 Sample fabrication . . . 102
3.3.1 MoS_2 crystal sources . . . 102
3.3.2 Mechanical exfoliation . . . 102
3.3.3 Optical identification of monolayer MoS_2 flakes . . . 103
3.3.4 Large area monolayer flakes . . . 105
3.3.5 Preparation of samples . . . 105
3.4 Introduction to spectroscopy techniques . . . 107
3.4.1 Introduction to Raman spectroscopy . . . 107
3.4.2 Confocal micro Raman spectroscopy set-up . . . 109
3.4.3 Introduction to Photoluminescence technique . . . 110
3.5 Extrinsic and intrinsic defect characterization using Raman and PL . . . 111
3.5.1 Raman spectroscopy signature of monolayer MoS_2 . . . 112
3.5.2 Photoluminescence signature of monolayer MoS_2 . . . 113
3.5.3 Reflectance spectroscopy of monolayer MoS_2 . . . 115
3.5.4 Strain and Doping from vibrational spectroscopy . . . 115
3.5.5 Excitonic complex in presence of strain, doping and defects . . . 119
3.6 Intrinsic defect confirmation in artificial HP/HT MoS_2 . . . 121
3.6.1 Scanning Tunneling Microscopy-nature of point defects . . . 121
3.6.2 Density functional theory (DFT) and STM simulations . . . 123
3.6.3 Field Effect characterization of artificial HP/HT MoS_2 . . . 126
3.7 Chapter conclusions and perspectives . . . 128
3.7.1 Conclusions . . . 128
3.7.2 Perspectives . . . 128

4 *hBN encapsulated MoS_2 Van der Waals heterostructures* 129
4.1 Brief introduction to the chapter . . . 130
4.2 Cathodoluminescence set-up . . . 132
4.3 Fabrication of hBN/monolayer MoS_2/hBN heterostructures . . . 133
4.3.1 hBN/monolayer MoS_2/hBN stack by PDMS method . . . 133
4.3.2 hBN/monolayer MoS_2/hBN stack by PPC method . . . 134
4.4 hBN encapsulation as passive component for enhancement of optical properties . 135
4.4.1 Homogeneous and inhomogeneous broadening . . . 135
4.4.2 Line-width reduction/improvement . . . 136
4.4.3 Four-wave mixing spectroscopy in monolayer MoS_2 . . . 137
4.5 hBN encapsulation as active component for efficient light generation in MoS_2 . 141
4.5.1 Probing Interlayer coupling . . . 141
4.5.2 Type I band alignment in hBN/ monolayer MoS_2/ hBN heterostructure 143
4.5.3 Non uniform cathodoluminescence and quenching . . . 144
4.5.4 Importance of hBN . . . 146
4.5.5 Raman studies on defects created by ion bombardment . . . 147
4.5.6 Raman analysis before and after electron beam irradiation . . . 148
4.5.7 Origin of defects . . . 152
4.5.8 Heterostructure fabrication for better interlayer coupling . . . 153
4.6 Chapter conclusions and perspectives . . . 154
4.6.1 Conclusions . . . 154
4.6.2 Perspectives: $MoSe_2$ heterostructure in tailored electromagnetic environments . . . 155

4.7 APPENDIX . . . 156
4.7.1 Photoluminescence spectrum fitting procedure . . . 156
4.7.2 Raman spectrum fitting procedure . . . 156
4.7.2.1 Residuals for quantitative fit analysis . . . 156
4.7.2.2 The spectral function . . . 158
4.7.3 Noisy spectra on large scale images . . . 162

5 *Enhanced composite silk nano-biomaterial by systemic intake of low dimensional materials* 164
5.1 Introduction: Nanomaterials integrated into composite silk fibers . . . 165
5.2 Single Walled Carbon Nanotubes (SWCNT) . . . 167
5.2.1 Mechanical properties of SWCNTs . . . 167
5.2.2 Growth of SWCNT by HipCO process . . . 169
5.2.3 SWCNT fibers . . . 170
5.3 Bombyx Mori Silk as high mechanical strength fibers . . . 171
5.3.1 Bombyx mori silk . . . 171
5.3.2 Mechanical properties of Bombyx Mori silk . . . 172
5.3.3 Recent developments in silk fibers . . . 173
5.4 Systemic process of SWCNT silk production . . . 174
5.4.1 Mulberry leaves and Bombyx Mori eggs . . . 175
5.4.2 Spin coating Nopo SWNTs on leaves . . . 176
5.4.3 Cocoon growth . . . 177
5.4.4 Reeling of silk fibers . . . 178
5.4.5 Key observations during the rearing and reeling of SWCNT silk fibers . . . 179
5.5 Characterization of SWCNT silk . . . 180
5.5.1 Raman spectroscopy on SWCNT silk . . . 180
5.5.2 Scanning electron microscopy of SWCNT silk . . . 182
5.5.3 Transmission electron microscopy on SWCNT silk . . . 184
5.6 Mechanical experiments of SWCNT silk . . . 186
5.6.1 Measurement setup for mechanical strength characterization . . . 186
5.6.2 Critical radius and Youngs modulus . . . 187
5.6.3 Breaking strength versus SWCNT concentration . . . 189
5.6.4 X- ray nano diffraction studies on SWCNT silk . . . 190
5.7 Conclusions and perspectives . . . 196

General conclusions and future perspectives 197

Bibliography 214

Preface

This thesis work addresses multitude of topics, that covers electronic, optical and mechanical properties of low dimensional materials accomplished under the protégé of Dr.Vincent Bouchiat. Such a broad range of activities were possible as a result of efficient team-work from Hybride group, Institut NEEL (Vincent Bouchiat, Nedjma Bendiab, Johann Coraux, Laetitia Marty and Julien Renard) specialized in different nanotechnological domains. This thesis was a result of collaborations, not only with the other members of the group but also with international entities.

The work based on graphene is collaboration between principal investigators Dr.Vincent Bouchiat (Institute NEEL, CNRS, Grenoble) and Dr.Aveek Bid (Indian Institute of Science, Bangalore) under the framework of CEFIPRA(Indo-french organization for science). All the sample fabrication were accomplished by me at Institut NEEL, Grenoble under supervison of Dr.Vincent Bouchiat and Dr.Julien Renard. The low temperature-high magnetic field quantum transport measurements were carried out in Indian Institute of Science (IISc), Bangalore under the supervision of Dr.Aveek Bid. In this regard, Dr.Kazi Rafsanjani Amin and Ramya Bhaskaran have supported me during the dilution fridge measurements who were PhD students in Dr.Aveeks's lab at that time. Weilai, a chinese visiting PhD student also supported me for preparing heterostructures at the end of my PhD.

The work based on monolayer MoS_2 is a result of collaboration between different team members of Hybride. In this work, all the synthesis and sample fabrications and optical characterization were carried out by me. Data analysis and figures were supported by Dr.Simone Lisi who was post-doc in the team. DFT simulations were supported by Van-Dung Nguyen and Laurence Magaud of our team. STM measurements were done in collaboration with Pierre Mallet and Jean-Yves Veuillen of QNES team in Institute NEEL and STM simulations by Yannick J. Dappe of CEA, Saclay. The FWM measurements and analysis were carried out by Tomasz Jakubczyk and Jacek Kasprzak of Institut NEEL. The low-temperature photoluminescence measurements were performed in collaboration with Maxime Richard, Petr Stepanov and low-temperature cathodoluminescence measurements were executed in collaboration Fabrice Donatini. hBN and MoS_2 synthetic crystals for the experiments were provided by K.Watanabe and T. Taniguchi of NIMS, Tsukuba, Japan.

Finally the work based on carbon nanotubes and silk were performed in collaboration with Mr.Gadhadar, CEO of Nopo Nanotechnologies, Bangalore under the guidance of Dr.Vincent Bouchiat. The growth and production of carbon nanotube silk were carried out by Nopo team. All the characterization techniques,mechanical measurements were performed by me at Institut NEEL except TEM data supported by Dipankar Kalita,Hanako Okuno of CEA/INAC and XRD-synchrotron measurements by Christian Riekel of ESRF,Grenoble and Manfred Burghammer (ESRF, ID13 beamline responsible).

Acknowledgements

First and foremost, I would like to thank Guido Groeseneken, Elke Delfosse from KU Leuven for giving me an oppurtunity to start in the field of nanotechnology. All of us, EMM Nano graduated students should be very grateful to them for being backbone and spine of this excellent program. In the same context, I would like to thank David Ferrand who is Grenoble EMM Nano co-ordinator who introduced me to numerous nanotech labs in Grenoble.

I am very grateful to my thesis director Vincent Bouchiat, who was my molecular electronics teacher during master studies. He gave me an oppurtunity to join master internship and PhD thesis. I had little to no hands-on experience in experimental physics or deep knowledge about nanophysics. He took a big risk at that time to recruit and train me. I would always remember him as my physics father (believe me, he knows everything) after spending 4 years under his guidance. He gave me complete freedom to learn or master whatever I am interested in, during my stay in the lab.

I am very thankful to my co-supervisor Julien Renard who joined as a permanent resercher at the same time I joined as a student. He was very knowledgable and at the same time very humble to give his support to my PhD. I have learnt a lot under him and was really great to work with him.

I would also like to thank my another co-supervisor Aveek Bid. I spent five months in his lab over three years and was able to integrate easily without difficulty. He gave his guidance, inputs and support inspite of his health concerns which are admirable.

I would like to thank specially Zheng Han Vitto for introducing me to world of exfoliation, heterostructures and lithography techniques. I have learnt a lot from this extremely good experimental physicist.

The best part of joining PhD in Hybride team was that you instantly get five supervisors who are specialized in different topics. I extend my sincere thanks to Nedjma Bendiab, Laetitia Marty and Johann Coraux for their time and support during my PhD inspite of not being my official supervisors. Nedjma is a very strong person who always encouraged and supported me like I was her own student. Laetitia is the nicest person in the team helping us regarding administrative to technical topics. Johann was very professional, giving inputs and technical boost to publications and presentations. I am honestly very grateful to all the members for supporting also for my future career prospects.

The fun part of joining Hybride team was that I met wonderful PhD and postdoc collegues. When I joined I was helped by Cornelia, Yani, Alexander, Dipankar and further during my thesis I have enjoyed my time in lab with Ana, Estelle, Simone, Sudipta, Felix, Van-Dung, Pauline, Riadh, Weilai, Brice, Priyank, Guilliame who make wonderful collegues. In the same context, I would like to thank Kazi, Ramya, Hemanto, Gopi, Suman and especially Sangram

and Anjali for helping me to integrate well in IISc.

I would like to thank CEFIPRA for providing me grant for conducting the PhD research. At the same time, I would like to thank all the CEFIPRA administrative members in particular Sathidevi for their continuos administrative support. In the same context, I would like to thank Institut NEEL administrative team, Othmane, Angelique, Cecile (Reprog) and Florence pois for helping with all the administrative procedure during my stay.

Coming to technical work at NEEL, I would like to thank Nanofab team (Jeff, Thierry, Seb, Bruno, Gwen, Latifa) for their support and training. They are maintaining a world class nanofab and were always available for any related problem. I have relished working with nanofab boss Jean Francois Motte both during fabrication and CNRS football tournaments. He really leads by example. Similarly I would like to thank microscopy team especially Simon for AFM traning and Richard Hattel for annealing my samples whenever I wanted.

I am very grateful to Cecile Berne for helping me to settle down in Grenoble during the start of PhD. She also helped me to learn many characterization techniques during my master internship.

I was very lucky to have plenty of friends in Grenoble. This made my life filled with fun and joy. I would like to thank Remy, Javier, Jorge, Shridevi, Swati, Nitika, Micheal, Beatrix, Nicolas, Louis, Coerntin, Marco, Alvaro, Hugo, Tomas, Vanni, Raquel, Marila, Curry(Dany). Sorry the list will go on. I am writing this at the end of my thesis. Little bit of stress may have made me to forget some really good friends. Sorry but you have been wonderful to me. Further I am grateful to my bff's Bob, Martina, Sergio, Thomas, Timothy, Yash, again many more...

I am also very grateful to Tony and family, Thierry and family for considering me like one among their own family. It was really wonderful to be among you during christmas, holidays or weekends.

Last but not the least, I would like to thank M.Guillaume CASSABOIS, M. Benoit JOUAULT, M. David FERRAND, M. Clemens WINKELMANN for accepting to be jury members for my thesis defense.

Outline of the thesis

Nanomaterials in particular one dimensional nanotubes and two-dimensional layered materials discovered with extraordinary properties have been touted as the components for next generation technologies. The discovery of Graphene has led to the innovation of a flurry of two dimensional materials. These include semimetals like graphene, insulators such as hexagonal boron nitride(hBN), and transition metal dichalcogenides(TMDC) semiconductors. Over the years graphene has bagged plenty of interest owing to its unique electronic properties especially its high mobility whereas most of the TMDCs attracted the researchers due to their direct bandgap at the monolayer limit that make them optically active. On the other hand carbon nanotubes discovered long before the 2D materials have been found to have excellent mechanical and electronic properties that could result in different kind of applications.

To obtain the potential outstanding property of the nano-material, it needs to be produced in the purest form and also processed and maintained in the same form even when used in different applications. This is a very challenging task where degradation could lead to catastrophic failures. Hence each of the steps such as the nanomaterial production, processing and behaviour in the environment needs to be studied in depth. This needs several characterization techniques to quantify the quality of the nanomaterial. Based on these studies, protection and enhancement solutions could be envisioned.

This thesis work is divided into five chapters starting from the introduction explaining the general concepts, motivation and questions that are being addressed in the thesis. The remaining four chapters are based on different physical properties of nanomaterials being probed. (electronic or optoelectronic or mechanical) In second, third and fourth chapter, a 2D material is interfaced with another 2D material in a layered fashion to form a stack kind of structure called Van der Waals heterostructure which basically enhances the electronic and optoelectronic properties of the 2D material. In the fifth chapter, 1D single walled carbon nanotubes are integrated with natural polymer fiber (Bombyx Mori silk) to enhance the mechanical property of the initial material.

In the second chapter, few layer of hexagonal boron nitride (hBN) is used with graphene to significantly boost its mobility and thus the quantum electronic properties. In this case the graphene is encapsulated between two few layered hBN flakes which acts as an ideal substrate and gate dielectric to improve its electronic properties. It was found out that the extraordinary intrinsic properties of 2D materials depends highly on the substrate upon which they are resting. The Si/SiO_2 substrates while convenient were later found not to be ideal ones due to roughness and charged impurity effects.

The quest to find an ideal substrate resulted in forming Van-der-Waals heterostructures with atomically flat and inert 2D hBN. A state-of-the-art method was introduced by Cory Dean group[1] to encapsulate the graphene in its pristine form between two hBN flakes with one-dimensional edge-contacts to obtain ballistic devices. These ballistic transport devices show

very high mobility of up to million $cm^2/V.s$ allowing the observation of fractional quantum Hall effect. We have also measured the 1/f noise behaviour at these regimes to better understand the transport dynamics in the bulk and along the edges.

In the third chapter, hBN is employed again and interfaced with monolayer MoS_2 to enhance its optical properties. Here h-BN acts as an atomically-flat buffer substrate to improve the optical properties of the direct band gap monolayer MoS_2. In these kind of samples, we have studied the possible origin of intrinsic and extrinsic defects which may affect the optical properties of the monolayer MoS_2. This is explained with detailed examination of the samples using different characterization techniques such as Raman spectroscopy, photoluminescence and scanning tunnelling microscopy.

In the fourth chapter,the same fabrication concepts as that in chapter two has been extended to monolayer MoS_2 where hBN encapsulation has been found to improve the excitonic features. Narrow linewidths approaching to intrinsic limit have been reported. We study again the influence of defects and disorder using four wave mixing spectroscopy technique. In addition, we describe a technique where hBN is no more just a passive buffer layer but has an active role while generating light from monolayer MoS_2. Further using a technique based on SEM called cathodoluminescence, we perform the probing of interlayer coupling in VdW heterostructures during generation of light where the spatial resolution is below the diffraction limit of light.

Finally, in the fifth chapter, single walled carbon nanotubes (SWCNT) are used to amplify the mechanical properties of the Bombyx Mori silk fibers. SWCNTs, one of the strongest known materials, is doped into the silk fibroin matrix by natural means to significantly improve its mechanical properties. The resulting nano-composite has been characterized using techniques such as Raman spectroscopy, scanning electron microscopy, transmission electron microscopy and X-ray diffraction. We further study the mechanical properties based on tensile load experiments of the nano-composite SWCNT silk where SWCNTs span over a large range of dose and found an optimum value for nanotube doping.

Chapter 1

Introduction: order/disorder in low dimensional materials

Contents

1.1 Motivation of the work 13
1.1.1 The Questions addressed in this thesis 15
1.2 Order in solids: crystals 16
1.3 Defects and disorder in 2D materials 17
1.3.1 Intrinsic defects 17
1.3.2 Extrinsic defects 17
1.4 Defect characterization techniques 18
1.5 Solutions for protection and physical property enhancements 19
1.5.1 Van der Waals (VdW) heterostructures 20
1.5.2 Nanocomposites 25

1.1 Motivation of the work

For any kind of applications whether it is electronic or optical or mechanical, pristine material in its purest form is very important. If not then the device may get degraded very easily and fails to reach its potential. Further it is also very important in any application to maintain over the course of events, the desired material in pristine form. The quality of the material could be degraded by various means such as irreversible defects in the material, surrounding environment affecting the material with reversible defects, and disorders formed due to manufacturing processes. Continuous improvements in processing and manufacturing have to be made in each of these factors to get best out of the material.

For example, in the microelectronic industry, ultra pure silicon is used for electronics and photovoltaics. The silicon used is perfect, defect-free single crystalline material where the purity is 99.9999999% famously called as 'nine-9'. Pure silicon has very low conductivity and in practice to enhance the conductivity, it is doped with small concentration of other elements. This doping improves the conductivity of silicon greatly and is used in semiconductor applications.

In this case, it is very important that the silicon used is very pristine and that the process of doping is also carried out in a controlled way. If these two basic points are not fulfilled, (i.e if the purity of starting material and the manufacturing process are not good enough) it may jeopardize the functionality and there would be severe degradation in the applications.

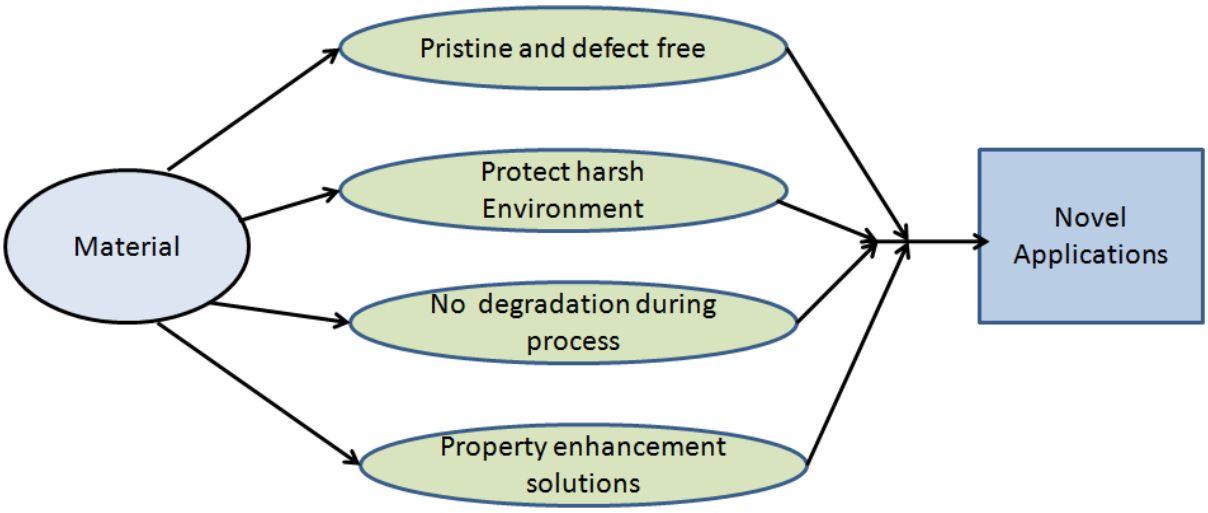

Figure 1.1 – Schematic block diagram with factors involving in the conversion of a material into sucessful application by harnessing their physical property.

The condition that we have discussed for 3D silicon is even more true when one reduces the dimensionality of the devices. In this thesis, the materials used are low dimensional nanomaterials like two-dimensional graphene and MoS_2 and one-dimensional carbon nanotubes. In the pristine form, each of these nano materials are wonder-materials with the potential of defining future electronics, optoelectronics and mechanical applications.

Nano objects or nanostructures can be categorized according to the number of its dimension in nanoscale. Nanoparticles including fullerenes have all the three dimension in the nanoscale and are named as 0-D nanostructures. One-dimensional nanostructures having two of their dimensions in nanoscale such as nanowires and nanotubes are considered to be ideal systems for

studying the effects of size reduction and quantum confinement on transport properties. Both 0-D and 1-D systems have also been used to embed in a bulk solid to form nanocomposites.

The two-dimensional nanostructures having at least one dimension in nanoscale, are starting to be explored by the microelectronics industry. They have gained a lot of scientific interest in the past few years after the discovery of graphene. Indeed, in the wake of Moore's law, there has been continuous efforts on reduction on the size of electronic devices.

1D and 2D nanostructures such as carbon nanotubes, semiconductor nanowires, graphene, transition metal dichalcogenides (TMDs) appear as strong candidates to be the building blocks for the fabrication of such devices. The properties like excellent electronic transport and direct bandgap have been stimulating the utilization of 1D and 2D nanostructures in a number of electronic and optoelectronic devices.

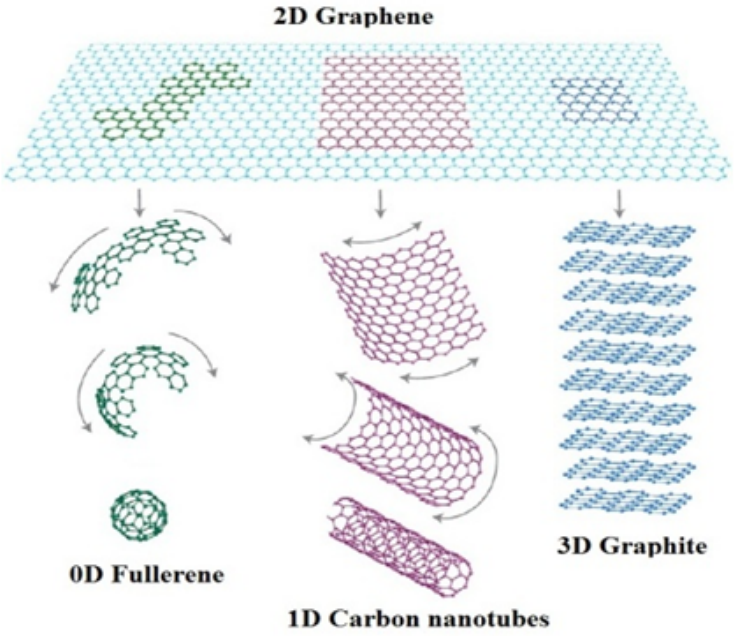

graphene family	graphene	hBN 'white graphene'	BCN	fluorographene	graphene oxide
2D chalcogenides	MoS_2, WS_2, $MoSe_2$, WSe_2	semiconducting dichalcogenides: $MoTe_2$, WTe_2, ZrS_2, $ZrSe_2$, etc.		metallic dichalcogenides: $NbSe_2$, NbS_2, TaS_2, TiS_2, $NiSe_2$, etc.	layered semiconductors: GaSe, GaTe, InSe, Bi_2Se_3, etc.
2D oxides	micas, BSCCO	MoO_3, WO_3	perovskite-type: $LaNb_2O_7$, $(Ca,Sr)_2Nb_3O_{10}$, $Bi_4Ti_3O_{12}$, $Ca_2Ta_2TiO_{10}$, etc.	hydroxides: $Ni(OH)_2$, $Eu(OH)_2$, etc.	
	layered Cu oxides	TiO_2, MnO_2, V_2O_5, TaO_3, RuO_2, etc.		OTHERS	

Figure 1.2 – (Top) Low dimension nanomaterials: structure of carbon-based 0D, 1D and 2D nanomaterials (Bottom) Classification of 2D materials. Figure adapted from [1],[2]

1.1.1 The Questions addressed in this thesis

Owing to their absence of bulk, these nanoscale few-atoms-layer materials could become easily defective either during its production or processing. In this thesis, I aimed at providing an in-depth study regarding how to preserve the nanomaterials during its pristine form and to optimize its environment.

How to identify or probe the defects if there are any and how to characterize or classify them? How external factors such as environment and manufacturing processes play a role in enhancing or degrading the quality? And finally what are the solutions to enhance the properties of the material regarding how to get the best property out of the material by combining different properties of distinct materials? In this work, the nanomaterials under test are graphene, MoS_2 and carbon nanotube, whereas the properties being tested are electronic, optical and mechanical respectively.

From past 15 years, graphene has been studied and it posses unique electronic properties. It took quite some time to grow/isolate the material in pristine form to obtain very high electron mobility as predicted. Here in this thesis, the state-of-the-art technique is used to maintain it in pure form. Another 2D material called hexagonal boron nitride (hBN) with completely opposite electrical property has been used to make a composite structure called Van der Walls heterostructures to get the best out of graphene.

Hence, here hBN protects graphene from external factors, optimize its environment and helps it to be itself and show its true worth. Further the probe used to characterize the defects is low frequency noise measurements. In this case we operate graphene in quantum Hall regimes (integer and fractional) and we obtain ballistic edge-transport. Still if the bulk part has higher defects it may affect the edge transport and this can be probed using low frequency noise measurements.

After the advent of graphene, flurry of 2D materials were discovered out of which the most prominent are the family of transitional metal di-chalcogenide (TMDC) materials. The uniqueness of these 2D-materials is that most of them become direct band gap in the monolayer limit. Hence these materials are touted as next generation semiconductors for opto-electronics. As expected, we study optical properties of MoS_2, a TMDC material in this thesis.

Especially for optoelectronics, pristine material is of utmost importance where even a tiny defect can affect its performance. Hence we perform in-depth studies ranging from defects already intrinsic to material to defects caused by environment and fabrication processes. Further to improve and obtain the optical properties close to its intrinsic potential, similar Van der Waals heterostructures discussed before are fabricated and studied.

Carbon nanotubes (CNT), one-dimensional materials discovered long before 2D materials have exceptional mechanical properties. In the previous chapters, a 2D material is coupled with another 2D material to enhance the physical property. In this chapter, a nano scale material has been incorporated into a macro scale natural polymer to get the best of both. When CNTs are mixed together to form a fiber, it has been seen that the mechanical properties degrade compared to just single CNT.Hence small quantities of CNTs have been added as fillers to a natural polymer matrix to enhance the possible mechanical property. However the mixing should be controlled as it may induce amorphization into polymer matrix. A thorough study is made to check the influence of CNTs in the natural polymer environment and how it changes the properties and the structure of the fiber.

Chapters	Materials	Out-standing property	Crystal defects	Degradation	Protection solutions
Chapter 2	Graphene	Electronic (High mobility 2D)	Structural defects	Substrate/process /environment (interfacing)	hBN embedded heterostructure
Chapter 3 Chapter 4	MoS_2	Optical (Direct bandgap)	Vacancy defects	Substrate/process /environment (interfacing)	hBN embedded heterostructure
Chapter 5	CNTs/ (silk)	Mechanic -al/ (protein crystal)	Amorpho -usization	Nano-enrichment of structure (composite)	Nanocomposites (bio systemic)

Figure 1.3 – Table describing the nanoscale and macroscale materials used in the thesis along with the physical properties being probed, the possible causes of deterioration and the enhancements solutions applied to improve the properties.

1.2 Order in solids: crystals

Crystals are solid materials arranged in a highly ordered microscopic structure. All the two dimensional materials are obtained from their respective crystals. Crystals are obtained naturally for example during mining but they can be manufactured artificially too. Graphene is isolated from graphite crystal, which is nothing but packed several layers of single layer carbon atoms held by forces called Van der Waals (VdW) explained in the coming paragraphs.

Similarly, monolayer MoS_2 is also obtained from natural occuring molybdenite crystal. To isolate defect-less monolayers, it is important that these natural crystals are very pure without any impurities. Normally , impurities such as amorphous elements, aggregates and other dopants from the environment can affect the quality of these natural crystals.

Hence to overcome these possible disorders in the crystal, artificial methods have been implemented to obtain pure synthetic crystals. In case of graphite, artificial methods like over heating of silicon carbide, graphitization or production of Kish-graphite crystals during cast-iron processing have been used to obtain synthetic crystal. When it comes to MoS_2, literatures have pointed out that natural crystals have many point defects and therefore they have been plenty of studies to grow the crystals artificially.

In this thesis, synthetic MoS_2 crystals grown by NIMS Lab in Tsukuba, Japan using their dedicated and unique high-pressure, high-temperature process have been used. An attempt is made to characterize and compare them against natural sources in order to produce future ultra-pure MoS_2 crystals. This has been explained in details in the chapter 3 of the thesis.

1.3 Defects and disorder in 2D materials

As explained before, defects are detrimental to the quality of the 2D materials and therefore the applications they have been used in. It is thus important to understand, classify them and identify their origin in order to engineer materials with optimized and sometimes enhanced properties. By studying the kind of defects and origin, we could engineer to obtain defect-less materials. In this section, we explain the different kind of defects, their origin and possible techniques to characterize and ways to find a solution to get rid of them. We can broadly classify the defects into two types, namely intrinsic defects that are internal to the material and extrinsic defects that are originating from external effects.

1.3.1 Intrinsic defects

Intrinsic defects are the disorders originating from the inner structure of material itself.(i.e degradation of the crystalline structure) There could be defects in the 2D material crystal during its synthesis or acquired while isolation to obtain 2D material from the crystal. The most common and abundant defects experimentally observed in 2D materials are point defects. The different kind of intrinsic point defects observed are single vacancies, double vacancies, complex or line vacancies, and substitutional impurities. The simplest single vacancy defect is nothing but a single missing atom in the crystal lattice structure. While in case of a substitutional defect, one of the dopant not belonging to the crystal structure occupies one of the atom site in the lattice.

The different kind of intrinsic defects explained in previous paragraph are shown in the figure 1.4.

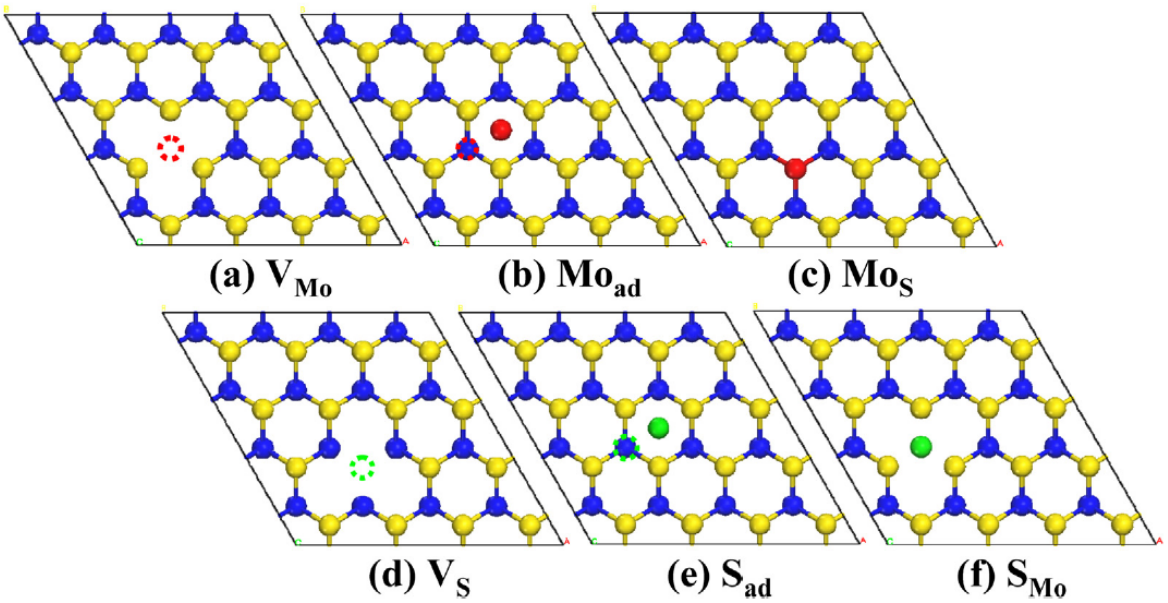

Figure 1.4 – Different types of point defects in MoS_2 2D crystal a) single Mo vacancy b)single Mo adsorption c) single substitution of S atom d) sulfur vacancy e) sulfur adsorption f) single substitution of Mo atom. Figure adapted from [3]

1.3.2 Extrinsic defects

Extrinsic defects are the disorder in the material originating from the external environment or external sources. We know 2D materials cannot stand by themselves but need a substrate to

hold them as they do not have any bulk and basically consist only two surfaces. These substrates may not be ideal as they introduce unnecessary charges into the 2D material system that may degrade its original property. So substrate induced charge effects are one of the extrinsic defects. Further, the environment to which the 2D material is exposed to can interfer with surface impurities. These impurities may just adsorb and deteriorate the quality or they can make a structural damage by covalent reactions or oxidations. These kind of extrinsic defects can be reduced and suppressed using proper substrate and protection techniques that will be discussed in the coming subsections.

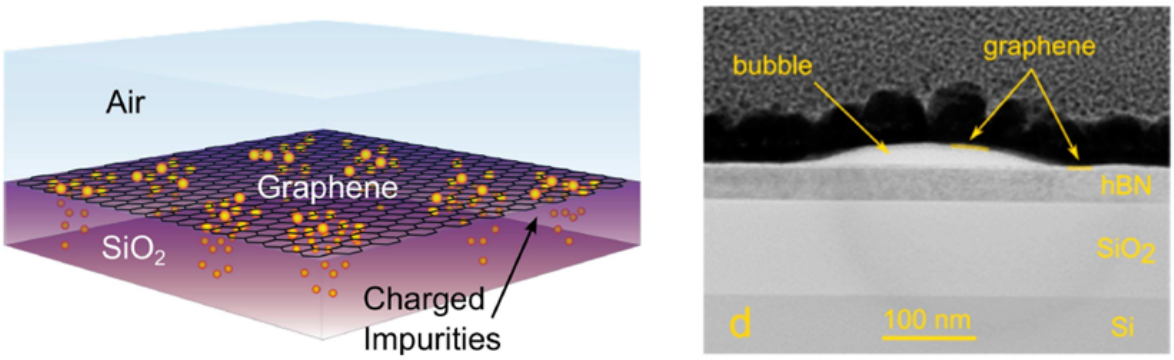

Figure 1.5 – (Left) Extrinsic defects originating from susbtrate, exposed environment. (Right) Extrinsic defects due transfer processes in form of blisters or bubbles. Figure adapted from [4], [5].

1.4 Defect characterization techniques

Characterization studies become very important during the defect study, where it is used to identify the nature of defects and quantify them. Over the years a wide range of characterization techniques have been used to study defects. The structural point defects have been studied by employing techniques such as transmission electron microscopy (TEM), scanning tunneling microscopy (STM) and X-ray photoelectron spectroscopy(XPS).While these techniques give a very good spatial resolution, it is difficult and complex to prepare the samples and also to characterize very large ones. Moreover, some of these techniques are invasive and highly detrimental to the samples, where there could be damages from the electron beam which could render the samples no more pristine for any further measurements.

This brings in a need to find new characterization solutions where there is sufficient spatial resolution, easiness to measure large structures and more importantly not to degrade the quality of the two dimensional material. So in this thesis work, optical spectroscopy techniques such as Raman and photoluminescence have been employed to characterize and differentiate different kind of defects. The advantages of using these techniques are that they are non-invasive and can be carried out easily at room temperature over large area samples in a time efficient manner.

As we know, the defects degrade the optical properties, by reverse engineering concept new features could be observed in these optical spectroscopic methods which classify and quantify the defects. Moreover, these techniques can probe and help to distinguish the different defects such as structural point defects, charge/doping effects from substrate or environment, strain or stacking. More details about these optical spectroscopic techniques will be discussed in the

chapter 3.

The spectroscopy techniques discussed above have maximum spatial resolution of half a micron determined by the minimum achieved laser spot size. In order to improve the spatial resolution below the diffraction limit of light, electron beam has been employed as a photon pump which creates probing source in a method called as cathodolminescence (CL). This technique allows us to have spatial resolution in order of few 10s of nanometers. Normally CL technique could be destructive, but using a special stack architecture, the optically-active 2D material could be protected. This has been discussed in detail in chapter 4 of this thesis.

Defect	Intrinsic	Extrinsic
Source of defect	Crystalline imperfections	Chemical/charge-fluctuations (spatial/temporal)
Origin of defect	Vacancy defects, substitutional defects	Substrate effects Surface contaminants
Characterization techniques	STM,XRD, Raman spectroscopy, XPS, Photoluminescence(PL) Cathodoluminescence (CL)	Raman spectroscopy Photoluminescence(PL) Cathodoluminescence (CL)

Figure 1.6 – Table of classification of defects in two dimensional materials with respect to their types and possible origin. Typical characterization techniques also included that are used to identify them.

1.5 Solutions for protection and physical property enhancements

In the previous section, we explained the different kinds of defects and ways to probe and characterize them. The next task is now to protect them from additional degradation over time in order to enhance the physical properties. The intrinsic defects related to the material could be overcome by optimizing the growth properties during the crystal generation. Although in this thesis we have compared the different crystal sources, the optimization of the growth parameters to get rid of internal defects is still an on-going topic.

This brings us to the second category of defects, the extrinsic ones, which could be avoided by using fabrication techniques that control the environment. In addition, these passive solutions enhance the physical property of the active 2D materials. As we know the corrugated non-atomically flat substrate cause charge transfer, atomically flat and inert/insulator substrates could be used to get rid of this substrate effect. In order to further protect the 2D material from the harsh environment, we can cover or encapsulate them again with an atomically flat or inert material. Hexagonal boron nitride (hBN) has been discovered as this atomically flat and inert material whose lattice constant almost matches that of graphene is explained in the next subsection. Hence with all these ideas, a new field in 2D materials, made like a composite of 2D materials called Van der Waals heterostructures was born.

Similarly, by using a macroscale materials, we can protect or enhance the property of a nanoscale material by forming composites. These called as nanocomposite are made up of low dimensional nanomaterial filler in a macroscale polymer matrix. Different physical properties such as mechanical, conductive etc can be enhanced using these nanocomposite solutions. The nanocomposites can be made naturally or by synthetic techniques explained in the further sub-sections. In this thesis, we embed single walled carbon nanotubes (SWCNT) in a natural polymer silk and study their possible enhancement in the mechanical properties.

1.5.1 Van der Waals (VdW) heterostructures

The period of layered two-dimensional materials started after the discovery of graphene by graphite exfoliation. Immediately, a flurry of 2D materials as shown in the table of the figure 1.2 were discovered with different physical properties than their bulk. In depth studies informed us that the bulk is nothing but several monolayer held together by Van der Waals forces.

In these layered materials, the strong covalent bond provide the required in-plane stability whereas the weak Van der Waals forces in the out-of-plane direction are barely enough to hold them together. This is the reason that monolayer sheets could be formed just by mechanical exfoliation. Hence upon exfoliation and Van der Waals adhesion of the flakes on Si/SiO_2 substrates, 2D insulators like hexagonal boron nitride, monolayer-semiconductors like transition metal dichalcogenides and monolayer semimetals such as graphene are available in the research labs for exotic experiments.

Previously we discussed that hBN plays an important role in carrying the 2D material in its pristime form and also protecting them from environment. Hence by employing flat hBN flakes with the major support of Van der Waals forces (both discussed in next subsection), we could build heterostructures where a single-atomic layer of 2D material is encapsulated between 20 to 40 layers of inert hBN. This superstructure keeps the monolayer material in its 2D form without any influence of external factors. Similarly these VdW heterostructures can be built at will using any desired 2D materials equivalent to playing a two dimensional LEGO game. In this section, we will describe about the different methods to fabricate these VdW heterostructures.

1.5.1.1 Van der Waals (VdW) forces

Van der Waals forces were firstly described by Johannes Diderik van der Waals in the year 1873. These interactions are noncovalent type and are dependent on distance where they quickly vanish at the longer distances. This VdW interactions are characterized by power laws in the distance R between the two or more objects. It could be characterized either by a short range strong repulsive core with a R^{-12} dependence or a long range attractive tail with a R^{-6} dependence. With the absence of any other forces, the equilibrium position at which this force begins to be repulsive rather than attractive determines the Van der Waals contact distance.

To generalize, if the interatomic distance is greater than 0.6nm (approximately), the force is found to be not strong enough to be observed whereas as the interatomic distance becomes less than 0.4nm the force exhibits repulsive character. Van der Waals forces are one of the weakest interaction forces in nature with a strength just between 0.4 and 4 kJ/mol (compared to covalent bonds that are 1350 kJ/mol), but are very strong during the multitudes of such interactions. Recently it has been shown that VdW interactions exhibit wave-like charge density fluctuations

at the nanoscale.

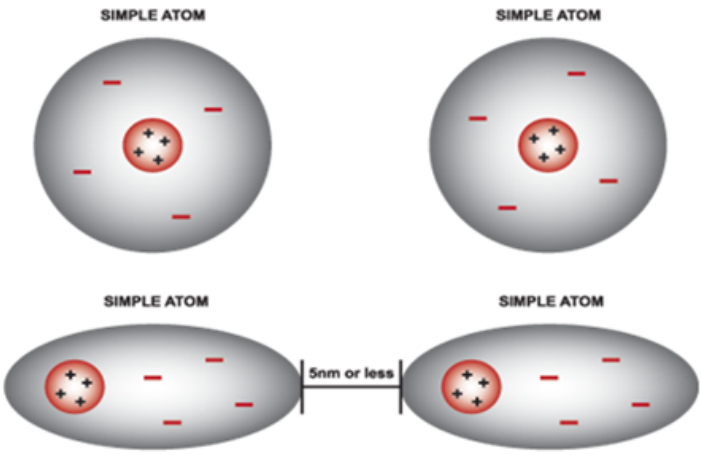

Figure 1.7 – Van der Waals force description resulting from attractive dipole-dipole interaction. (Figure adapted via agpa.uakron.edu)

Generally, there are four contributions for this intermolecular VdW forces. These include a repulsive component from Pauli exclusion principle, an electrostatic component (Kessom interaction) either attractive or repulsive arising due to charges, dipoles or quadrapoles, an attractive polarization interaction between the multipoles (Debye's force) and an attractive dispersion interaction (London dispersion) created by instantaneous multipoles.

However the classification of Van der Waals force is debatable as it has a composite origin. While some include only attractive forces, and others consider the totality of intermolecular forces including the repulsive ones. In this thesis, we consider only the attractive part of the VdW forces which promotes the adhesion between the surfaces that is the basic principle which enable the formation of artificial heterostructures.

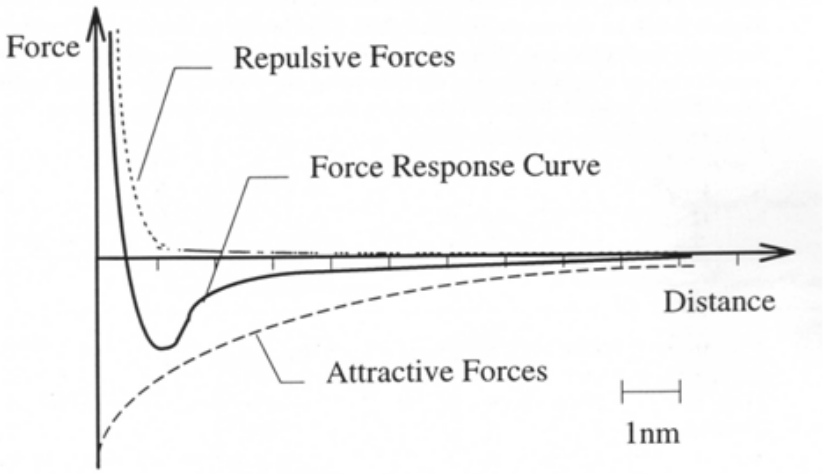

Figure 1.8 – Van der Waals force-distance curve description. The attractive force increases when distances between the interacting atoms increase until the point electron clouds touch each other where they repel electrostatically.

Van der Waals forces have some amazing characteristics such as their non-directionality, their independence against temperature, additive and unsaturable etc. However they are anisotropic and hence depend on the orientation of the objects (atoms, molecules, 2D layers) at stake. The polarization and dispersion interactions are always attractive irrespective of object orientation whereas the electrostatic interaction may change sign upon rotation. With these characteristics they can still support or hold together macroscopic mega-structures as the forces are additive.

Surface topography is another main parameter on which the VdW forces of adhesion depends upon. If there are surface asperities which provide larger area of contact, then VdW forces of attraction are higher. However the presence of impurities of any other kind could be unfavourable. These forces are effective when surface contact area is maximised. VdW forces affect flat surfaces and play a very important role during the assembly of complex heterostructures.

1.5.1.2 Hexagonal Boron Nitride (hBN), the work horse of 2D VdW heterostructures

Boron Nitride is a compound made of Boron and Nitrogen which has isoelectronic structure similar to that of Carbon lattice. The hBN is the most stable structure corresponding to graphite of Carbon where each layers are made of sp^2 conjugated boron and nitrogen atoms in a honeycomb structure, whereas the layers are held by weak van der Waals forces. hBN appears as white, inert and has excellent thermal, chemical stability and dielectric properties. hBN nanosheets are electrical insulators with a wide indirect bandgap[6] of 5.9eV which had lead to its usage in 2D electronics such as gate dielectrics and substrates. Recently it has been discovered that it is the best substrate to hold graphene owing to its similar lattice constant to that of graphene and hence it is used as a work horse to form heterostructures due to its affinity towards polymer films.

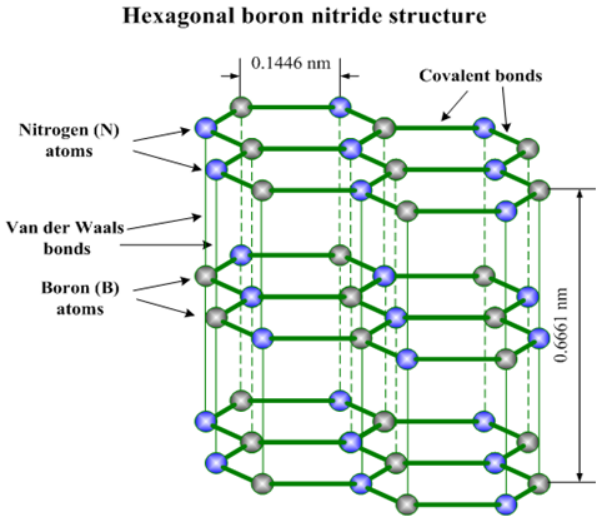

Figure 1.9 – Lattice structure of hexagonal Boron Nitride showing similar structure to that of graphene. The lattice mismatch with graphene is only 1.7%. Figure adapted from [7]

1.5.1.3 VdW heterostructures obtained by direct growth

After the discovery of graphene by exfoliation, there were plenty of research works going on after, to grow the monolayer 2D materials directly on the intended substrate. This was done using different types of chemical vapor deposition (CVD) and epitaxial methods. Many research

groups used metallic substrates because of their catalytic properties and were successful in producing graphene, MoS2 and many other 2D materials. However the problem was that they could not be directly used for experiments or applications as they were on metallic substrates. Since the growth on desired silicon or silicon oxide substrate was difficult, many solutions were devised to transfer them on to the desired substrates.

In Keun Soo Kim et al [8], they grew graphene on nickel layer and used PDMS film to hold on to the graphene, etch off the nickel and stamp it on the desired substrate. In another technique, they also etched the nickel film and fished the graphene floating on the solution. Various groups have made growth of graphene on copper sheets, spin coated PMMA on the graphene, etched the copper, fished the graphene on desired substrates and finally removed the PMMA on the graphene. The disadvantage of these methods are that they could not reach the minimal level of purity and kinetics of growth was another problem. Though several groups did excellent experiments with these 2D materials but fell short of their initial predicted potential by different theories. So the need of the hour was to develop transfer methods to preserve the intrinsic cleanliness of 2D-materials.

Recently, many experimetalists have succeeded in growing 2D materials directly on required substrates and even on hBN flakes. Shown in the figure 1.10 is graphene/hBN heterostructure by direct growth using CVD technique in our group. However it required further in-depth studies for direct growth of large scale heterostructure by CVD, ALD or epitaxial techniques.

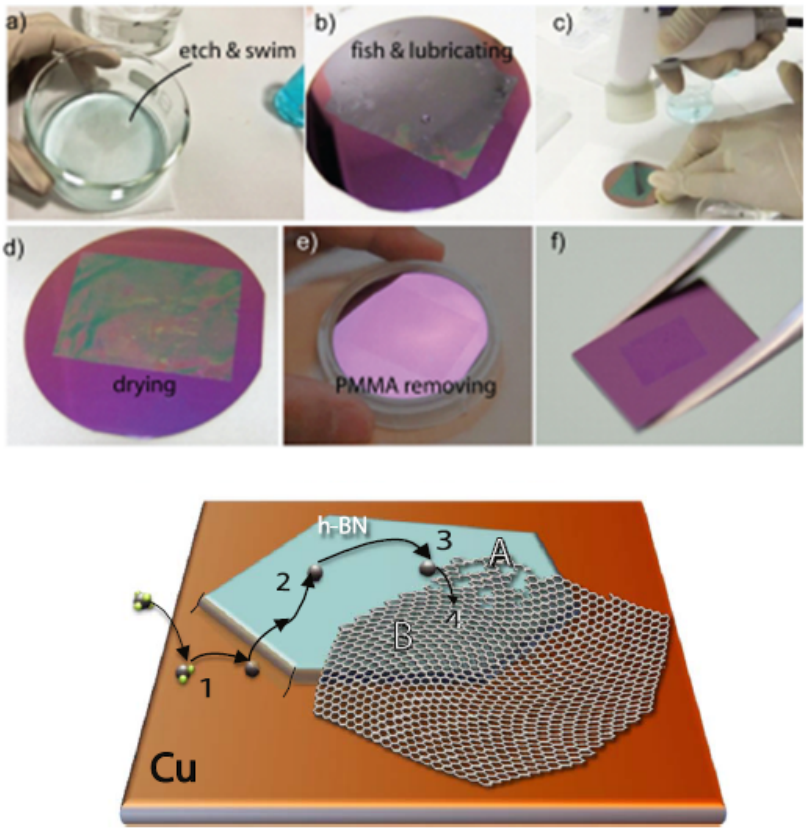

Figure 1.10 – (Top) Van der Waals heterostructures prepared by growth on metal followed by transfer to oxidized silicon wafers. (Bottom) Heterostructures produced by direct growth of graphene on hBN. Figure adapted from [9] [10]

1.5.1.4 VdW heterostructures by exfoliation and polymer transfer

With the advancement of smart transfer methods and innovation of atomically flat substrates, the first Van der Waals heterostructure was build by Dean et al [11] where exfoliated graphene was transferred on to an exfoliated hBN to form a graphene/hBN heterostructure. Boron Nitride having almost similar lattice, insulating large bandgap, inert and free of dangling bonds or surface charge traps, atomically planar surface became the most appealing and suitable substrate to bring the real predicted potential of graphene. They used a similar but upgraded transfer technique where PMMA was coated on graphene later separated from the substrate using a water-soluble layer. They aligned this graphene on PMMA on the intended hexagonal-Boron Nitride with the help of a glass plate and finally removed the PMMA. Electron transport measurements of graphene in these heterostructures showed electron mobilities three times higher than that of graphene on silicon oxide indicating the decrease in scattering caused by the charged impurities. Moreover , the Quantum Hall effects were observed at lower fields, more than a factor of two compared to that of graphene on SiO_2.

The employment of hBN as high quality ultra flat substrate for graphene was confirmed by scanning tunneling microscopy and spectroscopy by LeRoy group.[12] Just by using the hBN as a high quality substrate many new properties of graphene appeared or were found out by different research groups. At higher magnetic fields, multi-component fractional Hall effects were reported in graphene by CR Dean et al.[13] Multiple Dirac points were observed in graphene due to leakage of the insulating properties from the hBN into graphene when both are oriented at specific tilt angles.[14] This further opened a new branch in physics called Moiré superlattices and structures in which the additional periodicity gives to the material novel electronic properties.

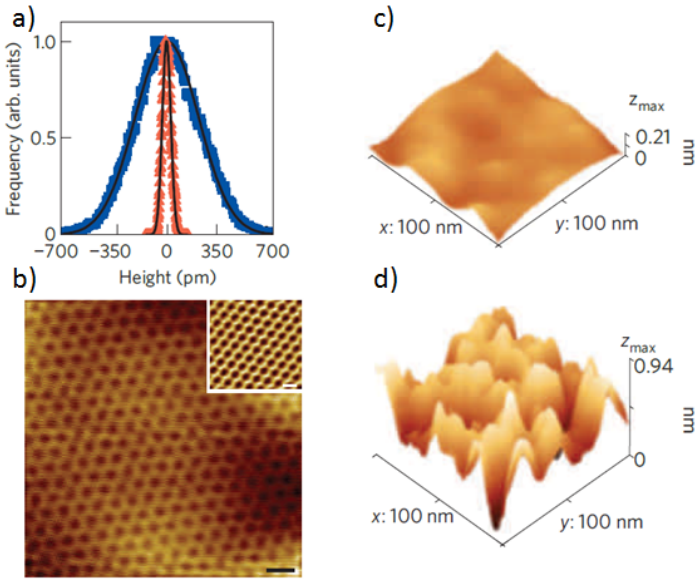

Figure 1.11 – (a)Histogram of the height distributions for graphene on SiO_2 (blue squares) and graphene on hBN (red triangles) along with Gaussian fits. (b)STM topographic images of a Moiré pattern produced by graphene on hBN. The scale bar is 2 nm. The inset is a zoomed region of 2nm area with a scale bar of 0.3 nm. (c) STM topographic image of monolayer graphene on hBN showing the underlying surface corrugations and d) monolayer graphene on SiO_2 showing increased corrugations. Figure adapted from [12].

This concept of VdW forces keeping the layers together has given rise to a new emerging

field of research called van der Waals heterostructures. These hetero-structures are artificially assembled structures with quality matching those of molecular beam epitaxy (MBE). This extraordinary process of making heterostructures opened a completely new field in 2D physics to fabricate high quality devices for transport to imaging and optics to applications. The idea in this VdW heterostructure is pretty simple to put one monolayer on the top of another monolayer or multilayer to form a stack which is made artificially.

This artificial assembly method gives you the additional freedom to choose any 2D materials and build up atomically flat 2D heterostructure which has been compared to atomic scale structure construction by A.K Geim et al.[1] Different methods or processes have been proposed and demonstrated to build these heterostructures in both large scale and small scale areas. There are several polymer based transfer techniques such as Polycarbonate PC method [15], PDMS viscoelastic stamping method [16] and polypropyl carbonate (PPC) method[17] to name a few.

The state of the art method is a Van der Waals attraction based pickup technique to make heterostructures using polymer called polypropyl carbonate[17]. In this technique, the quality of graphene/2D material is maintained prisitine as none of the polymer or wet chemicals come in contact with graphene. Hence graphene was encapsulated between two pristine, inert and insulating hBN flakes to overcome the charged substrate effects and also to protect the graphene from the possible environmental impurities on the top. One of the major challenge in these kind of structures were to provide good metal contacts to graphene to observe its potential intrinsic properties.

Further state-of-the-art high quality electrical contacts were realized again by C.R.Dean group [17] to provide graphene one dimensional electrical contacts where graphene edges were exposed by etching. Similar method is utilized to prepare the devices in this thesis and explained in the device fabrication section of chapter 2 in detail. With this architecture graphene has been found to manifest mobility up to few million cm^2/Vs allowing for ballistic transport of over 15 micrometers at low temperatures.

Another method called PDMS viscoelastic stamping method allows us to build the heterostructures quickly in time.[16] In this method, the 2D materials are directly exfoliated on the PDMS, aligned and stamped on another desired 2D material or any other substrates. This method enables us to build very large heterostructures. However, the disadvantage of this transfer technique is that the 2D material is in contact with the polymer PDMS and hence the prisitinity is not preserved. Nevertheless, major areas are clean to fabricate the required devices for measurements. This PDMS-method of stamping has been used and will be further presented in chapter 3 of this thesis.

In this thesis, we predominently use the so-called PPC transfer technique for assembling ultra-clean heterostuctures as well as PDMS transfer technique for large scale heterostructures. In chapter 4, we will compare the cleanliness and the quality of the heterostructures prepared using these two polymer transfer techniques.

1.5.2 Nanocomposites

Nanomaterials like nanotubes, fullerenes, graphene or other 2D materials could be used as ideal fillers in a matrix of a macroscale bulk material such as polymers or metals. The resulting nanocomposite is formulated to improvize one of the physical property of the bulk material. Van der Waals forces and hydrogen bonding also play an important role here where it could enhance or degrade the formation of such nanocomposites. If proper care is not taken, then

the nanomaterial fillers could agglomorate due to VdW attraction and destroy the purpose of nanocomposites. There were many theoretical and experimental reports where nanomaterials such as graphene, CNTs etc.. were used as nanofillers in different polymers such as PVA, nylon etc.. using various artifical processing methods. It was found out that by adding just a little quantity of nanomaterials, the mechanical properties can be boosted significantly. This high perfomance triggered rapid studies on nanocomposites.

During the studies, it was noted that there were issues of adhesion and dispersions which resulted in low-tensile loading and weak interfacial interactions, when higher quantity of nanomaterials were added. These issues in traditional polymer nanocomposites inspired to study the natural polymer fibers like cotton, Spider silk and Bombyx Mori silk, which then finally resulted in studies of bio inspired polymer nanocomposites. Further, these bio-inspired polymer nanocomposites can be processed using different techniques from artificial methods to natural systemic one where in particular, a living organism is used in preparing the composite as explained in the next subsections.

1.5.2.1 Nanocomposites by artificial processing methods

As explained before, many low dimensional nano-objects have been incorporated into natural polymers to enhance their mechanical properties. For these artificial processing methods such as layer-by-layer, evaporation, filtration, freeze casting, hydrogel casting and electrophoretic deposition have been employed to realize a homogeneous dispersion and good interfacial interactions. One of the nice example is silver nanoparticles that are homogeneously dispersed in the cotton fiber. This unique inorganic-organic hybrid structure changed the fiber morphology and demonstrated significant increase in tenacity and brittle failure behaviour.[18]

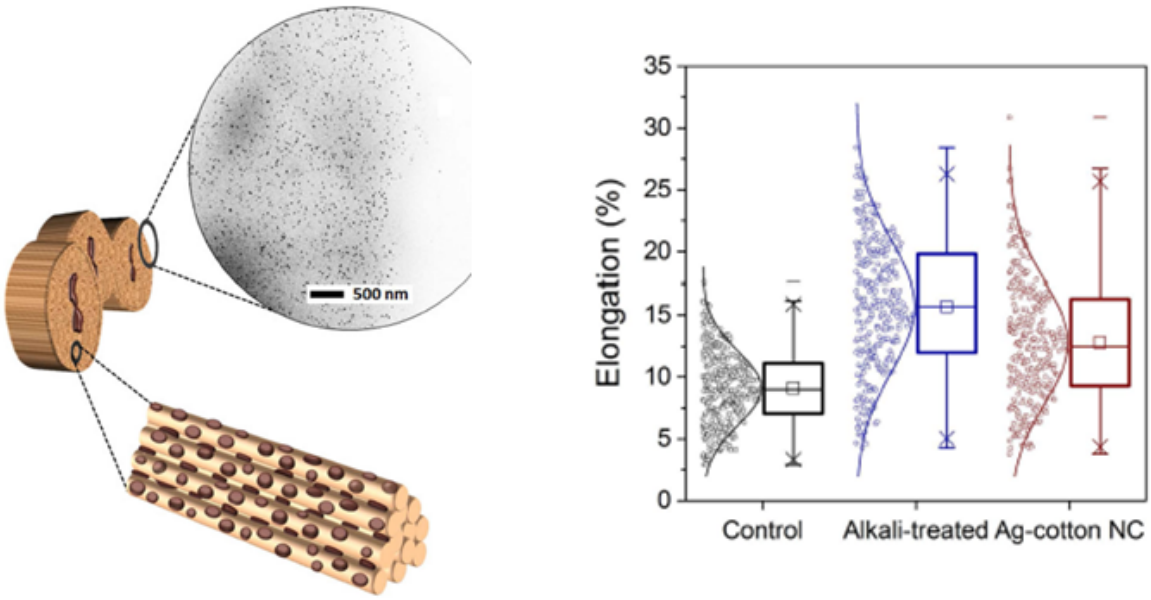

Figure 1.12 – (left) Schematics of the microfibrillar structure of cotton fiber modified by the in-situ synthesis of the silver nanoparticles and TEM images of the same. (right) Elongation for control, alkali treated and silver nanoparticle doped cotton. Figure adapted from Sunghyun Nam et al.[19]

However, these nanocomposites have their own disadvantages such as large scale production and precise control of the structures. Hence new methods have been identified where nanostructures are incorporated by natural method into these natural polymer fibers.

1.5.2.2 Nanocomposites by natural systemic approach

The novel method to integrate the nanomaterials into fiber is natural systemic approach. In this method, the low dimensional materials are fed to bio-organisms that prepare the natural fibers. By ingesting the nanomaterials, these bio organisms produce natural polymer fibers integrated with nanomaterials. The method is very facile and several experiments have reported that the mechanical properties have improved significantly. One such example is a reinforced spider silk, where spiders were fed with CNT and graphene resulting the production of CNT/Graphene spider silk with enhanced mechanical properties.

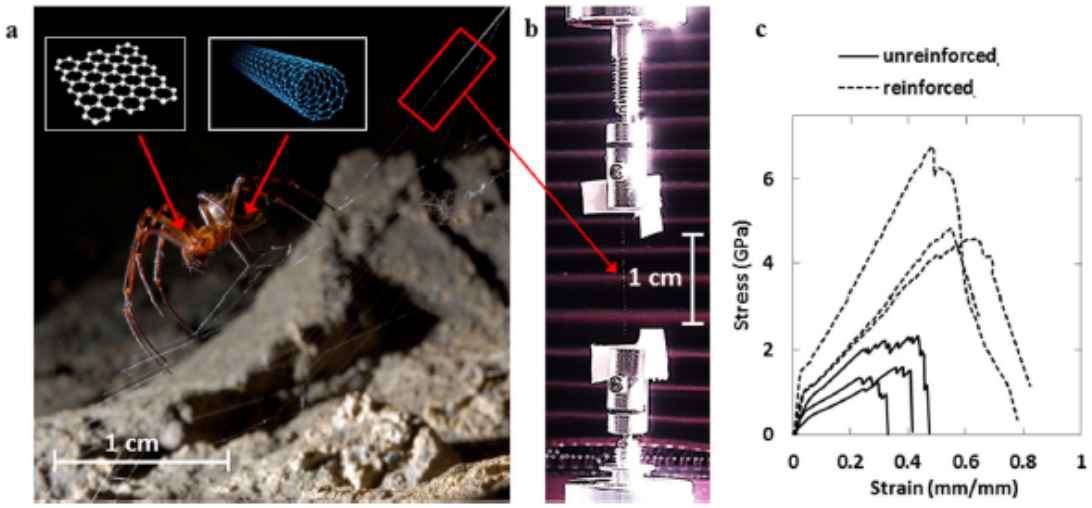

Figure 1.13 – a)Schematics of spider producing silk integrated with graphene and CNTs. b) Tensile-load set-up c) The stress-strain experiments for reinforced fibers show a significant increase in mechanical properties compared to the control spider silk fibers. Figure adapted from Emiliano Lepore et al.[20]

In the chapter 5 of this thesis, a similar approach has been adopted, where CNTs were sprayed on mulberry leaves and were fed to Bombyx Mori silkworm. These silkworms digest the leaves along with the low diamter (1nm) single walled carbon nanotubes (SWCNT) to produce the silk embedded with SWCNTs. The hence obtained SWCNT silk is expected to have improved mechanical properties. In the chapter we characterize the silk to confirm the presence of SWCNTs. We also perform characterizations to check the differences in structure of the SWCNT silk and probe if the mechanical properties indeed have improved.

Chapter 2

Novel technique to probe defects of the bulk in quantum Hall regimes in hBN/graphene/hBN heterostructures

Contents

2.1 Brief Introduction to the chapter 30
2.2 Electronic properties of Graphene 31
2.2.1 Crystal structure 31
2.2.2 Electronic band structure 32
2.2.3 Field effect properties 34
2.3 Sample fabrication 36
2.3.1 Mechanical exfoliation and identification of graphene and hBN 36
2.3.2 Stack preparation recipe using PPC Method 39
2.3.3 Nanofabrication of edge-contacted devices 45
2.4 Dilution fridge measurement technique 53
2.5 Quantum electron transport in the quantum Hall regime 54
2.5.1 Classical motion of electron in a magnetic field 54
2.5.2 Shubnikov de Haas effect 55
2.5.3 Landau quantization 56
2.5.4 Integer Quantum Hall effect 58
2.5.5 Relativistic iQHE in graphene 61
2.5.6 Devices and iQHE measurements 63
2.5.7 Ballistic transport and Landau-Buttiker formalism 66
2.6 Fractional Quantum Hall effect 67
2.6.1 Laughlin theory 68
2.6.2 Composite fermions 69
2.6.3 The curious case of 3/2 and 5/2 states 70
2.6.4 Fractional states in graphene 71
2.6.5 Fractional states in graphite backgated hBN encapsulated devices . . . 72
2.7 Noise in quantum devices 73
2.7.1 Different types of noise in electron devices 74
2.7.2 Low frequency 1/f noise 75

2.7.3 1/f measurement technique 78
2.7.4 1/f noise measurement in graphene 80
2.7.5 1/f noise in iQHE and fQHE regime 82
2.8 Conclusions and perspectives 86
2.8.1 Conclusions 86
2.8.2 Quantum point contacts for shot-noise measurements 86
2.8.3 Fabry Perot interferometers 87

2.1 Brief Introduction to the chapter

Graphene is an atomically-thin lattice of carbon atoms. Discovered in 2004 by K.Novoselov and A.Geim at University of Manchester, it is the world's first two dimensional material [21] and was soon found to display outstanding physical properties. In particular, the sp^2 hybridization of carbon lattice known to exist in graphite is preserved down to the monolayer. This property combined with quantum confinement associated to the reduced dimension, gives to graphene zero-bandgap semiconducting properties in a 2D gas of high mobility charges with electrostatic control of the density of charge carriers[22], a linear band structure and relativistic massless Dirac fermions. Such properties have attracted a huge interest in the community and culminated with the Nobel prize awarded to the discoverers in 2010.

Graphene is stable in air but, as a material without any bulk and thus reduced to two surfaces, its properties are super-sensitive to the environment and those can be strongly affected by adsorbates and interfacial charges. Also graphene usually needs a substrate as support and it has been found that properties of graphene are extremely dependent on the quality of the substrate used [23]. In order to bring in its intrinsic properties, the graphene layer can be suspended [24] to decouple it from its environment but with this solution it is very cumbersome to fabricate, not fully scalable and have limited gate control.

As explained in the introduction chapter, hexagonal boron nitride (hBN) flakes have been found to behave as ideal substrates [11]. Unlike silica, they do not have have any dangling bonds nor charged adsorbates and their lattice symmetry and parameters are similar to graphene. Such properties associated with a full encapsulation strategy [17], greatly help graphene to maintain his pristine electron transport properties. Ballistic transport combined with the specificity of Dirac fermions has lead to a complete new range of electronics devices where electrons trajectories behave like optical beams. [25]

In this chapter, we are going to present the design, fabrication methods and characterization of edge-contacted hBN-encapsulated graphene devices suitable for high-quality quantum electron transport. These state-of-the-art devices show charge mobilities reaching one million $cm^2/V.s$ at very low temperature. The Integer quantum Hall effect (i-QHE) together with the fractional quantum Hall effect (f-QHE) that is observed under high magnetic fields are further proofs for the high quality of these devices. As a further development beyond the current state-of-the-art, we present preliminary results of a novel technique to further investigate the nature of charge carrier, especially in the regime of f-QHE by studying the noise behaviour in graphene in the low frequency regime.

2.2 Electronic properties of Graphene

This section gives a short overview about structure and properties of graphene regarding its crystal lattice, dispersion relation with complete band structure and resulting electric field effect. It is based on references [26][27] where more detailed explanation can be obtained.

2.2.1 Crystal structure

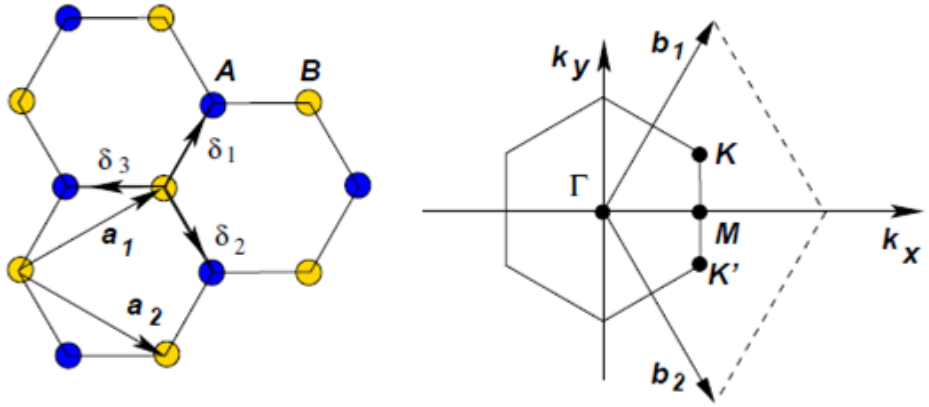

Figure 2.1 – Graphene lattice represented in real-space and reciprocal space. (Left) Lattice structure of graphene, made out of two interpenetrating triangular lattices. (a_1 and a_2 are the lattice unit vectors, and δ_i, $i = 1, 2, 3$ are the nearest neighbour vectors.) (Right) Corresponding Brillouin zone of graphene with two Dirac points located at the K and K' points. Figure adapted from Castro Neto et al. [26]

Graphene lattice is composed of carbon atoms arranged in a honeycomb structure where neighboring carbon atoms (blue dots and yellow dots) withstand inequivalent cristalline environment. As a consequence, it can be described as two inter-twinned triangular lattices A and B with two atoms per unit cell. One has to note, however, that the honeycomb lattice is not a Bravais lattice as this latter can be seen as the rombi defined by a_1 and a_2 vectors. The atoms in graphene occupying the two sublattices are identical. The existence of these two sub-lattice has important implications to its electronic band structure.

The vector a_1 and a_2 represent the corresponding basis of the Bravais lattice given by:

$$a_1 = \frac{a}{2}(3, \sqrt{3}), a_2 = \frac{a}{2}(3, -\sqrt{3}). \tag{2.2.1.1}$$

The nearest neighbour vector δ_1, δ_2 and δ_3 are:

$$\delta_1 = \frac{a}{2}(1, \sqrt{3}), \delta_2 = \frac{a}{2}(1, -\sqrt{3}), \delta_3 = -a(1, 0). \tag{2.2.1.2}$$

The reciprocal lattice is also a hexagonal structure but rotated by $\pi/2$ in comparison to real space lattice. The corresponding first Brillouin zone with its centre Γ and the reciprocal vectors b_1 and b_2 given by:

$$b_1 = \frac{2\pi}{3a}(1, \sqrt{3}), b_2 = \frac{2\pi}{3a}(1, -\sqrt{3}). \tag{2.2.1.3}$$

As shown in the figure 2.1 the Brillouin zone (BZ) comprises of two in equivalent points K and K' at corner where Dirac cones are located and their momentum space coordinates are given by:

$$K = (\frac{2\pi}{3a}, \frac{2\pi}{3\sqrt{3}a}), K' = (\frac{2\pi}{3a}, -\frac{2\pi}{3\sqrt{3}a}). \tag{2.2.1.4}$$

2.2.2 Electronic band structure

Graphene exhibits sp^2 orbital hybridization which constitutes in a combination of orbital s, p_x and p_y that forms an σ-bond with each of its three neighboring carbon atoms. The carbon–carbon σ-bonds are 0.142 nm long and are 120 degrees apart. These very strong bonds are responsible for the planar structure of graphene and for its exceptional mechanical and thermal properties. The remaining p_z electrons make up the π-bond that is oriented out of plane.

These π-bonds hybridize together to form the π-band and π^*-band. Each carbon atom contributes one electron to this band so that it is only half filled. Hence due to these delocalized π-electrons over the full area, graphene exhibit a surface exposed 2D electron/hole gas of high mobility. The anomalous electronic properties of graphene is due to its 2D structure, honeycomb lattice and the fact that all the sites on its honeycomb lattice are occupied by the same atoms, which introduces inversion symmetry.

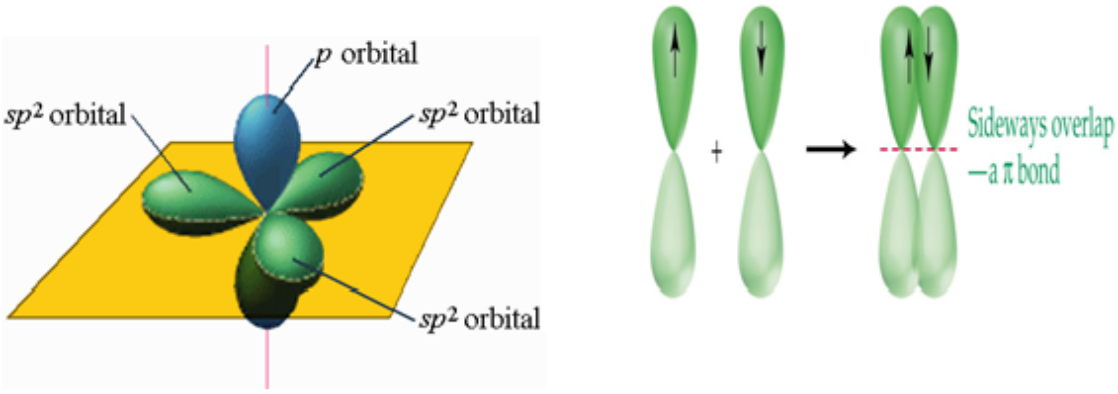

Figure 2.2 – Depiction of sp^2 hybridization in graphene with σ-bonds(left) and π bonds(right). Figure adapted from [28]

Band structure due to these π-band electrons in graphene is approximated by tight binding approach. In this model an electron can hop between the nearest neighbor(nn) and the next nearest neighbor(nnn). When we consider an independent atom, its wavefunction is $\phi^a(r)$. But in a crystal lattice, atoms are not independent and hence on the application of Bloch wavefunction, we obtain:

$$\psi_k(r) = \sum_{R_j} exp(ik.R_j)\phi^{(a)}(r - R_j), \tag{2.2.2.1}$$

where $R_j = m_j a_1 + n_j a_2$ are the Bravais vectors of the lattice.

Also in graphene the unit cell has two atoms and two sublattices A and B. There is lack of symmetry between these sublattices and hence must be considered separately represented by different wavefunction. The trial wavefunction of the two electrons would be:

$$\psi_k(r) = a_k\psi_k^A(r) + b_k\psi_k^B(r). \tag{2.2.2.2}$$

where a_k and b_k are complex wavefunction of the wave vector k.

The solution of time dependent Schrödinger equation gives the energy dispersion:

$$\hat{H\psi}_k(r) = \epsilon_k\psi_k(r). \tag{2.2.2.3}$$

The energy dispersion relation takes the form of:

$$\epsilon_k^\lambda = 2t'_{nnn}\sum_{i=1}^{3}\cos(k.a_i) + \lambda t_{nn}\sqrt{3 + 2\sum_{i=1}^{3}\cos(k.a_i)}. \tag{2.2.2.4}$$

where t_{nn} is the nearest neighbor hopping amplitude and t'_{nnn} is the effective nnn hopping amplitude considering the overlap correction yielding the renormalized hopping amplitude. $\lambda = \pm 1$ corresponds to two solutions representing the two bands, conduction band (π^*) and the valence band (π) respectively.

As we could see from the figure 2.3 the valence and the conduction band touch at the point where the equations ϵ_k^λ become zero. The valence band is filled with electrons and the conduction band is empty , then the Fermi level is located above the last filled state at the point where equation ϵ_k^λ is zero. These points are called as Dirac points.

Hence there are six Dirac points out of which only two are independent and are represented as K and K'. If we expand the equation 2.2.2.4 around K point until the second order in qK with $k = K+q(\mid q \mid \ll K)$, the dispersion relation can be linearised in the vicinity of Dirac point under the long wavelength limit and low energy excitations. Thus we obtain first order approximation:

$$E_\pm(q) = \lambda\bar{h}v_F \mid \vec{q} \mid \tag{2.2.2.5}$$

where $v_F = 1 \times 10^6$ m/s is the Fermi velocity.

This equation 2.2.2.5 indicates the existence of two Dirac points K and K' where the linear energy bands of electrons and holes touch with no energy gap leading to two fold valley degeneracy in graphene. This linear energy dispersion appears similar to that of relativistic particles whose dynamics could be described by massless Dirac equations. The group velocity of charge carriers is independent of energy unlike the parabolic dependence of energy in case of two dimensional electron gas in III-V heterostructures (2DEG).

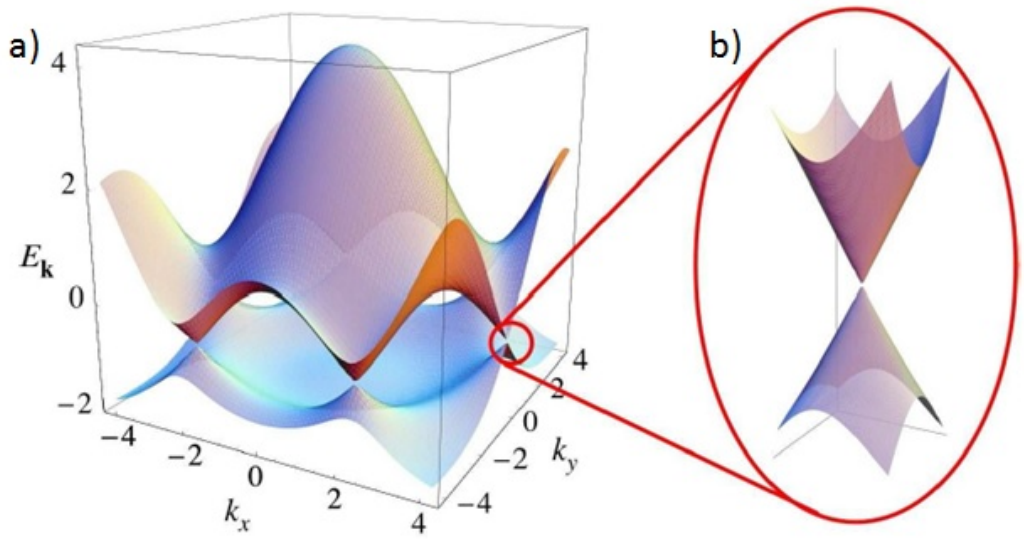

Figure 2.3 – (a) Graphene band structure. (b) Zoom in to low-energy dispersion at one of the K points shows the e–h symmetric Dirac cone structure crossing the zero energy plane. Figure adapted from A. Castro-Neto et al.[26]

2.2.3 Field effect properties

The figure 2.4a describes the electrical field effect behavior in graphene. The inset shows conical low-energy spectrum E(k) of graphene, indicating changes in the position of the Fermi energy E_F with changing gate voltage V_g. Positive V_g induce electron-doping while negative V_g induce hole-doping . This implies that graphene exhibits a strong ambipolar electric field effect such that charge carriers can be tuned continuously between electrons and holes in concentrations up to few $10^{13} cm^{-2}$ and room-temperature mobility up to 50,000 cm^2/Vs can be induced by applying a gate voltage (for example of a few tens of volts on the back-substrate) .

As shown in the figure 2.4a, under negative gate bias, the Fermi level drops below the Dirac point, introducing a significant population of holes into the valence band; while under positive gate bias, the Fermi level rises above the Dirac point, promoting a significant population of electrons into the conduction band. The rapid decrease in resistivity ρ on adding charge carriers indicates their high mobility.

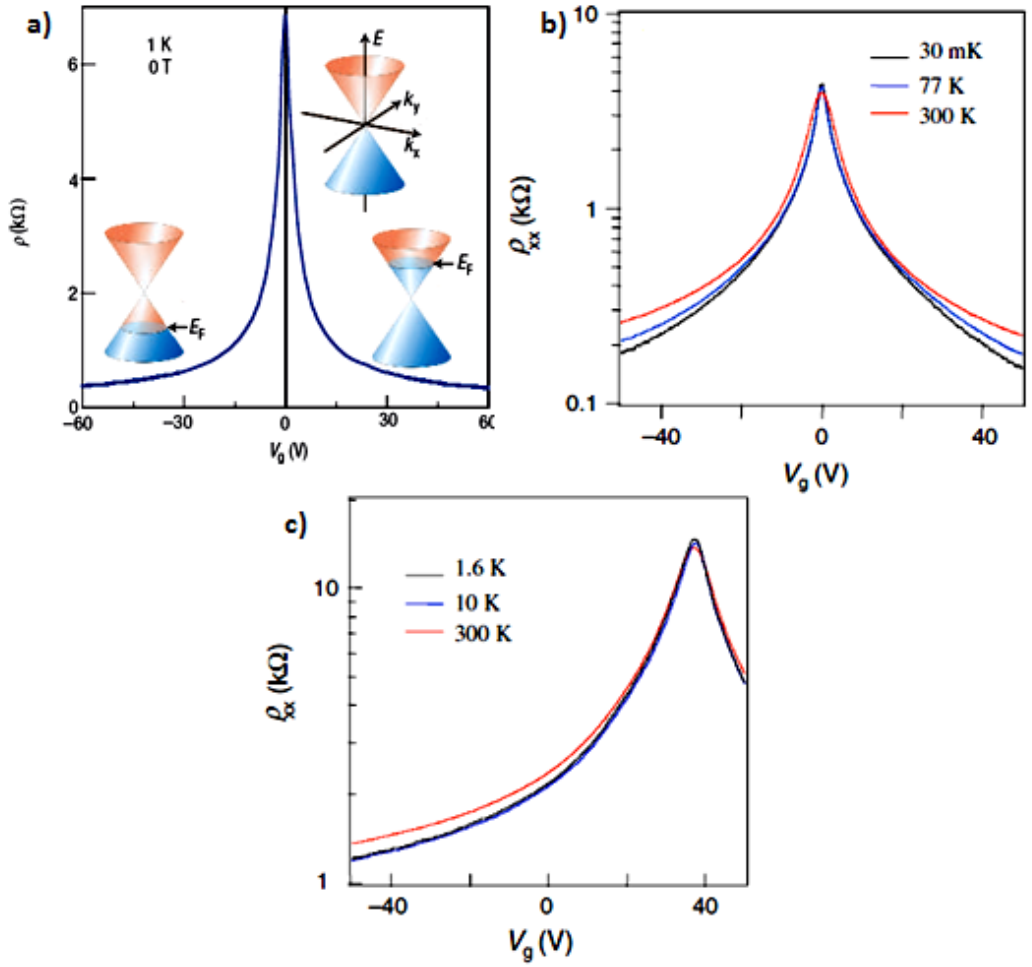

Figure 2.4 – (a) Ambipolar field effect in mono-layer graphene . (b) The gate voltage and temperature dependence of resistivity of the high mobility sample ($\mu = 20,000 cm^2/Vs$), ρ versus V_g at three temperatures, $T = 0.03K$, 77K, and 300 K.(c) The gate voltage and temperature dependence of resistivity of the low mobility sample ($\mu = 2,000 cm^2/Vs$), ρ versus V_g at three temperatures, $T = 0.03K$, 77K, and 300K. Adapted from Geim et al [2] and Y-W. Tan et al.[29]

Moreover as shown in the figure 2.4b, the observed mobility weakly depends on temperature, which means that mobility at 300K is still limited by impurity scattering and therefore can be improved significantly. From the peak position in resistance, we obtain a corresponding gate voltage for the charge neutrality point. A finite value of this indicates an unintentional doping of the graphene samples whose origin may be from electrostatic effects caused by surface charged impurities.

In the figure 2.4c for low mobility sample, the Dirac point is shifted to a large positive gate voltage value. Such a large shift of the charge neutrality point indicates that there is heavy doping of the sample due transferred charges from the environment. Ionized charge traps in the substrate or adsorption of molecules on the graphene surface may locally induce a chemical doping that might be partly responsible for the low mobility observed in this sample.

2.3 Sample fabrication

This section gives the complete process flow for fabricating graphene devices from flakes preparation to bonding the device pads. As explained in the introduction chapter, to improve its mobility graphene has been encapsulated into two thin atomically flat hBN flakes and are provided with one dimensional contacts. This preparation of Van der Waals heterostructure will be discussed in deep to obtain a stable recipe. The difficulties experienced during critical step of etching for the realization of 1D contacts would be discussed. Also state-of-art lithography techniques used to fabricate these devices will be shown in detail.

2.3.1 Mechanical exfoliation and identification of graphene and hBN

During the mechanical exfoliation, a natural graphite crystal is placed in a scotch tape, pressed together and peeled repeatedly to obtain thinner layers of graphite. Nobel prize winners A.Geim and K Novoselov were the first to introduce this method to obtain monolayer Graphene. In our case we use a 3M Magic scotch tape in which a $1mm^2$ size piece of crystal is placed on adhesive side, folded and pressed beside itself repeatedly without gaps or overlaps to obtain a homogeneous square like structure as shown in the figure 2.5. This structure on the scotch tape could be attached to any desired substrate and peeled down slowly at different angles to which leaves behind some of the flakes on the target substrate out of which some would be monolayers. We also use application of heat up to 100°C while peeling to obtain larger flake coverage on the substrates.

Figure 2.5 – Homogeneous square-like structure of flakes obtained after repeated exfoliation steps on the same scotch tape

Variety of substrates could be used as the host substrate after rubbing of scotch leaving behind the ultrathin flakes. These can be Si /SiO_2 substrate, metals like copper, quartz, glass or even polymers like PDMS. It is very important to start with very clean and high-quality substrate for exfoliation to obtain clear-cut clean flakes. Generally highly-doped Silicon with 290nm of SiO_2 as capping oxide is used as a common substrate in labs for fabricating devices. There are two basic but important advantages in using this substrate. The structure of SiO_2 capping layer acts as a dielectric which is convenient to be used a gate oxide during applicaiton of a voltage on the substrate. Another advantage is that 290nm of SiO_2 is at a sweet spot for optical interfererometry so that monolayers of graphene deposited on top could be identified with ease with an optimized contrast [30].

As said before, to obtain ultra clean Si/SiO_2 substrates several methods are employed. These Si/SiO_2 wafers are cut into $1cm \times 1cm$ squares and while cutting using a diamond cutter, care is taken that none of the residue fall on the surface which may change the surface adhesion of the substrate. Any particles or residues are detrimental for exfoliation or for the future steps of fabrication. If the substrates are maintained clean while cutting, then virgin substrates could be used for exfoliation without the need of cleaning it.

In case there are Si/SiO_2 particles everywhere, then it needs cleaning procedures. Several complicated cleaning procedure such as RCA cleaning, Piranha solution, Nitric acid based cleaning are being employed to obtain a clean substrate. In our case we use a simple method where we ultrasonicate the substrates in acetone for about 5 mins followed by rinsing in iso propyl alcohol (IPA) for a minute. The substrates were then dried by blowing with Nitrogen gas. Further sometimes a minute of 10 Watt oxygen plasma is carried out to get ultra clean substrates with hydrophilic properties.

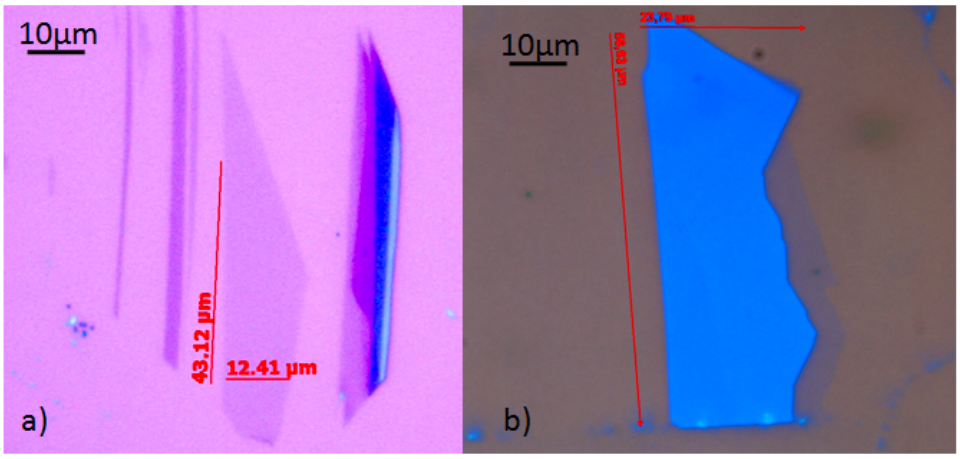

Figure 2.6 – a) Optical image of monolayer graphene mechanically exfoliated on Si/SiO_2(290nm) substrate. Visible contrast is maintained down to the monolayer. b) Optical image of 20nm-thick hBN flake mechanically exfoliated on Si/SiO_2(290nm) substrate.

Selection of flakes with proper size, homogeneity and color is a critical step before preparing a Van der Waals heterostructure. In our graphene devices, we need strictly monolayer graphene and few layer hBN about 20 to 25nm in thickness. Optical microscopy is the technique that is usually used to identify the monolayers. Based on contrast difference and color, it is easy after a while, to identify with rapid visual inspection under a simple optical microscope strictly monolayered flakes with reasonable yield. While the monolayer graphene appears as a faint purple or violet in colour as shown in the figure 2.6a, with increase in thickness the colour turns out to be darker version of violet.

Further we could use a more reproducible and quantitative approach to establish correspondence between optical contrast and number of layers for a given material (graphene, hBN, but also dichalcogenides...) and illumination. Note that it is easier to identify the adequate hBN flakes as, for our usage, thickness uncertainty of ±5nm have little to no significance on the device properties.

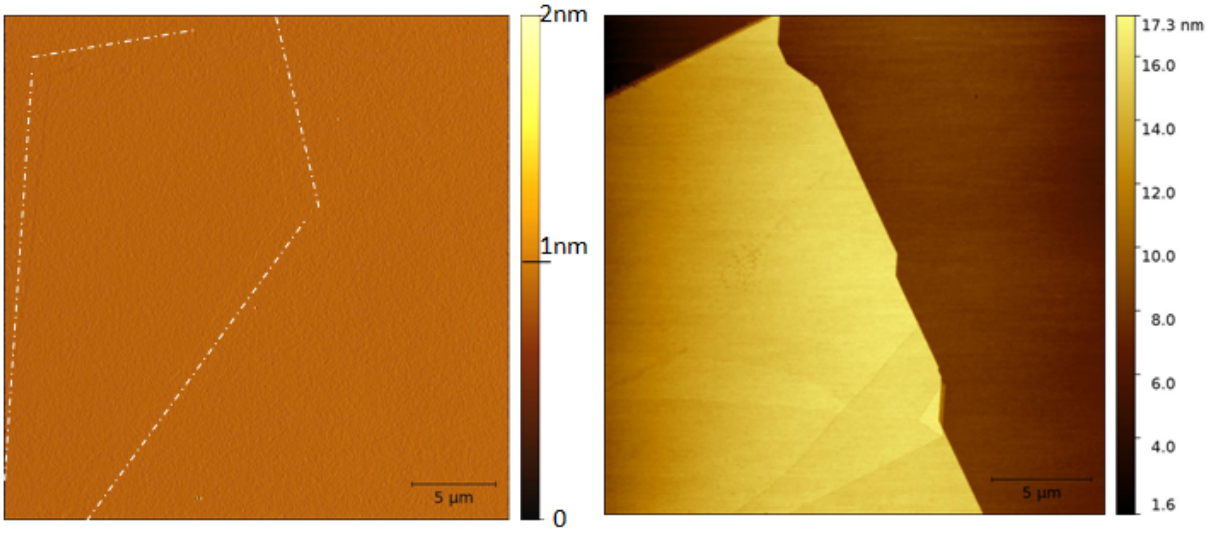

Figure 2.7 – AFM topography image of ultra-clean graphene(left) and hBN flakes(right).

In order to further confirm the monolayer nature of graphene, Raman spectroscopy (explained in detail in next chapter) could be used. When excited with green laser 532nm , monolayer graphene has a characteristic Raman signature as shown in the figure 2.8. There are two peaks around 1580cm^{-1} and 2700cm^{-1} which are assigned to G band and 2D band of graphene respectively. Furthermore absence of defect peak D at 1350cm^{-1} indicates the high quality of graphene without defects or disorder. The single peaks with full width at half maximum which is around 22cm^{-1} confirms that the graphene is single layer. In case of bilayer graphene the full width at half maximum of 2D peak broadens to be above 40cm^{-1} as the peak starts to divide into two.

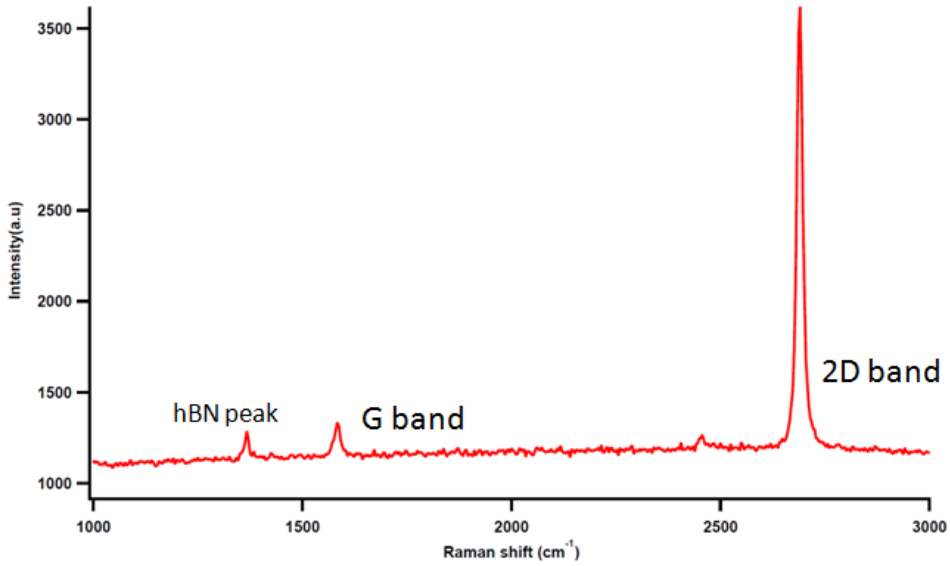

Figure 2.8 – Raman spectrum of hBN-encapsulated graphene, exhibiting characteristic G and 2D band of monolayer graphene and signature of hBN peak.

In the previous paragraphs, we have emphasized the importance of cleaning substrates. While super-clean substrates are important as starting materials, the cleanliness of the exfoliated flakes deposited on top are equally crucial for good devices. All the optically identified

flakes that are suitable for preparing a heterostructure are then scanned using Atomic Force Microscopy (AFM) to determine their flatness and tidiness. Any flakes contaminated with scotch tape glue residues or with any other particle impurities are rejected from the further steps of fabrication. Only atomically-flat and residue-free hBN flakes of thickness of about 20 to 25nm are selected. Another bare minimum criteria for selection of the hBN flakes is that they should be larger in size than the monolayer graphene which are used to make the stack so that they are fully protected. hBN flakes produced from the crystals provided by our collaborators (K. Watanabe and H. Taniguchi at NIMS, Tsukuba, Japan) have lateral size repeatedly exceeding 100 micrometers with homogeneous thickness, giving ample surface for hosting further top layers.

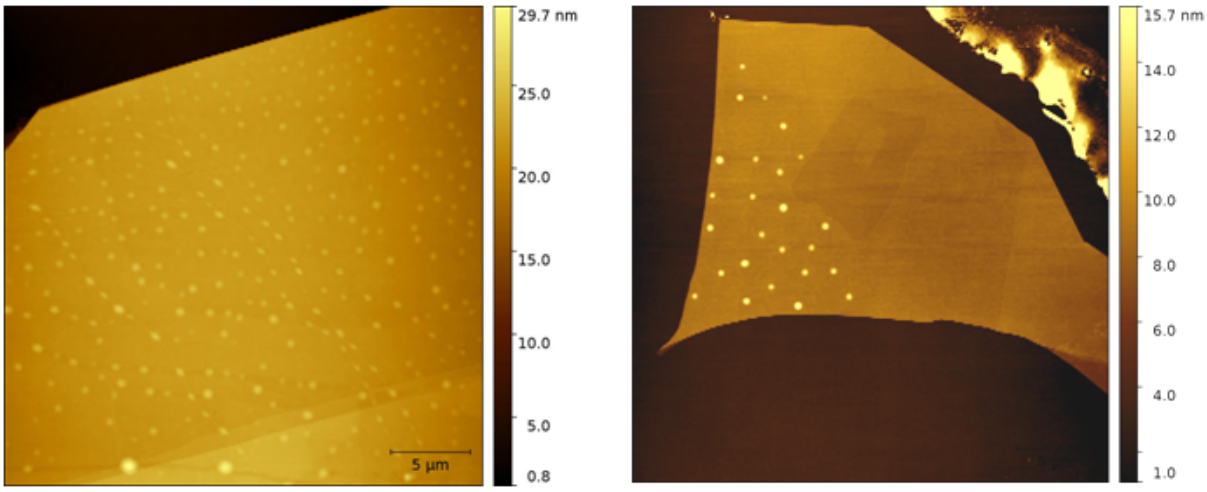

Figure 2.9 – AFM topography image of hBN flakes showing impurities on its surface caused by contamination during processing (possibly from scotch tape glueduring repeated cleaving.)

2.3.2 Stack preparation recipe using PPC Method

Here we present the process and recipes for preparation of hBN/Graphene/hBN heterostructures using the pickup technique method first demonstrated by Dean et al. [17] . This technique is based on the principle that graphene is picked-up by hBN previously exfoliated on a Polypropylene Carbonate (PPC) Stamp. This picking of graphene is based on the strong graphene/hBN Van der Waals adhesion force caused by their respective flatness optimizing the contact area. As a consequence, the graphene has a stronger interaction with hBN compared to silica which enables the pickup with good reproducibility. This so-called "PPC method" provides the cleanest heterostructures with pristine graphene encapsulated as never in the process graphene is placed in contact with polymers . Further, one-dimensional contact to graphene is realised by side-contacting to obtain high mobility graphene devices. In this context, lithography techniques used to fabricate the devices are explained in detail.

2.3.2.1 Polypropylene Carbonate (PPC) Stamps

In this polymer transfer method, we use a copolymer called Polypropylene Carbonate (PPC) that is made of carbon dioxide and propylene oxide. PPC is a low-weight polymer that has a glass-transition temperature between 25°C to 45°C and a melting temperature of about 120°C. It is soluble in polar solvents. We prepare a PPC solution as follows: 3 grams of PPC crystals are dissolved in 20 ml of Anisole. This solution is stirred continuously using a magnetic stirrer and is maintained at 50°C temperature for about 24 hours. Later the solution is purified using

a 0.2μm filter paper and stored under ambient conditions.

To obtain a homogeneous PPC film, we spin coat for 60sec the PPC solution on 1×1 cm^2 silicon substrate which is further peeled for later use. Speed and acceleration for this spin coating are 4000 rpm and 4000 rpm/s respectively. This is followed by hard-baking for 5 mins at temperature of 90 ˚C. Below is the recipe to make the PPC stamps on the glass slide.

1. A square shaped PDMS of 1×1 cm^2 is cut out and placed at centre of a clean glass slide at 1cm from one of the end.
2. A crystal clear tape is taped down on it to get a dome shaped surface over the PDMS.
3. Take a piece of 3M magic scotch tape and cut out a small circular hole that is enough to cover the PDMS piece.
4. Take the PPC film that was previously spinned over Si substrate and make a scratch at one end of the substrate.
5. Stick the tape with circular hole over the centre of PPC film on the Si substrate and peel off such that the PPC film is attached to the tape having circular hole.
6. Paste the PPC film on tape with circular hole on the glass slide such that the circular hole with PPC covers the PDMS piece on the glass slide.
7. Heat the thus prepared stamp on a hot plate at 90˚C for about 30s so that the PPC homogeneously sticks over the PDMS without any air bubbles.

Figure 2.10 – Picture of a glass-slide stamp prepared using the steps explained above. The PPC film is exposed in the circular hole region above PDMS for the pick-up.

2.3.2.2 Microtransfer setup

The figure 2.11 shows the custom-built micro-transfer setup which basically consists of an optical microscope(A) (equiped with long focal distance objectives with 10X and 50X magnification), a camera connected to computer (B), a X-Y-Z motorized stepper-motor stage(C/D), a manual 3-axis micromanipulator(E) and a temperature controller(F). The whole setup is placed on a vibration-isolated table to provide stable conditions during the transfer. The stage (holding the sample to be stamped) can be moved in X, Y and Z direction using a joystick coupled to a PC controller with a precision control of 20nm in Z and 0.2 micron in X,Y (Micos GmbH). There is a variable temperature, vacuum-assisted sample holder at the middle of the stage and the stage could also be heated from room temperature up to 200 ˚C and cooled using nitrogen gas

circulation inside the stage . A high precision PID temperature regulator(F) has sensitivity of up to 0.1°C for slow heating. Further the glass slide holder/ manual micromanipulator could be fixed on the thick steel plate at desired angle. This holder can be moved in X, Y and Z directions manually with the help of the knobs. Both the movable stage and the glass slide holder/ manual micromanipulator help in alignment of the desired flakes.

The substrate holding stage as shown in the figure 2.11(bottom) is fixed on lower elevator stage. It is a nickel plated copper(1) with a size of 2 inch diameter assisted with vaccum (11). The copper plate is integrated with a Type-J thermocouple(2) that is heated uniformly by two 175 W heating cartridges. The whole unit is supported by a stainless steel plate(3) mounted via insulating fiberglass pedestals(4) on a fibregalss screening plate(5). This screening plate has three adjusting screws(6) with spherical bearing surfaces(7), thereby giving an angular adjustment $\pm 2^{\circ}$ with respect to the XY plane, for bringing the substrate and the glass side exactly parallel. After the transfer process, rapid cooling of copper plate could be realized by nitrogen gas circulation, fed via a flexible coaxial metal tube(10), through a dissipator chamber(9) inside.

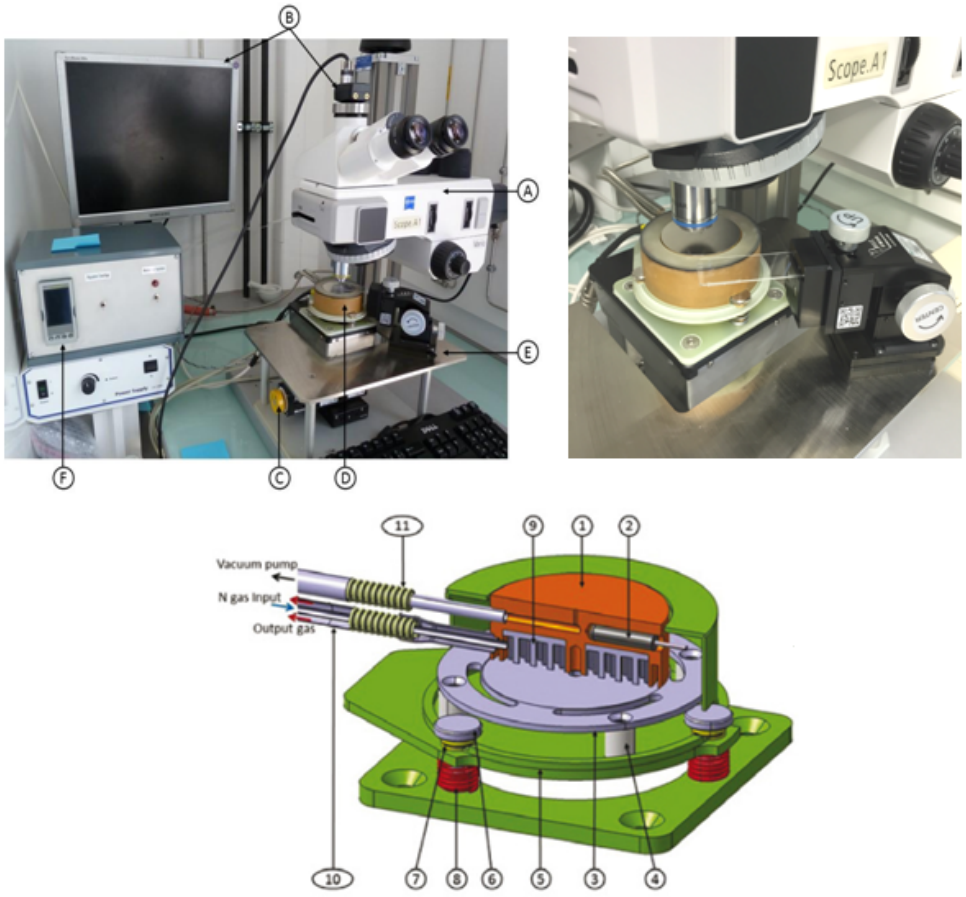

Figure 2.11 – (top) Pictures of microtransfer setup used to build the heterostructures. The micro-transfer apparatus: the microscope and display, the XYZ displacement elements, the sample-holding stage and temperature controller.(bottom) Inside picture of the temperature controlled sample-holding stage.

2.3.2.3 Pick-up transfer technique Recipe using PPC

Following are the steps executed during the pick-up transfer technique to produce heterostructures involving graphene encapsulated between two hBN flakes. To begin with, we prepare

the raw materials required for the preparation of heterostructures. We exfoliate hBN and the graphene flakes on two respective Si/SiO_2 substrates. We then select and identify the flakes that have to be picked up in the micro-manipulator. Optical images and AFM images helps in selecting clean and flat flakes as explained before. We also prepare the PPC stamp placed on a PDMS cushion and fixed on the glass slide following the instruction given in the previous sections.

2.3.2.3.1 First pick-up of top hBN After the PPC stamp on glass slide has been prepared, we place the substrate with hBN flake to be picked up first (final top (i.e. capping) hBN layer) under the microscope on the stage that is firmly held by vacuum. One makes sure that the thickness of hBN flake is above 10nm. We fix the glass slide which was preheated at 80 $^{\circ}$C for 30s (PPC surface placed upside down) on to the glass slide holder and we align it such that the circular PPC area is exactly over the hBN flake. We then focus on the selected hBN flake through the transparent and optically clear (glass/PDMS/PPC) stamp to get a clear image of the flake that is aligned versus the stamp using X and Y motorized manipulator. We focus on hBN as well as PPC and align the hBN flake to be at the centre of circular PPC area on the PDMS using the fine tuning manual XYZ micromanipulator holding the glass slide stamp. We move down using the Z direction of the glass slide holder and bring the glass slide with PDMS very close to the hBN flake . As you go down towards the flake while the PPC touches the substrate, choose a contact point which is not very far from the hBN flake appears and is clearly seen as a black contact contour/line. The dome shape of the stamp allows the PPC to be touched on to a very small area of the substrate.

When the PPC touches the surface of the substrate, there is around the contact area, optical interference patterns (equal thickness fringes) called Newton rings that help a lot in monitoring the approach. As we go down these Newton rings move along with the contact line. When these rings are very close to the flake to be picked up, we gradually increase the temperature of the stage from 38°C in steps of 0.5°C until the flake is completely covered. Thermal effect allow fine control of the contact line and also makes PPC sticky. The Newton rings move over the hBN flake due to temperature gradient as the PPC softens. When these rings have completely crossed the flake, we reduce the temperatures in the steps of 0.5°C back to 38 $^{\circ}$C along with tiny upward movements in Z direction of the holder.The spreadover PPC surface over the substrate should move back very slowly and in the process the hBN flake will be picked up by the PPC. Here the hBN is picked up due to its very strong adhesiveness towards polymer film PPC. It has been found out that the thick hBN flakes of 10nm and above readily adheres to PPC when brought in contact along with change in temperature as discussed before. Once the first hBN flake is picked up, move the glass slide away from the substrate using the Z direction upward movement of the glass slide holder.Verify in the optical microscope if the desired hBN flake is picked up and take the picture. The hBN flake would appear whitish in color on the PPC.

2.3.2.3.2 Further pick-up steps for any 2D material After a very flat hBN flake above 10nm has been picked-up as explained in the previous paragraph, we heat the glass slide again at 90°C for approximately around 30 seconds before the pickup of any other 2D material (graphene in this case). This step should be performed every time before pickup. Now we place the substrate with graphene flake on the stage and align it such that the hBN flake on PPC film and graphene flake on substrate are overlapping such that hBN covers the complete area of graphene. We then increase the temperature by gradual steps of 0.5°C from initial temperature of 38°C as explained before, but during this time we stop when the graphene flake is fully covered by PPC, but not the whole hBN flake. This allows for an easy pick up of graphene as some part of hBN flake would be still on PPC and would ensure that the stack is picked up. In subsequent

pickups, it is always convenient to keep a part of first hBN still on PPC during the cool down and pickup step for the same reason. In this case the graphene is picked up as a result of stonger Van der Waals attraction towards the hBN upon contact.

2.3.2.3.3 Graphene encapsulation in pristine condition After the graphene has been picked up, again we heat the glass plate at 90°C for approximately around 30 seconds. Again we place the substrate with bottom hBN flake to be picked up, on the stage and align with the already picked top hBN + graphene on PPC film so that the latter could be encapsulated between two hBN flakes. Use the ritual pickup steps of increasing and decreasing the temperature by gradual steps that cover and pickup the required bottom hBN flake. In this way the graphene is maintained pristine where it is not in contact with any polymer or chemicals during the transfer process. Further by encapsulating it into two hBN flakes, it is maintained in pristine condition without any contact with the environment. Hence by employing this method, we can obtain the cleanest heterostructure as possible almost comparable to the vacuum conditions as any surface impurities would be pushed outside the heterostructure. The same ritual steps could be used to pick up as many 2D material flakes as possible, almost up to 4 to 6 layers of different 2D materials.

2.3.2.3.4 Drop-down of stack from PPC to desired substrate After the desired 2D material flakes have been picked-up, the entire heterostructure would be on the PPC and could be landed on to desired target substrate (Si/SiO_2 in this case) for further fabrication steps. For that purpose, we take a clean Si/SiO_2 substrate, we place it on the stage such that stack is aligned at the desired location. As described before, we move the glass slide downwards and with gradual increase in temperature and with the movement of PPC over the substrate, the stack comes in contact with substrate. We then heat the stage to 110°C to 120°C gradually in steps of 20°C upon which PPC softens and would be at semi melting stage. After about 10 minutes, slowly move the glass slide away from the substrate in small steps. The PPC film with the heterostructure melts on to the substrate and detaches from the glass slide.The substrate with the stack and residual PPC could be washed with acetone followed by rinsing in IPA to remove the PPC. But there are high chances that the stack would flow away with PPC in acetone.To avoid any wash away of the heterostructure, we anneal the stack for 30 minutes under high vacuum conditions up to temperatures of around 350°C. In this way the heterostructure could be built without the use of any solvents. After the annealing one could perform AFM characterization to check the quality and cleanliness of the stack.

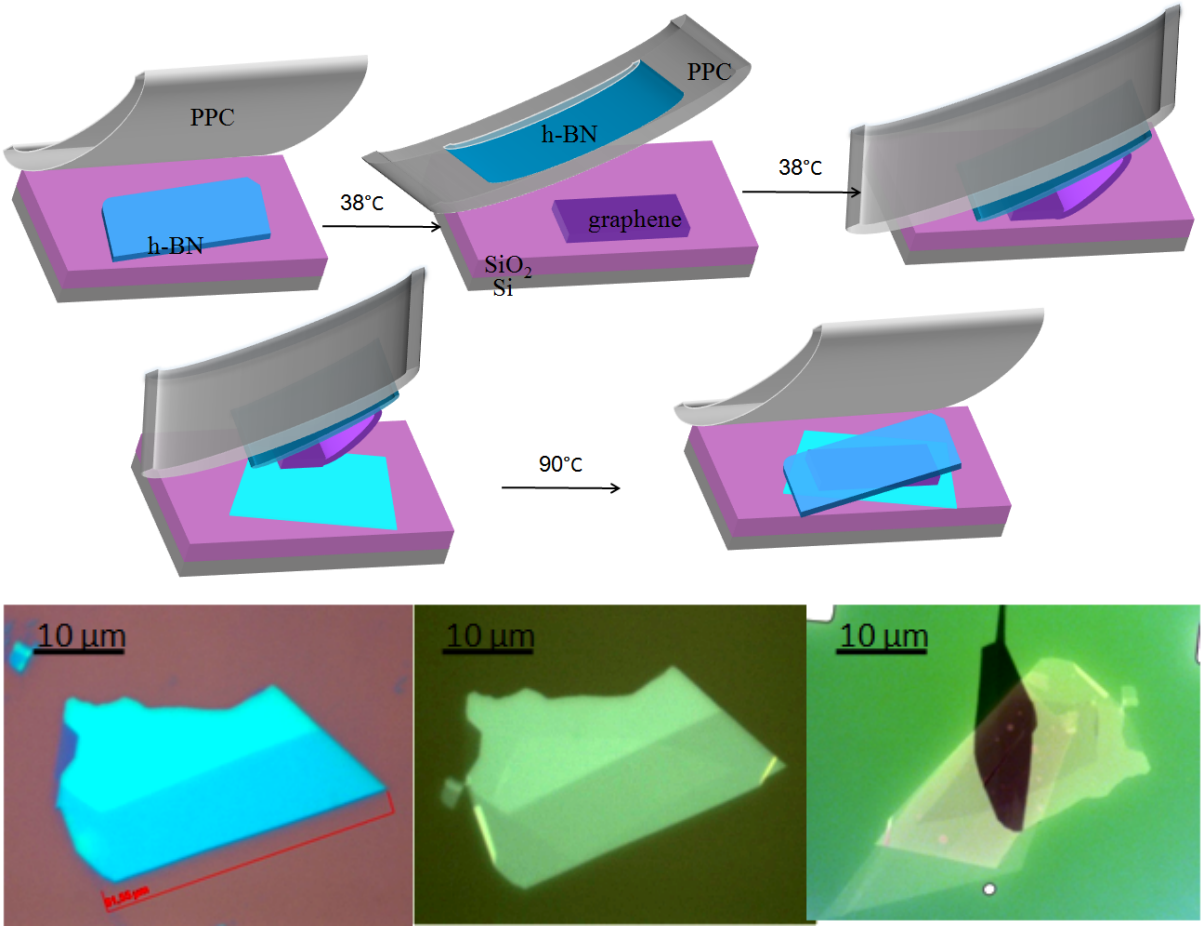

Figure 2.12 – (Top) Process flow diagram of PPC pick-up technique. In the first image hBN is already on PPC film and aligned with graphene for pickup. Second image the graphene is picked up as explained by the recipe. Third image depicts the drop down of the stack from the PPC to the target substrate as explained by recipe. (bottom) The optical images of the stack first with hBN, second with graphene/hBN on PPC film, third the complete stack dropped down on Si/SiO_2 substrate.

2.3.2.4 Improvements in the stacking process

The quality of the heterostructures prepared depends not only on cleanliness of the flakes used but also the time used for its fabrication. As explained before the PPC or PPC/hBN spreads over the flake to be picked up by gradually increasing the temperature. If this temperature is increased very fast during the pick-up, bubbles trapped with air or impurities could be formed as shown in the figure 2.13 a,b,c. These bubbles could degrade quality of the stacks and thus electronic properties. We can get rid of these bubbles to some extent by long annealing of the stack at 350˚C for about 2 hours. As a result of annealing the bubbles move over the surface and get accumulated at the edges of graphene as shown in the 2.13d. Further, we could avoid any bubbles by slow pick-up process where the pick-up temperature is increased slowly by uniform gradual steps of 0.2/0.1 ˚C. The 2.13 e,f shows the bubble free stacks prepared using such a slow pick-up process.

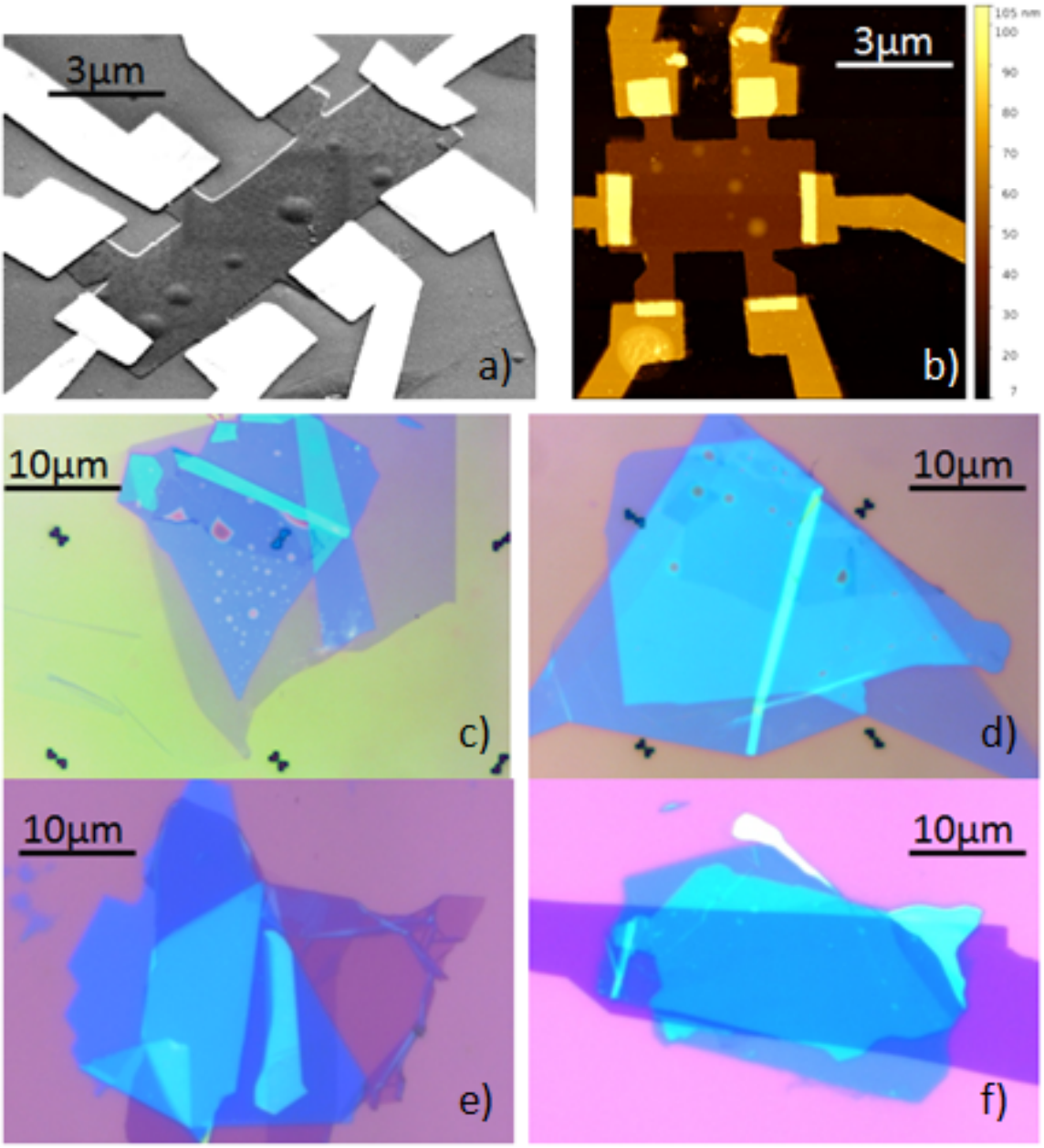

Figure 2.13 – a) Scanning electron microscopy image of a hBN/graphene/hBN Hall bar with bubbles that may effect the mobility. b) Atomic force microscopy image of a hBN/graphene/hBN Hall bar with bubbles. c) Optical image of the as obtained stack with bubbles. d) Optical image of the long annealed stack with bubbles moved to the graphene edges. e,f) Bubble-free heterostructures prepared using slow pick-up process.

2.3.3 Nanofabrication of edge-contacted devices

After the preparation of the heterostructure, one can proceed to devices design and fabrication. For the fabrication of edge-contacted device, we need several steps of lithography for alignment marks, stack shaping and etching, gate buffer deposition and finally for the metal contacts. Here we use a three-step lithography process with the help of both the optical lithography for markers and electron beam lithography for etching and metal deposition. We also present the very critical etching process to obtain one dimensional contacts by depositing metal layer on the sandwich edge. The figure 2.14 shows the process flow of the fabrication that was developed, stabilized and further refined during the course of the thesis. Each sub-step is described in

details in the following subsections.

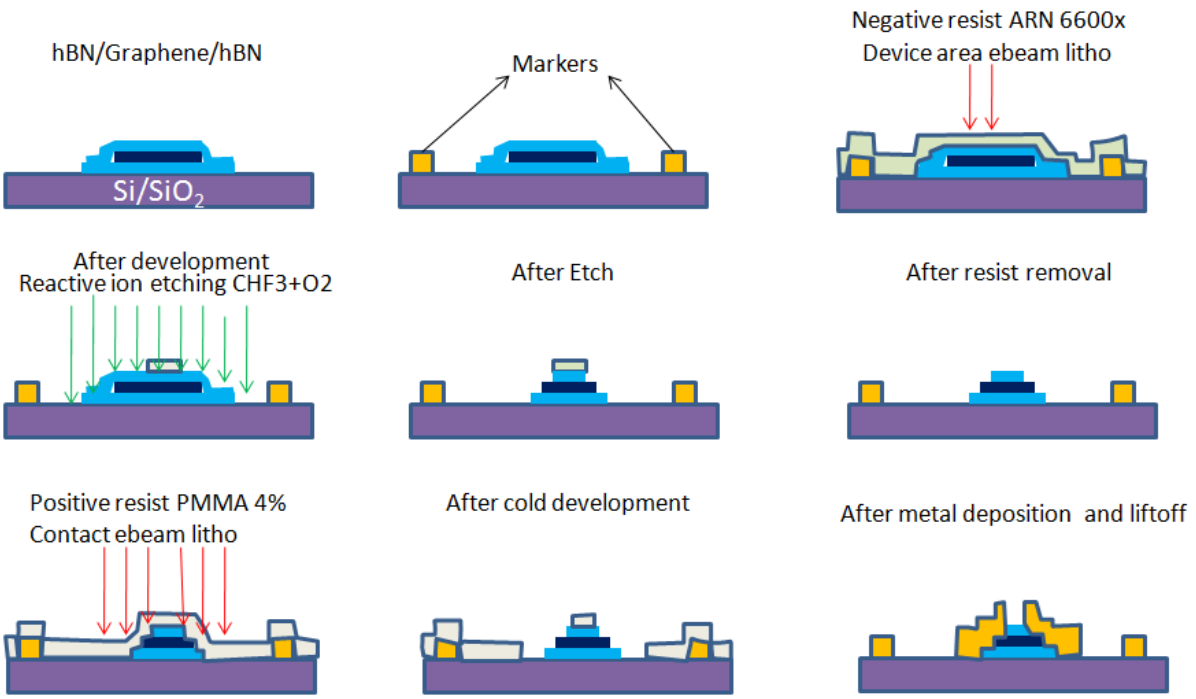

Figure 2.14 – Process-flow for the fabrication of the edge-contacted devices. The process includes realizing markers by laser lithography, EBL using negative resist for device area follwed by reactive ion etching(RIE) and resist removal, and then final EBL using positive resist for metal contacts followed by metal deposition and liftoff to obtain the edge contact devices.

2.3.3.1 Markers using Laser Lithography

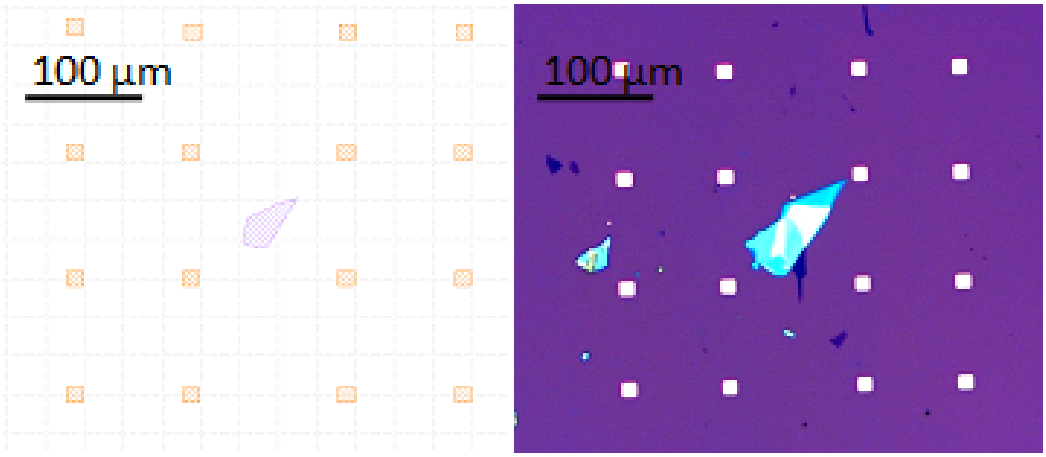

Figure 2.15 – (Left) Design file with markers for laser lithography. (Right) Optical image of markers on the desired location on the susbtrate after laser lithography followed metal deposition and liftoff.

In this step of lithography, we basically design markers for alignment case for the further electron beam lithography procedures. When we place the final stack, it is possible that it would

be randomly distributed on the substrate. The relative position of the stack should be very precisely known especially when we do electron beam lithography. Hence we use a markers around the stack as shown in the figure 2.15a which could be used for design of the device using the CAD software and for the precise alignment while doing the ebeam lithography (EBL) .Relative errors during the alignment process can be reduced down to 10 nm or less using NanoBeam Mini-Masker EBL writer as it is equipped with an interferometric stage.

Here we use an automated optical lithography called Laser lithography which is fast and dynamic for this kind of marker design which does not require a very high precision of below a micron. Here we design 8x8 micron square shapes around the stack to recover the exact positions of the stacks during further EBL steps. Since it is based on direct writing optical lithography, we spin coat an optical resist (S1805) on the stack-stamped substrate . Lithography will be always followed by development using different developers. All the parameters of spinning, development and liftoff are presented below.

UV Resist : S1805
Spinnning parameters: speed 6000 rpm, acceleration 4000 rpm/s, time 30s
Baking parameters: 115°C for 1 min
Exposure Dose: 15mJ/cm^2
Development: Microposit Developer/DI water 1:1, 1 min dip followed by DI rinse and Nitrogen blowdry
Metal deposition: Ti/Au 5nm/50nm at any rate
Liftoff: Acetone dip 2 hours, IPA rinse 1 min followed by Nitrogen blow-dry.

2.3.3.2 E-Beam Lithography (EBL) for device area definition

We take the optical images after the deposition of the markers around the stack. These images are imported into the CAD design so that we can get very precise alignment and positioning of the device design in the required area of the stack. The basic device shapes are designed using the design software, (KLayout/AutoCad in our case) by aligning the optical image on the underlying markers as shown in the figure 2.16a. Since we need relative alignement between the steps better than 50nm, we use ebeam lithography for the design of the devices that would be further etched into required shapes.

EBL requires resists which are sensitive to electrons. These resists are of two types, a positive-tone resist, which upon exposure by electrons see its polymer chains modified and is dissolved during the development and a negative-tone resist which upon exposure gets cross-linked and remains non-soluble after the development. For the etch lithography, we use negative resist like HSQ or ARN to get the desired shapes on the stack upon development. During the etching time, it is found out that HSQ/ARN resist further solidify and occasionally becomes glassy which indeed is difficult to remove during the liftoff. Hence when we use HSQ/ARN we need a another layer of resist PMMA underneath so that it is easy for removal during the liftoff process. Below are the parameters presented for the HSQ and ARN processes.

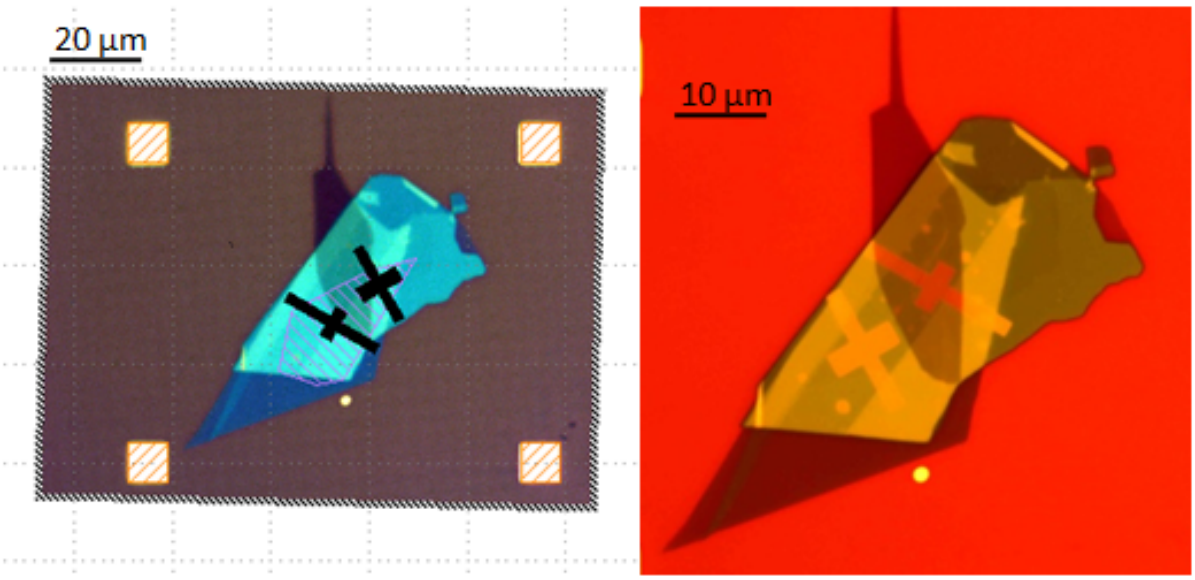

Figure 2.16 – (Left) CAD design file with device area (in black) defined for electron beam lithography. (Right) Optical image of the device area on the stack after ebeam lithography followed by development.

2.3.3.2.1 HSQ (hydrogen silesquioxane) process: 2-Layer Resist

1st Layer: PMMA 950K 2%, speed 4000 rpm, acceleration 4000 rpm/s, time 60s, bake 200˚C/ 5mins
2nd Layer: HSQ 6%, speed 4000 rpm, acceleration 4000 rpm/s, time 60s, no bake
Dose: 600 microC/cm^2 at 80keV
Development: MF26 90s, DI water rinse 60s, Nitrogen blow dry
Liftoff: Acetone dip 2 hours, IPA rinse 1 min and Nitrogen blowdry.

Since HSQ has a very short shelf life and is expensive, we developed another recipe based on the negative resist ARN 7700.18 which could be directly used or in a bilayer configuration with PMMA underneath for better liftoff and resist cleanliness.

2.3.3.2.2 ARN 7700.18 process: 2-Layer Resist

1st Layer: PMMA 950K 2%, speed 4000 rpm , acceleration 4000 rpm/s, time 60s, bake 200˚C/ 5mins
2nd Layer: ARN 33%, speed 4000 rpm, acceleration 4000 rpm/s, time 60s, bake 85˚C/ 1mins
Dose: 1200 microC/cm^2 at 80keV
Development: Hard bake 105˚C/ 2mins, DI water : AR 300-46 1 : 4, 60 sec, DI water rinse 60s, Nitrogen blow dry
Liftoff: Acetone dip 2 hours, IPA rinse 1 min and Nitrogen blowdry.

2.3.3.3 Reactive ion etch process

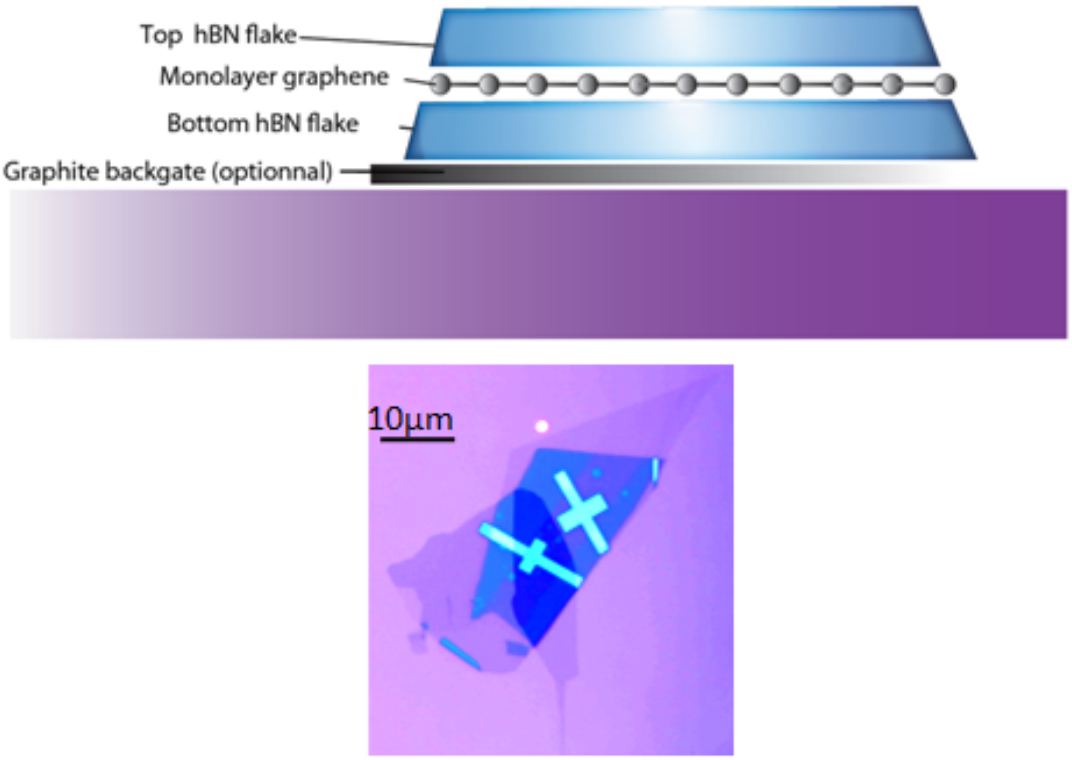

Figure 2.17 – (Top) Single layer graphene edge-atoms exposed for realizing the 1D contacts after the etching process. (Bottom) Optical image of the stack after the reactive ion etching process.

After the development of the device shape, graphene needs to be exposed at the edges so that low-resistance one-dimensional edge contacts (as pioneered by Cory Dean group at Columbia) could be realized in the forthcoming steps. This is achieved by reactive ion plasma etching process of the hBN/G/hBN stack. It should be noted that the thicknesses of both top and bottom hBN flakes are typically 30 to 40 times that of graphene and hence a recipe that specifically etch hBN and is less efficient on graphene (to preserve the edge protrusion) must be found and optimized. In the seminal paper of Wang et al.[17], they show that a small angle arises at the etched sidewalls (pyramid like stack edge as seen in figure 2.17) which is of paramount importance for obtaining reliable electrical contacts of the deposited metal film connecting graphene edges. The recipe and parameters that was developed during the thesis and used during RIE etching are presented below.

1. Oxygen plasma etch:

Power 10 Watt, temp 15°C, pressure 5 mBar, 20 sscm for 1 min.
This etch step is for removal of bottom PMMA layer. We need to confirm from optical images that indeed all PMMA has been removed.

2. CHF_3-Oxygen plasma etch:

Power 60Watt, temp 15°C, pressure 5 mBar, CHF3:O2 in 5:1 ratio, 20 sscm: 4 sscm, etch rate 36nm/min.

It should be also noted that the etching step is the most critical step to get the cumbersome one-dimensional contacts and it should be executed in a super clean stable environment with

respect to pressure and temperature. It is always helpful to execute a 10-min oxygen plasma to clean the chamber from previous process residues followed by dummy etching process before the actual etching. Sometimes if the chamber is not clean or the used resist was outdated or impure, the etching would not be as good and thus partial or no contacts would be established. One such example is shown in the SEM figure 2.18, where we could see the deposition of the resist impurities at edges of the sample. This residues cover the graphene edges and no contacts were established in such kind of devices.

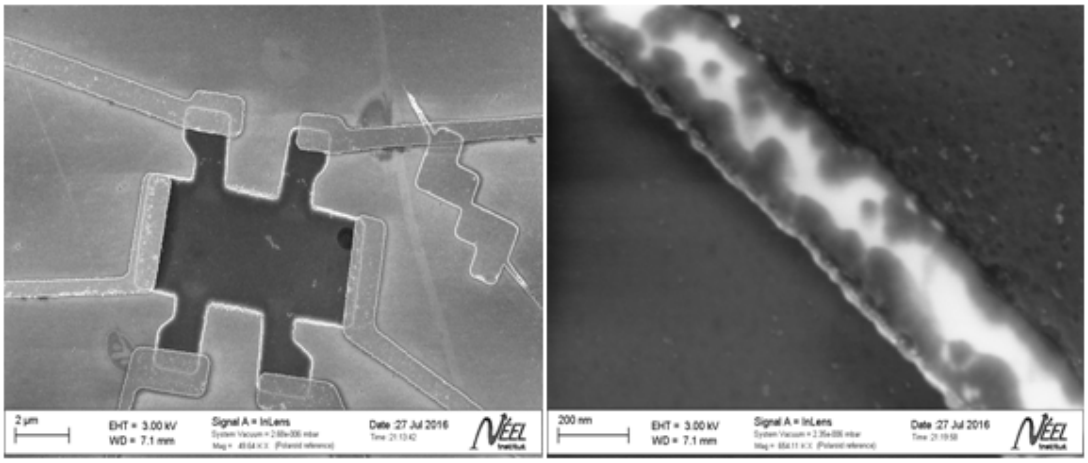

Figure 2.18 – (Left) Optical image of the stack after the flawed etching process. (Right) Electrically insulating residues (shinny deposits in SEM image) could be seen at the stack edges which prevent the realization of graphene edge contacts.

2.3.3.4 Ebeam Lithography (EBL) for contacts electrode definition

A second electron beam lithography step is carried out after the etching process in order to incorporate metal contacts. We use low current (1.1nA) during the lithography of the fine contacts and higher currents (15nA) for larger contacts and pads. Here we use the positive resist, double layer PMMA to realize the contacts. The double layer serves for the precision in the critical size and also during the liftoff process. The recipe parameters of this step used during the thesis are presented below.

Bi layer PMMA Resist:
1st Layer: PMMA 4% , speed 5000 rpm, acceleration 4000 rpm/s, time 30s, bake 200˚C/ 5mins
2nd Layer: PMMA 950K 2%, speed 1500 rpm, acceleration 2000 rpm/s, time 60s, bake 180˚C/ 5mins
Dose: 1000 microC/cm^2 at 80keV

Developers:
MIBK : dip 30s , rinse in IPA, blow dry
Cold developer: DI Water: IPA (1:3) at 4˚C, dip 90s, rinse IPA, blow dry

Liftoff:
Acetone dip 2 hours, IPA rinse 1 min and Nitrogen blowdry.

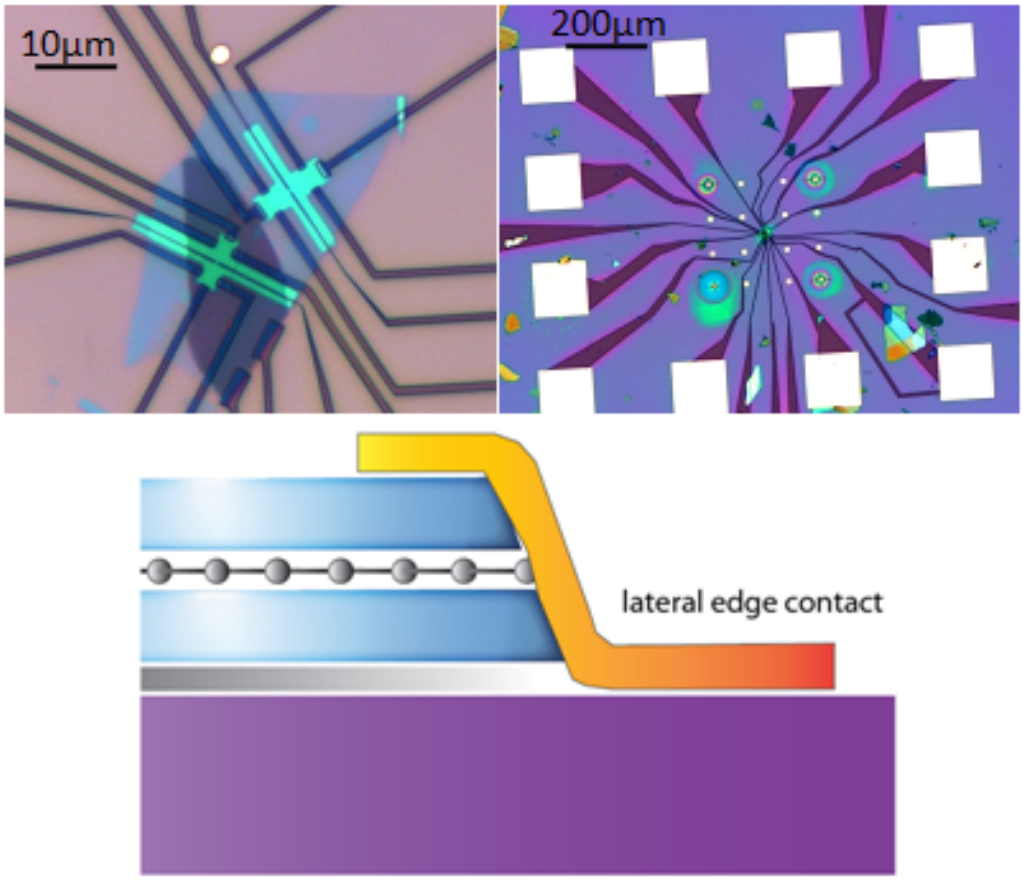

Figure 2.19 – (top) Optical image of the device after the lithography and development that defines the contacts. The contacts and the pad area used for bonding could be seen in the figure. (bottom) Diagram showing the one dimensional lateral edge contact realized for 2D graphene.

2.3.3.5 Metal deposition and lift-off process

After the electron beam lithography of the contacts, a very short 2-4 seconds, 10 Watt oxygen plasma is carried out just before the metal deposition process. This is to ensure that there are no residues of PMMA left at the edges of the stack which would degrade the contacts. We use the electron beam deposition technique to evaporate the desired metal as the contacts. The evaporation must be uniform and homogenous for which reason we use a rotating stage with a small angle tilt of about 2 degrees. We use a thin adhesion layer of chromium which is found to stick well on graphene surface followed by a thicker gold layer.

Gold Au thickness 70nm, deposition rate 0.5nm/s
Chromium Cr thickness 2nm, deposition rate 0.11nm/s

Finally the pads of the device are carefully micro-bonded to the chip holder and device should be ready for electrical test.

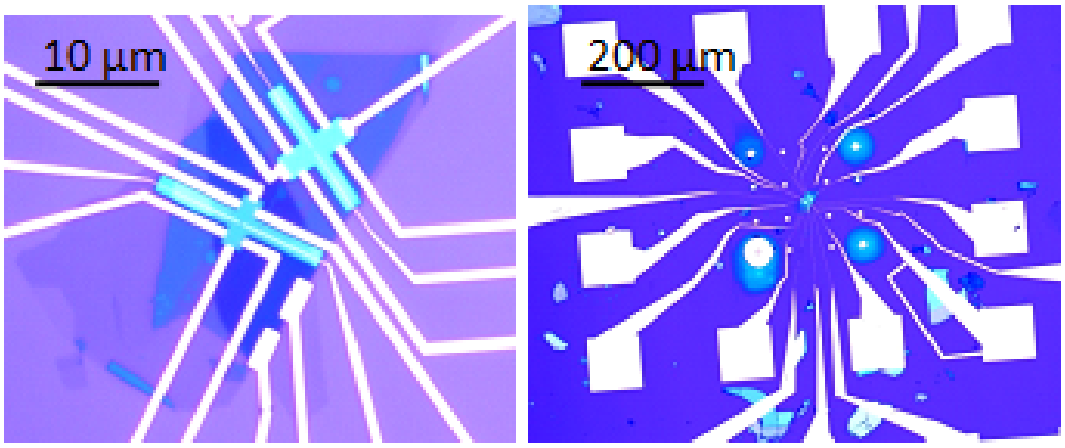

Figure 2.20 – Final device structure after the metal deposition and liftoff.

2.3.3.6 Top gate backend process

Most of the times it is difficult to have an arrangement where the top gate or quantum point contacts gates to be realized during the contact and pads lithography. Since the contacts are edge-contacted, the graphene is exposed at the edges and not possible to design the top gates with out a work-around as gates might contact the graphene. In this case, I have developed a process where we use a over-exposed-glassy reticulated PMMA patch just near the edges to sufficiently cover them. Care is also taken that the PMMA patch doesnt extend too much over the heterostructure which may diminish the gate effect. Taking this into account only 50-100nm of patch is fabricated on the heterostructure as shown in the figure 2.21.

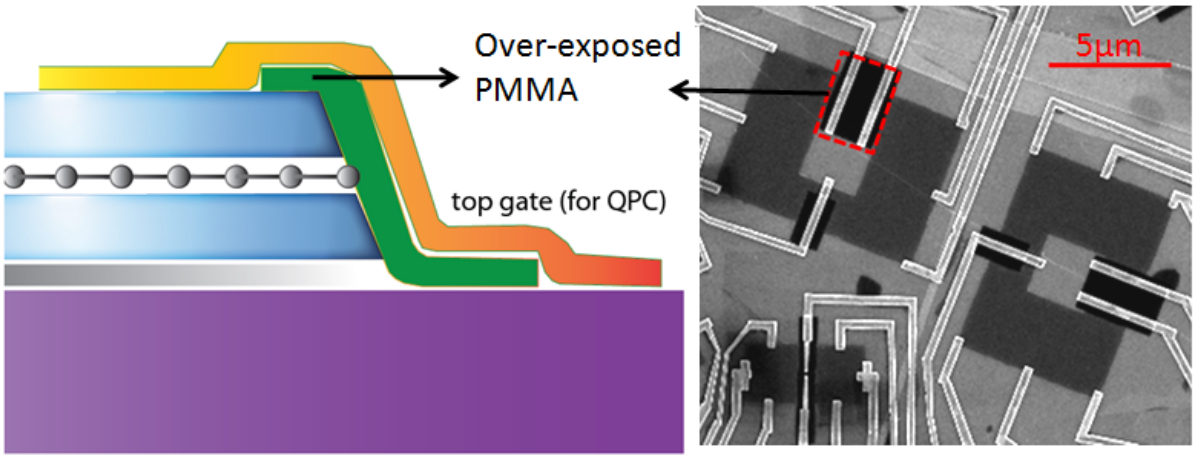

Figure 2.21 – (Left) Top gate process depiction to avoid the exposed graphene at the edges. (Right) SEM image of graphene edge-contacted device where red dotted lines shows the PMMA patch that was over-exposed to solidify it into a glass non removable structure so that the gate metal contact can pass over it without coming into contact with graphene exposed at the edge.

In this gate-last process, in continuation to previous processes, fourth and fifth steps of e-beam lithography is utilized for PMMA patch and gate contacts . We use a single layer PMMA as positive resist, design the required small structures to cover the edges, develop them and highly overexpose the PMMA during lithography. This over-exposed PMMA turns solid and glassy because of cross-linking of its polymer chains. The liftoff is not necessary here and even

if one carries out the liftoff process, glassy PMMA remains stable.

PMMA patch:
PMMA 2% , speed 4000 rpm, acceleration 4000 rpm/s, time 60s, bake 200°C for 5mins
Dose: 5000 microC/cm^2 at 80keV

2.4 Dilution fridge measurement technique

All the measurements in this chapter of the thesis were executed in Oxford Triton 400XL cryogen-free dilution refrigerator integrated with a superconducting magnet . This system can reach a base temperature lower than 20mK, thanks to the dual pulse-tube refrigerators producing 1.5 Watt and 1 Watt @ 4.2 K respectively. The sample stage is inserted inside a 57 mm-bore superconducting solenoid with a huge mass of 130kg, an inductance of 60H and an operating current of 140 A that gives a provision of applying high-magnetic fields up to 16 T. As shown in the figure 2.22, the Oxford-Instruments Triton system consists of a cryostat with a pulse-tube cooler, gas handling and control rack, magnet power supply rack, pump rack and a pulse tube compressor which occupies almost a big room of $40m^2$. The system is equipped with a bottom-loading stick allowing samples to be changed while the cryostat is still cold.

When we are performing very low temperature measurements that requires low-noise high precision electronic measurements, the suppression of external source of noise becomes extremely important. Coaxial cables were used to achieve good shielding. Isolation transformer was used to reduce the electrical noise originating out of the raw power supply. The main goal of the isolation transformer was to separate the measurement system's ground from the raw power supply's ground. Any floating wires in high magnetic field could also generate noise and for the same reason all the cables were well anchored inside the dilution fridge. In order to suppress the high frequency noise above a cut-off frequency of $f_c = 50$ MHz, the electrical lines inside the dilution fridge were filtered using three-stage passive low-pass RC filters. These filters integrated on PCBs were mounted on the mixing chamber plate of the dilution fridge.

Our measurements are carried-out generally at sub-Kelvin temperatures and cooling down the electrons down to this temperature is highly strenuous task as filterings of measurement lines is necessary. Lattice cooled down to certain temperature does not also mean that electron were also cooled-down to that temperature as the electron phonon coupling are suppressed at lower temperatures. Several steps were ensured in the dilution fridge in cooling down of electrons. To minimize thermal loads from the room temperature components to the target device, resistive coaxial cables were used from room temperature connectors to the mixing chamber plate inside the dilution fridge. A thin layer of General-Electric varnish was used for thermal coupling of all the cables. Sample holder was anchored to the mixing chamber connector using thin long copper wires which were well-clamped to the mixing chamber plate.

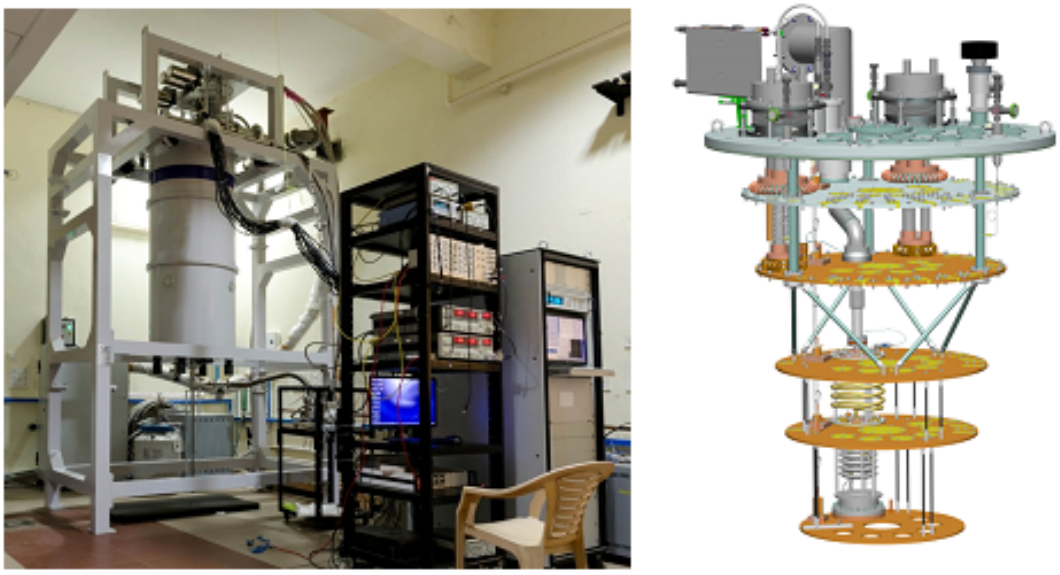

Figure 2.22 – (Left): Cryogen-free dilution refrigerator used for measurements situated at Prof. Aveek Bid Lab, IISc, Bangalore. Note the large cryostat vessel cylinder hosting the dry 16T superconducting magnet surrounding the dilution fridge. (Right): block diagram of the 4-cold stage inside dilution fridge (the sample is placed on the lowest (coolest) part which is coupled to the mixing chamber of the dilution fridge (base temperature 20mK).Figure adapted from [31]

2.5 Quantum electron transport in the quantum Hall regime

In this section, we shall discuss about the electrical transport characteristics in graphene. We start by introducing the concept of diffusive transport regime and classical motion of electron in the magnetic field. It is then followed by transport in 2DEG system of how low dimension, low temperatures and high fields induce quantization effects in the electron transport leading to the introduction of interesting concepts in the ballistic regime such as Integer Quantum Hall effect. We would explain then how graphene has different integer quantum Hall effect compared to conventional 2DEG systems. The theory explained is based on[32][27][33][34] could be referred for detailed description.

2.5.1 Classical motion of electron in a magnetic field

In the diffusive transport regime, the electronic charge carriers experience elastic scattering because of the instantaneous collision with the impurities indicating that the conductivity would be better with less impurities. The average time between the subsequent collisions of an electron is τ also called as relaxation time. If we apply an electric field to the system , then according to the Drude model the momentum based equation of motion reads:

$$\frac{dp}{dt} = -\frac{p}{\tau} + eE. \tag{2.5.1.1}$$

The carrier mobility can be defined as $v_d = \mu E$ where v_d is carrier drift velocity and hence the mean free path of electron would be $l = v_d\tau$.

These equations imply that higher the mobility means the conductivity would be higher and the electrons would have a higher mean free path.

Now for the above system having transverse electric field in the x direction, the electrons are restricted to move in (x, y) plane resulting a constant current I in the x direction. If we apply a constant magnetic field in the z-direction , it induces a voltage V_h in the y direction. This effect is called as Hall effect discovered by Edwin Hall in 1879.

This classical Hall effect arises due to the fact that the applied magnetic field causes the charged particles to move in form of circles. The corresponding equation of motion would be:

$$m\frac{dv}{dt} = -ev \times B. \tag{2.5.1.2}$$

The frequency with which the charged particle rotating as a circle in the magnetic field, called as cyclotron frequency is given by:

$$\omega_B = \frac{eB}{m}. \tag{2.5.1.3}$$

The Hall resistance and the longitudinal resistance ρ_{xx} and ρ_{xy} could be derived from the Drude model given as:

$$\rho_{xx} = \frac{m}{ne^2\tau}, \rho_{xy} = \frac{B}{ne}. \tag{2.5.1.4}$$

2.5.2 Shubnikov de Haas effect

The classical Hall effect equations show that the longitudinal resistance is independent of the magnetic field while the Hall resistance is linearly proportional to the magnetic field. Meanwhile, during the transport measurements of 2D electrons in a strong magnetic field, Shubnikov and de-Haas found out that, above some critical value, longitudinal resistance starts oscillating as a function of the magnetic field. This so-called Shubnikov de Haas (SdH) effect is the first demonstration of possible quantum phenomena in the 2D electron systems. SdH effect is a direct consequence of energy quantization of the 2D electrons systems in a strong magnetic field. This quantization of cyclotron radius of electron in a magnetic field is called as Landau quantization which would be explained in detail in the next section.

As a result, the kinetic energy also gets quantized into Landau levels(LLs) given by:

$$\epsilon_n = \hbar\omega_C(n + 1/2). \tag{2.5.2.1}$$

Using the Einstein's diffusion relation longitudinal conductivity could be defined as:

$$\sigma_L = e^2 D_\rho(E_F). \tag{2.5.2.2}$$

From the equation it can be seen that the longitudinal conductivity depends rather on density of states (DOS) at Fermi energy instead of electronic density.

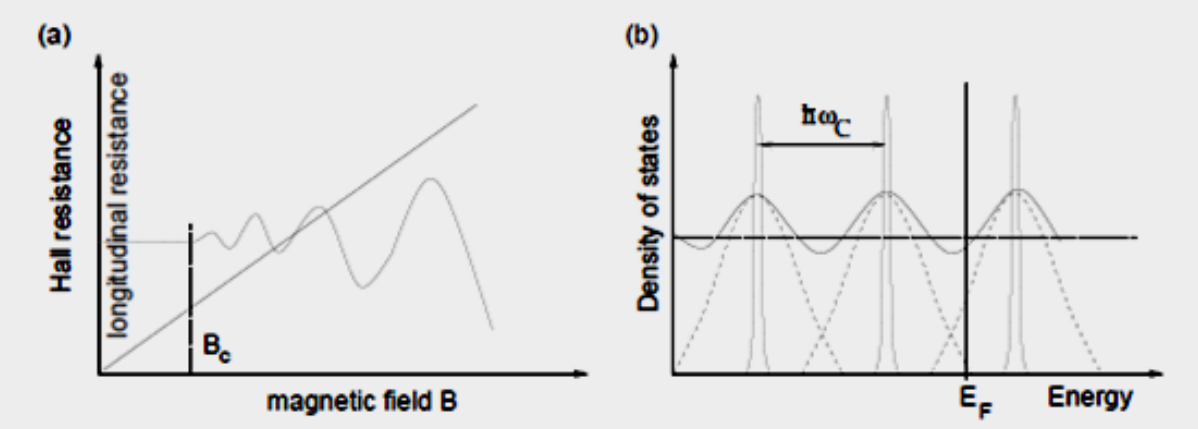

Figure 2.23 – a) Graph explaining the Shubnikov-de Haas effect. Above a critical field B_c (black dotted line), the longitudinal resistance (grey) starts to oscillate as a function of the magnetic field. The Hall resistance varies linear with respect to B. b) Density of states (DOS). In a clean system, the DOS consists of equidistant delta peaks (grey), whereas in a sample with a stronger impurity concentration, the peaks are broadened (dashed lines). The continuous black line represents the sum of overlapping peaks, and E_F denotes the Fermi energy. Figure adapted from Mark Goebirg notes[32].

As a consequence of Landau quantization, the DOS of the clean system forms a sequence of delta peaks as seen in the figure 2.23. These peaks would be broadened due to impurities in the system and may also overlap. During the increase in the magnetic field, the energy distance between the Landau levels increases and as a result DOS becomes maximum when Fermi energy coincides with the energy of a LL and minimum if Fermi energy lies in between two adjacent LLs. From the diffusion equation we have seen that the longitudinal resistance is a function of DOS. Hence the above mentioned oscillation in DOS as a function of magnetic field directly translates into the oscillation of longitudinal resistance and hence the SdH oscillations.

2.5.3 Landau quantization

In the previous section we discussed about the quantization of 2D electron on the application of magnetic field resulting in SdH oscillations. We will discuss this quantization called Landau quantization in detail here. As explained in previous subsection , after a critical magnetic field value, Landau quantization occurs. This magnetic field must be strong enough so that electron completes at least one complete circle without any collision that is $\omega_c.\tau > 1$. This Landau quantization of kinetic energy into discrete energy levels called Landau levels could be calculated by solving the Schrodinger equation in external magnetic field.

Considering a conventional 2D electron system with quadratic energy dispersion given as:

$$\left[\frac{(\vec{p}+ \mid e \mid \vec{A})^2}{2m^*}\right]\psi(\vec{r}) = \epsilon\psi(\vec{r}), \tag{2.5.3.1}$$

where $\vec{A}$ is the vector potential with Landau gauge $\vec{A} = -B_y\hat{e}_y$ where magnetic field is in the z direction perpendicular to the motion of 2D electrons in x, y plane. On simplification with these parameters,

$$\left[\frac{(p_x - \mid e \mid B_y)^2 + p_y^2}{2m^*}\right]\psi(x,y) = \epsilon\psi(x,y). \tag{2.5.3.2}$$

If we consider electron as a plane wave propagating in x direction, $\psi(x,y) = exp(ik_x x)\eta(y)$

$$\left[\frac{p_y^2}{2m^*} + \frac{1}{2}m^*\omega_c^2\left(y - \frac{\hbar k_x}{\mid e \mid B}\right)^2\right]\eta(y) = \epsilon\eta(y). \tag{2.5.3.3}$$

This equation is similar to ordinary one dimensional Schrodinger equation for a simple harmonic oscillator.The eigenvalues of the equation is given as:

$$\epsilon_N = \hbar\omega_c\left(N + \frac{1}{2}\right). \tag{2.5.3.4}$$

where N=0,1,2 .... are Landau levels that are equally spaced with the cyclotron gap $\hbar\omega_c$.

Hence with the increase in the magnetic field, the DOS splits into discrete energy levels as shown in the figure 2.24. Initially until the critical magnetic field, the DOS peaks overlap and causes the longitudinal resistance to oscillate as a function of magnetic field called SdH oscillation. Further increase in the magnetic field results in larger spacing between the peaks than their width. During this regime the longitudinal resistance falls to zero and the transverse resistance take specific constant values in the form of plateaus which is called as Quantum Hall Regime discussed in the next section.

From the eigenenergy values in the equation ϵ_N one can notice that it only depends on the quantum number n and this shows that Landau levels are highly degenerate. The number of allowed states per unit surface area in a Landau level n_L depends on the sample dimensions where the centre coordinate y_0 has to lie within the width of the sample.

$$\epsilon_N = \hbar\omega_c\left(N + \frac{1}{2}\right), n_L = \frac{eB}{h} = \frac{B}{\Phi}. \tag{2.5.3.5}$$

Hence as many electrons as magnetic flux quanta (h/e) penetrating the sample could be accommodated in a Landau level. In this context filling factor defined as the number of Landau levels filled with electron could be calculated as:

$$\nu = \frac{n_e}{n_L} = \frac{n_e h}{eB}, \tag{2.5.3.6}$$

n_e being the electron density.

Until now we have not considered the role of electron spin on the quantization subject. When an electron spin is placed in a magnetic field, an additional energy called Zeeman energy E_z is contributed.

$$\nu = \frac{n_e}{n_L} = \frac{1}{g_s}\frac{n_e h}{eB}, \tag{2.5.3.7}$$

where g_s corresponds to spin degeneracy. Thus the Zeeman effect splits the Landau level into spin up and spin down branches which doubles the density of states in a Landau level. This

spin effect is more pronounced at higher magnetic fields as Zeeman energy increases linearly with the magnetic field.

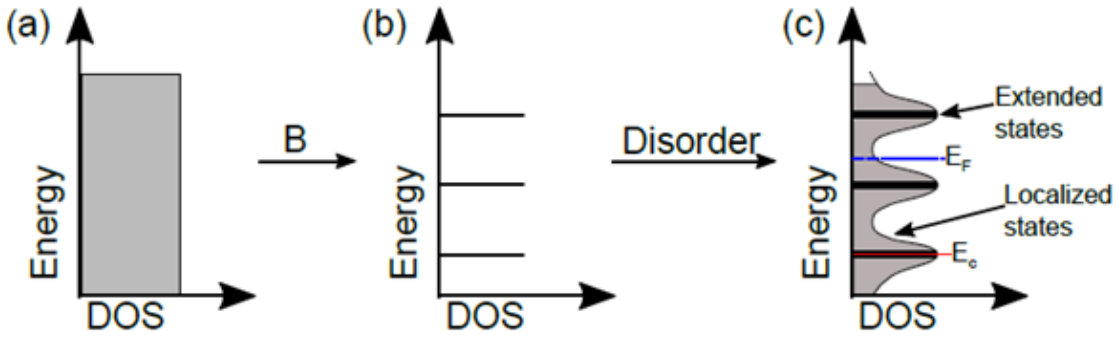

Figure 2.24 – Density of states under application of magnetic field. (a) Typical plot of density of states (DOS) versus energy E in 2D. (b) The 2D DOS splits into discreet Landau levels in presence of large transverse magnetic field. (c) In presence of disorder, the Landau level splits into band of extended states, separated by localized states. Figure adapted from [35].

2.5.4 Integer Quantum Hall effect

The Landau quantization theory assumes an infinite plane without any physical boundary conditions. However, in reality, the samples are finite in size and have a physical boundary. Classically speaking, at the edges of the sample we can imagine that the charged particles moving in circles at the edge must collide with the boundary and in the presence of magnetic field the only option for this particle is to bounce back and carry on with the forward motion. Quantum mechanically, at the edges of the sample, the electron density drops to zero and introduces a confining potential in the y direction $V(y)$:

$$\left[\frac{p_y^2}{2m^*} + \frac{1}{2}m^*\omega_c^2\left(y - \frac{\hbar k_x}{\mid e \mid B}\right)^2 + V(y)\right]\eta(y) = \epsilon\eta(y). \tag{2.5.4.1}$$

At the edges, the confinement potential causes the Landau levels to be lifted upwards and forces them to cross the Fermi energy at a finite distance, shown in figure 2.25a is the main reason for the Hall quantization. Hence even though the bulk having no states is insulating, at the edges there are non zero DOS where Landau levels cross the Fermi energy. At these crossover points , there emerges one dimensional edge channels. These edge channels are chiral and only propagate in one direction and hence back scattering occurs only if there are some means to transport the electron to the counter propagating edge at the opposite edge of the sample and given that the edges are macroscopically separated, backscattering is nearly impossible in the Quantum Hall regime.

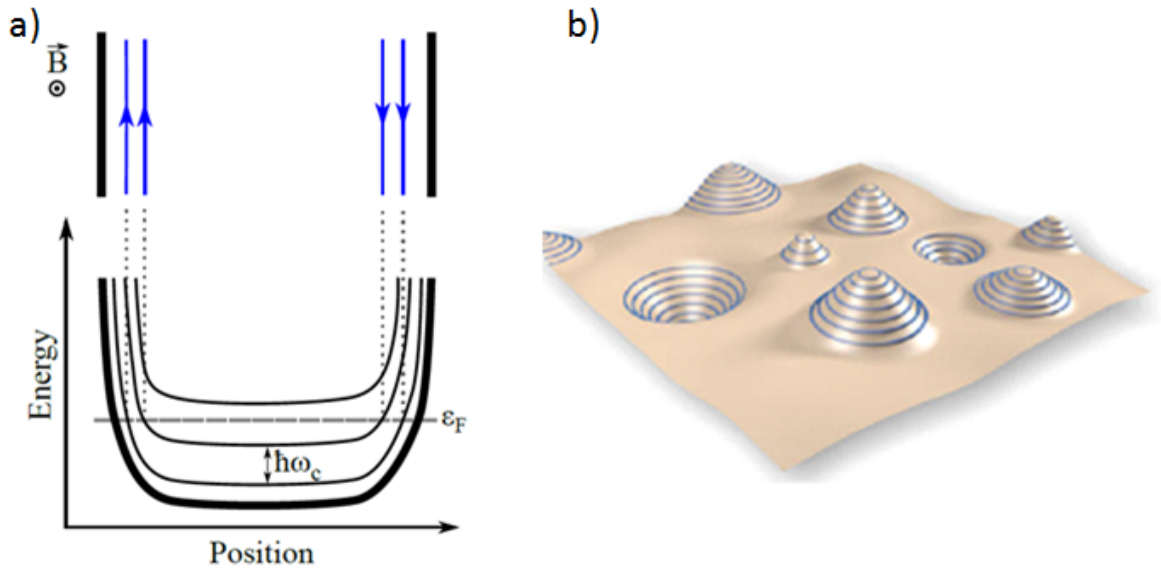

Figure 2.25 – a) Landau levels bending up at the edges due to confining potential of the physical edge. One dimensional edge channels emerge when landau levels cross the fermi level. Figure adapted from [36]. b) Localized states depiction in a single particle picture. Spatial varaiation of electrostatic potential due to disorders in the sample. Electrons are trapped in the valleys and hills of the disorder landscape.(Their orbits are indicated in blue.) adapted from [34]

Using the edge concept, the conductance of a completely filled single Landau level could be calculated as $G_n = \frac{e^2}{h}$.

Hence the conductance due to n completely filled Landau levels would be:

$$G_n = n\frac{e^2}{h}. \tag{2.5.4.2}$$

This explains that the Hall resistance is quantized when 'n' Landau levels are completely filled with filling factor ν=n . However, it does not explain the formation of plateaus as such why the Hall resistance remains constant even though the filling factor is varied using the magnetic field around ν=n. Here comes the important role of disorder or impurities which strongly influences the width of the resistance plateaus.

In reality, samples are seldom ideal and disorder is present due to possible impurities due to internal or external factors. These impurities lead to broadening of the Landau levels as shown in the figure 2.25b. The disorder potential causing the broadening of the Landau levels also divides the electron system into localised states and extended states. As shown in the figure 2.25b, the electrons could be localised either in randomly distributed hills and valleys created by the disorder potential. Using this concept of separation of DOS into localized and extended states, it is possible to explain the zero longitudinal resistance and the constant transverse resistance plateaus for wide range of magnetic field.

As shown in the figure 2.26a, let us consider a situation where there are 'n' completely filled Landau levels with the n^{th} Landau level being unoccupied. When we decrease the magnetic field, the Landau level 'n' is being filled by electrons. These electron occupy the hills or valley sites, at the equipotential lines that enclose the disorder as shown in the previous figure 2.25b. The Fermi level falls into the region of localized states. Thus these added electrons are localized

somewhere in the bulk and do not contribute to the electronic transport measured at the edges. As a result Hall resistance remains constant at the plateau and the longitudinal resistance at zero in spite the increase in the magnetic field.

On further decrease of the magnetic field, the extra added electrons enclosed in the disorder equipotential line in the bulk almost touches the opposite edges as shown in the figure 2.26c. Hence the longitudinal resistance takes a non zero value as the electron leaks from the upper edge to the lower as it is backscattered due to its chirality. During the same time transverse Hall resistance is no more quantized and is in the process to jump to the next lower possible plateau called as plateau transition state. A clear transition of the Hall resistance between the plateaus is accompanied by a peak in the longitudinal resistance.

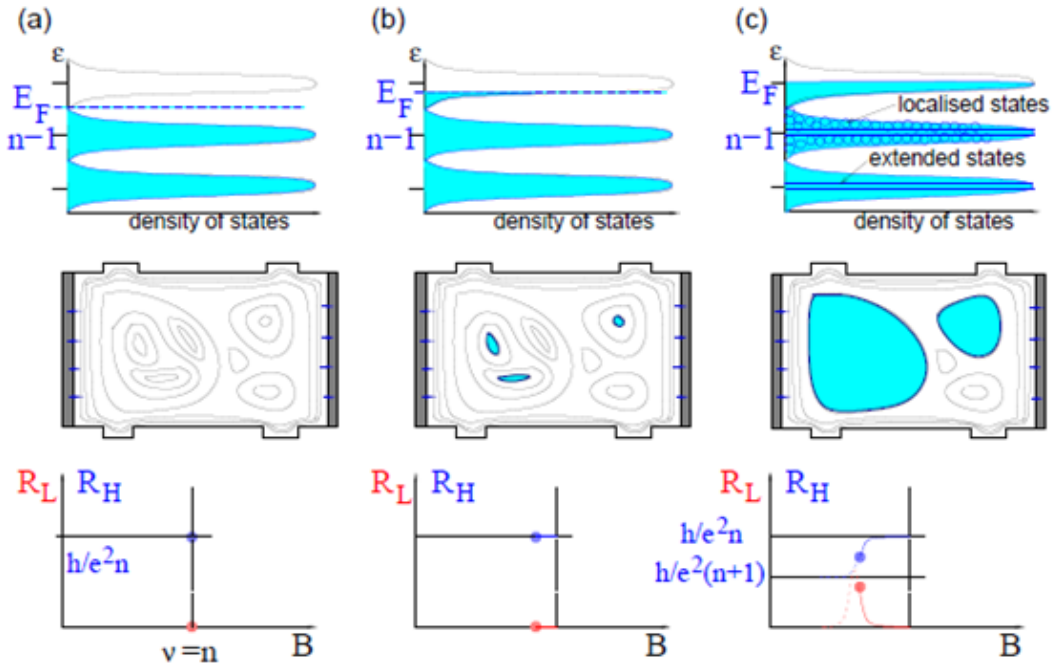

Figure 2.26 – Description of Quantum Hall effect. The (impurity-broadened) density of states are shown in the first row for increasing fillings (a)-(c) described by the Fermi energy E_F . The second row represents the impurity-potential landscape the valleys of which become successively filled with electrons when increasing the filling factor, i.e. when lowering the magnetic field at fixed particle number. The third row depicts the corresponding Hall (blue) and the longitudinal (red) resistance measured in a six-terminal geometry, as a function of the magnetic field. The first figure in column (c) indicates that the bulk extended states are in the centre of the DOS peaks, whereas the localised states are in the tails. Figure adapted from Mark Goerbig chapter.[32]

Thus the formation of localised states due to disorder forms a crucial role to observe quantum Hall plateaus. In the absence of disorder, the plateaus and thus the zero longitudinal resistance would be observed only when Fermi level jumps from one Landau level to another shrinking the plateaus to a single point.

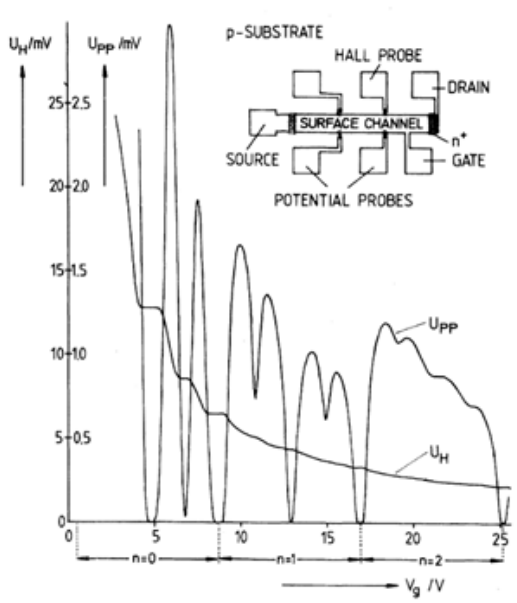

Figure 2.27 – First experimental observation of quantum Hall effect showing quantized transverse resistance plateaus with corresponding zero longitudinal resistance. Original data of iQHE by Klitzing in 1980. Figure adapted from [37]

Hence the Integer Quantum Hall effect exhibits constant transversal resistance plateaus or the steps quantized to few parts per billion to $R_h = h/ne^2$, where n is an integer. This was first discovered by Klaus von Klitzing in a two-dimensional electron system of a silicon MOSFET transistor [37] at the high magnetic field lab in Grenoble. Similar plateaus were observed in a two dimensional electron system in GaAs/AlGaAs heterostructure. After the advent of two dimensional materials like graphene which are strictly two dimensional electron system, Quantum Hall effect studies have gathered momentum.

2.5.5 Relativistic iQHE in graphene

Quantum Hall effect in graphene is distinctive and differs from those observed in conventional 2D electron systems. Graphene has linear energy dispersion and is ambipolar where the charge carriers are both electron and holes. This anomalous Quantum Hall effect was observed by Novoselov et al [38] during the discovery of graphene. Considering the four-fold degeneracy in graphene Quantum Hall plateaus occur at:

$$G_{xy} = \nu \frac{e^2}{h}, \nu = \pm g_s g_v \left(n_l + \frac{1}{2} \right). \tag{2.5.5.1}$$

where g_s and g_v have two-fold spin degeneracy and two-fold valley degeneracy respectively giving four-fold degeneracy for each Landau levels. The sign +/- in the filling factor ν corresponds to the charge carriers electron and holes. Thus the QH plateaus are expected in the position centred around:

$$\nu = \pm 4n + 2 = \pm 2, \pm 6, \pm 10, ... \tag{2.5.5.2}$$

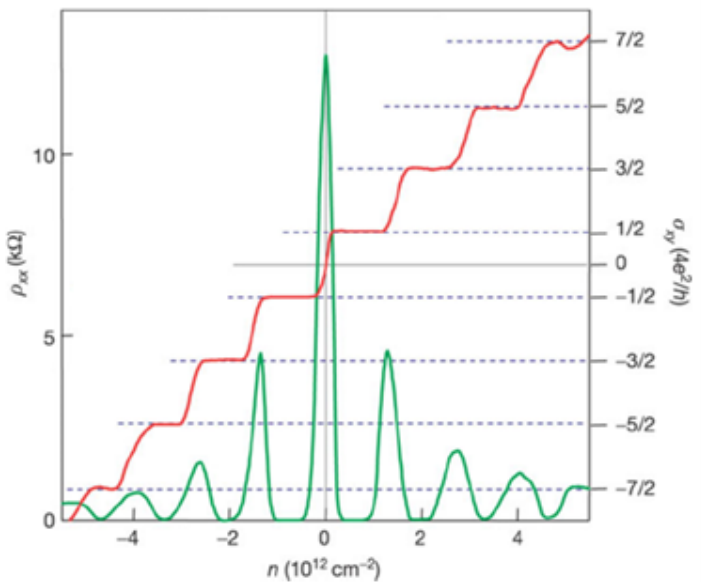

Figure 2.28 – Experimental observation of Quantum Hall effect for massless Dirac fermions. Shown in the figure are Longitudinal resistivity ρ_{xx} (green) and Hall conductivity ρ_{xy} (red) with carrier concentration n at B = 14T and T= 4K. This shows that the half-integer QHE is exclusive to 'ideal' graphene. Figure adapted from Novoselov et al.[38]

We can derive the energy spectrum of relativistic Landau levels in case of graphene using the Dirac equation in presence of magnetic field given as:

$$E_{n_l} = \pm\sqrt{2e\hbar v_F^2 \mid n_l \mid B}, \tag{2.5.5.3}$$

where $n_l = 0, \pm1, \pm2, ...$ and $\pm$ corresponds to Landau levels of electrons and holes respectively.

This equation signifies that the relativistic energy dispersion has a square root dependence on the magnetic field and Landau level index whereas in the previously discussed QHE in case of 2D electron systems had a linear dependence. Hence the Landau levels are no more equally spaced in energy but the adjacent Landau level energy increase according to:

$$\Delta\epsilon_n = v_F\sqrt{2\hbar eB}\left(\sqrt{n+1} - \sqrt{n}\right). \tag{2.5.5.4}$$

Secondly, the equation also points that there is a Landau level at zero energy occupied by both electron and holes unlike the case of 2DEG systems. In case of zeroth Landau level, it has been found that while transverse conductance shows a step-like feature neither of the resistances longitudinal and transverse exhibit a plateau or the zero resistance. Highly insulating behaviour is observed in case of longitudinal resistance which further increases under higher magnetic fields.

Further, as the sample preparation techniques improved, graphene becomes cleaner with higher mobility, and many groups have then found many additional plateaus in Quantum Hall effect. At high magnetic fields the Kim group at Columbia U.[39] discovered QH plateaus at filling factors ν =0, +1, +4. Later Dean et al [11] in the same lab observed the QH plateaus at

all the integer values of the filling factor in the graphene supported by atomically-flat hBN flakes.

The appearance of these plateaus has been attributed to breaking of spin and valley symmetry of the Landau levels. The breaking of spin symmetry is due to Zeeman energy splitting which is enhanced further by exchange interactions between electrons in graphene and 2DEG. The breaking of valley symmetry is attributed to valley anisotropy induced by lattice distortion arising from short range electron interactions and electron phonon interactions. The lifting of degeneracy causes intermediate filling factors at ν =1,2,3.. and the quantization of Hall conductance becomes:

$$G_{xy} = \pm\nu\frac{e^2}{h}, \nu \in N. \tag{2.5.5.5}$$

The Landau levels due to broken symmetry have small energy gap and thus difficult to observe them during the experiments. If the disorder level is more compared to the energy gap, the adjacent Landau levels would mix and the observation of well defined plateaus would be difficult. However due to advanced fabrication techniques such as hBN encapsulated graphene devices, the disorder level is reduced significantly and the broken symmetry Landau states are seen well resolved. The integer Quantum Hall effect in one of our edge contacted hBN encapsulated device measured at 16T magnetic field and 20mK temperature is shown in the figure 2.30.

2.5.6 Devices and iQHE measurements

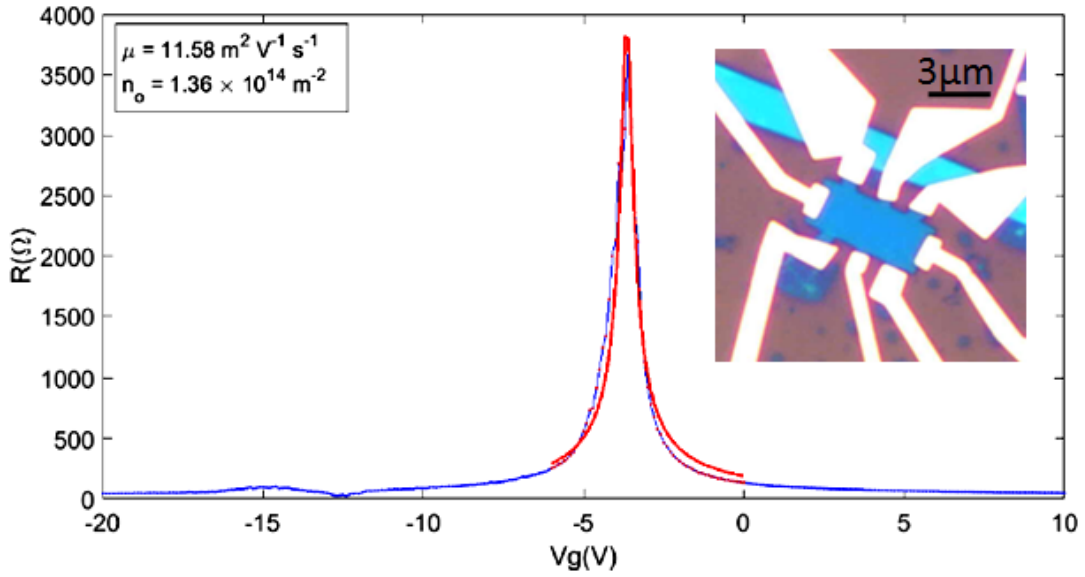

Figure 2.29 – (inset)Edge-contacted hBN/Graphene/hBN Hall bar (device109). Plot of field effect curves (in blue) for device109 at low temperature of 20mK. The red curve is the fit to calculate the mobility of graphene.(Formula 2.5.6.1)

An example device (Device109) which is a edge-contacted hBN-encapsulated device is shown in the figure 2.29(left). All the measurements were carried out in a dilution refrigerator explained in the section 2.3 along with the help of low-frequency lock-in measurement techniques. The device field effect characteristics at lower temperatures is shown in the figure 2.29 right. The

Dirac point is observed close to zero indicating no extra doping by impurities. The on state resistance is as low as 25 Ω. The mobility at 20 mK temperature for this device was found out to be $115,800 cm^2/V.s$ using the fit (red curve in figure 2.29) with the formula as a function of gate voltage given below.

$$R = \frac{L}{We\mu\sqrt{(n_0)^2 + [7.56 \times 10^{10}(V_g - V_d)]^2}} + R_C \tag{2.5.6.1}$$

where L and W are length and width of the device, V_d is the Dirac volatge and R_c is the contact resistance. Mobility of the device μ and residual carrier concentration n_0 are the unknown variables are estimated by fitting the experimental data.

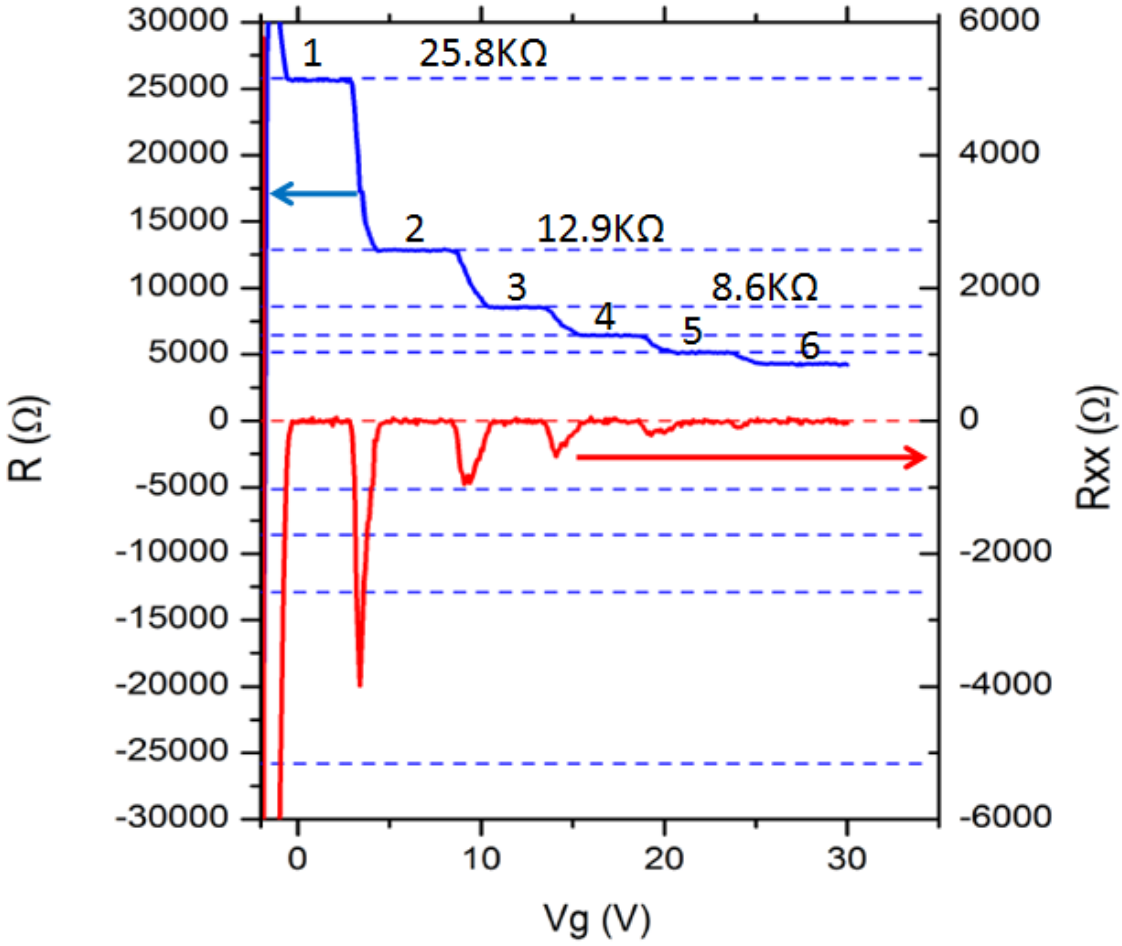

Figure 2.30 – Integer quantum Hall effect showing all integer plateaus (ν=1,2...6) taken at temperature 20mK and magnetic field of 16T for the device109. R_{xx} longitudinal resistance in red and R_{xy} transverse resistance in blue.

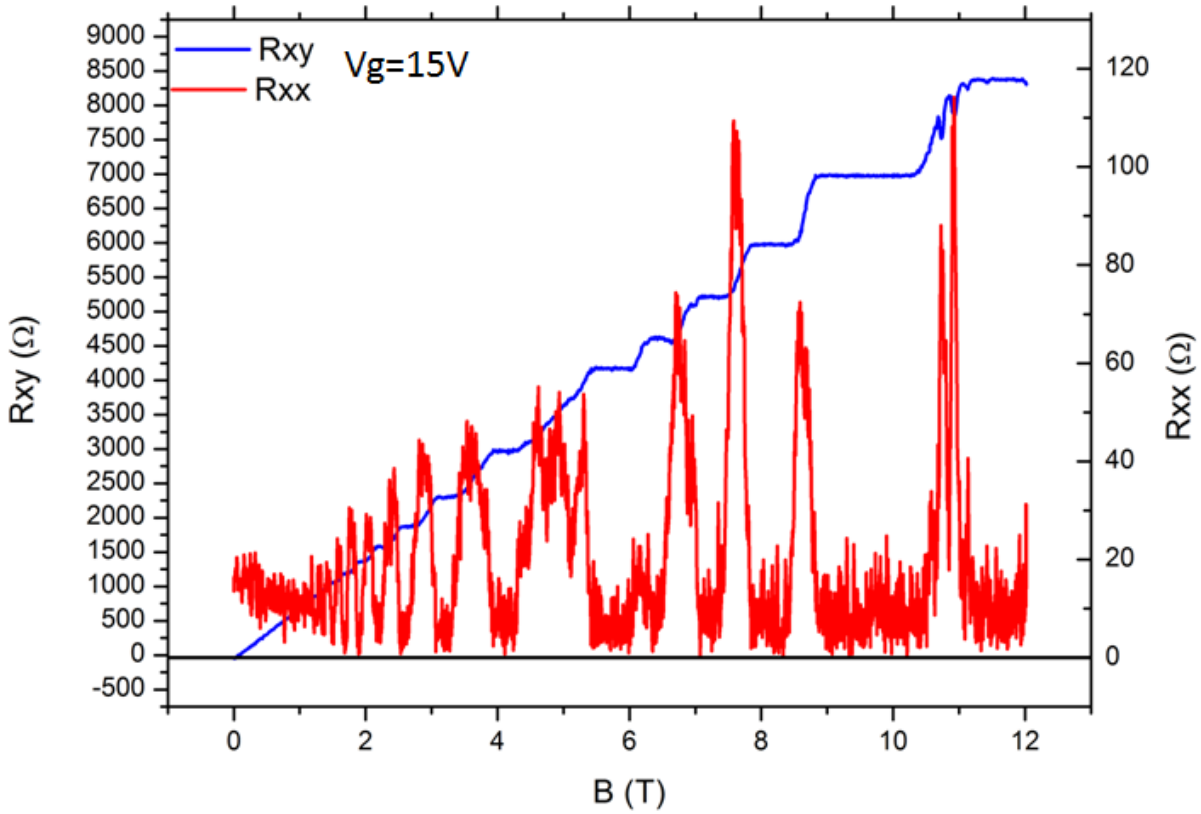

Figure 2.31 – Magneto-resistance measurements at gate voltage 15V and temperature 20mK with magnetic field varied from 0 to 12T for the device109. R_{xx} longitudinal resistance in red and R_{xy} transverse resistance in blue.

The figure 2.31 shows the magneto-resistance characteristics of the device with a gate voltage of Vg=15 V. It could be seen that well defined QH plateaus are observed with vanishing longitudinal resistances. It could be noted that after 6T the symmetries are broken we could observe n=3,4,5 and 6 plateaus at integer multiples. The quantum Hall effect can also be studied by fixing the magnetic field knob and varying the electric field that is the gate voltage of the device.

The figure 2.30 shows the plot of R_{xx} and R_{xy} versus the varied gate voltage of the device at fixed magnetic field of 16T. It can be seen that the degeneracy is completely lifted at 16T and we could observe all the integer valued plateaus from G= e^2/h to $6e^2/h$. The figure 2.32 is called a Landau fan diagram which is a 2D plot where conductance G_{xy} is measured versus gate voltage V_g at different magnetic fields. Different colour in the plot represents each e^2/h plateau and all the plateaus from 1 to 8 could be observed in the graph.

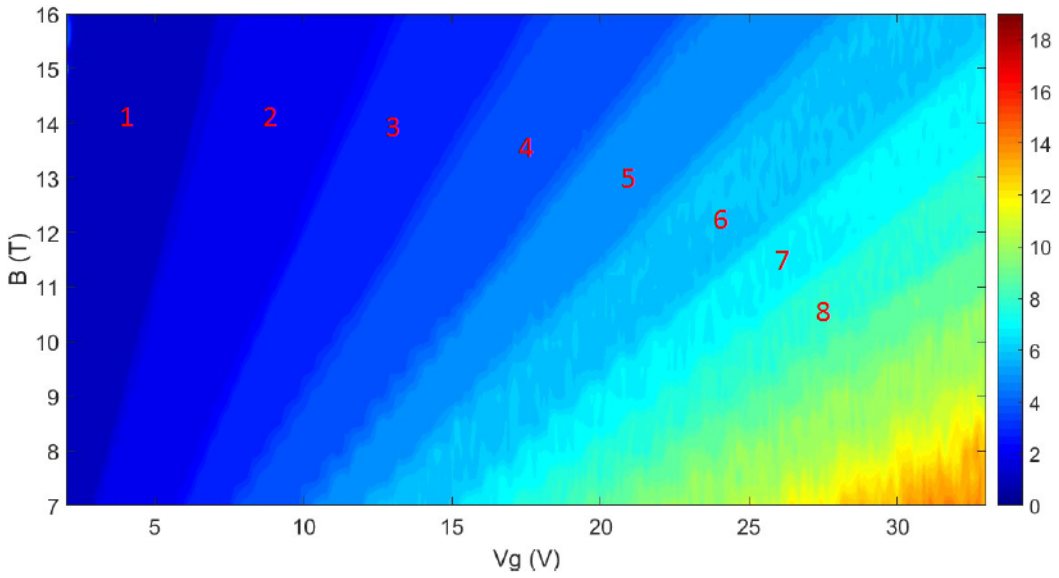

Figure 2.32 – "Landau fan" diagram at temperature 20mK and varying magnetic field(0-16T) and electric field(0-30V) for the device shown in the figure 2.29. Each plateau has its filling factor assigned in red.

2.5.7 Ballistic transport and Landau-Buttiker formalism

In the section of classical transport, we discussed about the diffusive transport because of the collision and that mobility is higher when mean free path increases. when the mean free path is very large such that it exceeds the dimensions of the device, then the transport is said to be ballistic transport. Hence this can no more be explained using the Drude diffusion transport model instead could be described as electronic conduction similar to wave propagation in a waveguide as explained by Landauer-Buttiker formalism.[40] In this model, it was defined that the conductance is quantized in the ballistic regime and the current transport occurs through the number of transverse mode M allowed in the waveguide. The two terminal conductance of such a ballistic conductor is given by:

$$G = \frac{2e^2}{h} M T_r, \tag{2.5.7.1}$$

where T_r is the transmission probability between the conductor and the contacts.

If we consider low-contact resistance and the complete transmission of the modes from conductor to contacts, the device is completely ballistic and the conductance is quantised given by:

$$G = \frac{2e^2}{h} M. \tag{2.5.7.2}$$

We can recognize that this ballistic transport formula is similar to that of quantized conductance in case of the integer QHE. Hence it could be explained that in case of the QHE the transport that happens at the edges is ballistic. These edge modes are topologically protected and could be considered as perfectly ballistic one-dimensional channels.

2.6 Fractional Quantum Hall effect

Over a period of time, due to improvement in many factors from novel 2D electron systems, better fabrication techniques together with the availability of higher magnetic fields, the devices and measurement techniques improved significantly in terms of mobility approaching the ballistic regime at low temperatures. These 2D electron samples exhibited excellent integer Quantum Hall regimes. For the first time in the history, D. C. Tsui, H. L. Stormer, and A. C. Gossard[41] observed an anomalous Hall plateau at transverse resistance $3h/e^2$ accompanied by a dip in the longitudinal resistance in a high mobility sample where the lowest level spin polarised Landau level was 1/3 filled. Initially this result was surprising and it was attributed to formation of Wigner solid or charge density wave state with triangular symmetry.

Meanwhile Laughlin [42] had already deduced that the Hall resistance is the ratio of the magnetic flux quanta (h/e) and the electronic charge. From this purview, they had suggested that quasiparticles with fractional electronic charge could be the reason for the 1/3-filled quasi one dimensional system. Later the same people observed strikingly new structures at Landau filling factors ν=1/3, 2/3, 4/3, 5/3, 2/5, 3/5, 4/5, and 2/7. [43] These results suggested the existence of fractional quantization of the Hall effect. One of the first results of HL Stomer et al. [41] is presented in the figure showing the fractional Hall plateaus in transverse resistance and corresponding minimums in the longitudinal resistance.

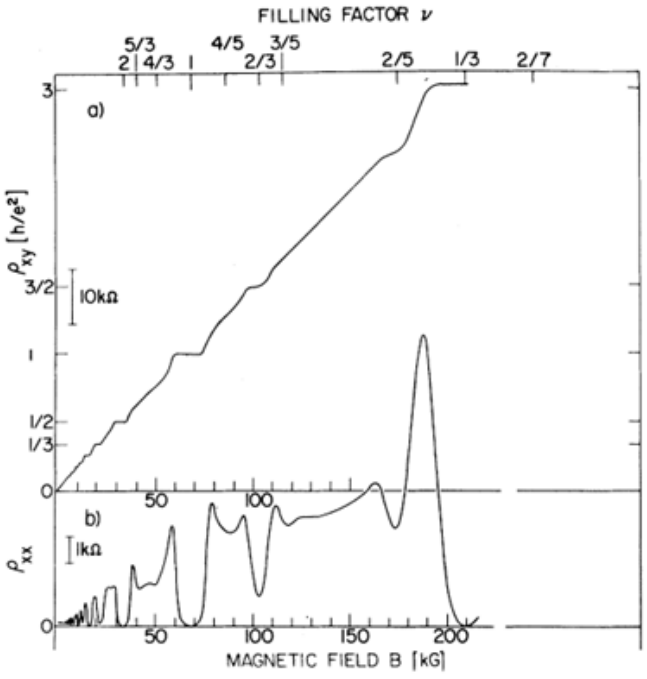

Figure 2.33 – First experimental observation of fractional quantum Hall effect in 2DEG GaAs/AlGaAs in 1983. Transverse resistance exhibits plateaus at fractional steps at 1/3,2/3 etc.. with corresponding dips in longitudinal resistance. Devices were measured at T=0.55K. Figure adapted from [41].

As we explained previously, integer Quantum Hall effect has edge transport where the electrons are non-interacting. It is a single particle effect and Coulomb interactions are neglected for the study. The fractional Quantum Hall Effect (fQHE) could be understood on the basis of interaction between the electrons and hence is a many particle problem. In case of fQHE the

charged electrons can avoid one another in energetically advantageous way unlike iQHE where electrons are packed closely without any possibility of avoidance. The electrons can rearrange themselves to reduce the Coulomb energy while maintaining kinetic energy constant. Several theoretical concepts and models have been put forward by many to understand the concept of fQHE. In the following section we would discuss the two important theories, Laughlin's wavefunction theory by Laughlin[42] and composite fermions theory by J.Jain.[44]

2.6.1 Laughlin theory

In order to explain the electron correlated fractional quantum Hall theory, Laughlin came up with a concept of attaching vortices to an electron where vortices are nothing but one flux quantum h/e of the magnetic field. Hence for example in the fQHE state ν=1/3, each electron is occupied by three vortices to minimize the Coulomb energy as such to reduce the electron-electron repulsion. In general for ν=1/q, there would be q vortices attached to each electron. Based on the concept, Laughlin[42] proposed a many body wavefunction which describes the formation of fractional Hall states at filling factors ν=1/q in the lowest Landau level given by:

$$\psi_{1/q} = \prod_{i<j}(z_i - z_j)^q exp\left(-\frac{1}{4l_B^2}\sum_i \mid z_i \mid^2\right), \tag{2.6.1.1}$$

where z_i is the position of i^{th} electron. This wavefunction includes the Coulomb interaction term and a Gaussian wavefunction representing the ground state of non interacting charge particles.

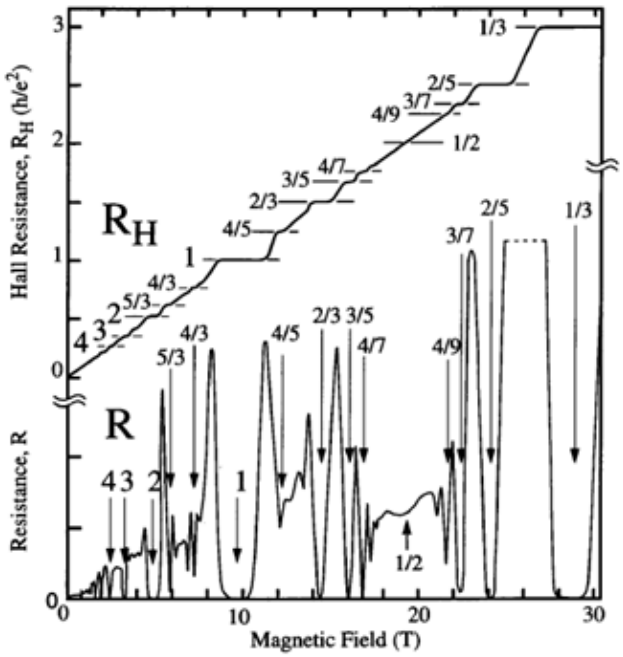

Figure 2.34 – Further more fractional plateaus were observed in ballistic 2DEG systems. Figure adpated from [45]

The above wavefunction was based on the assumption that all the electrons are spin polarised in the lowest Landau levels and thus pushing the q to be an odd integer number. In

fact the proposed waveform could be accounted only for the ν=1/q fractional states where q is an odd integer. Meanwhile, several other plateaus were experimentally discovered of the form, filling factor ν =p/q where q was an odd integer, such as 4/3, 5/3, 2/5 etc. On the same lines, Laughlin's wavefunction was generalised for the fractional states with filling factor $\nu = 1 - 1/q$ taking into account the particle hole symmetry. Further to explain the other fQHE states, Haldane[46] and Halperin[47] [48] extended Laughlin's theory with iterative hierarchical model where a daughter state occurs in presence of a parent state. Parent state are of form Laughlin like and condense into daughter state due to Coulomb interaction. This scheme could explain the fractional states of type $\nu = 1/(2q + 1)$ where denominator is odd. However the fractional states having even denominator filling factors could not be explained by the current approach which brings us to an alternative elegant model called composite fermion theory discussed in the next section.

2.6.2 Composite fermions

The Laughlin's quasiparticles were complex in the part that they do not obey Fermi-Dirac statistics or the Bose Einstein's statistics instead are found to follow a more general "anyonic" statistics. With the experimental observation of even denominator fractional states, there needed a new unified theory to shed light on these new fractions. Jainendra Jain proposed [44] [49] a new unified theoretical approach to explain both the integer quantum Hall effect and also the additional fractional plateaus of the form:

$$\nu = \frac{p}{2kp \pm 1}, \tag{2.6.2.1}$$

where k and p are integers.

This theory is again based on the concept of coupling electrons and vortices. However in this case when electrons are coupled with the even number of vortices, the new quasi particle is called as composite fermion (CF). An electron dressed with odd number of flux quanta (vortices) are called as composite boson which obey the Bose Einstein's statistics whereas composite fermions defined before follow Fermi-Dirac statistics. Since the magnetic field is integrated to electron in form of flux quanta, these composite particles are virtually in a magnetic field free region. Thus the composite bosons condensate into the ground state with an energy gap in accordance with Bose condensation which are seen as fractional states. The plateau formation is similar to that of iQHE due to disorder fluctuation and carrier localization but with new kind of fractionally charged quasi particles.

In the case of composite fermions, instead of condensation they fill up according to Fermi statistics forming a compressible Fermi sea and cannot form a plateau like composite bosons. If from now, the magnetic field is increased, the effective magnetic field would be:

$$B^* = B - B(\nu = 1/2). \tag{2.6.2.2}$$

Increase in the magnetic field will lead to Quantum Hall states but with integer values of the effective filling factor[47]:

$$\nu^* = \frac{n_e h}{(eB^*)}. \tag{2.6.2.3}$$

Hence this theory deduces that fractional quantum Hall effect is nothing but the integer Quantum Hall effect of weakly interacting composite fermions. The generalised filling factor in accordance to this theory would be:

$$\nu = \frac{\nu^*}{p.\nu^* \pm 1}, \tag{2.6.2.4}$$

where p is an even integer number denoting the number of flux quanta coupled to every electron.

Composite fermion theory has been pretty successful in explaining the different observed fractional states. However still additional states like 4/11, 5/13 observed could not be supported by this theory. Further the fractional quantum Hall effect of composite Fermions because of weak residual interaction between the same has been proposed and observed. Finally, the fractional charge in the quasi particles of fQHE is not just a theoretical concept but has been proven experimentally. Shot noise measurements where the current fluctuations are proportional to the carrier charge have been measured to confirm the fractional charges in the fractional states.[50]

2.6.3 The curious case of 3/2 and 5/2 states

All the odd denominator fractional states have fairly been explained by Laughlin's theory or extensions of it like composite fermion theory. The even denominator states like 1/2 were explained by composite fermion theory but one could not observe plateaus in transverse resistance or a falling longitudinal resistance. Strikingly further even denominator fractional states were experimentally observed such as 3/2, 5/2 [51], 7/2 [52] and 1/4[53] and a pronounced plateau was observed in the case of 5/2. The 5/2 state was postulated to be a 1/2 state in the next higher Landau level. But mysteriously one could observe a well defined plateau at ν =5/2. Many possibility such as composite fermions forming pair like cooper pairs have been speculated[54],[55]. The another peculiarity of this state is that they follow the fractional statistics of anyons [56]. Nevertheless, at present there is no clear explanation for the occurrence of this state which explains the labyrinthine behaviour and origin of fQHE.

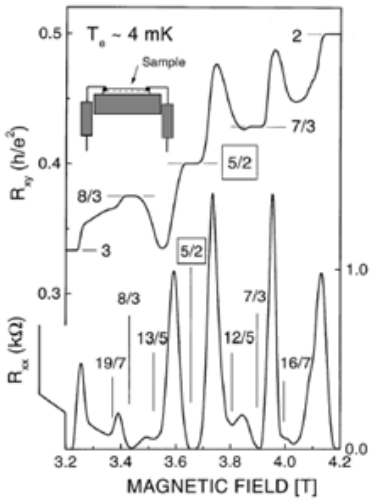

Figure 2.35 – Experimentally observed even denominator fractions. Figure adapted from W.Pan et al [57]

2.6.4 Fractional states in graphene

As explained in the beginning of the chapter, graphene is a unique and special material compared to conventional 2D electron systems where graphene's electrons are massless relativistic particles. It has inequivalent Brillouin zone corners K and K' which results in four-fold symmetry. This four-fold spin valley symmetry is described by SU(4) group which includes SU(2) spin and SU(2) valley isospin. They are broken by lattice effects resulting in anomalous Quantum Hall effect discussed in previous section. Due to the same reason the fractional states in graphene are also different to that of convention 2D electron systems.

Disorder in the system makes it difficult to observe any possible fractional Hall effects. With the improvement in the mobility of the graphene either by suspending it or using an atomically flat hBN substrates, fractional Hall plateaus for $\nu < 1$ [58],[59] were observed my many groups. Later in course of time, mobility in graphene improved multi-fold with the advent of edge contacted hBN encapsulated graphene stressed throughout in this chapter lead to discovery of fractional states with higher filling factors $\nu > 1$ [13],[60] [61],[62].

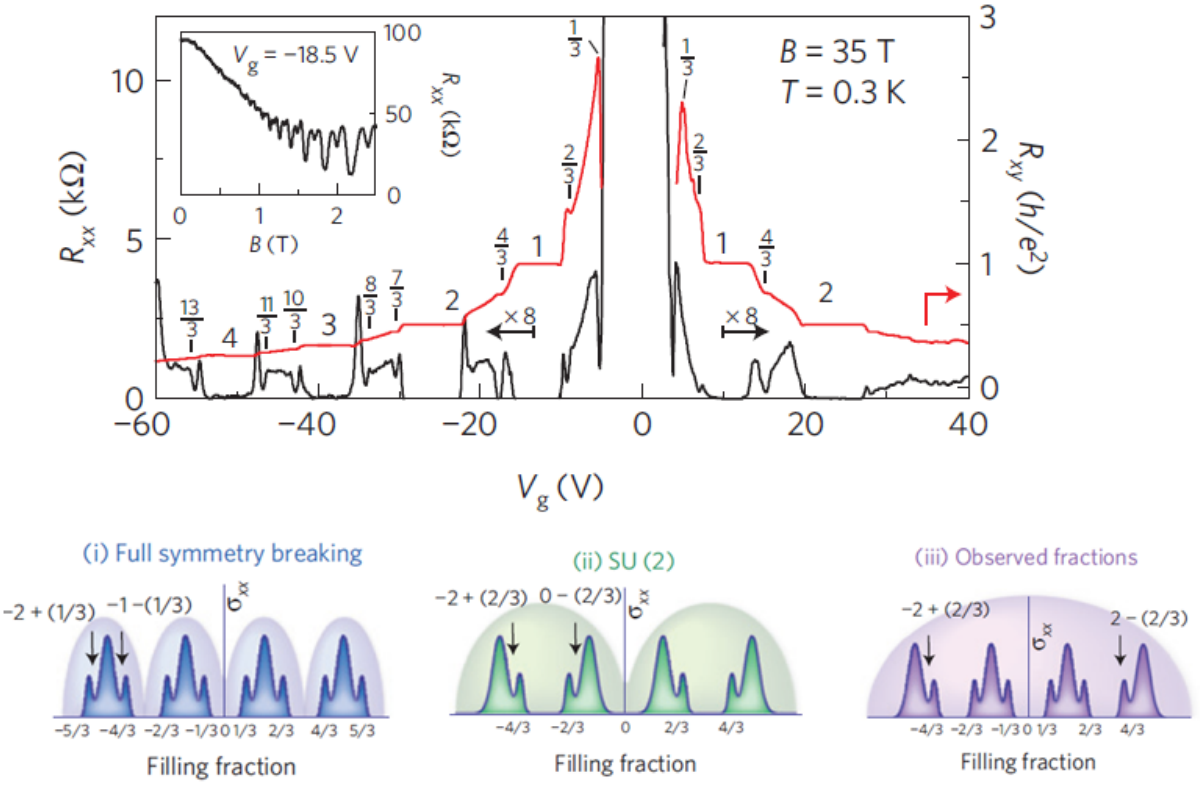

Figure 2.36 – Multi-component fractional Hall effect in graphene/hBN samples:(Top) plot of longitudinal (left axis) and Hall resistance (right axis) versus gate voltage at B = 35T. Inset depicts SdH oscillations at gate voltage of -18.5 V. (Bottom) Representation of the FQHE hierarchy observed by Dean et al[13]. The expected electron–hole symmetry is shown with assumptions (i) full lifting of all internal degeneracies (ii) full breaking of only one degeneracy (iii) schematic diagram of the fractions observed in the article. Arrows explains particle–hole conjugate pairs in each scenario.

The multi-component fractional Hall effect in graphene was observed by Dean et al[13] group where they measure fractions at filling factors ν=1/3,2/3 and 4/3 in n=0 Landau level and at ν=7/3,8/3,10/3,11/3 and 13/3 in the n=1 Landau level as shown in the figure 2.36. The figure 2.36b gives the representation of possible fourfold symmetry breaking of graphene.

In figure2.36b i) we could notice that all the degeneracies have been lifted due to coupling to the external magnetic field and that fQHE states could not mix spin/valley branches. In the figure 2.36b ii) only spin or valley degeneracy is broken and it is possible to see even numerator fractional states and finally in figure 2.36b iii) case the spin and valley fQHE states mix due to small Zeeman and valley splitting leading to Coulomb interaction mixing the branches.

Taking into account of this SU(4) symmetry in graphene Landau levels M.O Goerbig et [63] all propose a trial wavefunction based on Halperin approach for explaining the two component fQHE states. The Laughlin wave function explained in the Laughlin's theory section given as:

$$\psi_m = \prod_{j<k}(z_j - z_k)^m exp\left(-\frac{1}{4}\sum_l \mid z_l \mid^2\right). \tag{2.6.4.1}$$

This was generalised by Halperin to SU(2) symmetry taking spin degree of freedom into consideration. Here similar to his approach Laughlin's wave function was extended to SU(4) symmetry to include spin and valley degeneracies:

$$\psi^{SU(4)}_{m_1,.....,m_K;n_{ij}} = \phi_{m_1,.....,m_4}\phi^{inter}_{n_{ij}} e^{-\sum_{j=1}^{k} - \sum_{k_j=1}^{N_j}|z^{(j)}_{k_j}|^2/4}. \tag{2.6.4.2}$$

The first term consists of product of four N_j particle Laughlin's function given by:

$$\phi^L_{m_1,....m_K} = \prod_{j=1}^{4}\prod_{k_j<l_j}^{N_j}\left(z^{(j)}_{k_j} - z^{(j)}_{l_j}\right)^{m_j}, \tag{2.6.4.3}$$

which is a product for each spin valley component denoted by m_1, m_2, m_3 and m_4.

The correlations between the different components denoted by indices i,j=1,...4. is given by:

$$\phi^{inter}_{n_{ij}} = \prod_{i<j}^{4}\prod_{k_i}^{N_i}\prod_{k_j}^{N_j}\left(z^{(i)}_{k_i} - z^{(j)}_{k_j}\right)^{n_{ij}}. \tag{2.6.4.4}$$

Here m_j must be odd to take into account of Fermionic statistics of electrons whereas n_{ij} that defines the correlation between i and j states could also be even.

Based on specific spin and valley configurations $1 = (\uparrow, K), 2 = (\uparrow, K'), 3 = (\downarrow, K)$ and $4 = (\downarrow, K')$, they derive independent filling factors given by:

$$\nu_f = \frac{1}{m}; \nu_f = \frac{2}{2m-1}; \nu_f = \frac{4}{4m-3}. \tag{2.6.4.5}$$

2.6.5 Fractional states in graphite backgated hBN encapsulated devices

Our previous devices graphene encapsulated between the two hBN flakes showed mobility of up to 200,000 cm^2/Vs and exhibited a well-defined Quantum Hall effect. However we were not able to observe the fractional states in them owing to lower mobility in our system and being restricted to 16T of magnetic field. We decided to go for graphite back gate to further improve the screening from Si/SiO2 substrate. This device gave us a very good mobility exceeding 500,000 cm^2/Vs and also we were able to observe many fractional states as explained in the

following.

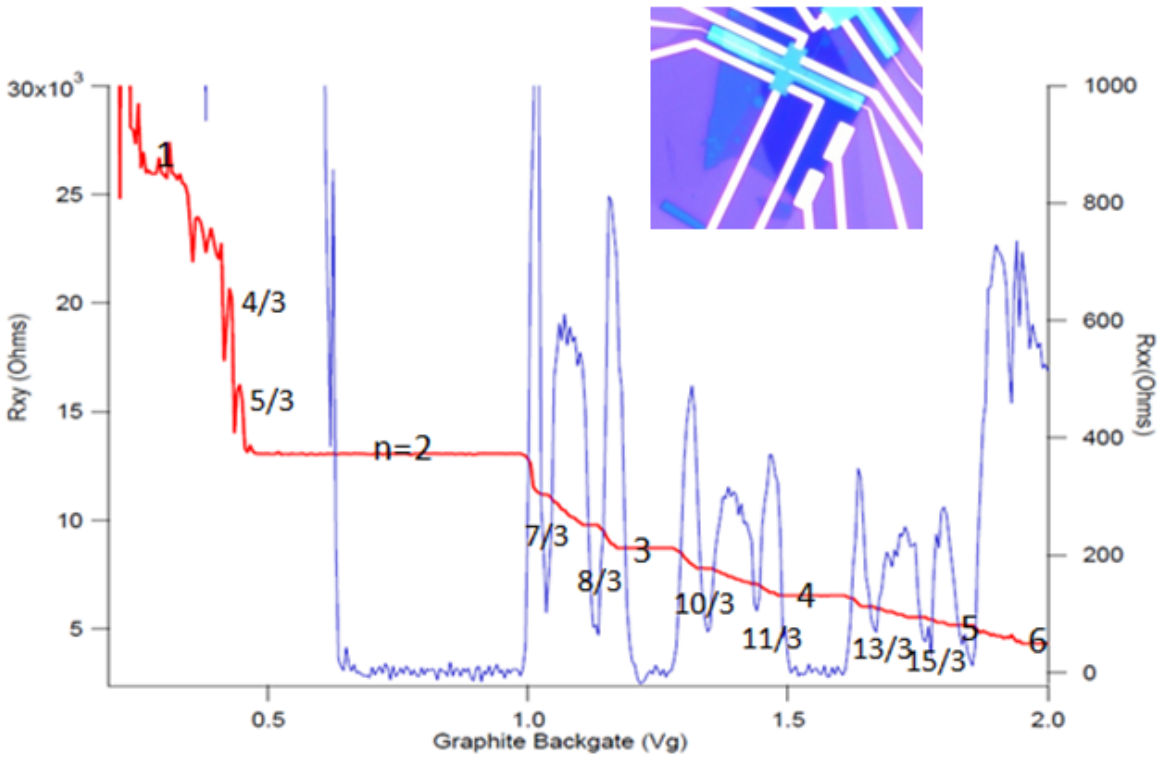

Figure 2.37 – Multi-component fractional Hall effect in our hBN/graphene/hBN/graphite sample. R_{xx} in red and R_{xy} in blue. Inset shows the Hall bar device with graphite back gate.

These electron transport measurements were carried out in a dry dilution refrigerator integrated with maximum 16T transverse magnetic field during IISc visit in Bangalore, India. The base temperature was maintained at around 20mK. The device exhibited many fractional states at n=1 Landau level at ν=7/3,8/3,10/3,11/3 and 13/3. We were also able to observe fractional states in n=0 Landau levels with the filling factor ν=4/3 and 5/3. The fractional states 1/3 and 2/3, we were not able to observe due to competing insulating phase at low density.

2.7 Noise in quantum devices

Electrical noise is an undesirable electrical signal that interferes with or distorts the original electrical signal of interest. The signal to noise ratio is important when we consider about the electronic applications. The output signal measured is a combination of original output signal along with the summation of several different types of noises, in fact modified by the device characteristics. Hence study of noise is an important specification during the electron transport measurements. When it comes to the electron transport, noise in specific, resistance noise are the dynamic fluctuations in the resistance around its time averaged mean value $\langle R \rangle$ given by:

$$\Delta R(t) = R(t) - \langle R \rangle. \tag{2.7.0.1}$$

The fluctuating resistance could give information about the dynamics of charge carriers in the devices.

According to Weiner-Khinchine theorem the power spectral density (PSD), $S_R(f)$ defined as the Fourier transform of the autocorrelation function is given by:

$$S_R(f) = \int_{-\infty}^{\infty} d\tau C_R(\tau) exp(-2\pi i f \tau), \tag{2.7.0.2}$$

where

$$C_R(\tau) = \lim_{T\to\infty} \frac{1}{2T} \left[\int_{-T}^{T} \delta R(t+\tau)\delta R(t) dt \right]. \tag{2.7.0.3}$$

is the autocorrelation function of R(t).The squared magnitude of Fourier transform of R(t) is given by:

$$S_R(f) = \lim_{T\to\infty} \frac{1}{2T} \left[\int_{-T}^{T} \delta R(t) exp(-2\pi i f t) dt \right]^2. \tag{2.7.0.4}$$

This expression is used as PSD as we measure finite length data sequences during the experiments.

2.7.1 Different types of noise in electron devices

The above explained resistance noise or electrical noise can be broadly classified into three types as given below. The differentiation is based on their spectral nature and by the dependence on the bias of the circuit.

2.7.1.1 Thermal noise or Johnson-Nyquist noise

The fluctuations across the leads of any conductor due to random motion of electrical charges at non zero temperature even without application of any current is called as thermal noise also named as Johnson Nyquist noise after the experimental observation of it. Thermal noise of the resistor could be represented by a simple model consisting of a noise voltage source in series with a noiseless resistor. Using this model the power spectral density PSD of voltage fluctuations because of thermal noise of the resistor maintained at a temperature T is given as:

$$S_V = 4k_bTR. \tag{2.7.1.1}$$

Therefore from the equation we can notice that the PSD of thermal noise is dependent only on the equilibrium temperature and the resistance. The PSD also indicates that it is independent of frequency and hence referred sometimes as White noise. This thermal noise does not give any information on charge carrier dynamics of the system. However it is very useful while calibrating the measurement setup for noise measurements as we exactly know the thermal noise of the system.

2.7.1.2 Shot noise

The time dependent fluctuations in an electrical current is referred as Shot noise. The shot noise is a non equilibrium noise due to discreetness and stochastic nature of charge carriers during the transport. In a truly Poisson type electron emission process, that is number of electrons in a given time interval is a Poissonian distribution, the power spectral density of current fluctuation

is given by

$$S_{shot} = 2e\langle I\rangle \tag{2.7.1.2}$$

where $\langle I\rangle$ is the mean current and e the unit of electronic charge.

Shot noise is predominantly used in mesoscopic physics for experimental measurements of the charge and statistics of the current carrying quasiparticles in the system. In such systems different charges like cooper pair charges (2e), fractionally charged quasiparticles have been understood because of shot noise measurements[50].

2.7.1.3 Flicker noise/ low frequency noise or 1/f noise

1/f noise is a low frequency noise whose spectral density depends inversely on the frequency, degrades the performance of devices and circuits. This has been observed in wide variety of devices including current carrying resistor and its power spectral density could be given as:

$$S_{1/f}(f) \sim 1/f^{\alpha}, \alpha \approx 0.8 - 1.2 \tag{2.7.1.3}$$

2.7.2 Low frequency 1/f noise

In electronics, 1/f noise is also called as flicker noise and is generally found below the frequency $f < 100$KHz. The low frequency noise has been widely studied to probe phenomenon such as structural phase transitions, quantum phase transitions[64] and super conducting transition[65] experiments. The electrical current fluctuations can be represented as:

$$\delta I \propto q(\delta N)\mu + qN(\delta\mu), \tag{2.7.2.1}$$

where N is the number of charge carriers, q is the electronic charge and μ is the mobility. Hence 1/f noise has been described using mobility fluctuation approach and carrier number fluctuation mechanism.

2.7.2.1 'du Pre' interpretation of 1/f noise

du Pre introduced a mechanism to understand the behaviour of spectral density of 1/f noise as represented in the figure 2.38[66]. When we consider a system with arbitrary double well potential having two accessible states separated by an energy difference E_a, the system fluctuates between these two states with a characteristic time scale T which depends on E_a. The time series of any measurable quantity of the system fluctuates randomly between the two values. If we consider this fluctuation in terms of resistance, then one of the state should correspond to R_{low} and another to R_{high}. The time series of the resistance of the system measured would fluctuate randomly between these two values. This time-series is called as Random Telegraphic Noise (RTN) as shown in the figure 2.38. The power spectral density of such a fluctuation is a Lorentzian given by:

$$S(f) \propto \frac{2\tau}{1 + (2\pi f\tau)^2}, \tag{2.7.2.2}$$

where τ is the characteristic time scale of the relaxation.

The power spectrum would be determined by $1/\tau$; For $f_\tau \gg 1$, $S(f) \propto 1/f^2$

and for $f\tau \ll 1$, PSD would be frequency independent (i.e white noise). A system will usually have a wide distribution of τ , maybe due to distribution of defect configuration.

If we consider this distribution with time scale D(τ), the power spectrum would result to:

$$S(f) = \int d\tau D(\tau) \frac{2\tau}{1 + (2\pi f\tau)^2}. \tag{2.7.2.3}$$

If we consider $D(\tau) \propto \tau^{-1}$ over a time scale $\tau_1 \leq \tau \leq \tau_2$, then

$S(f) \propto 1/f$ for a frequency range $2\pi/\tau_2 \ll f \ll 2\pi/\tau_1$.

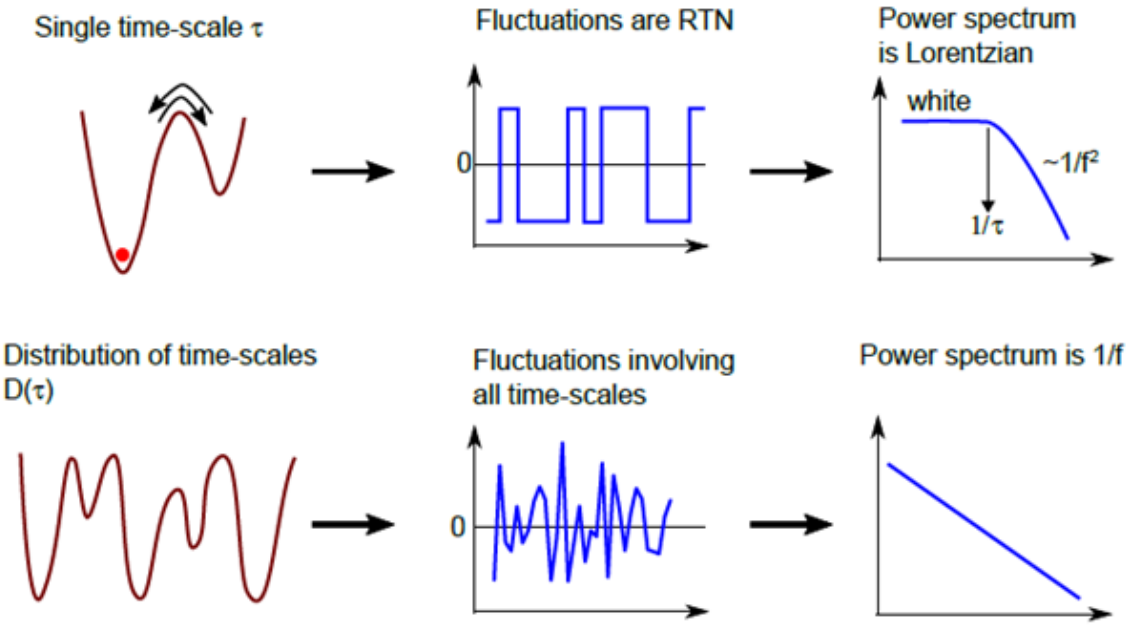

Figure 2.38 – Figure explaining the origin of 1/f PSD. During a single time scale τ, a Lorentzian PSD originating from a defect relaxation in an arbitrary double-walled-potential. Due to superposition of fluctautions with a distribution $D(\tau)$ of relaxation times in an arbitrary potential landscape, the above Lorentzian PSD develops to a 1/f PSD. Adapted from [35].

2.7.2.2 McWhorter's model

In context of semiconductors, in the same lines as du Pre interpretation, the idea got developed into McWhorter's model based on fluctuation of charge carriers[67]. In semiconductors according to this model, the major source of 1/f noise is due to trapping and detrapping of charged impurities at semiconductor-oxide interfaces. This would be activated process E_a corresponding to the depth of the trap. If defects that act as carrier traps are distributed throughout the width of the oxide and if the rate limiting process for trapping and detrapping is tunneling of carrier from bulk into the traps, then the distribution D(T) will depend on the distribution D(l) which is the distribution of distances of the trap from the interface.

Hence for a tunneling process, $\tau \propto exp(l/l_0)$

$$D(\tau) \propto | \frac{\partial l}{\partial \tau} | D(l) \propto l_0 D(l)/\tau. \tag{2.7.2.4}$$

This results in 1/f power spectrum of the resistance fluctuations if we consider a uniform distribution of the depth of the traps making D(l) constant and $D(\tau) \sim \tau^{-1}$.

2.7.2.3 Dutta and Horn model

The above explained idea of activated random process was re-casted by Dutta and Horn to understand the process behind 1/f noise mechanism [68]. It was suggested by them that the low frequency noise arises from superposition of thermally activated random processes with broad range of energies. Considering T to be thermally activated process with $\tau = \tau_0 exp(E_a/k_B T)$ then:

$$S(f) \propto \frac{k_B T}{2\pi f} D(E'), \tag{2.7.2.5}$$

where

$$F(E, f) = \frac{\tau_0 exp(E_a/k_B T)}{1 + (2\pi\tau_0)^2 exp(2E_a/k_B T)}. \tag{2.7.2.6}$$

and E' is the energy value at F(E) peak.

This Dutta-Horn model for 1/f noise provides a suitable explanation of the spectral shape for a wide range of frequency.

2.7.2.4 Mobility fluctuations model

Meanwhile, mobility fluctuations mechanism has also been used to explain the low frequency 1/f noise in which the cause is interpreted as a result of superposition of elementary scattering events where scattering cross section σ fluctuates from σ_1 to σ_2. From the mobility fluctuation model [69] the noise spectral density is given by:

$$\frac{S_I}{I^2} \propto \frac{N_t^\mu}{V} \frac{\tau\zeta(1-\zeta)}{1 + (\omega\tau)^2} \Lambda^2 (\sigma_1 - \sigma_2)^2. \tag{2.7.2.7}$$

where N_t^μ is the concentration of the scattering centres, Λ the mean free path of the charge carriers, ζ is probability that scattering centre would be in the state σ_1.

2.7.2.5 Hooge's model

It is complicated to generalize the 1/f noise mechanism and hence very difficult to obtain a meaningful figure of merit for 1/f noise. However the most commonly used figure of merit is Hooge parameter α_H which is based on the empirical formula built by Hooge[70],[71] given as:

$$\frac{S_R}{R_2} = \frac{\alpha_H}{Nf}. \tag{2.7.2.8}$$

where N is the number of charge carriers and $S_R \sim (\delta R)^2$ is the power spectral density of the fluctuations at frequency f. This model was particularly based on the mobility fluctuations of the charge carriers but later extended to other 1/f noise mechanisms.

During the experiments, it is convenient to use relative variance $\delta R^2/R^2$ for the comparison of 1/f noise magnitude defined as:

$$\frac{\delta R^2}{R^2} = \frac{1}{\langle R \rangle^2} \int_{f_{min}}^{f_{max}} df S_R(f), \tag{2.7.2.9}$$

where $\langle R \rangle$ is the average resistance, f_{min} and f_{max} lower and upper cutoff of the measured bandwidth. $\delta R^2/R^2$ parameter could be studied while varying the external parameters such as temperature, magnetic field or gate voltage.

2.7.3 1/f measurement technique

1/f noise measurement techniques have been well developed and established in Indian Institute of Science, Bangalore.[72][35][73] Below is the brief explanation about the measurement techniques followed during the thesis.

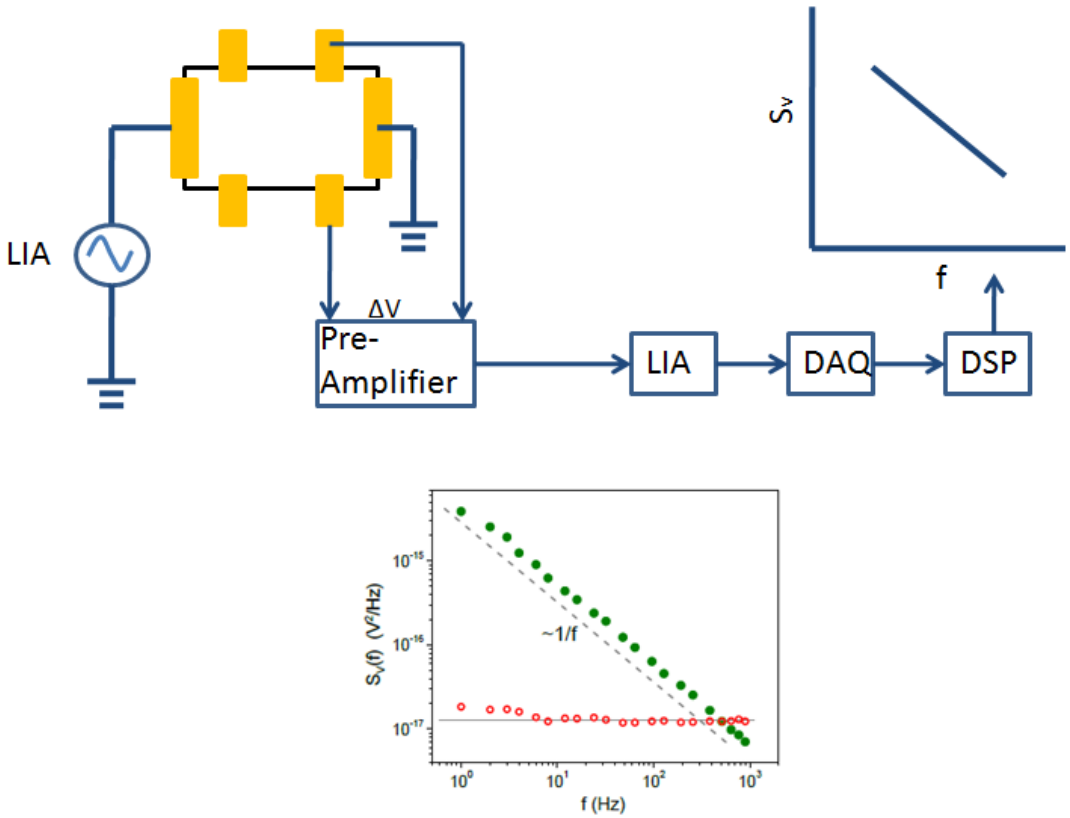

Figure 2.39 – (Top) Schematic of 1/f noise measurement technique used to measure resistance fluctuation of the device in 4-probe configuration. LIA is lock-in amplifier. (Bottom) Typical 1/f noise power spectrum for graphene in green dots and background noise in open red cirles. The grey lines indicate expected PSD.

As explained in the previous section, dynamical resistance fluctuations $\Delta R(t)$ is required in

the measurement of 1/f noise which is given as:

$$\Delta R(t) = R(t) - \langle R \rangle. \tag{2.7.3.1}$$

where $\langle R \rangle$ is the time averaged mean resistance value. The power spectral density of $\Delta R(t)$ is used in the noise characterization of the device.

In our experiments, we have used ac method introduced by John et al [74] to calculate the PSD of the resistance fluctuations. The complete noise measurement setup block diagrams is given by the figure. A constant amplitude AC current $i_{ac} = i_0 sin(2\pi f_0 t)$ is used to bias the device and the voltage fluctuations $\delta v(t)$ across the device was measured. As described in the figure 2.39, a low noise room temperature pre amplifier(SR552 or SR 554) amplifies the voltage $\delta v(t)$ which is later measured with a lock in amplifier (LIA SR380). The phase sensitive detector of the lock in amplifier demodulates the amplified voltage. We record the X and Y output voltage of the lock in amplifier simultaneously with a data acquisition card (NI-USB 6201) which are further processed by digital signal processing techniques. We use the average periodogram technique developed by Peter D Welch[75] for estimating the PSD from the measured time series. The DSP techniques used are described in the references [76][72].

According to ac method[74] of measuring low frequency noise, the PSD is given by:

$$\sum_v (f, \delta) = G_0^2 \left[S^0_{v_{BG}} (f_0 - f) + I_0^2 S_R(f) \cos^2 \delta \right]. \tag{2.7.3.2}$$

where G_0 is the total gain which is the product of the gain of used preamplifier and LIA, f is the measurement frequency ($f \ll f_0$), f_0 is the excitation frequency and δ is the phase angle of detection of the input voltage to the lock in amplifier with respect to the phase of source current. $S_R(f)$ is the PSD of the device due to resistance fluctuations and $S^0_{v_{BG}}$ is the PSD of voltage fluctuations because of background fluctuations. This $S^0_{v_{BG}}$ has noise contributions arising from various electrical components used in the measurements set up such as pre amplifier, current sources etc. in addition to Johnson Nyquist noise.

While the in phase component ($\delta = 0$) containing noise contributions from both the sample and the background is given as:

$$\sum_v (f, \delta) = G_0^2 \left[S_{v_{BG}} (f_0 - f) + I_0^2 S_R(f) \right]. \tag{2.7.3.3}$$

the quadrature component ($\delta = \pi/2$) giving only the background noise is given by :

$$\sum_v (f, \delta) = G_0^2 \left[S_{v_{BG}} (f_0 - f) \right]. \tag{2.7.3.4}$$

Thus the estimate of $S_R(f)$ is obtained by subtraction the quadrature component from the in phase component. The most important advantage of this ac technique is that the background noise is measured simultaneously with the current noise.

The figure 2.39c shows a typical graph of PSD of graphene measured at room temperature 300K. The red circles represent the measured Johnson-Nyquist noise background data which is in excellent agreement with the expected value of the Johnson-Nyquist noise represented by the grey solid line. The green filled circles is the signature of the measured PSD of 1/f noise of the

graphene device.

2.7.4 1/f noise measurement in graphene

Low frequency 1/f noise has been extensively studied in graphene[77][78]. All the reports point to the fact that the low frequency noise in graphene is scale invariant and shows a 1/f spectral dependence in the range 1KHz to 100KHz. There are so many factors affecting this one atomic layer graphene where the carriers are not only exposed directly to disorder and traps of substrate or gate oxide but also to the environmental conditions of oxygen and humidity. However interestingly it has been found out that 1/f noise amplitudes are relatively low compared to other bulk systems. Experimental studies reported on 1/f noise with different channel area explain that 1/f noise most probably originates from graphene itself rather than the contributions from metal contacts. It has also been observed that defects on edges of the graphene channels contributed to low frequency noise spectrum. There have been different reports consistently reporting noise spectrum ranging from 10^{-9} to 10^{-7} Hz^{-1} for graphene devices.

It has been describe that 1/f noise in graphene has an unusual gate dependence where the noise amplitude attains a minimum at the Dirac point with maximum resistance and growing with the increase in the gate voltage[79][80][81]. This V-shape characteristic has been reported by various groups despite the varied design and different fabrication techniques used. The same V-shape dependence was extended to M-shape dependence where noise amplitude starts decreasing beyond a critical value of gate bias voltage. The M-shape dependence has been attributed to spatial charge inhomogeneities related to the presence of electron and hole puddles in graphene. It has also been shown that the M-shaped behaviour before annealing transforming into a V-shape behaviour after annealing. The mechanism of interplay between long-range and short-range scattering play an important part in this transformation. Any water vapour or impurities adsorbed to graphene would be removed by thermal annealing, leading to the suppression of the long-range scattering effects.

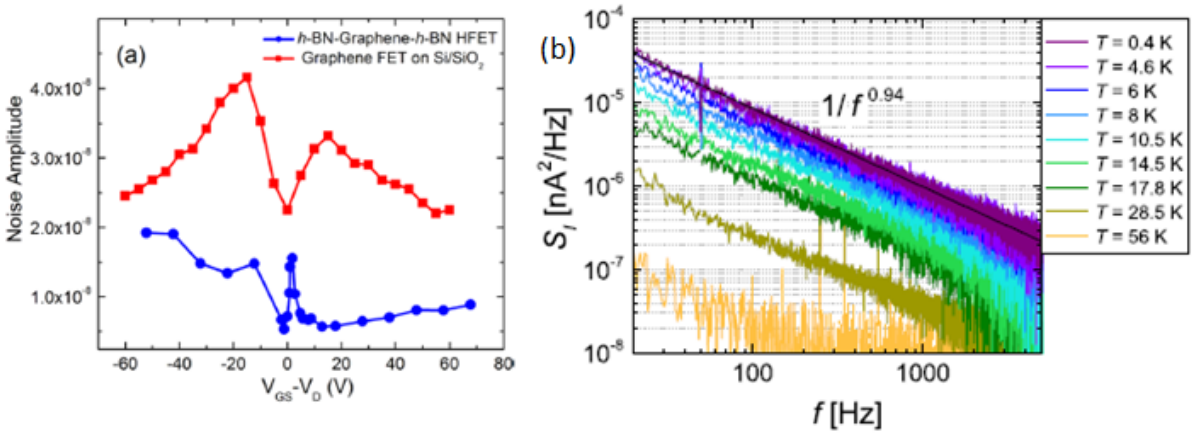

Figure 2.40 – 1/f noise studies in graphene: a) Plot of noise amplitude as a function of gate voltage with respect to Dirac point for graphene on Si/SiO_2 and hBN/graphene/hBN heterostructure. b) 1/f noise power spectral density spectrum measured at different temperatures with zero magnetic flux density, and a current of I = 10μA. A power-law fit at T = 0.4K is shown by the black solid line. Figure adapted from [82] and [83].

It has been found out by many experiments that due to the unusual gate dependence be-

haviour, the 1/f noise in graphene does not follow conventional McWhorter model. The deviation was attributed to contacts, inhomogeneous trap distribution or even significant contributions from mobility fluctuations. On the same lines, many recent studies observed the fact that there was dominant contribution to 1/f noise by the mobility fluctuations originating from fluctuations in the scattering cross-section[77].

Long environmental exposure leading to degradation of graphene has been found out to have higher level of noise amplitudes. Suspended graphene devices have been found to exhibit significantly lower 1/f noise levels compared to that of graphene devices on SiO_2[84]. Top or bottom gate electrodes deposited on graphene have been found to have similar or lower noise level in spite of mobility degradation suggesting that capping of graphene which prevents to exposure of water or organic contaminants could be used to suppress the noise magnitude. On the same lines, graphene encapsulated in hBN devices show significant reduction of noise amplitudes as compared to graphene on SiO_2 devices as depicted in the figure2.40 [82][85].

In micro or nano-electronic devices, the flicker noise (also called 1/f noise) is a serious problem limiting the development of practical applications and pushing toward the use of high frequency. Graphene with its high mobility could be used for many of the future applications such as sensors, metrology, ultrafast transistors, transparent electrodes and interconnects. From long time its been reported that the origin of 1/f noise in graphene is either due to charge density fluctuations or mobility fluctuation. Majority of them claim that 1/f noise arises from mobility fluctuations, owing to both short-range (defect configuration) and long-range (Coulomb) scatterings.

At very low temperatures, it has been found out that the origin of 1/f noise in mesoscopic graphene devices is due to quantum interference effects [86]. It was also reported that mesoscopic conductance fluctuations were the origin of 1/f noise at low temperature and in presence of magnetic fields. It was observed that 1/f noise strongly depends on temperature and also on magnetic fields. The 1/f noise increased with the increase in the magnetic field indicating that conductance fluctuations in the inhomogeneous landscape, with network of compressible and incompressible subregions, as the origin.[83]

Beyond a certain characteristic magnetic field, further increase in the magnetic field reduced the 1/f noise amplitude and with resulting quantum Hall plateau, the noise became immeasurably small and vanishes, confirming that current noise and quantized Hall resistance being inseparable[87]. In addition it was also reported that the 1/f noise spectral density significantly increases during the regime of quantum Hall transitions[88]. Hence measurement of 1/f noise was proposed as an alternative way of confirming resistance quantization in graphene.

However there were no detailed reports describing the 1/f noise fluctuations in the high mobility samples to examine its behaviour at the plateaus and the transition. Any possible correlation between the transverse and longitudinal resistances with respect to the 1/f noise had to be studied [89]. The possible origins of the 1/f noise in these quantum Hall and fractional Hall regime needed to be studied to understand the noise behaviour at the edge modes and the bulk of the system. The noise behaviour at these regimes could provide an idea of charge dynamics in the bulk of the system. It can also provide information about charge localization in the bulk and about the origin of mesoscopic conductance fluctuations (seen in narrow devices). Therefore in this thesis we have studied the 1/f noise behaviour at low temperature and high magnetic fields at the quantum Hall regime, both in integer quantum Hall and fractional quantum Hall regime to explain its origin and the charge dynamics.

2.7.5 1/f noise in iQHE and fQHE regime

The localised bulk state play a very important role in precise quantization of Hall resistance in quantum Hall regime. Eventhough the edge channels have been studied very well in this regime, the behavior of the bulk has been seldom documented and is difficult using conventional electron transport techniques. Hence the study of 1/f noise behavior at the QHE regime can shed light about the electron dynamics happening in the bulk states.It can provide significant information of QHE breakdown, scattering mechanisms and electron overheating.

Quantum interference effects come into picture in 1/f noise measured at very low temperatures in mesoscopic regime of graphene devices[86]. As shown in the figure 2.40b, the noise amplitude increases exponentially with the decrease in the temperature(56 K to 400 mK). Increase in the magnetic field even by small scales of 0.3T leads to a significant reduction of almost 4 orders of magnitude in 1/f noise. With further increase in magnetic field up to 4T, it was noticed that 1/f noise increases by order of magnitude indicating a presence of different mechanism during these regimes.

It has been suggested that during the increase of magnetic fields, the conductance fluctuations in the inhomogeneous landscape form a network of compressible and incompressible sub regions leading to increase in the noise magnitude[83]. It has been described that the noise amplitude increases sharply during Shubnikov de Hass regime and decreases below the measurement threshold during the Quantum Hall regime. It is also been vaguely pictured that noise is qualitatively correlated to the longitudinal resistance in Quantum Hall regime. Hence a detailed analysis is required to understand the behaviour of 1/f noise at the plateaus and plateau to plateau transition in Quantum Hall regime and Fractional Quantum Hall regime.

The noise measurements were recorded at magnetic field of 16T and at very low temperature of about 20 mK. At these experimental conditions, we observe integer quantum Hall effect and also fractional quantum Hall effect in clean higher mobility devices as explained in the previous sections. It is noticed that during these quantum Hall regimes, the 1/f noise is suppressed if the conductance is quantized. This is attributed to conductance quantization where transmission probability is almost close to unity due to the strong magnetic field that suppresses any residual back-scattering.

During the switching between the plateaus, that is, in the transition between the plateaus, the 1/f noise is observed to be the highest with the data recorded showing more than four order increase. This is similar to increase of the longitudinal resistance during the transition between the plateaus. Hence the 1/f noise follows or is correlated to the longitudinal resistance of the Hall bar and the origin of the noise can be traced back to the concept of resistance fluctuation in the longitudinal resistance.

In the figures 2.41, 2.42, we can see the noise fluctuations both at the plateau (n=2) and transition between the plateaus. It could be seen that the fluctuations are not exactly like RTN as explained in the figure 2.38, but similar to RTN fluctuations. The power spectral density of such fluctuation gives a noise spectrum as shown in the figure 2.41, 2.42. By fitting the data, we understand that the power spectrum is 1/f related to 1/f noise. In the figure 2.41, 2.42, we could see two curves red and black, corresponding to background noise and 1/f noise.

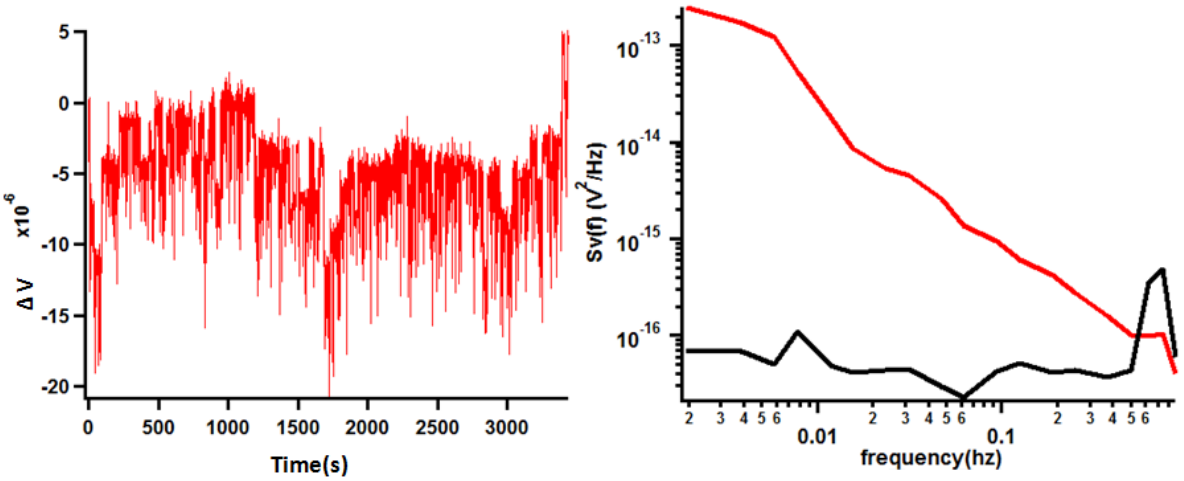

Figure 2.41 – (left) Noise fluctuations during the transition from ν=1 to ν=2 and its power spectral density showing low noise amplitude. (right)1/f noise spectrum in red and background noise spectrum in black.

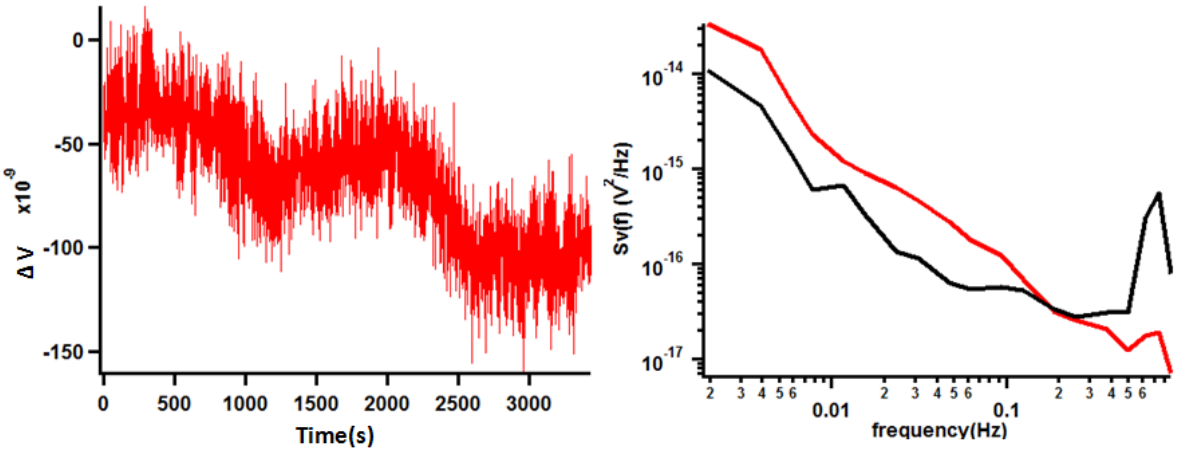

Figure 2.42 – (left) Noise fluctuations at the plateaus ν=2 and its power spectral density showing very low noise amplitude compared to previous figure 2.41 taken at the transition. (right)1/f noise spectrum in red and background noise spectrum in black.

It could be seen that behavior of noise is 1/f both at plateaus and the transition. However the power spectral density is four orders of magnitude lesser at the plateaus when compared to the transition. This could be explained using an illustration as shown in the figure 2.43. During QHE regime, the electron transport happens at the counterflowing edges channels seperated by the bulk insulating state. In the figure 2.43, the edge channels are shown in thick red lines at the edges. Further in the bulk, electron and holes are in form of puddles and are localized as depicted by dotted red lines.

At the plateaus, the Fermi level would be at the zero-gap metallic state at the edge and at the energy gap in the bulk. This bulk state energy gap protects the backscattering of electrons and hence there is no interaction between the edge states and the bulk states. But during onset of the transition between plateaus, the edge state could hop/tunnel to the localised bulk state or vice versa. This gives rise to the RTN-kind of fluctuation in the noise and hence the 1/f behavior of noise. Therefore at the dissipationless edge modes, the electrons are not interacting and the noise is supressed. But during the transitions, the electrons in the bulk and the edge

modes could interact and significantly increase the 1/f noise.

The 1/f noise measurement was executed at diferent gate voltages in iQHE and fQHE regime covering all the plateaus and trasitions. The noise spectral density at each gate voltage point was integrated to obtain the 1/f noise amplitude at that gate voltage. Hence the figure 2.44 is the graph of 1/f noise amplitude measured at different gate voltages covering the iQHE and fQHE regime. It could be seen from the graph that, at the plateaus the 1/f noise is supressed and in between the transition they are four order higher. It could be seen that this effect is more pronounced at iQHE plateaus than the fQHE plateaus.

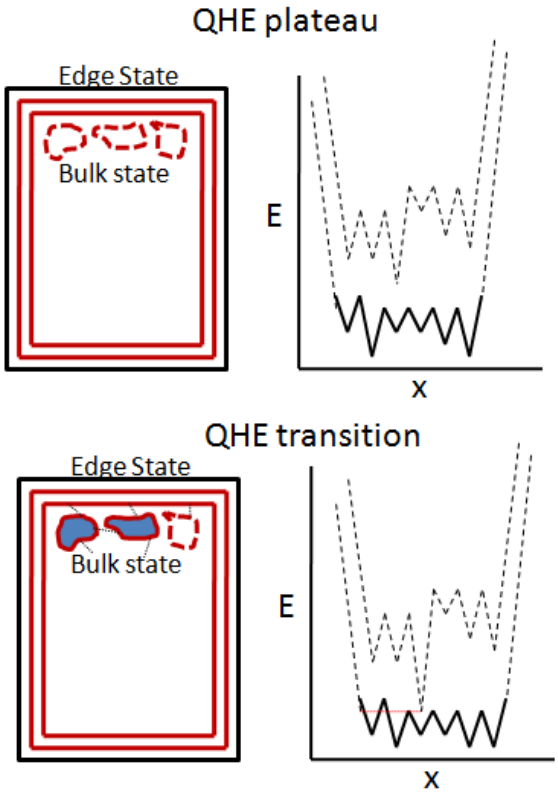

Figure 2.43 – Illustration of QHE behavior and possible tunneling/hopping events between the edge states and the bulk states. The red dashed curve represents unoccupied state while the red solid as occupied. The black dashed line illustrates the possible hopping/tunneling between the states.

It could be noted that, these fQHE edge states might have not been formed completely as they still show residual resistance in R_{xx}. This longitudinal resistance is non zero because of possible backscattering or interaction with the bulk states. It could also be seen that the 1/f noise amplitude curve is in correlation with the longitudinal resistance. Hence our theory of hopping or tunneling between the edge states and the bulk states is the origin of the 1/f noise during the iQHE and fQHE regime.

In hand waving terms, we could explain these results in terms of McWhorter model where the origin of the 1/f noise was due to the charge traps in the insulating dielectric positioned above or below the semiconductor. Similarly quantum Hall transport in graphene is a phenomena where at the edges the graphene is ballistic but the majority of the bulk is an insulator. Hence the hopping charges between the insulating bulk to the edges during the transition of

the plateaus can lead to significant increase in the 1/f noise observed.

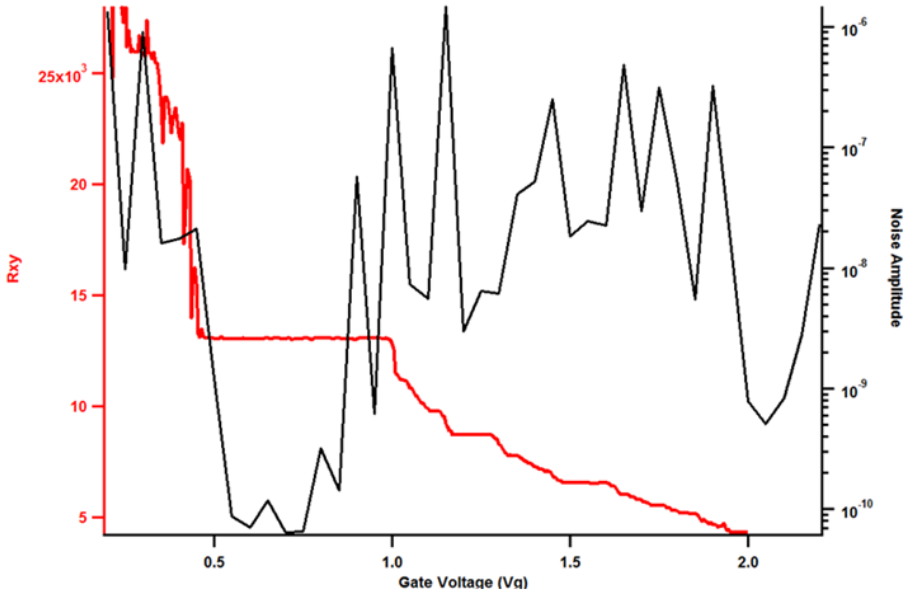

Figure 2.44 – 1/f noise and transverse resistance comparison in graphene at quantum Hall and fractional quantum Hall regime

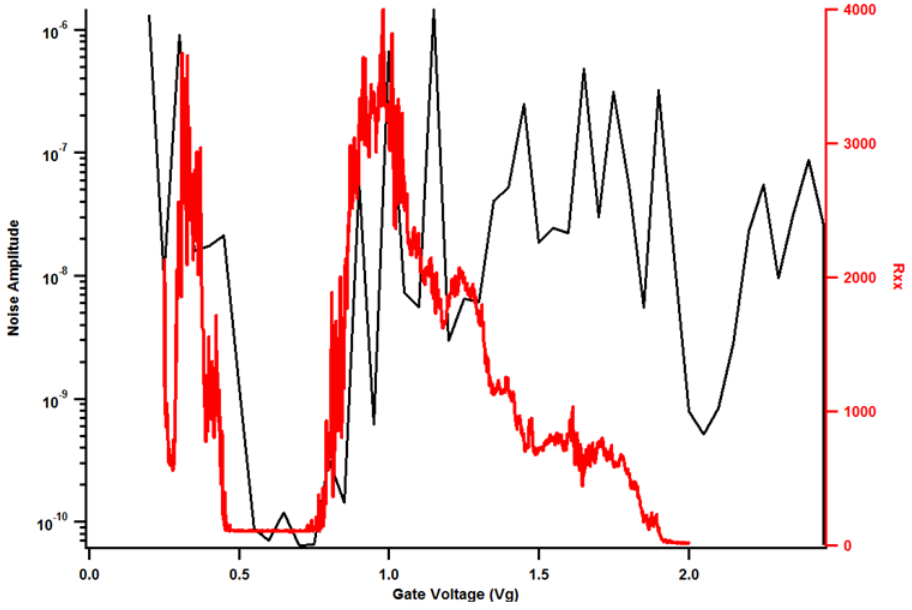

Figure 2.45 – 1/f noise and longitudinal resistance comparison in graphene at quantum Hall and fractional quantum Hall regime

Further it is observed that the 1/f noise is also suppressed at fractional Hall plateaus which are due to quasi-particles. We see the reduction in the 1/f noise but not as much compared to the quantum Hall plateaus. One reason being that these fractions not being formed completely as there is still residual longitudinal resistance at these fractional plateaus. Hence it requires more comprehensive study to check if the 1/f noise falls to similar levels as that of quantum Hall plateaus.

2.8 Conclusions and perspectives

2.8.1 Conclusions

A detailed methodology for fabrication of edge-contacted BN/Graphene/BN devices has been depicted in the thesis. The importance of etching and edge contacts has been explained to obtain high mobility ballistic samples with low resistance edge contacts.

These high quality devices exhibit Integer Quantum Hall plateaus. The spin and valley symmetry of graphene is broken at very low magnetic field of up to 2T further revealing the anomalous Quantum Hall effect of graphene.

In these high quality devices, with mobility above 250,000 cm^2/Vs approaching the ballistic regime, Fractional Quantum Hall Effect has been observed. All the n/3 plateaus except 1/3 have been visible as a clear plateaus. However the longitudinal resistance has not been reduced completely to zero having a residual resistance indicating that fractional plateaus are not completely formed.

Further, 1/f noise experiments were conducted on these graphene samples at QHE and fQHE regimes to understand the origin of noise behaviour during these regimes. The noise amplitude was found to be at the lowest during the plateaus and increasing during the transition between the plateaus. More studies are on-going to study and understand more about 1/f behavior in these regimes.

2.8.2 Quantum point contacts for shot-noise measurements

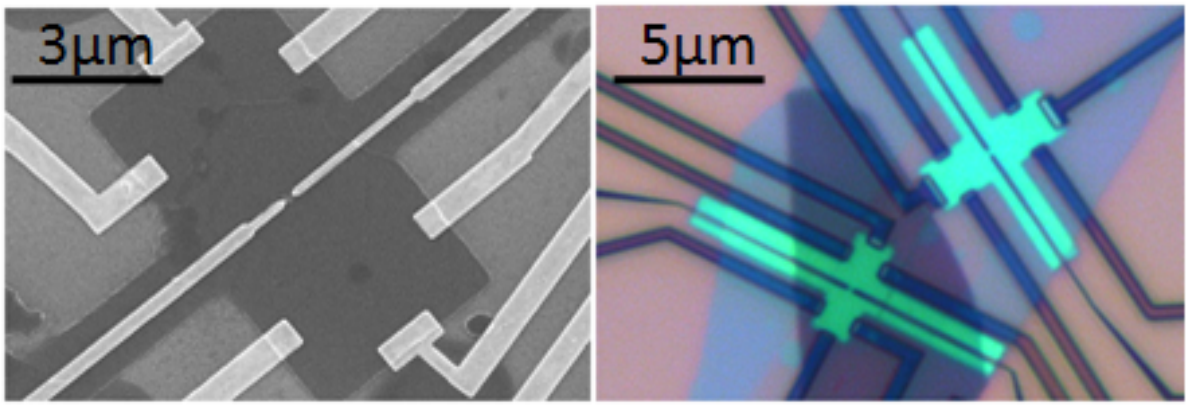

Figure 2.46 – Hall bar devices with split top gates to implement quantum point contacts (QPC).

We propose to develop top-gated devices based on high mobility hBN-graphene-hBN heterostructures. The metallic top gates will be used to realize quantum point contacts (QPC)[90] and gate controlled tunnel junctions which will form the basic building block of the devices for shot noise and interference measurements. We propose to probe the tunnelling charge and statistical phase of the quasiparticles in the Fractional Quantum Hall Regime in these materials using Shot noise measurements. We also propose to perform detailed measurements of Shot noise in the fQHE states to better understand the effect of magnetic field, temperature and transmission co-efficient on the tunnelling charge. An observation of anyonic statistics of the charge carriers in such devices would open up these materials to possible applications in Quantum computation. In addition, observation of fractional tunnelling charge would be a definite

proof that Laughlin's theory of fQHE is indeed universal in nature.

We propose to carry out extensive studies of the charged and neutral modes in FQH states based on shot noise measurements to probe the ground state of the system, test its stability to local perturbations and to understand the temperature dependence of the quasiparticle decay lengths. We also propose to study their phase using electronic Fabry-Perot interferometers to gain an insight into their mutual interactions and their phase correlation length scales. The energy gaps seen in such systems, especially the fragile 5/2 state is of the order of a few tens of milli Kelvins. It has also been established from our previous experiments[91]that the effects of neutral modes die out significantly by about 50 mK. These two points justify the requirement of carrying out the proposed experiments at temperatures of the order of 10 mK, achievable only using a dilution refrigerator.

2.8.3 Fabry Perot interferometers

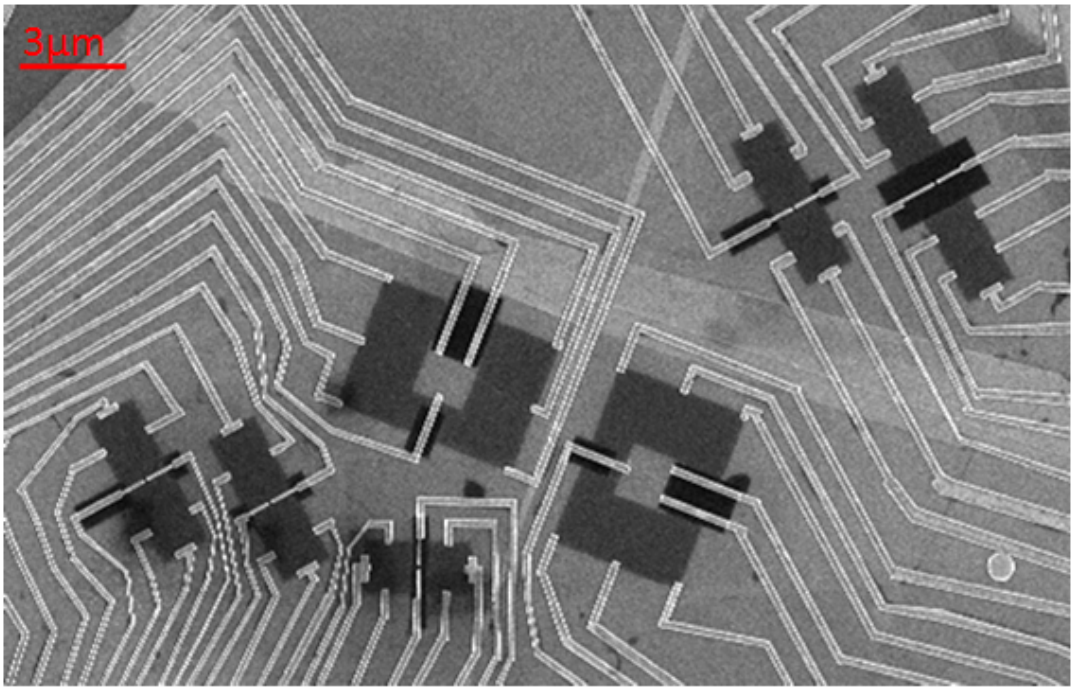

Figure 2.47 – Fabry-Perot interferometer devices with loops and Quantum point contacts fabricated on hBN/Graphene/hBN heterostructures.

We propose to probe the effect of Coulomb interactions on the charge and statistics of charge carriers in graphene in the fQHE regime as a function of device geometry, heterostructure parameters and edge-state configuration to deconvolute the Aharonov-Bohm like oscillations peaks (which contains information regarding the statistics of the quasiparticles) from the Coulomb energy dominated Coulomb blockade like single particle charging peaks.

Chapter 3

2D Synthetic MoS_2 versus Natural MoS_2 : Influence of defects on optical properties

Contents

3.1 Brief introduction to the chapter 89
3.2 Electronic properties of monolayer MoS_2 92
3.2.1 Crystal structure 92
3.2.2 Band diagram 93
3.2.3 Excitonic properties in monolayer MoS_2 94
3.2.4 Vibrational properties in monolayer MoS_2 98
3.3 Sample fabrication 102
3.3.1 MoS_2 crystal sources 102
3.3.2 Mechanical exfoliation 102
3.3.3 Optical identification of monolayer MoS_2 flakes 103
3.3.4 Large area monolayer flakes 105
3.3.5 Preparation of samples 105
3.4 Introduction to spectroscopy techniques 107
3.4.1 Introduction to Raman spectroscopy 107
3.4.2 Confocal micro Raman spectroscopy set-up 109
3.4.3 Introduction to Photoluminescence technique 110
3.5 Extrinsic and intrinsic defect characterization using Raman and PL111
3.5.1 Raman spectroscopy signature of monolayer MoS_2 112
3.5.2 Photoluminescence signature of monolayer MoS_2 113
3.5.3 Reflectance spectroscopy of monolayer MoS_2 115
3.5.4 Strain and Doping from vibrational spectroscopy 115
3.5.5 Excitonic complex in presence of strain, doping and defects 119
3.6 Intrinsic defect confirmation in artificial HP/HT MoS_2 121
3.6.1 Scanning Tunneling Microscopy-nature of point defects 121
3.6.2 Density functional theory (DFT) and STM simulations 123
3.6.3 Field Effect characterization of artificial HP/HT MoS_2 126
3.7 Chapter conclusions and perspectives 128
3.7.1 Conclusions 128
3.7.2 Perspectives 128

3.1 Brief introduction to the chapter

Molybdenum di sulfide is an inorganic compound naturally occurring in the form of Molybdenite, having a layered structure of several layers of MoS_2 held together by weak Van der Waals interactions. It belongs to group VI transition metal di chalcogenides (TMDC) family of the form MX_2 where M is a transition metal and X is a chalcogen. The in plane or intra layer covalent bonds are strong but the interlayer Van der Walls forces are weak in multilayer MoS_2 which on application of proper forces can be cleaved down to a few layers and monolayers.

Like other TMDC's, the bulk MoS_2 is known to be an indirect bandgap semiconductor which on thinning down to a monolayer turns out to be a direct bandgap semiconductor. The direct band gap paves way for interesting optoelectronic properties that has promoted the research of these 2D monolayer MoS_2 based devices. Eventhough these monolayers are thought to be stable under the ambient conditions, they are found to degrade over time when exposed to the environment which may affect their electrical or optical properties.

Natural diamonds are produced over 120 to 130 km deep inside the earth in an extreme environment of 1,500 $^{\circ}$C and 4.93 GPa (50, 000 atmospheric pressure). However, we cannot get them until magmas bring them up above the ground. Ultrahigh pressure diamond press can provide these processes artificially in a short time. In recent years, there was a similar kind of process carried out in case of natural hexagonal boron nitride (hBN). In this occasion, a synthetic hBN was fabricated using a special high pressure, high temperature (HP/HT) technique by K.Watanabe and T.Tanuguchi, NIMS [92], where it was found that hBN was close to prisitine with very less amount of defects. In addition, it was found that the exfoliation of such crystals yields large-scale flakes useful for experiments.

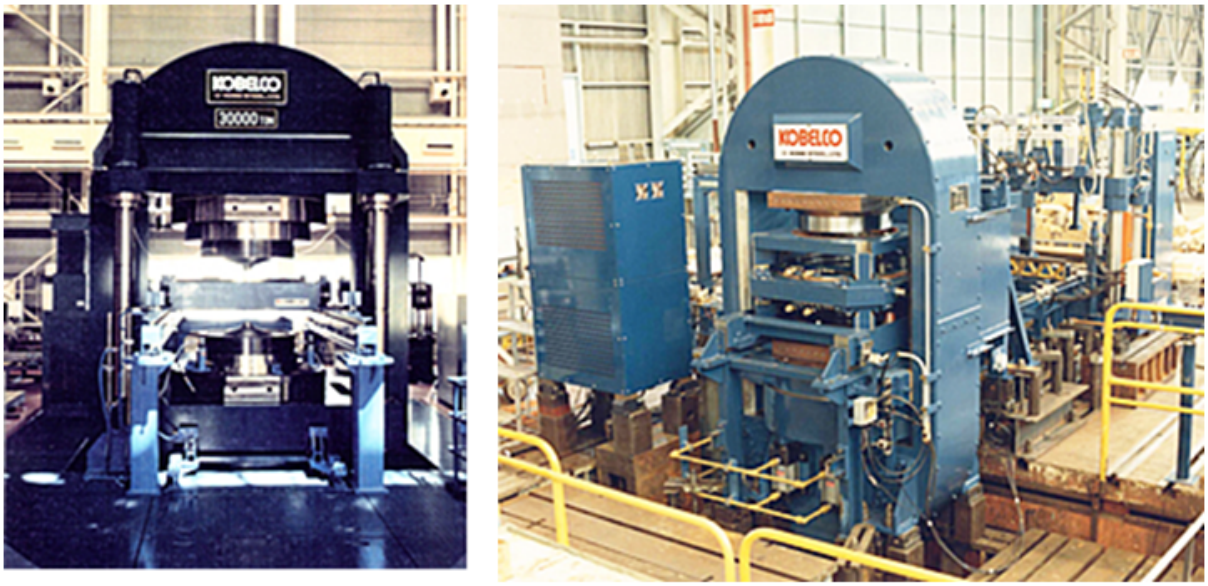

Figure 3.1 – **High pressure, high temperature press machine used for production of synthetic crystals such as Diamond, hBN and MoS_2.** (left) 294 MN (30,000 tf) Flat Belt Type Press (right) 39.2 MN (4,000 tf) Flat Belt Type Press

Natural MoS_2 obtained from molybdenite is found to have some structural defects. The most common and abundant defects that were found and studied in depth were simple vacancies like sulphur vacancies.[93] Hence to improve the quality of the crystal, extensive studies and experiments have been going on. Similar strategy as that of HP/HThBN has been applied by the same group from NIMS to produce an alternative source of MoS_2 crystal. In this process 99.9% pure MoS_2 powder is encapsulated in a hBN capsule and brought to a high pressure of 5 GPa and high temperature of about 1800 c for 20 mins by using a belt type high pressure apparatus. The sample is slowly cooled down from this molten state to room temperature at a rate of 0.8 $^{\circ}$C/min. After releasing the pressure, the MoS_2 crystal is recovered by crushing the h-BN capsule. We obtain a typical 1-2 mm crystal size after the execution of this HP/HT process.

Hence, in this chapter we compare the quality of the natural MoS_2 and synthetic HP/HT MoS_2 crystals. In this thorough study, we check if we can obtain larger and better quality flakes in case of HP/HT MoS_2 similar to that of previously observed HP/HT hBN. Further, we compare them with the studies of possible defects and disorders with the help of various characterization techniques.

When we talk about these crystals, we have to look deep into the material itself first, the possible intrinsic defects in it and the way to characterize them to select the best samples for the experiments or applications. As discussed in the introduction of the thesis, the intrinsic defects include simple to complex vacancies in the structure or/and the substitutional impurities by other atomic species in the crystal structure. The other important component for bringing disorder in the crystals/flakes are extrinsic defects arising from the environment around, non ideal substrate that are carrying the 2D materials or the manufacturing processes.

There lies a challenge to identify the nature of these defects and quantify them. Different characterization techniques have been employed such as transmission electron microscopy, scanning electron microscopy and scanning tunneling microscopies.While these techniques give a very good spatial reolution, it is difficult and complex to prepare the samples and also to characterize very large ones. Moreover, some of these techniques are detrimental to the samples, where there could be damages from the electron beam which could render the samples no more pristine for any further measurements.

This brings in a need to find new characterization solutions where there is sufficient spatial resolution, easiness to measure large structures and more importantly not to degrade the quality of the two dimensional material. So in this thesis work, optical spectroscopy such as Raman and photoluminescence have been employed to characterize and differentiate different kind of defects. The advantages of using these techniques are that they are non invasive and can be carried out easily at room temperature over large area samples in very less time.

Defect	Intrinsic	Extrinsic
Source	Crystalline imperfections	Chemical/charge influence
Origin	Vacancy defects Substitutional defects	Substrate effects Surface contaminants
Characterization techniques	STM, XRD Raman spectroscopy Photoluminescence Cathodoluminescence	Raman spectroscopy Photoluminescence

Figure 3.2 – Table for classification of defects in two dimensional materials with respect to their types and possible origin. Typical characterization techniques also included that are used to identify them.

In general, several solutions are proposed to enhance the physical properties of the monolayer MoS_2 material to get the best intrinsic property out of the 2D direct bandgap semiconductor. Similar to graphene, hBN has been proposed as an atomically flat substrate and along with encapsulation has been shown to improve the electronic and optical properties. In this chapter we address several questions in relation to the nature of the material and quality of the process or solutions proposed and fabricated to enhance its properties. Hence there are several key messages which come from this profound experimental work.

First, we discuss about how to clearly distinguish between internal defects and external defects and their influence on the physical properties using optical probes such as Raman spectroscopy and photoluminescence. The defects could be intrinsic to the monolayer MoS_2 itself such as sulfur vacancies and/or substitutional atoms. They could also be extrinsic where charged impurities may come from the substrate underneath or the atmosphere above it. Nevertheless, both the impurities have thought to limit the electronic and optical properties of the monolayer MoS_2.

Hence this chapter that has resulted in a publication [94] covers multitude of information about TMDC materials, in particular monolayer MoS_2, where we have discussed about the use of different crystal sources like natural and artificial, different substrates to carry them, different polymer transfer techniques to build the heterostructure samples and variety of complementary characterization techniques that give distinct defect information. With all these useful information and measures, we could build near perfect 2D MoS_2 samples showing its intrinsic properties for the future optoelectronic devices.

3.2 Electronic properties of monolayer MoS_2

In this section, we will describe some of the electronic properties of monolayer MoS_2 which would be helpful for the understanding of the work carried out in the thesis. Here we basically explain the crystal structure and thus resulting band diagram.The excitonic properties and the vibrational properties of single layer MoS_2 form the basis on which the thesis has been built upon.

3.2.1 Crystal structure

The monolayer of MoS_2 has three atomic layers S-Mo-S in which each layer of Mo or S atoms form a 2D hexagonal lattice. The Mo atoms in the middle plane are surrounded by three nearest neighbour S atoms at both top and the bottom layer giving the crystal a D_{3h} symmetry. The crystal structure is characterized by in plane lattice constant a_0 and the distance between the two chalcogen planes d_{x-x}. The top view of a monolayer MoS_2 has similar hexagonal lattice structure to that of graphene.

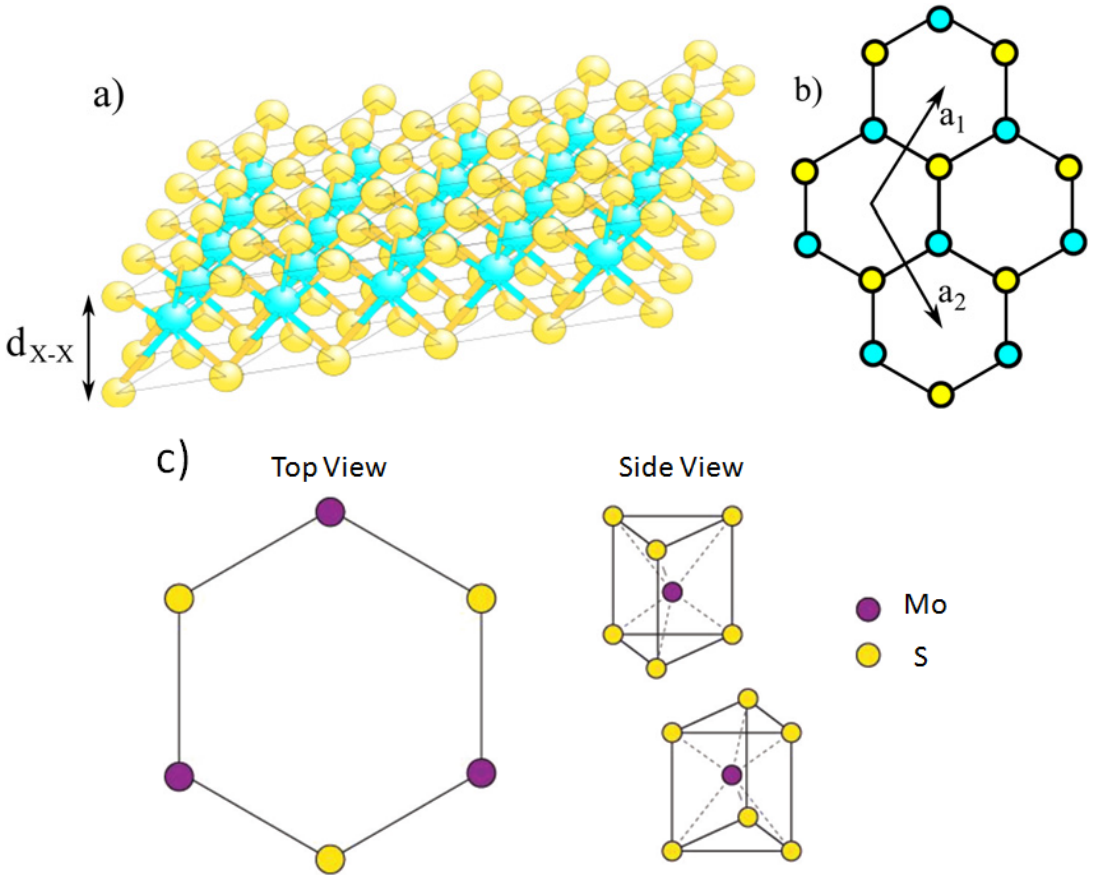

Figure 3.3 – **Crystal structure of monolayer MoS_2.** a) Description of monolayer MoS_2 structure with hexagonally arranged Molybdenum atoms (Mo in color cyan) that are sandwiched between two layers of Sulfur (S in color yellow) atoms. b) Top view of the structure with lattice vectors a_1 and a_2 (adapted from Kormanyos et al. [95] c) Figures describing the top view and the side view of the structure where the top view has a hexagonal structure with the real structure shown in the side views being of the form trigonal prismatic coordination.(adapted from Xiao et al. [96])

A monolayer 2H-MoS_2 has 2 chalcogen layers per unit cell stacked in hexagonal symmetry with each molybdenum atom at the center of a trigonal prismatic coordination sphere and is covalently bonded to six sulfide ions whereas each sulphur atom has pyramidal coordination and is bonded to three molybdenum atoms. Here we study the crystal in the 2H phase and would be just referred as MoS_2 in the forthcoming instances. The 2H phase breaks the inversion symmetry in a monolayer but is restored in case of even number of layers. Inversion symmetry is broken as the two sublattices are occupied, respectively, by one molybdenum and two sulphur atoms.

3.2.2 Band diagram

The electronic band structure of bulk and monolayer MoS_2 calculated using density functional theory by Splendiani et al [97] is shown in the figure 3.4. We could see that in case of bulk, the top of the valence band and the bottom of the conduction band are located at the Γ point and the midpoint along the $\Gamma - K$ line, respectively resulting in an indirect bandgap. In the case of a monolayer, band extremas are located at finite momentum $K+$ and $K-$ points of the hexagonal Brillouin zone. As we can notice from the figure 3.4 that the direct excitonic transition energy at the K point of the Brillouin zone hardly changes with the change in the layer thickness. Instead we could see a significant change in the indirect band gap between Γ and the midpoint of $\Gamma - K$ monotonically increases with the increase in the layer thickness and finally making MoS_2 a direct band gap semiconductor in the monolayer.

This change is a result of characteristic d-electron orbitals that comprise the conduction and the valence bands of MoS_2. At the K amd K' point, the conduction band states are mainly composed of strongly localized d-orbitals at Mo atom sites in x-y plane, to be specific, d_{z^2} orbital of Mo atom along with small contribution from p_x and p_y of the sulfur atom. And the states at valence band have $d_{x^2}+id_{xy}$ of transition metal Mo atom slightly mixed with chalcogen sulfur p_x+ip_y orbitals.[98]

These d- orbitals have minimal coupling with other layers as the Mo atoms are located in the middle of S-Mo-S unit cell. The states near the Γ point and at the indirect bandgap point originate due to the linear combination of d_z^2 orbitals on Mo and p_z orbitals on S atoms both of which are delocalized and of antibonding nature. Here there is strong coupling between the layers and their energy depends on the thickness of the layers which results in decrease in the indirect bandgap.

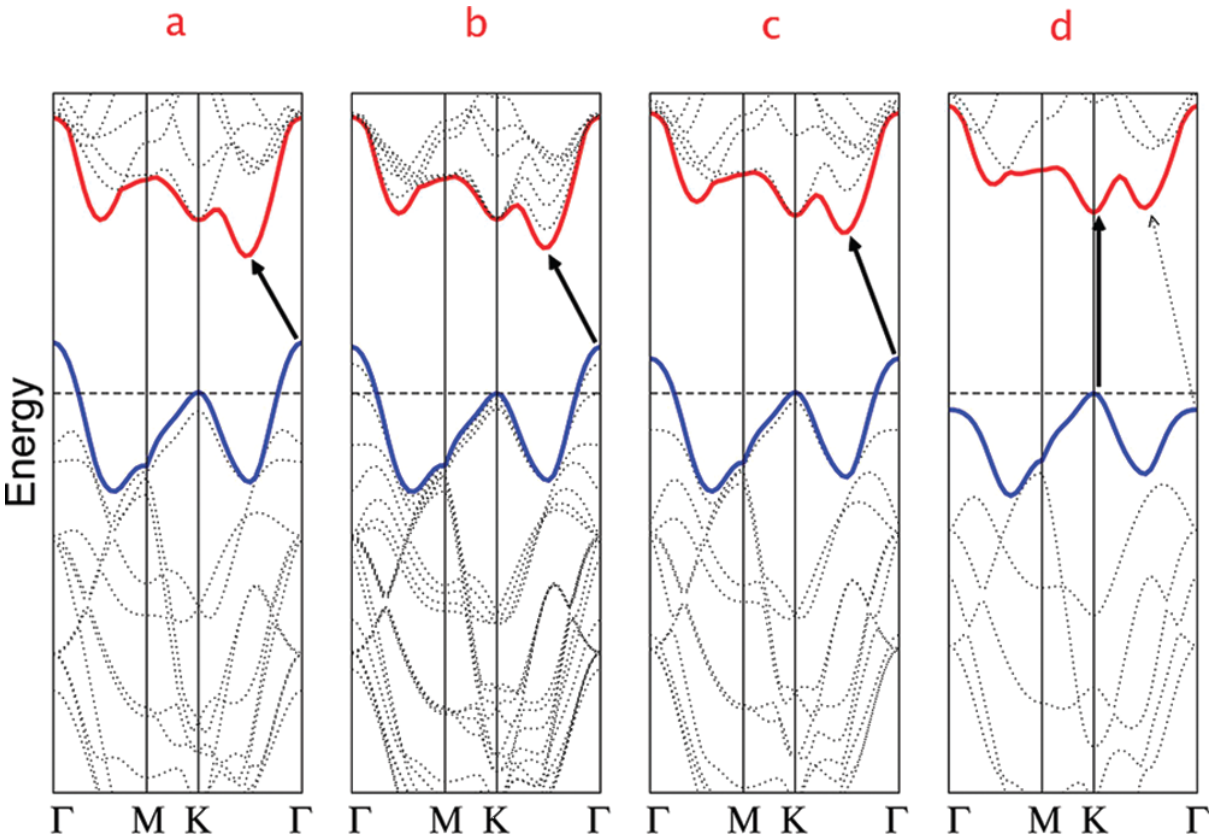

Figure 3.4 – **Calculated band structure diagram for MoS_2 by density functional theory.** (a) Bulk MoS_2 (b) Quadrilayer MoS_2 (c) Bilayer MoS_2 and (d) Monolayer MoS_2 showing transition from indirect bandgap semiconductor to a direct bandgap one. The lowest energy transition at conduction (in red) and valence band (in blue) extremas are shown in the solid lines. Figure adapted from Splendiani et al [97]

3.2.3 Excitonic properties in monolayer MoS_2

A bound state created by a negatively charged electron and a positively charged hole because of coulomb attraction is called an exciton. The nature of exciton is similar to that of an hydrogen atom in terms of internal structure and excited energy states. In the bulk form of the semiconductors exciton has small binding energy of 1-10 meV due to large dielectric screening whereas in two dimensional monolayer semiconductors there is large coulomb interaction due to spatial confinement and reduced dielectric screening with excitons having 100-500 meV of binding energy.

The excitonic properites of monolayer MoS_2 discussed in this section are based on the review article of Gang Wang et al. For further in depth information please refer to the article. [99]

As discussed before an electron and a hole can form a bound state namely neutral exciton as shown in the figure 3.5 (a) and we can represent this as two particle problem where a negatively charged conduction electron interacting with a positively charged valence hole. The Bloch function of the empty electron state in the valence band is given by $\mid v\rangle = \mid s_v, \tau_v, k_v\rangle$ where $s_v(v = c, v)$ denotes the spin index, $\tau_v = \pm 1$ is the valley index and k_v is the wave vector for a valence (v) or conduction (c) state.

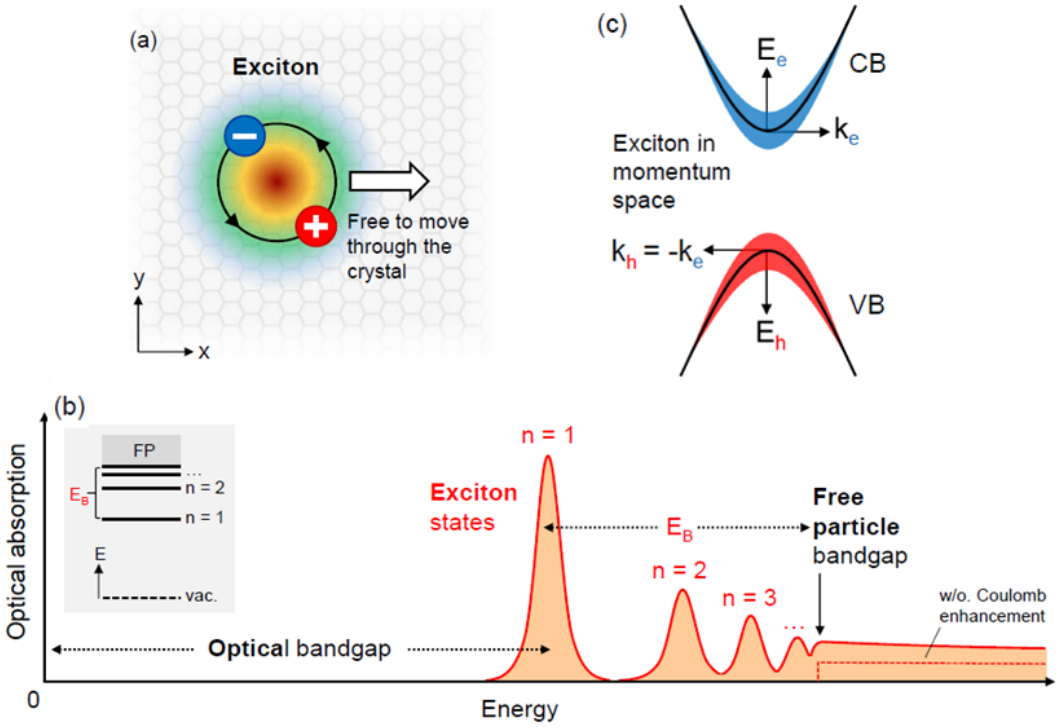

Figure 3.5 – a) A real space representation of a bound electron hole pair in form of a Wannier-Mott exciton showing a very strong spatial correlation between the two constituents. The arrow points the motion of the exciton as a whole from the centre of mass wavevector. b) Representation of an ideal 2D semiconductor with a series of bright exciton transitions below the renormalized quasiparticle bandgap.The inset represents atom like energy level diagram of the exciton states assigned by their principal quantum number n, with binding energy E_B of the ground state exciton below the free particle gap.(FP) c) exciton represented in the reciprocal space. The width of the shaded regions shows the contribution of electron and hole quasi particles in the conduction band and the valence band respectively. Figure adapted from Gang Wang et al.[99]

By the application of the time reversal operator $\mid h\rangle = \hat{K} \mid v\rangle$ on it, we obtain the valence hole Bloch function represented by $\mid h\rangle = \mid s_h, \tau_h, k_h\rangle$. Here the hole wavevector would be opposite to that of the empty electron state as orbital part changes to its complex conjugate and the spin part flips upon the application of time reversal operator given by $k_h = -k_v$. Hence the hole valley and spin quantum number would also be opposite to that of empty electron state represented as $s_h = -s_v$, $\tau_h = -\tau_v$.

Upon the interaction of MoS_2 monolayer with a σ^+ photon having a wavevector projection $q_\parallel$ to the plane, creates an electron with a wavevector k_e with spin $s_e = +1/2$ and $\tau_e = +1(K^+)$ valley index and an unoccupied state in the valence band with wavevector $k_v = k_e - q_\parallel$. The corresponding hole wave vector is given by $k_h = -k_v = q_\parallel - k_e$ with valley index $\tau_h = -1$ and spin $s_h = -1/2$. Hence the centre of mass wavevector of the electron hole pair as a whole is given by $K_{exc} = k_e + k_h = q_\parallel$. Similarly a σ^- photon results in formation of electron hole pair with $\tau_e = -\tau_h = -1, s_e = -s_h = -1/2$.

In MoS_2 monolayers, the electrons and holes are tightly bound together as excitons by attractive coulomb potential with large binding energies of order 0.5eV. They have small Bohr radius in real space of order $a_B \simeq 1nm$ and hence the spread of exciton in the K space is very significant .

Hence exciton wavefunction with phase locked or coherent electron states $\mid e\rangle = \mid s_e, \tau_e, k_e\rangle$ and hole states $\mid h\rangle = \mid s_h, \tau_h, k_h\rangle$ around the respective band extrema in the k-space can be denoted as

$$\psi^X = \sum_{e,h} C^X(k_e, k_h) \mid e; h\rangle \tag{3.2.3.1}$$

where C_X is expansion coefficient that describes the relative contribution of electron and hole states to the exciton. The values of C_X are represented by the shaded regions near the bands in figure 3.5c.

The exciton can propagate freely around the centre of mass in the plane of the material as described by the Bloch theorem. Hence the resulting exciton states is given by $X = \{K_{exc}, s_e, \tau_e, s_h, \tau_h, (n, m)\}$ where K_{exc} is the centre of mass wavevector, s_e, τ_e, s_h, τ_h are electron and hole spin and valley indices and (n,m) are relative motion labels. This relative motion states (n, m) can be represented by principal and magnetic quantum number with n=1,2,3.. and $m \in Z$ and $\mid m \mid < n$ respectively. This is similar to that of a hydrogen atom where principal quantum number $n = 1$ results in a ground state and $n > 1$ are excited state of Wannier Mott excitons as depicted by the energy level diagram in the inset of figure 3.5b. The magnetic quantum number m and the set of spin and valley indices $s_{e.h}$ and $\tau_{e,h}$ determine the selection rules for optical transitions further dividing the exciton states into optically active bright states and dark states which would not be the focal point of this thesis.

Coulomb interactions play a major role during the exciton formation process with a contribution of self energy. Self energy is related to the repulsive interaction between the identical charges leading to overall increase of the quasiparticle bandgap of the semiconductor. This energy required to create an unbound electron hole pair in the continuum is called as free particle bandgap. The optical adsorption of an ideal 2D direct bandgap semiconductor is described in the figure 3.5b. The excitonic resonances occur below the renormalized free particle bandgap as consequence of strong Coulombic interactions. This is called as optical bandgap which is defined with respect to ground state of exciton which has lowest energy feature in the absorption. Hence the optical bandgap is different from free particle bandgap which could be described also as n=∞ limit of the bound exciton state.

Reduced dielectric screening from the environment and an ideal 2D confinement in these monolayer TMDC materials like MoS_2 results in very strong coulomb interactions between the electron and hole pairs when compared to conventional quasi 2D systems. This Coulomb interaction can be separated into two namely direct and exchange contributions where both again have sub divisions called long range and short range interactions. The Coulomb interactions taking place at inter particle distances in real space larger than the inter atomic lattice distances are long range interactions. It could also be termed that long range interactions arise for small wavevectors in reciprocal space when compared to the size of the Brillouin zone. While the short range contributions are due to electron and hole wavefunctions overlapping at the scales of order of the lattice constant.

The interaction of positive and negative charge distributions corresponding to electron and hole comprises the direct part of Coulomb interactions. Further the long range interactions in this direct part arises from dimensionality and dielectric properties of the system and they are electrostatic in nature and hence provides a major contribution to the exciton binding energy E_b. The envelope function of the electron hole pair that are weakly sensitive to certain type of valley and spin Bloch functions represent this long range direct interactions.

Coulomb term	Impact	Interaction	Result
Direct	**Exciton binding Energy**	**long-range**	**neutral excitons (500meV)**
		short-range	**charged excitons, biexcitons (50meV)**
Exchange	**Exciton fine structure**	**long-range**	**neutral exciton spin/ valley depolarization (1...10meV)**
		short-range	**splitting of dark and bright excitons (10's of meV)**

Table 3.1 – Different Coulombic interaction affecting the optical properties of excitons in monolayer MoS_2.

In general it could be described that direct long range interactions are attractive Coulomb forces between the opposite charges which form a bound state of electron and hole called neutral exciton with strongly correlated relative motion in the real space as shown in the figure 3.5a. The short range part of the direct interaction arises due to coulomb attraction of the electron and hole at same or neighboring unit cells. This short range direct interaction is sensitive to spin and valley state Bloch functions and normally considered with corresponding part in the exchange interaction.

In case of exchange interaction, the contribution originates from Coulomb interaction incorporated with Pauli's exclusion principle. Similar to exchange interaction in atoms, the mutual orientation of electron and hole spins on the quasi particle valley states determines the energy of the excitons. Further, exchange interactions can also be divided into long range and short range interactions. The long range exchange interaction is electrodynamic in nature where an exciton interacts with the induced electromagnetic field during the virtual electron hole recombination state.

The back action of the electric field produced by exciton which is like a microscopic dipole, on the exciton corresponds to long range part of exchange interactions. This interaction promotes the transitions between individual exciton states excited by the light of different helicity thus dictating the spin valley relaxation of the excitons. The short range part of exchange interaction are dependent mainly on spin and valley states of the quasi particles and thus controls the separation between bright and dark excitons.

The excitonic properties of monolayer TMDC materials discussed above are pertaining to low density regime. However, at intermediate and higher density regimes, as a result of photo-excited carriers, that are either in form of Coulomb-bound or free-charges, can alter the excitonic properties significantly. At elevated carrier density regimes there would be major scattering events, both elastic and inelastic. As a consequence of these scattering events there would be spectral broadening of the exciton resonances due to relaxation of the exciton phase, energy, momentum and spin.Further due to inelastic scattering with free charge carriers, an exciton can catch an additional charge to form a trion which is a bound three particle state with two electron and a hole. In the same lines, two excitons can interact together to form a biexciton state which is a bound two exciton state. In addition, at higher density regimes, dynamic Coulomb interaction screening can occur leading to decrease in electron hole attraction and thus the red shift in exciton energy.

3.2.4 Vibrational properties in monolayer MoS_2

Phonon is a quantized unit of vibrational energy of oscillating lattice or atoms in the crystalline solid. It has both wave and particle like properties. Phonons are bosons and are not subjected to Pauli exclusion principle.

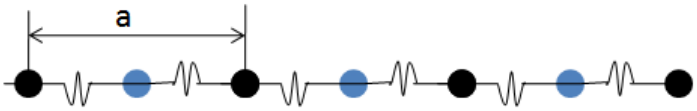

Figure 3.6 – One dimensional Bravais lattice with two different atoms or ions.

Figure 3.6 is a schematic of one dimensional Bravais lattice with two different atoms or ions having different masses M_1 and M_2 per unit cell such that $M_1 > M_2$ with lattice constant a.

Assuming that each atom interacts only with its nearest neighbours and on application of harmonic oscillator model, we obtain the solution of the problem in form as

$$\omega_{\pm}^2 = K\left(\frac{1}{M_1}+\frac{1}{M_2}\right) \pm K\sqrt{\left[\left(\frac{1}{M_1}+\frac{1}{M_2}\right)^2 - \frac{4\sin^2\left(\frac{qa}{2}\right)}{M_1 M_2}\right]} \tag{3.2.4.1}$$

where K is the force constant.

This solution is called as phonon dispersion relation for diatomic linear chain of two different mass and is plotted in the figure 3.7a. We could see that there are two branches in the dispersion map. The first branch ω_- which tends to become zero at $q = 0$ is called as acoustic mode. In this mode the atoms vibrate in unison or coherence out of their equilibrium position. When the displacement is in the direction of propagation, some atoms would be closer and others would be farther apart like a sound wave in air and hence they are called as acoustic phonons. These phonons have a linear relationship for long wavelengths between the frequency and phonon wavevector.

The other solution ω_+ is called as an optical mode where the atoms in the unit cell vibrate out of phase as if the atoms are independent of the neighbours. In this case the two sublattices of the two types of atoms move rigidly in opposition to one another. From the figure 3.7a, we could see that optical phonons at the Brillouin centre show non zero frequency and near the long wavelength limit, they do not show any dispersion. Optical phonons can interact with the light and scatter them called as Raman scattering discussed in the next section.

Figure 3.7c shows the arrangement of atoms in the acoustic and optical modes in a one dimensional chain with two atoms per unit cell. In this system of linear chain of atoms, we obtain the dispersion relation for longitudinal acoustic (LA) and longitudinal optical (LO) phonons. In the same lines if we continue with two atoms per primitive cell in a three dimensional lattice, there would be two branches in the dispersion relation corresponding for each polarization mode in a direction of propagation. Therefore there exists transverse acoustic(TA) and transverse optical (TO) phonons as depicted in the figure 3.7c. In case of the optical phonons, figure 3.7(bottom a,b) shows the vibrational displacement of the atoms in TO and LO modes of oscillation.

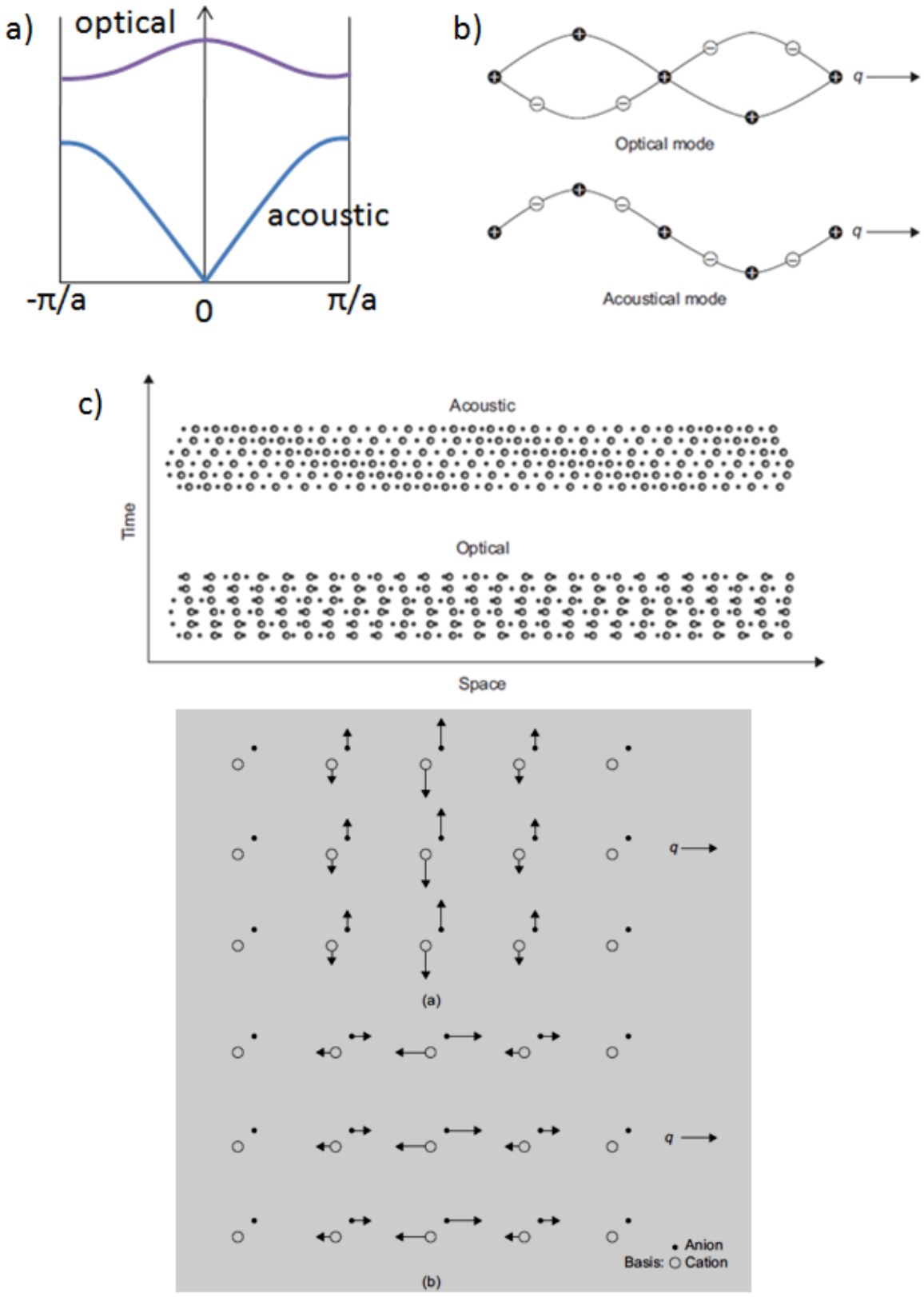

Figure 3.7 – (TOP) a) Optical and acoustic phonon branches of a diatomic linear chain. b) Transverse optical and acoustical waves for the same wavelength in a diatomic linear lattice. c) Configuration of atoms in acoustic and optical modes in the diatomic linear chain. (BOTTOM) The direction of displacement of individual ions in (a) transverse optical (TO) and (b) longitudinal optical (LO) modes of oscillation. (Adapted from 'physics of condensed matter' Prasanta Kumar Mishra.[100])

This is continued on the same lines with the bulk MoS_2, having Bravais lattice that is hexagonal and with $P6_3/mmc$ space group (D_{6h} non-symmorphic group). The unit cell possesses 6 atoms with two being Mo and remaining four sulphur atom sites with point group symmetry C_{3v}. Using these parameters along with an approach called density functional perturbation theory (DFPT), the phonon dispersion maps for bulk MoS_2 and monolayer MoS_2 has been calculated by Molina-Sanchez et al [101] as shown in the figure 3.8 along with the density of states represented in the right panels.

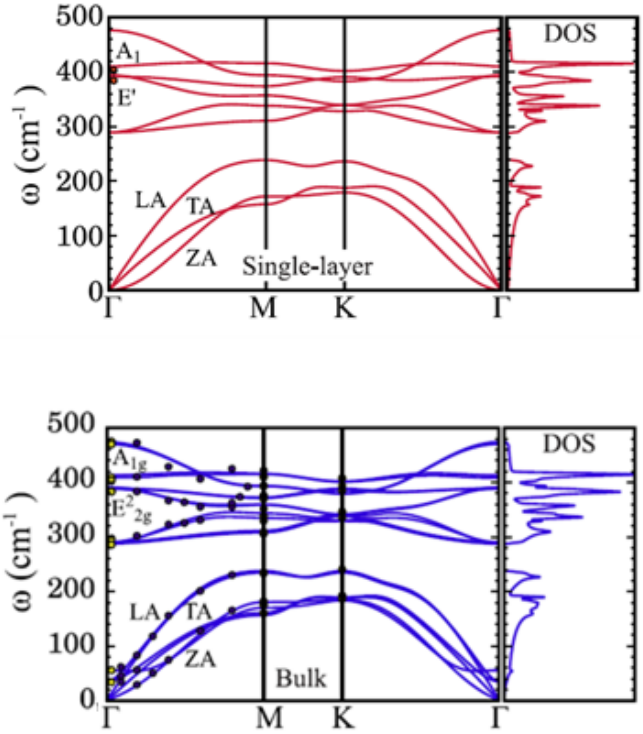

Figure 3.8 – Phonon dispersion maps and density of states for (top) monolayer MoS_2 and (bottom) bulk MoS_2. Figure adapted from Molina-Sanchez et al. [101]

We could notice from the figure 3.8 that there are not much differences between the phonon dispersions of single layer and the bulk for in-plane dispersion. In case of bulk, all the single layer modes are split into two branches. The splitting is very low since the interlayer interaction are weak. The significant noticeable difference between the two is the splitting of the acoustic modes of bulk MoS_2 around Γ point. From the phonon dispersion curve of bulk MoS_2, we notice the three acoustic modes, longitudinal acoustic(LA) and transverse acoustic (TA) are the in plane vibration modes which have a linear dispersion near the gamma point and also higher energy than the out of plane acoustic mode(ZA).

Along with these there are low frequency optical modes corresponding to interlayer interaction with rigid layer motion in plane called shearing mode and an out of plane layer breathing mode. The monolayer MoS_2 has a similar resemblance to that of bulk with phonon branches being reduced to nine. As one can expect, the lower frequency shearing and breathing modes are absent.

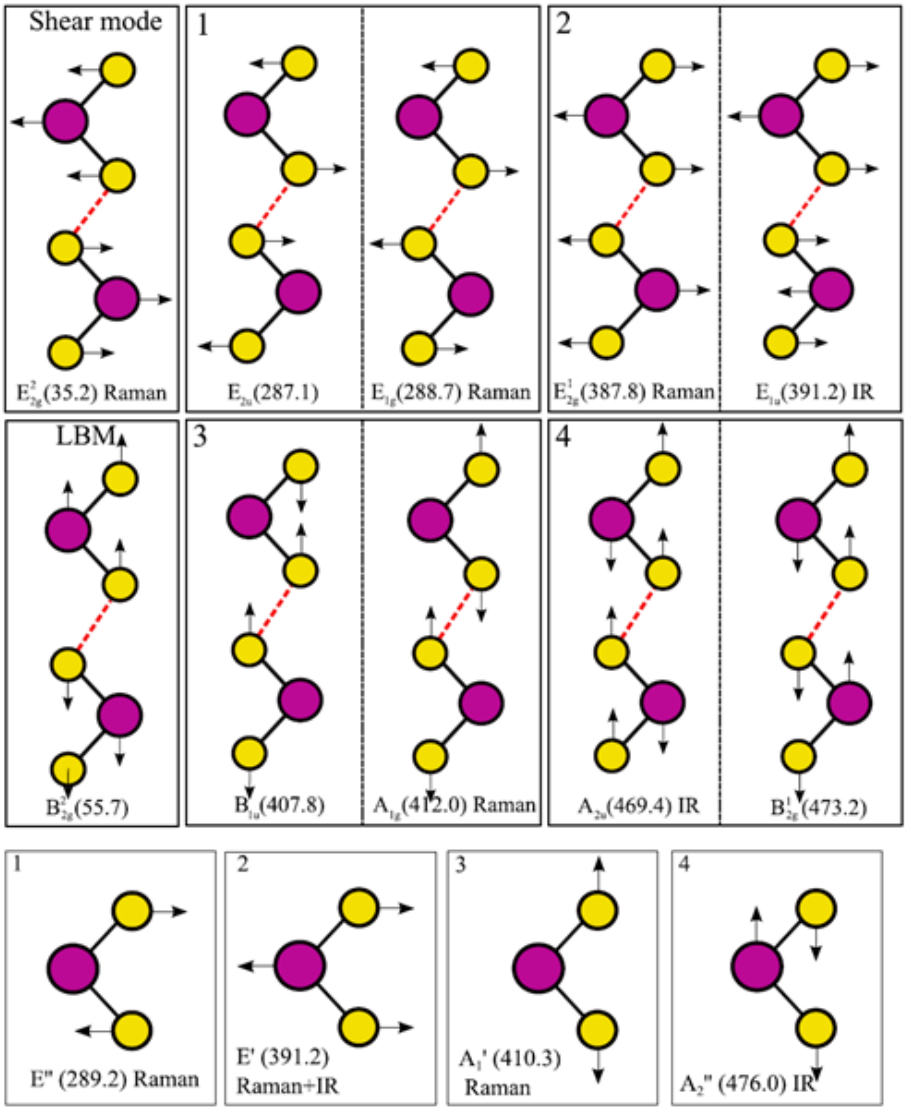

Figure 3.9 – Pictorial representation of optical phonon modes for bulk MoS_2. The first row represents the modes with parallel polarization to the layer. The perpendicular modes are shown in the second row. The third row shows the optical phonon modes for monolayer MoS_2. The figure is adapted from A.Molina Sanchez et al. [101]

Group theory analysis yields 18 normal modes of vibration at q=0 with irreducible representation given as $A_{1g} \oplus A_{2u} \oplus 2B_{2g} \oplus B_{1u} \oplus E_{1g} \oplus E_{1u} \oplus 2E_{2g} \oplus E_{2u}$ where A_{2u} and E_{1u} correspond to TA modes, A_{1g}, E_{1g}, and E_{2g} are associated as Raman active optical modes and E^2_{2g} corresponding to low frequency shear mode. When reduced to monolayer with three atoms in the unit cell, there would be nine phonons at the Brillouin zone centre (Γ point) and could be represented as $A_1^{'} \oplus A_2^{''} \oplus E^{'} \oplus E^{''}$ where A_1' and E' are optical Raman active modes and the other acoustic modes.

The atomic displacements of the optical phonon modes of bulk and monolayer MoS_2 at Γ point are shown in the figure 3.9. Each of the E modes are doubly degenerate and hence correspond to in plane vibrations of either Mo and/or S atoms whereas the modes A and B are non degenerate corresponding to out of plane movement of the atoms. In case of bulk MoS_2, inversion center lies half way between two S atoms of neighboring layers. Hence there are gerade (g) modes and ungerade (u) modes which are symmetric and anti symmetric with respect

to inversion. The gerade mode corresponds to anti-phase movements and ungerade mode, the in-phase movement. The gerade and ungerade modes come in pairs while also being close in frequency. The A and B modes could be distinguished by rotating the crystal by $2\pi/6$ around the principal rotation axis.

In the simplified 2D representation in the figure 3.9, the third row corresponds to translation of the 3 upper atoms onto the 3 lower atoms. In other words, if the direction of arrows changes, the mode is A. The subscript used shows which modes are symmetric or antisymmetric. If the subscript used is 1 then modes are symmetric whereas the subscript 2 are antisymmetric modes. In the case of monolayer MoS_2, the inversion symmetry is absent leading to no differences between gerade and ungerade modes. The subscripts 1 and 2 are dropped for doubly degenerate E modes and instead symmetric modes are denoted with a prime (E') and antisymmetric with double prime (E'').

3.3 Sample fabrication

Before going into physical or optical experiments on monolayer MoS_2, here is a brief description of how very high quality samples are fabricated. In this section, we discuss about the different crystal sources used, exfoliation techniques and identification process of monolayer MoS_2 using physical characterization.

3.3.1 MoS_2 crystal sources

In our experiments, the MoS_2 flakes are obtained from two different sources of bulk crystals. One of them is a natural source MoS_2 bought from SPI(Structure Probe Inc.) supplies while the other is a synthetic crystal prepared at high temperature(HP) and high pressure(HT) complex process by NIMS, Tsukuba. In this process 99.9% pure MoS_2 powder is encapsulated in a h-BN capsule and brought to a high pressure of 5 GPa and high temperature of about 1800 $^{\circ}$C for 20 mins by using a belt type high pressure apparatus. The sample is slowly cooled down form this molten state to room temperature at a rate of 0.8°C/min. After releasing the pressure, the MoS_2 crystal is recovered by crushing the h-BN capsule. We obtain a typical 1-2mm crystal size after the execution of this HP/HT process.

3.3.2 Mechanical exfoliation

Mechanical exfoliation is an easy and very effective procedure to obtain high quality monolayer flakes at as short time as possible for conducting laboratory experiments. The discovery of graphene and electrical experiments on these samples by Novoselov et al [21] was possible because of the very same exfoliation method. In the mechanical exfoliation method a scotch tape (3M magic scotch in our case) is used to micromechanically cleave the sample and thin them down. In this method a piece of MoS_2 crystal is placed on the adhesive side of the scotch tape. This adhesive side is pressed on to itself many times to thin down the crystal and to form a square like structure as shown in the figure 3.10 which could pressed on to the desired substrates.

Variety of substrates could be used such as Si /SiO_2(290nm) substrate, metals like copper, quartz, glass or even polymers like PDMS. The tape with the already thinned down crystals is pressed onto the surface of the target substrate. It is caressed slowly from the top so that the tape gets nicely adhered to the substrate. The tape is peeled off slowly which leaves behind

some of the flakes on the target substrate out of which some would be monolayers.

Figure 3.10 – (left) Picture of exfoliation on scotch tape executed by the above explained method using (right) natural and HP/HT crystal of MoS_2.

3.3.3 Optical identification of monolayer MoS_2 flakes

Generally the MoS_2 flakes would be first exfoliated on Si /SiO_2(290nm) substrate to get an idea about the thickness of the flakes and isolate the monolayer flakes for the future use. These substrates are mainly used because the 290nm of Si/SiO_2 on the top helps to optimize the contrast for monolayers during optical microscopy. Optical microscopy is the technique that is usually used to identify the monolayers. Based on contrast difference, it is easy to recognize the monolayer flake. However its matter of experience to be able to exactly identify the monolayer just by optical contrast. Further we could use an approach to establish correspondence between optical contrast that can vary with number of layers and the optical wavelength.

In this regard ,we find that in the red channel of the digital optical images, the contrast is the lowest (0.22 ± 0.08) for a monolayer. This characteristic contrast can be used as criterion for the fast identification of the monolayers of MoS_2. We chose the contrast of the RBG images with respect to the surrounding SiO_2 surface in the red channel (red channel contrast, RCC) as a relevant quantity, defined as the difference between the signal from SiO_2 ($I_{silicaR}$) and from the flake (I_{flakeR}), normalized by $I_{silicaR}$:

$$RCC = \frac{(I_{silicaR} - I_{flakeR})}{I_{silicaR}} \tag{3.3.3.1}$$

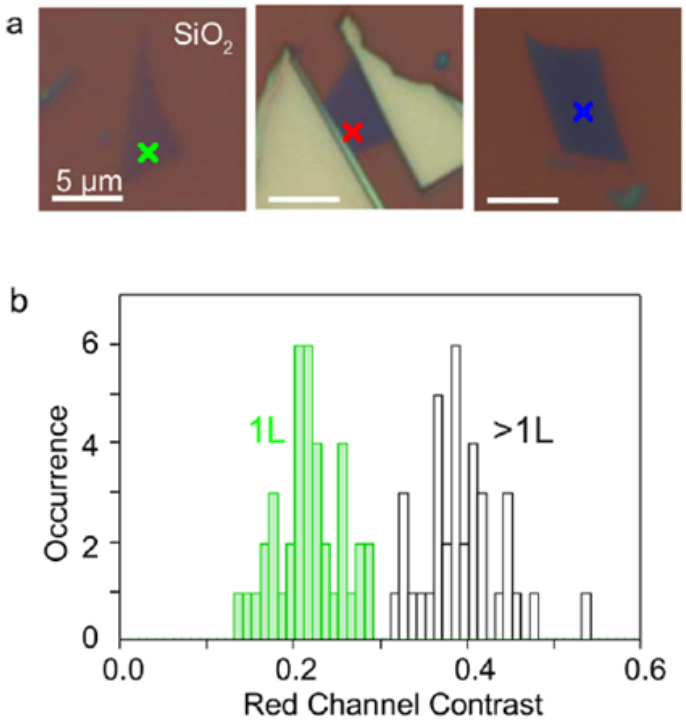

Figure 3.11 – (a) Optical micrographs of (from left to right) single-(1L), bi- (2L), and tri- (3L) layer MoS_2 flakes exfoliated on SiO_2 with Scotch tape.(b)Occurrence of all MoS_2 1L flakes (green bars) showing a characteristic optical contrast relative to SiO_2 in the red channel in numerical images. For comparison, some flakes of more than one layer in thickness (black bars), showing a higher optical contrast, are shown: 75 flakes have been measured in total. Green bars signal single-layer flakes, as ascertained with Raman spectroscopy, and black bars signal flakes of more than one layer in thickness.

Further to confirm we could do atomic force microscopy(AFM) to check the thickness of the deposited flake. In case of a monolayer MoS_2 flakes the thickness should be around 0.8nm. We could also confirm them using Raman spectroscopy or Photoluminescence which would be discussed in the later sections of the chapter.

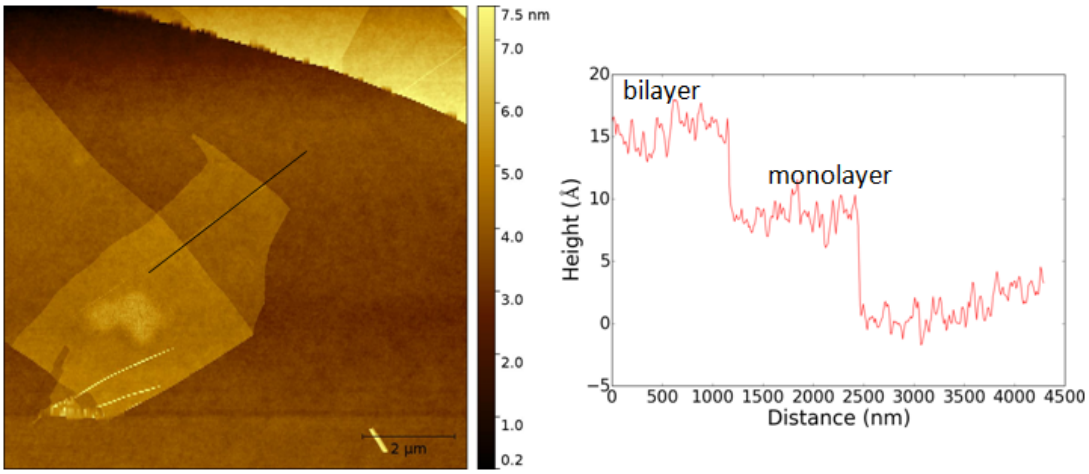

Figure 3.12 – Atomic force microscopy image of exfoliated MoS_2. Shown in the figure are monolayer and bilayer MoS_2 with typical thickness(height) of 0.8nm and 1.6nm respectively.

3.3.4 Large area monolayer flakes

One of the disadvantage of exfoliating on Si $/SiO_2$ is that irrespective of the source of MoS_2 whether natural or artificial, the typical area is of the order few to $20 - 50\mu m^2$. We have seen that if we use polydimethylsiloxane (PDMS) Gelpak 4 as the substrate instead of Si $/SiO_2$, the area of the exfoliated flakes substantially increases by almost 10 folds. In this case, the tape with already thinned down MoS_2 is gently pressed on the PDMS substrate and peeled slowly to obtain flakes.

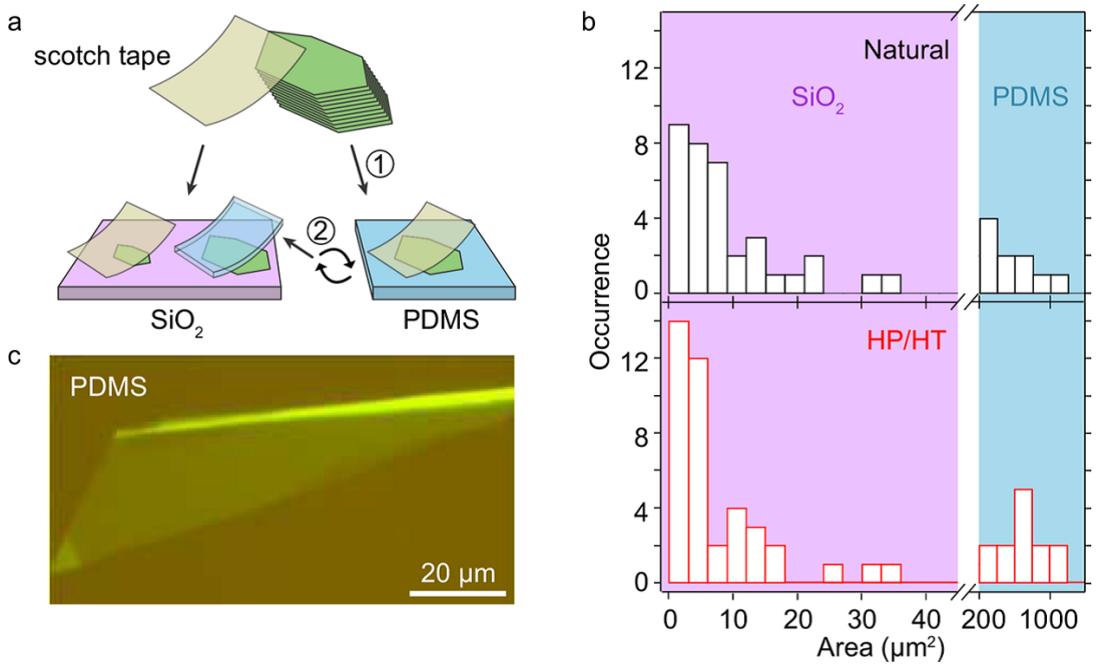

Figure 3.13 – (a) Schematics of the process for exfoliation with scotch tape toward a SiO_2 surface and PDMS. (b) Occurrence of MoS_2 flakes of less than four layers in thickness, obtained by scotch tape exfoliation on SiO_2 (light-pink-shaded regions) and stamping on PDMS (blueshaded regions), in the case of a natural source of MoS_2 (top) and the HP/HT-MoS_2 (bottom) for both Scotch tape and PDMS: 45 and 52 flakes have been measured for the two sources of MoS_2. (c) Optical micrograph of a large bilayer MoS_2 flake obtained by exfoliation on PDMS.

In above figure 3.13, there is also a comparison of exfoliation between the natural and HP/HT MoS_2 sources. We wanted to confirm with the statistics if the synthetic MoS_2 is any better in terms of number and the area of the monolayer flakes obtained. Whether the substrate is Si $/SiO_2$ or PDMS, we see that the quantity of flakes and their area are approximately same. Hence we cannot conclude that synthetic MoS_2 is better than the natural one.

3.3.5 Preparation of samples

As explained in the introduction in case of monolayer MoS_2, we try to enhance its optical properties by transferring it onto hBN flakes to form a MoS_2/BN heterostructure. For the transfer, we use a polymer transfer technique called PDMS viscoeleastic transfer method.

In the case of PDMS method, first the h-BN crystal is placed on a scotch tape and was mechanically exfoliated onto a Si/SiO_2 substrate. A very flat hBN flake with thickness around 20nm is identified. Meanwhile, the MoS_2 crystal is exfoliated onto a gelpack PDMS thin film. A

large monolayer MoS_2 is identified on PDMS based on optical contrast. This monolayer MoS_2 is aligned and transferred onto the h-BN on Si/SiO_2 by viscoelastic stamping method discovered by Castellanos et al.[16]

This process is similar to stamping but at very slow speed. During the stamping, the monolayer MoS_2 gets transferred on to hBN flake. A pictorial representation of this process is shown in the figure 3.14. While this process is known to yield clean MoS_2/h-BN interface, at some areas there maybe air blisters, puddles and cracks. These may form as a result of the exerted mechanical stress, but a negligible amount of contaminants is expected which was verified using AFM or TEM.

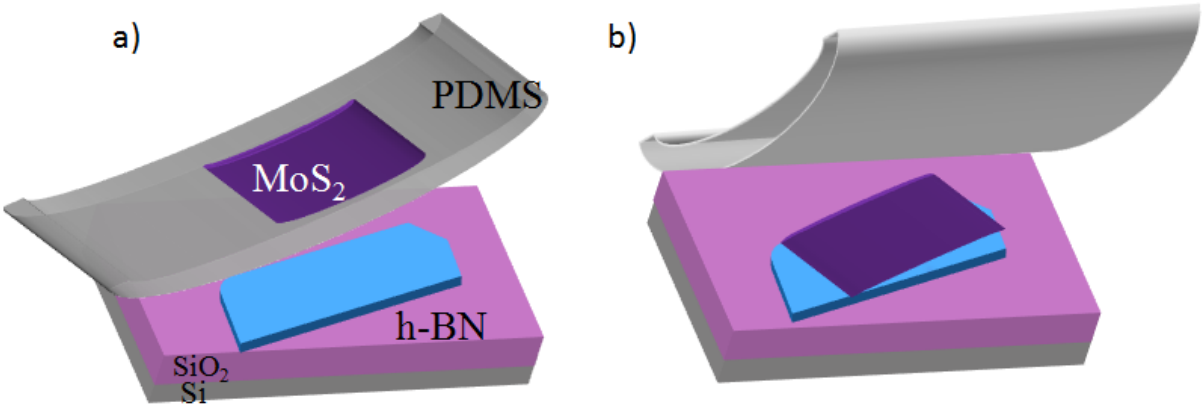

Figure 3.14 – Flow diagram for preparation of MoS_2/BN heterostructure using PDMS. a) MoS_2 is exfoliated on gelpak thin film of PDMS and a monolayer is identified and aligned to clean and flat hBN flake b) After the PDMS stamping process, the monolayer MoS_2 is transferred on to the selected hBN flake.

Using the PDMS method explained above, two kind of samples were fabricated. In the first kind, natural monolayer MoS_2 was stamped on to the hBN flake. This sample had two parts, one where monolayer MoS_2 was on Si/SiO_2 substrate and another on hBN flake. Similarly in the second kind of sample, synthetic HP/HT monolayer MoS_2 was stamped on to the hBN flake. This second sample also had monolayer MoS_2 lying on Si/SiO_2 and hBN respectively. The optical images for the same is shown in the figure 3.15.

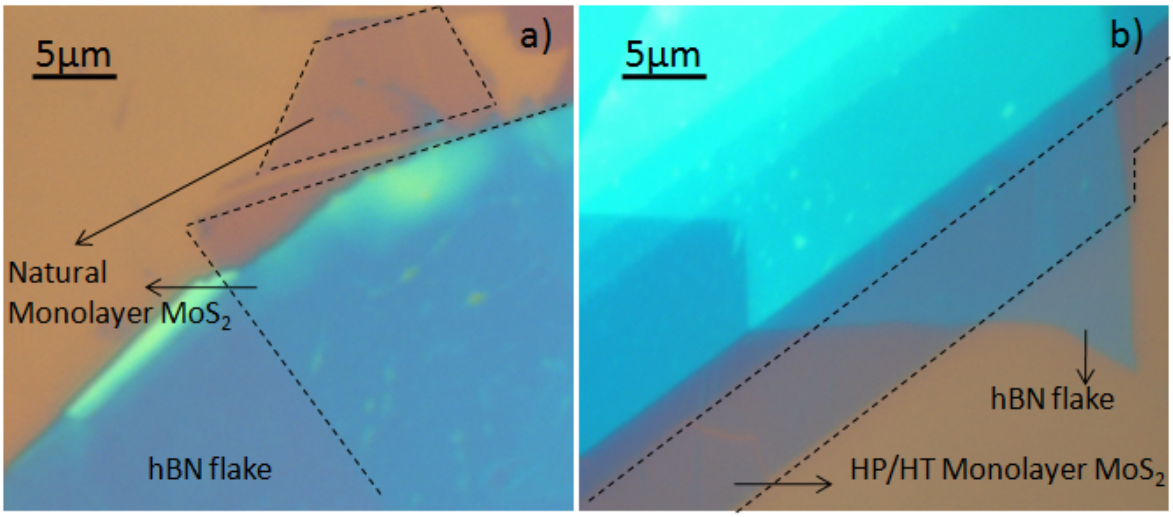

Figure 3.15 – a) Natural MOS_2/BN heterostructure b) Synthetic MoS_2/BN heterostructure both prepared using PDMS technique of viscoelastic stamping.

3.4 Introduction to spectroscopy techniques

In this section we provide basic introduction to the different spectroscopy techniques such as Raman, photoluminescence and reflectance spectroscopy that are used in the further course of the thesis.

3.4.1 Introduction to Raman spectroscopy

Raman spectroscopy is a non contact, non destructive vibrational spectroscopic technique used to obtain information on molecular vibration and crystal structures. When a material is illuminated with light, often a part of it is transmitted, a part that is reflected and the remaining part interacts with the material in form of absorption, emission or scattering. This scattering of light is majorly an elastic process where there is no change in the energy called Rayleigh scattering. However there would be a infinitesimal amount of inelastic scattering where the scattered light has different energy from the incident light called as Raman scattering. The difference in energy is hence the energy of the optical phonon involved in the process.

Raman scattering could be classified into two types called as Stokes Raman scattering and anti-Stokes Raman scattering. In case of Stokes Raman scattering, an electron that is excited from the ground level falls to a vibrational level and involves energy absorption by the material resulting in scattered light having lower energy than the incident light. In contrast, during anti-Stokes Raman scattering an electron is excited from the vibrational level to an excited state and thereby scattered light having more energy than the incident. Hence, when temperature is increased during the measurement process the intensity of anti-Stokes increases when compared to that of the Stokes scattering and due to this reason, intensity ratio of anti-Stokes and Stokes could be used to measure the temperature of the sample.

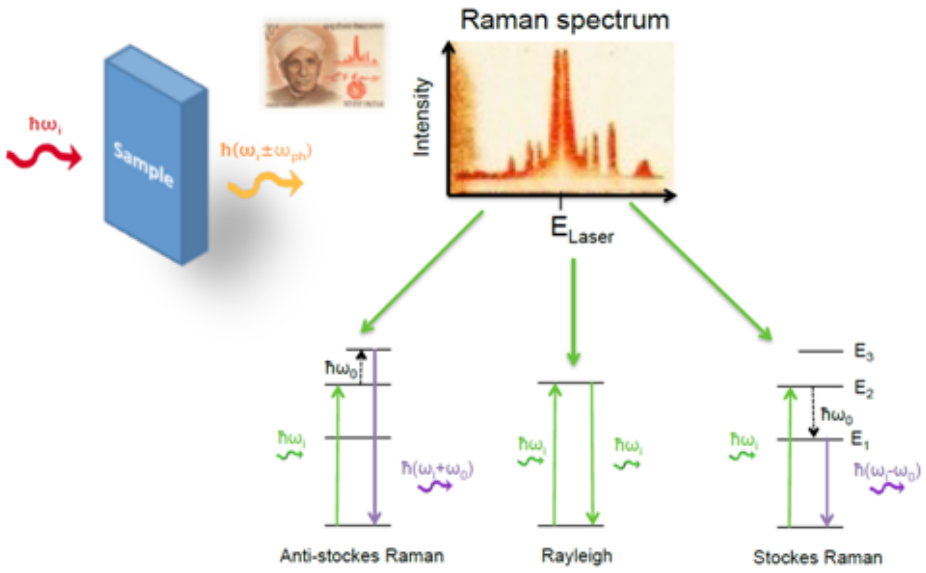

Figure 3.16 – Inelastic Raman scattering process: Schematic of the Raman diffusion. An example of Raman spectra exhibiting different peaks both in the Stokes Raman and anti-Stokes Raman region. (Figure adapted from Nedjma Bendiab HDR)[102]

Raman scattering can be represented as an incident photon of energy $h\omega_i$ and momentum k_i that scattered into a photon of energy $h\omega_{sc}$ and momentum k_{sc} in accordance with energy and momentum conservation laws.

$$h\omega_i = h\omega_{sc} + h\Omega_{ph}. \tag{3.4.1.1}$$

$$k_i = k_{sc} + q_{ph}, \tag{3.4.1.2}$$

where Ω_{ph} and q_{ph} are the energy and the momentum of the phonon.

The Raman scattering intensity according to Fermi golden rule is proportional to the total transitional probability given as:

$$I \propto \left| \sum_{n,n^*} \frac{\langle \omega_{sc}, ph, i \mid H_\rho \mid 0, ph, n^* \rangle \langle 0, ph, n^* \mid H_{e-ph} \mid 0, 0, n \rangle \langle 0, 0, n \mid H_\rho \mid \omega_i, 0, i \rangle}{[h\omega_i - (E_n - E_i)] \cdot [h\omega_i - h\Omega_{ph} - (E_{n^*} - E_i)]} \right|^2 \cdot \delta\left(\omega_i - \Omega_{ph} - \omega_{sc}\right) \tag{3.4.1.3}$$

where H_ρ represents electron photon interactions, H_{e-ph} contains the electron phonon interactions. Here the quantum state of the system which are influenced by photonic, phononic and electronic nature of the system are represented as:

The term $\langle 0, 0, n \mid H_\rho \mid \omega_i, 0, i \rangle$ describes the electronic excitation from state i to n due to absorption of an incident photon of specific energy $h\omega_i$.

The term $\langle 0, ph, n^* \mid H_{e-ph} \mid 0, 0, n \rangle$ explains the phonon emission by the excited electron due to its scattering from state n to n^*.

Finally the term $\langle \omega_{sc}, ph, i \mid H_\rho \mid 0, ph, n^* \rangle$ is the recombination of excited electron in the state n^* with the hole so that it returns to its initial state i.

In the above equation, when the difference between the incoming photon energy and the scattered photon energy is equal to an electronic transition, the denominator term tends to zero resulting in maximal intensity. This phenomena is called as Resonant Raman scattering. In addition, the above discussed process is the first order Raman process which are result of photon interaction with one phonon in the material. The selection rule $q_{ph} \approx 0$ allows the phonon to be accessed only near the centre of the Brillouin zone. However we can access the phonons far from the gamma point because of higher order Raman scattering processes.

Higher order processes occur either when two phonons are excited which are of the same phonon branch resulting in overtones of a particular mode or two phonons of different branches generate modes that are superposition of different modes. These higher order scattering process are generally due to phonon scattering at defects which would be discussed briefly in the next chapter of the thesis.

3.4.2 Confocal micro Raman spectroscopy set-up

A confocal micro Raman consists of a laser excitation source with well defined wavelength and beam profile, sample illumination system and light collection optics, wavelength selector typically a filter and a detector such as a photodiode or a CCD. Typically laser wavelengths such as 633 nm, 532 nm, and 488 nm are used in the laboratory setup. The intensity of the Raman scatter is proportional to $1/4\lambda$, so short excitation laser wavelengths deliver a much stronger Raman signal.

In this technique, a confocal microscope with typical objectives 10X, 50X or 100X aids us to probe a required spot with good precision. Here the resolution is limited to diffraction limit of light of approximately 500nm called as spot size. Along with the microscope is a mechanical stage to place a sample which can move in X, Y and Z directions that is used to focus the laser spot on the required position of the sample.

An important element is a piezoelectric element that can perform precise movements down to some tens of nm during Raman imaging. Scattered light from the sample is collected by a large numerical aperture objective which is guided by a fiber to the spectrometer which further will be dispersed by the grating. In our setup there are 600gr/mm grating with resolution of $3cm^{-1}$ and 1800gr/mm grating with resolution of 0.5cm^{-1}. These wavelength dispersed photons are then collected by a CCD camera maintained at low temperatures. Typically notch filters are used to cut off the high intensity elastic Rayleigh scattering from the low probable inelastic scattering.

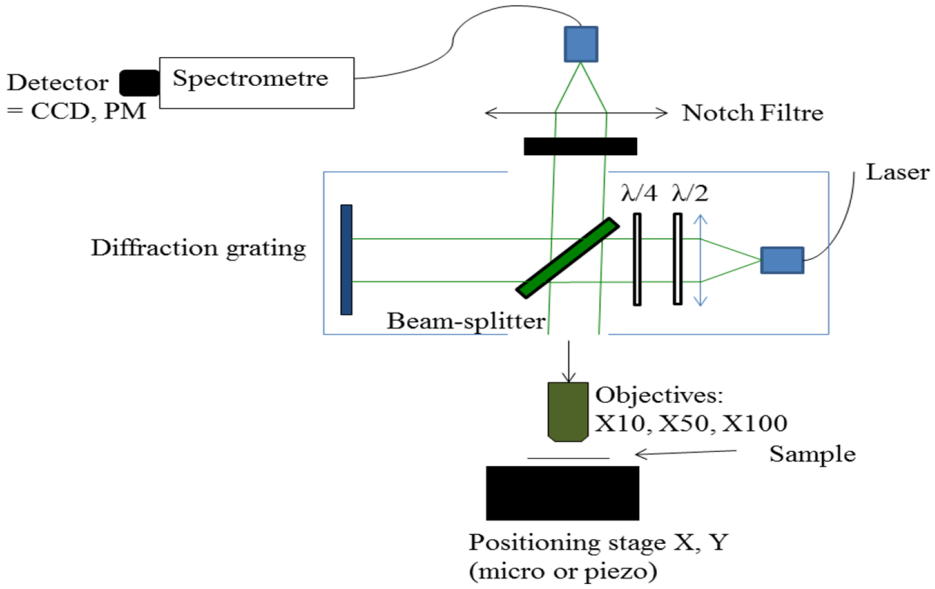

Figure 3.17 – Scheme of a Raman spectrometer. The incoming laser reaches the sample, goes then through notch filter (in this case a holographic notch filter), passes through a system of lenses and a slit and is diffracted by a grating, which divides its spectrum with respect to its frequencies. (Figure adapted from master-intership Martina Ballerio)[103]

3.4.3 Introduction to Photoluminescence technique

Photoluminescence spectroscopy is a widely used contact less and non destructive technique for characterisation of the optical and electronic properties of semiconductors. Photoluminescence (PL) is a light emission by any material after the absorption of photons that excite electron to a higher energy level. The electrons are photo excited into allowed excited states by light, upon relaxation electrons return to their equilibrium states and may include the emission of photon to be called a radiative process where as the result of no emission is called to be a non radiative process.

The energy of the emitted light (photoluminescence) will be the difference in energy levels of the two electron states involved in the transition between the excited state and the equilibrium state. While this explanation is general , other more complex phenomena occur during photoluminescence in many body systems like that of semiconductors. We would discuss in details the photoluminescence in case of semiconductors in the following paragraph.

The set-up used in photoluminescence technique is similar to that of the confocal Raman one instead the detector collects the photon emission. If the extrema of the conduction band and the valence band are at the same point in k, then the semicondcutor is called to be direct bandgap semiconductor. In this case upon excitation by laser, electron is excited from valence band to conduction band while creating a hole in valence band. This electron and hole pair called exciton is bound together and upon relaxation emits the photon pertaining to the optical bandgap of the direct bandgap semiconductor. This anhiliation of exciton resulting in photon emission is called radiative recombination.

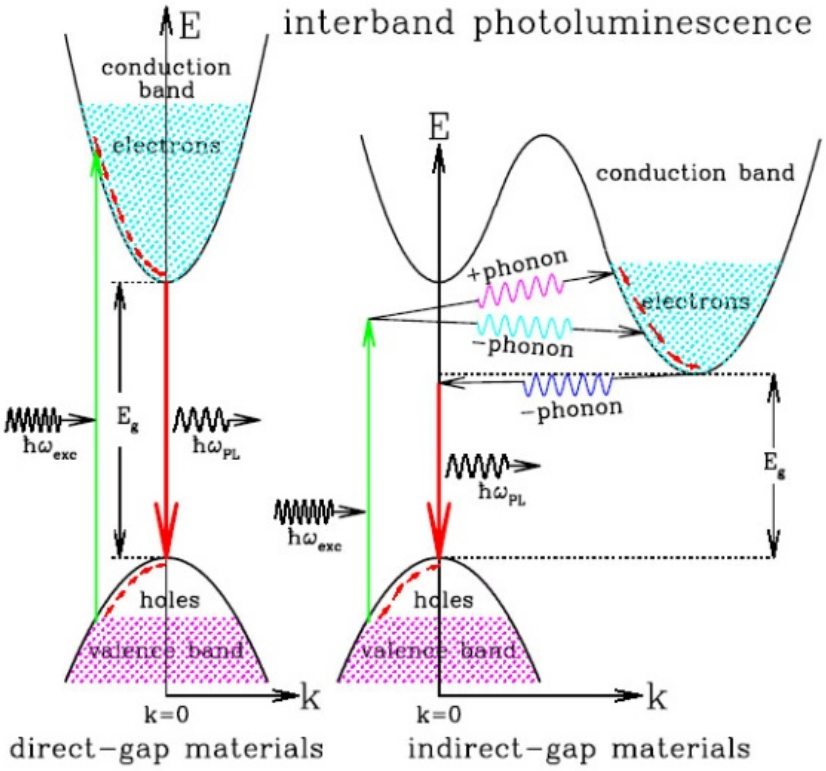

Figure 3.18 – Band diagram for direct bandgap semiconductors (left) and indirect bandgap semiconductors (right). Direct bandgap semiconductor showing direct transition of electron hole pair to form a photon whereas indirect bandgap needs phonon assistance for the photon emission. Figure taken from (Li, caltech.edu)

However, in some of the semiconductors, the extremas are not at the same point resulting in indirect bandgap semicondutor as shown in the figure 3.18. In this case the electron hole pair annihilates in non radiative recombination where photon emission is absent. Moreover, in some cases a phonon of suitable energy may assist the electron hole pair to recombine radiatively but the probability of this is very low. Hence for the significant photon emission, the semiconductor must be direct bandgap material unless profoundly assisted by phonons (in case of hBN [6]).

3.5 Extrinsic and intrinsic defect characterization using Raman and PL

In this context, we perform a comparative discussion about the two different samples namely natural monolayer MoS_2 and artificial HPHT monolayer MoS_2 standing on two different kind of substrates of SiO_2 and h-BN. Using the PDMS viscoelastic stamping method discussed before, MoS_2 was exfoliated on PDMS, identified using optical microscope and transferred onto Si/SiO_2 substrate and h-BN substrate (which was exfoliated on Si/SiO_2 beforehand) such that a part of monolayer MoS_2 is on the latter and the other part on the former. This is shown clearly in the figure 3.15. Hence the comparison is between the four samples all having monolayers: a) natural MoS_2 on Si/SiO_2 b) natural MoS_2 on hBN c) HP/HT MoS_2 on Si/SiO_2 and d) HP/HT MoS_2 on hBN.

3.5.1 Raman spectroscopy signature of monolayer MoS_2

The typical signature of MoS_2 Raman spectrum includes in plane $E^{'}$ (E^1_{2g} in multilayer) mode and out of plane $A^{'}_1$ mode(A_{1g} in multilayer) along with the low frequency modes depending on whether the MoS_2 is monolayer or not. Conventionally the difference between the high frequency modes $E^{'}$ and $A^{'}_1$ has been used to determine the thickness of the MoS_2 layers. It could be noted from the figure 3.19b that the frequency of $E^{'}$ mode decreases with increasing number of layers whereas the $A^{'}_1$ mode frequency increasing with the number of layers.

The out of plane mode $A^{'}_1$ increases with layer thickness due to interlayer interaction caused by weak Van der Waals attraction of the S atoms of the nearby layers. While this result is expected as the layer stacking can be seen as addition of a spring between S atoms of the nearby layers, but unexpectedly in case of $E^{'}$ it shows opposite trend. This anomalous behaviour has been still debated with explanations attributing from long range Coulomb interaction to weakening of nearest neighbour Mo-S force constant.

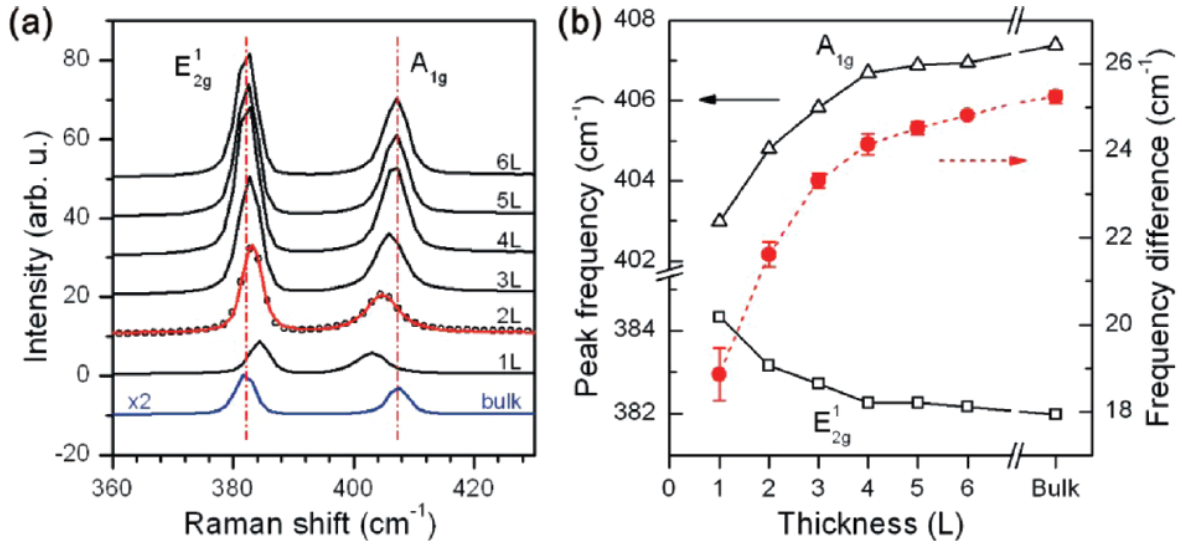

Figure 3.19 – a) Raman spectrum of MoS_2 having different layer thickness b) Plot of position of A_{1g} and E^1_{2g} modes ($A^{'}_1$ and E' in case of monolayer) and their frequency difference as a function of thickness of MoS_2 layers. Figure adapted from Lee et al. [104]

The figure 3.19a shows the thickness dependence of MoS_2 on its characteristic high frequency Raman modes. If the frequency difference between the high frequency mode is in between 18 to 20 cm^{-1}, it has been considered to be a monolayer MoS_2. While most of the times this is true, the positions of E' and $A^{'}_1$ and thus the frequency difference depends on the underlying substrate, stress and doping contributed by the substrate and also the doping contributed by internal or external defects. Hence sometimes it may not be right to use just the frequency difference to characterize the monolayer MoS_2. For example, monolayer MoS_2 grown using CVD methods on Si/SiO_2 substrates and monolayer MoS_2 transferred on hBN have been found to have this frequency difference a bit higher up to 21 cm^{-1}.

However, there is other reliable way to measure the number of layers using Raman spectroscopy on MoS_2 flakes [105][106]. These are the low frequency modes of MoS_2 namely rigid layer shear mode (S1) and layer breathing mode (B1) corresponding to vertical rigid layer vibrations as represented in the figure 3.20. We can notice that the monolayer MoS_2 Raman spectra has no signature of the low frequency modes. The occurrence and position of these shear (S1)

and breathing (B1) modes indicates that the flake is not a monolayer MoS_2.

Further these low frequency Raman active modes display stronger dependence on frequency than the high frequency modes where the two modes are stiffer in trilayer than in the bilayer as shown in the figure 3.20. Due to presence of these low frequency Raman active modes very close to Rayleigh, sometimes it is difficult to measure them easily. In that case, the most reliable way to identify the monolayer MoS_2 is by combination of high frequency Raman modes and photoluminescence technique that is explained in the next sub section. Since only monolayer MoS_2 has a direct bandgap, it displays strong photoluminescence.

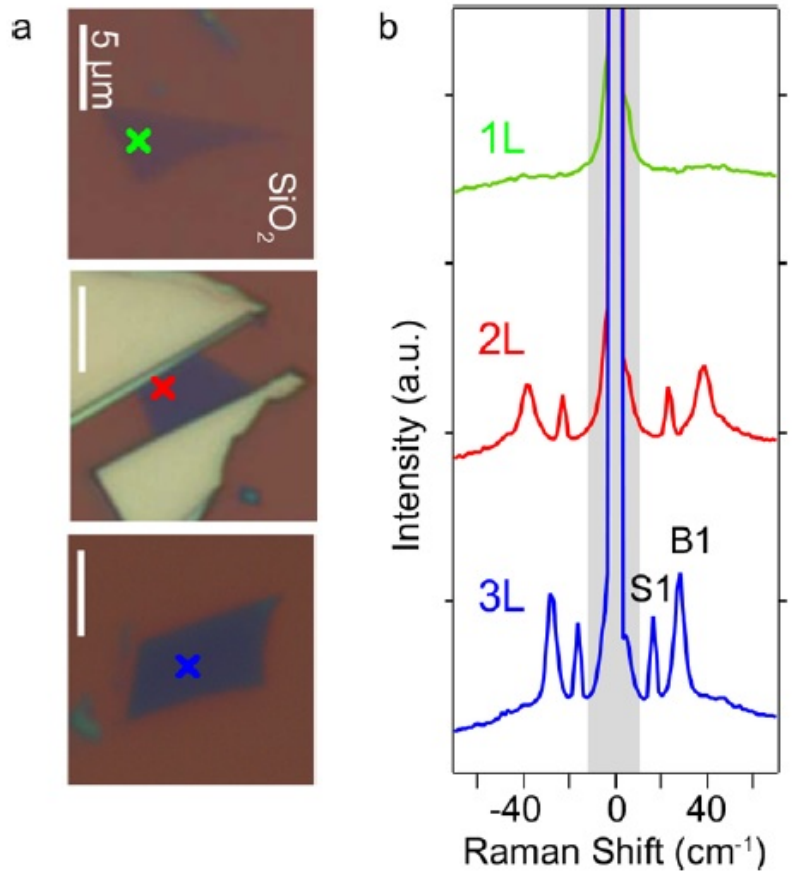

Figure 3.20 – (a) Optical micrographs of (from top to bottom) single-(1L), bi- (2L), and tri-(3L) layer MoS_2 flakes exfoliated on SiO_2 with Scotch tape. (b) Raman spectra of the interlayer shear (S1) and breathing (B1) modes measured at the locations marked with a cross in (a). The three spectra are vertically shifted for clarity; the grey-shaded area corresponds to the stop band of the notch filter (within which the measured intensity is not informative).

3.5.2 Photoluminescence signature of monolayer MoS_2

In the case of semiconductors like MoS_2, photo-excitation generates a pair of bound electron and holes typically with binding energies 0.5eV (for monolayer MoS_2), that behave similar to hydrogen atoms called as excitons. When the recombination of these electron hole pairs occurs, a photon is emitted which is observed as PL. The behaviour explained is true in the case of direct bandgap semiconductor such as monolayer MoS_2. In the indirect bandgap semiconductors like bulk MoS_2, phonons are needed to assist the photoluminescence process as shown in

the figure 3.18. However the probability of the occurrence of this case is very low compared to former because of which the monolayer MoS_2 has a very strong photoluminescence compared to its multilayer. Hence PL could be used a tool to identify and differentiate the monolayers of MoS_2.

Photoluminescence spectra were acquired with a 532 nm Nd:YAG laser using a commercial confocal WITEC spectrometer at room temperature under ambient conditions. The laser spot size is 0.5 micron. The signal was collected through a 50X objective with a numerical aperture of 0.75. A low power of 8 microW was used with a grating of 600 lines/mm. The photoluminescence spectra were taken with an integration time of 30 s to improve signal-to-noise ratio, and the spatially resolved photo-luminescence maps were taken with an integration time of 5 s.

The spectrum shown in the figure 3.21b is a typical PL signature of monolayer MoS_2. We could observe two major peaks which could be fit with three lorentzians called as trion (A-), exciton (A) and exciton(B). The excitons can bind to extra electrons called as trions which are nothing but charged excitons. In MoS_2, there is very strong spin orbit interaction due to relatively heavy element which gives rise to a significant spin orbit splitting of the valence band and hence the two peaks neutral exciton(A) and neutral exciton(B), due to holes from the upper and lower spin band respectively. At the conduction band there is very small but significant spin splitting also which gives rise to concept of bright and dark exciton which will not be discussed in this thesis.

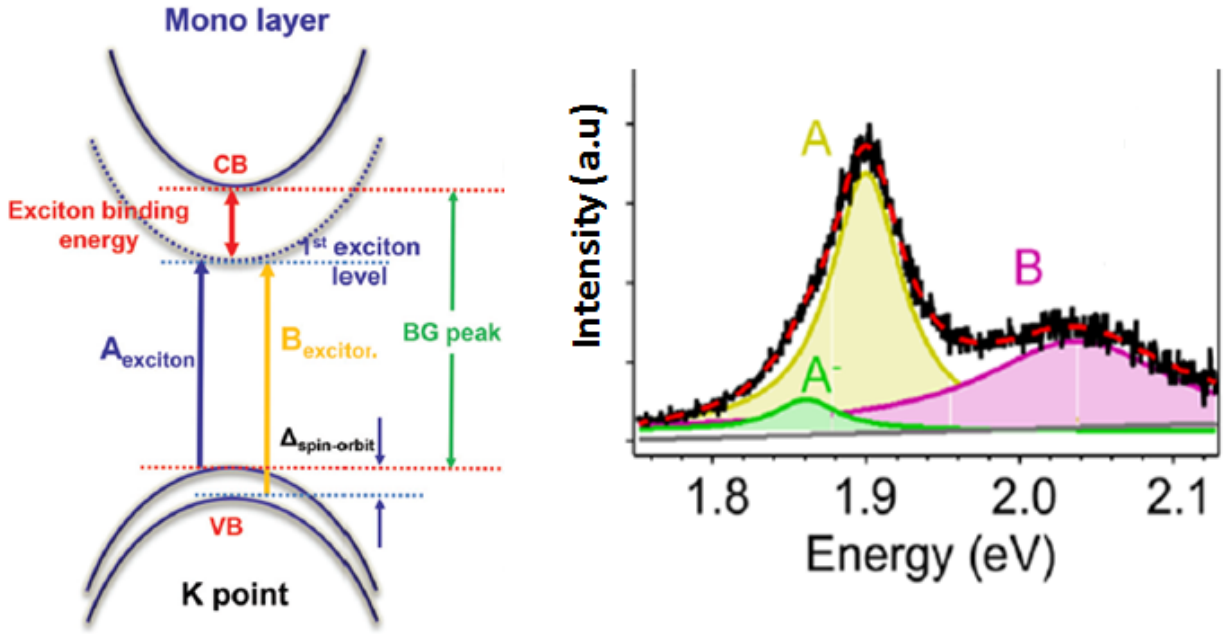

Figure 3.21 – (left) Schematic band diagram of monolayer MoS_2 explaining the optical transition at K point. Background peak (BG) corresponds to the difference in conduction band and valence band energy. Figure adapted from Dhakal et al. [107]. (right) Typical PL spectrum recorded during the experiments showing trion (A-), exciton (A) and exciton(B) peaks.

3.5.3 Reflectance spectroscopy of monolayer MoS_2

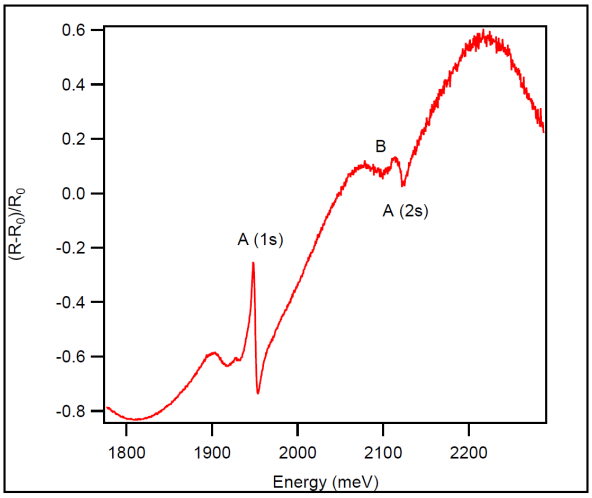

Figure 3.22 – Reflectivity signature of monolayer MoS_2.

Along with Raman spectroscopy and photoluminescence techniques, reflectance spectroscopy is a simple and powerful technique to probe 2D-materials and in particular, the thickness/layers. The figure 3.22 illustrates the differential reflectence spectra of monolayer MoS_2. It could be seen that the spectra has two prominent peaks occuring at energy 1.95eV and 2.1eV respectively. These peaks correspond to the optical absorption resulting from the direct transition at K point of the Brillouin zone. These peaks A(1s) and A(2s) are associated to generation of the A and B excitons during PL respectively.

3.5.4 Strain and Doping from vibrational spectroscopy

The high frequency Raman modes for each of the four samples is shown in the figure 3.23. In the high frequency modes of monolayer MoS_2, the in plane mode E' is susceptible majorly to strain[108], [109], [110] caused by the substrate or other effects while the out plane mode $A_1^{'}$ is susceptible mostly to electron doping [111] due to its sensitivity to electron phonon coupling effects. The first difference among the samples we could readily observe from their corresponding spectrum is that the position of $A_1^{'}$ varies according with the substrate underneath the monolayer MoS_2. We observe a blue shift of 1.0 ± 0.1 and 0.8 ± 0.1 cm^{-1} from SiO_2 to the h-BN substrate both in natural and HP/HT samples respectively. These blue shift are maybe due to mechanical strain translating the anharmonicity of the interatomic potential or electron doping arising as a effect of electron phonon interaction or both. Therefore we define and use a method to decouple and quantify the strain and electron doping effects as explained in detail by A.Michail et al.[112]

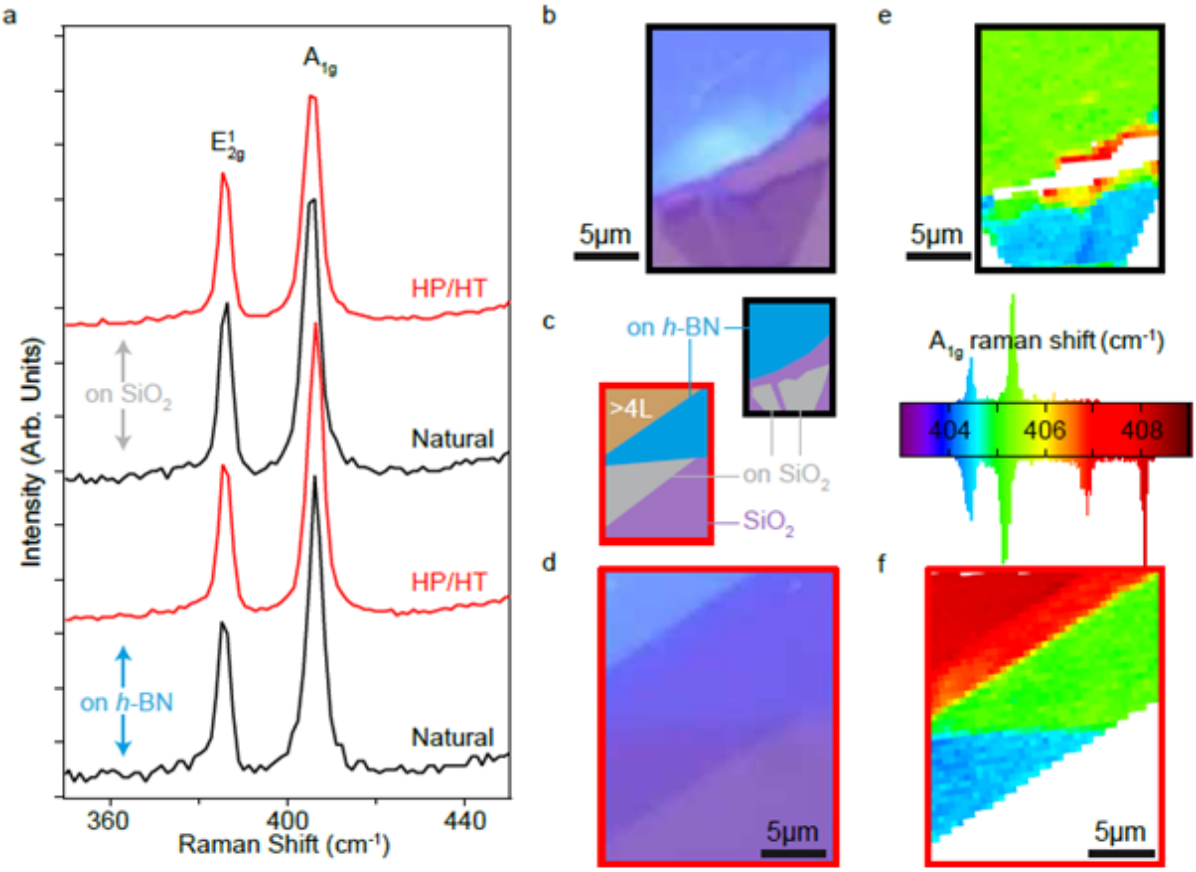

Figure 3.23 – (a) Raman spectra (532 nm wavelength laser) for MoS_2 single layers exfoliated from a natural crystal (black) and from a HP/HT source (red), on SiO_2 and hBN. (b, c, d) Optical micrographs for MoS_2 exfoliated from the two kinds of crystals. The cartoons (c) clarify the stacking of MoS_2 on hBN and SiO_2. (e, f) Raman maps of the position of the $A_1^{'}$ mode for the region corresponding to (b) and (d) for the two kinds of MoS_2 samples. The distribution of the mode position is shown for the top and bottom maps. The thick black and red frames in (b) to (f) refer to two MoS_2 sources, natural and HP/HT.

For the sake of calculation of the effect of strain, we define a parameter called Gruneisen parameter (γ) [113]which quantifies the effect that changing crystal lattice has on its vibrational properties. In our case it denotes the change in the frequency of a mode with respect to strain applied on the substrate. The phonon frequency shift in a particular mode induced by the strain can be calculated using the relation

$$\delta\omega = 2\gamma\omega_0\epsilon \tag{3.5.4.1}$$

where ω_0 is the frequency of a mode at zero strain, γ is the Gruneisen parameter of that mode, and ϵ is the applied biaxial strain.

However, it is difficult to obtain the frequency of the mode with no strain or no doping experimentally as it is an unrealistic situation. Hence we use the mean value of the observed frequency of the flake as an estimate for this unperturbed phonon frequency. This Gruneisen parameter has been calculated for in plane mode E' and found to lie between 0.64 to 1.1 whereas for the out of plane $A_1^{'}$ mode it takes a value around 0.15. Hence its usually assumed that the E' mode is more suceptible to strain effects. In our case we take a mean value of 0.86 for in

plane E' mode and 0.15 for the out of plane $A_1^{'}$ mode.

Electron phonon coupling (EPC) occurs due to increased electron doping where the anti-bonding states are at the bottom of the conduction band, positioned at the K-point of the Brillouin zone. These arising electron phonon coupling alters the Raman active modes of MoS_2. It has been found out that the effect of EPC is much lower for the in plane E' mode when compared to out of plane $A_1^{'}$ mode. Further, the EPC is proportional to the phonon linewidth. Hence the linewidth of $A_1^{'}$ mode increases with electron doping upto 6cm $^{-1}$ whereas the E' mode does not display any significant variation as a function of electron doping. This coexisiting strain and electron doping could be expressed linearly in terms of Pos($A_1^{'}$) and Pos(E') with assumption that strain and electron doping effects are decoupled at low levels of the same. Hence a linear transformation between the vector spaces $\delta Pos(A_1^{'}) - \delta Pos(E')$ and $\epsilon - n$, n being electron doping, could be formulated which is explained as below.

The relative difference between the strain and doping induced phonon frequency shift of the Raman mode E' and $A_1^{'}$ and their mean values taken as unperturbed frequency is given as

$$\Delta Pos(E') = Pos(E') - Pos(E')_0 \tag{3.5.4.2}$$

$$\Delta Pos(A_1') = Pos(A_1') - Pos(A_1')_0 \tag{3.5.4.3}$$

where $Pos(E')_0$ and $Pos(A_1')_0$ are the mean position values taken as unperturbed frequency.

These equations can be expressed as functions of strain ϵ and electron concentration n, given as

$$\Delta Pos(E') = -2\gamma(E')Pos(E')_0\epsilon + k_n(E')n \tag{3.5.4.4}$$

$$\Delta Pos(A_1') = -2\gamma(A_1')Pos(A_1')_0\epsilon + k_n(A_1')n \tag{3.5.4.5}$$

where $\gamma(E')$ is the Gruneisen parameter of the E' mode, $\gamma(A_1')$ is the Gruneisen parameter of the A_1' mode and k_n corresponds to the shift rate with the carrier concentration.

These equations could be written in terms of ϵ and n as

$$\epsilon = \frac{k_n(A_1')\Delta Pos(E') - k_n(E')\Delta Pos(A_1')}{2\gamma(A_1')Pos(A_1')_0k_n(E') - 2\gamma(E')Pos(E')_0k_n(A_1')} \tag{3.5.4.6}$$

$$n = \frac{\gamma(A_1')Pos(A_1')_0\Delta Pos(E') - \gamma(E')Pos(E')_0\Delta Pos(A_1')}{\gamma(A_1')Pos(A_1')_0k_n(E') - \gamma(E'')Pos(E')_0k_n(A_1')} \tag{3.5.4.7}$$

with their unit vectors of the ϵ-axis and n-axis respectively given as

$$\hat{\epsilon} = \frac{\gamma(E')Pos(E')_0\hat{i} + \gamma(A_1')Pos(A_1')_0\hat{j}}{\sqrt{[\gamma(E')Pos(E')_0]^2 + [\gamma(A_1')Pos(A_1')_0]^2}} \tag{3.5.4.8}$$

$$\hat{n} = \frac{k_n(E')\hat{i} + k_n(A_1')\hat{j}}{\sqrt{k_n(E')^2 + k_n(A_1')^2}} \tag{3.5.4.9}$$

where $\hat{i}$ and $\hat{j}$ are the unit vectors of the $\Delta Pos(A_1')$ and $\Delta Pos(E')$ respectively.

For our experimental case we have used the mean $Pos(E')$ and $Pos(A_1')$ as $385cm^{-1}$ and $405cm^{-1}$ respectively. The Gruneisen parameter values used are $\gamma(E')$ as 0.86 and $\gamma(A_1')$ as 0.15 and the k_n values used are $k_n(E') = -0.33 \times 10^{-13}cm^{-1}$ and $k_n(A_1') = -2.22 \times 10^{-13}cm^{-1}$. Using these we can construct a $\epsilon - n$ reference space with positions of E' and A_1' modes as axes

system as represented in the figure 3.24.

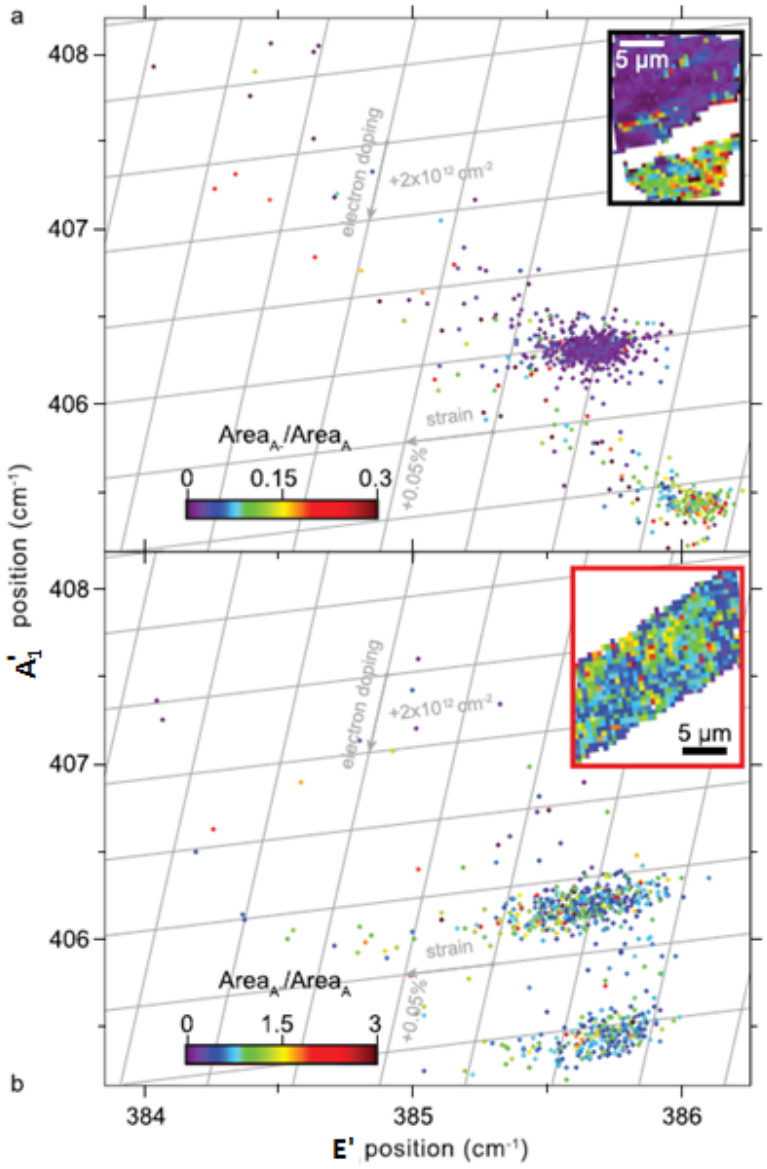

Figure 3.24 – Positions of the A_1' and E' modes of the Raman spectra (532 nm wavelength laser), each point corresponding to a point in the maps shown in figure 3.19 e,f. The grid of the strain vs electronic doping has increments of 0.05% and $2 \times 10^{12} cm^{-2}$. (a and b) The two MoS_2 sources, natural and HPHT, respectively. Each point is coded with a color corresponding to the ratio of areas of the two contributions to the main excitonic feature in the photoluminescence spectra, shown in the insets (see Figure 3.25).Inset shows spatial dispersion of area ratio.

The figure 3.24 shows the graph for the four types of samples explained at the beginning. Just by the visual analysis of the graph, we could notice that there are two groups of points. The two groups of points correspond to MoS_2 on hBN sample having a higher A_1' position and MoS_2 on Si/SiO_2 respectively. This trend is similar despite that the MoS_2 comes from two different sources pointing that the effect is caused by external means possibly the nature of the substrate [114], [115] [116]. Additionally, it is found out that the electron doping is higher by 2.5×10^{12} and 2.0×10^{12} electrons/cm^{-2} on Si/SiO_2 samples for both the natural and HPHT sources respectively. This is attributed to phenomena of substrate induced doping where the

charged impurities in SiO_2 dope the two dimensional material resting over it. These effects are absent in case of h-BN which is a crystalline inert atomically flat substrate. Hence this doping effect on MoS_2 induced by charged impurties in the substrate are classified as extrinsic defects to monolayer MoS_2.

We can also notice from the figure 3.24, that the two clusters of points are scattered within a range of 0.05% to 0.1% in strain. This comes from the fact that a small extent of non uniform strain could be generated during the transfer by PDMS method explained in the previous sections. Further a strain difference of 0.05% to 0.1% is reported between the two clusters of points, corresponding to the sample of natural MoS_2 on hBN and the sample of natural MoS_2 on SiO_2 respectively. However such a difference is not found in the case of HPHT MoS_2 samples. This observed difference is attributed to the possiblity of different mechanical efforts exerted during the fabrication of the samples rather than internal strain induced by the defects.

3.5.5 Excitonic complex in presence of strain, doping and defects

Similar to previous section, both electronic doping and strain influence the excitonic properties of monolayer MoS_2.[108],[117],[118],[119],[120] Photoluminescence spectroscopy measurements were performed on the same samples addressed before at room temperature using a 532 nm green laser excitation at low power of about 0.1 μW. The figure 3.25 displays the characteristic spectra after the optical interference effect corrections. As expected for monolayer MoS_2, we observe two peaks designated as A exciton and B exciton corresponding to different transition involving one or the other spin polarized valence band. [121]

In this section we will consider only the A exciton. Further while fitting the spectrum, we could notice that the peak actually comprises two components namely neutral exciton simply called as exciton and charged exciton named as trion.[120] The peak positions of these are seperated by 40meV called as trion binding energy and the peaks have a full width at half maximum of several 10meV dominated by electron phonon coupling.[122] The trion prominently depends on electron doping and is higher with the increase in doping.[123]

Conventionally electron doping is extracted from photoluminescence spectra where the ratio of trion and exciton gives the level of electron doping. This is estimated to be typically on the order of several 10^{12} electrons $/cm^{-2}$. The inset in the previous figure reveals a distinctive trion vs exciton population whether MoS_2 lies on SiO_2 or $h-$BN. The ratios of A^- to A areas, typically $0.01-0.02$ and 0.1, respectively, on these two substrates are consistent with changes of electronic doping levels, due to charged impurities in SiO_2, found in the analysis of the Raman data (on the order of a few $10^{12}cm^{-2}$).

The position of the two peaks (Figures 3.25b) is changing by 12 meV whether MoS_2 lies on SiO_2 or h-BN. As Raman spectroscopy suggests, this is a result of the preparation process causing a spatial strain variation, a compression on SiO_2 relative to the case on h-BN, by about 0.1%. The magnitude of the strain-induced energy shift fits with that corresponding to previously reported strain-induced electronic band gap change.[108]

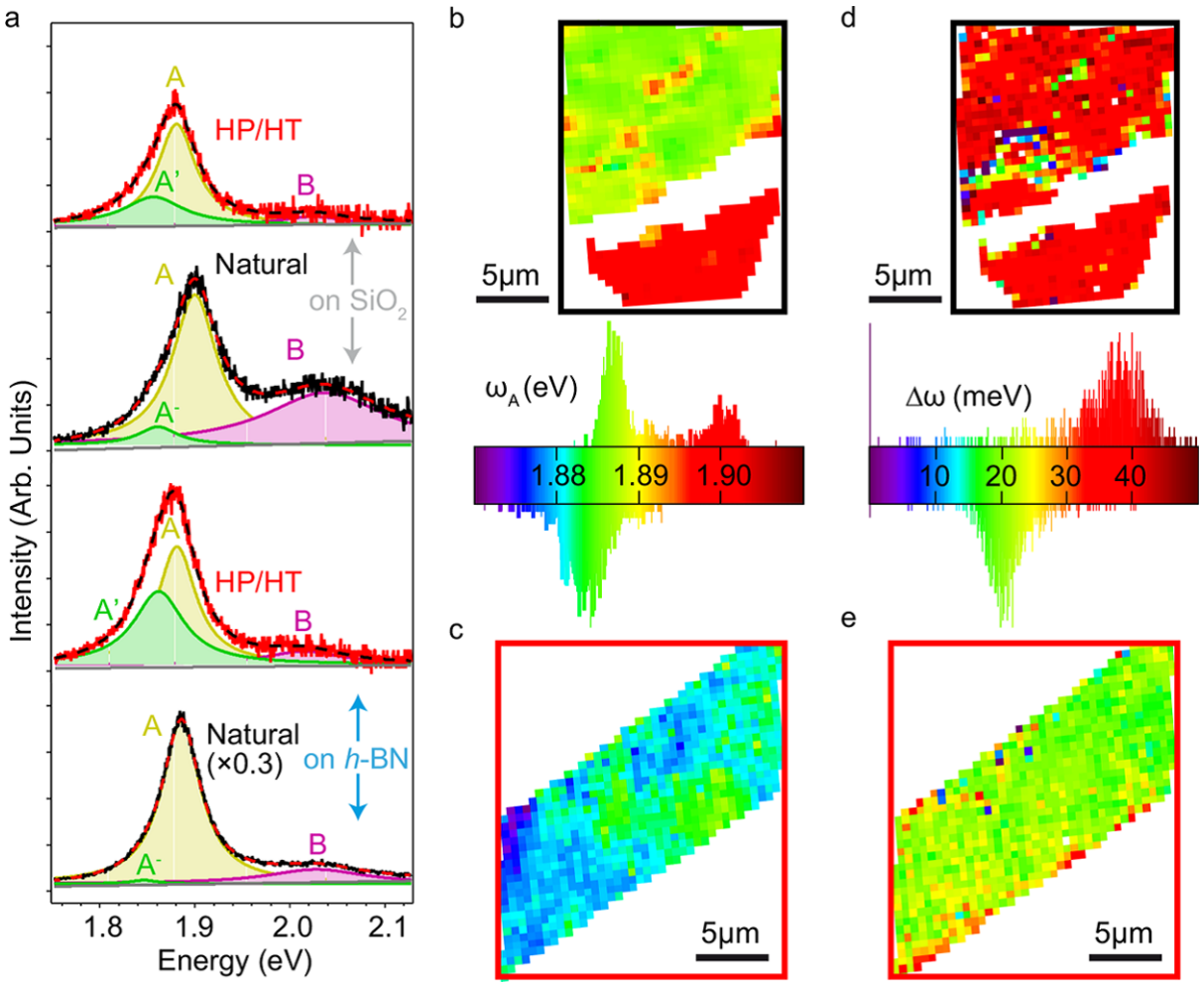

Figure 3.25 – (a) Room-temperature photoluminescence spectra for single layer MoS_2 prepared by exfoliation from natural (black) and HP/HT(red) crystals, deposited on the surface of SiO2 (top) and hBN (bottom). The spectra have been corrected for interference effects associated with the presence of the MoS_2/hBN, MoS2/SiO_2, hBN/SiO_2, and SiO_2/Si interfaces. The spectra are fitted with three Lorentzian components, respectively corresponding to the lowest energy direct transition, for the exciton (A), the trion for natural MoS_2 (A-), or the defect-bound exciton for HP/HT MoS_2 (A), and the second lowest energy direct transition for the exciton (B). The dotted lines are the best fits to the data. (bcde) Maps of energy of the A component, ω_A (b, c), and of the difference in energy $\Delta\omega$ of the A- and A (d,e)components, for the same area as in Figure 3.23 b,d, for natural (thick black frames, b, d) and HP/HT (thick red frames, c, e) MoS_2 single layers.

Let us now turn to the photoluminescence signatures in the case of HP/HT-MoS_2. In this case also, we find that the main excitonic feature does not consist of a single component. While the above-discussed energy difference between the two components was about 40 meV for natural MoS_2, consistent with the expected trion binding energy corresponding to electron doping levels on the order of few 10^{12} electrons/cm^{-2} [120], here the two components are separated by a substantially lower energy difference (20 meV), regardless of the substrate (Figure 3.25e).

Such an energy difference cannot correspond to a trion under the influence of strain or electronic doping: the variations of strain and electronic doping in our samples are in the range of a few 0.1% and $10^{12} cm^{-2}$,respectively, which have only a marginal influence on the binding energy of the trion (a few meV or below).[120][124] What is then the nature of this low-energy

emission? The corresponding component is not the A^- found in natural MoS_2. In fact, such a component is also expected (the main excitonic feature would hence consist of three components), but appears to represent a negligible one in the case of HP/HT MoS_2. Its spectral weight is globally high and strikingly, unlike the A^- feature for natural MoS_2, does not correlate with the kind of substrate and corresponding doping level revealed by Raman spectroscopy (Figure 3.23b). This is at variance with the behavior expected for trions.

A rational explanation for this low-energy feature (in the case of HP/HT MoS_2) is that it relates to a defect-bound exciton. Defect bound excitons were previously invoked in MoS_2 and attributed to sulfur vacancies, divacancies, and metal vacancies.[125],[126] While they were found to be associated with a binding energy of the order 100 meV, here we find a binding energy of 20 meV. The limited variations of strain or electronic doping in our samples do not allow us to reveal a possibly different influence of these effects on the A', A^-, and A features. As we will see, samples from the HP/HT source comprise a larger amount of defects. In the following, we determine the nature and density of these defects using additional probes.

3.6 Intrinsic defect confirmation in artificial HP/HT MoS_2

Further to confirm the defect bound exciton probed by photoluminescence technique explained in the previous section, additional characterization was utilized. In this section we show the nature of these internal defects using scanning tunneling microscopy. To support and describe the findings from STM, we employ DFT technique. Finally, field effect transistor of monolayer MoS_2 is fabricated to study any further change in the electronic properties due to the internal defects in MoS_2.

3.6.1 Scanning Tunneling Microscopy-nature of point defects

A large variety of defects have been considered in MoS_2, including sulfur vacancies [127],[125], [128],[129], substitutional atoms replacing either the metal or the sulfur atom [130],[127],[125], [128],[131],[129], and individual atoms (the electron-donor alkali atoms) adsorbed onto the surface [130].Only the latter kind has been reported to be associated with shallow donor levels, which could account for usually reported n-doping in monolayer MoS_2 at room temperature. The chemical analysis of the starting material in the HP/HT process does not seem compatible with the presence of alkali atoms, though. On the contrary, based on this analysis, potential candidates as impurities are iron and carbon prominently, or boron and nitrogen from the capsule used to seal the MoS_2 during the HP/HT treatment.

The impurity levels in MoS_2 are too low to be reliably assessed with standard macroscopic chemically sensitive probes such as X-ray photoelectron spectroscopy [132]. High-resolution microscopy circumvents this issue, by addressing the defects individually. We used STM for this purpose, as implemented in a ultra high vacuum environment that limit spurious interactions of the defects with, for example, small molecules. Very few reports in the literature have in fact been devoted to STM measurements on single or fewlayer flakes. Mostly, this is due to the small size (few 1 to 10 μm^2) of the exfoliated flakes, which if deposited on a nonconductive substrate, must be electrically contacted with finely designed electrodes. The observation of such small features with a short field of view technique such as STM is obviously very laborious.

This is probably why most reports for the last 20 years rely on cleaved bulk MoS_2.[114], [133],[132],[134], [132] Two workarounds have been recently implemented : one, taking benefit of large area growth of MoS_2 on graphite[135], [136] and the other the strong adhesion of MoS_2

exfoliated on a gold surface [137]. As far as we are concerned, we chose an alternative strategy and once more exploited PDMS exfoliation (Figure 3.13a), which yields large flakes of sizes approaching 1000 μm^2, using as a host substrate a (conductive) graphene-covered silicon carbide surface. To ease the localization of the (fewlayer) flake, we further deposited micrometer-sized gold markers as shown in the figure 3.26.

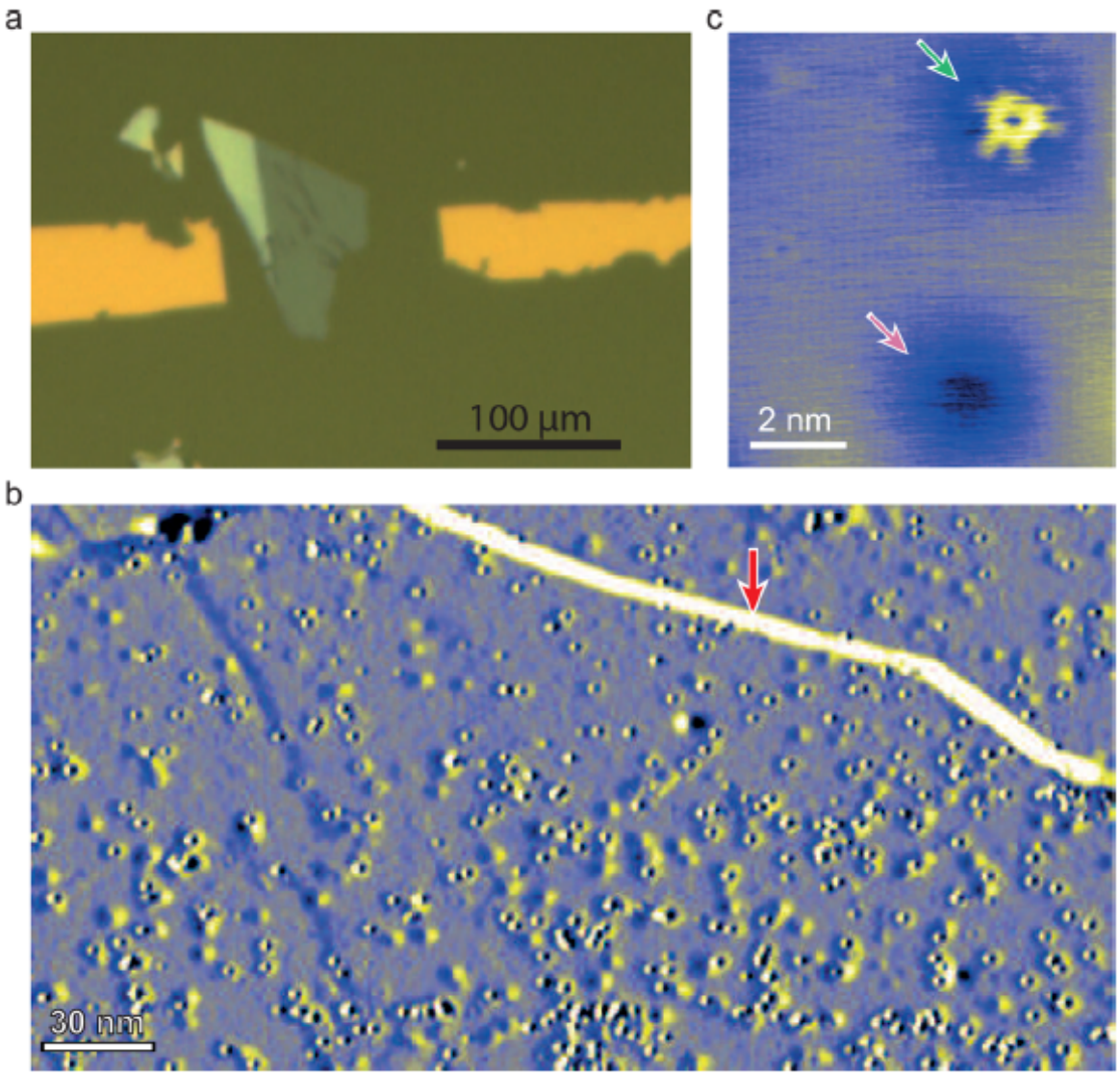

Figure 3.26 – (a) Optical micrograph of the five-layer HP/HT MoS_2 deposited on graphene/SiC, with gold markers. (b) STM image measured with a bias voltage of $V_b = -2$ V and a tunneling current of $I_t = 0.2$ nA. The image shows the derivative of the apparent height as a function of the horizontal spatial coordinate to enhance the contrast of the atomic size defects. The red arrow points to an atomic step edge of the substrate, with a height of 0.75 nm. (c) STM topograph ($V_b = -2V, I_t = 0.2nA$) close-up view on some defects. The green and pink arrows point to two kinds of defects.

The five-layer MoS_2 flake (typically $100 \times 80 \mu m^2$) prepared from the HP/HT source was transferred by PDMS stamping onto graphene grown over the SiC substrate. The average graphene coverage on 6H-SiC(0001), as deduced from Auger electron spectroscopy and STM images, was between one and two layers. Gold markers were evaporated on this substrate,

served as alignment marks, further helping to locate the MoS_2 flake in STM experiments. STM measurements were performed in an ultra high vacuum (UHV) environment at 300 K using a homemade microscope (Measurements were performed by Pierre Mallet and Jean-Yves Veuillen team, Institut NEEL). The samples were gently outgassed in UHV (typically at 300 °C for 1 h) before being loaded in the STM setup. The tips were made from mechanically cut PtIr wires. The data were analyzed using the WsXM software.

This rather advanced sample preparation allows imaging single defects with STM (yet it should be noted that the measurements are in no way straightforward). A high density of defects is observed (Figure 3.26b), on the order of $1 \times 10^{12} cm^{-2}$, varying from 0.6 to $4 \times 10^{12} cm^{-2}$ from one place to the other. A spatially inhomogeneous distribution of defects was already quoted in previous STM analyses from MoS_2 samples. The density we find on the HP/HT sample is larger than the one observed on samples prepared by exfoliation of natural molybdenite, which is in the few $10^{11} cm^{-2}$ range or less ($3.5 \times 10^{10} cm^{-2}$). Conversely, a much larger density of defects (from $5 \times 10^{12} cm^{-2}$ to $5 \times 10^{13} cm^{-2}$) has been reported for MoS_2 prepared by exfoliating synthetic crystals.

In the HP/HT MoS_2 we find two prominent populations of point defects, which appear as a bright feature and a depression, respectively (Figure 3.26c). Depression like defects of the same extension ($1 - 2nm$) or slightly larger (in the few nanometer scale) have been reported previously. Among them, one appears as a depression at negative tip-sample bias as in our observations and is a characteristic defect in natural MoS_2 that is ascribed to missing S-Mo-S fragments located either in the top or in a buried MoS_2 layer.

The second kind of defect (the bright one) has not been observed in natural MoS_2 samples and is hence generated during the preparation of the HP/HT sample. It has a characteristic shape resolved with sharp STM tips, consisting in a ring with three pairs of radial legs. The size of the ring is typically 0.7 nm. Defects featuring a ring shape in STM have also been reported previously and were ascribed to alkali atoms adsorbed on the surface. Neither the HP/HT process nor the ultra high vacuum chamber where the STM measurements were performed seems to yield such adsorbates, though.

3.6.2 Density functional theory (DFT) and STM simulations

Both electronic and structural information contribute to the STM images. To determine the nature of the defects, DFT simulations provide key insights to interpret the observed STM contrasts. The comparison of experimental STM images with spatially resolved information provided by DFT is a well established approach to study defects. To our knowledge such a comparison has not been made in the case of defects in MoS_2 beyond the case of lattice vacancies. We computed the stable configurations of five defects corresponding to the impurities that are detected in the chemical analysis of the raw MoS_2 or present in the h-BN capsule used in the HP/HT process.

This includes a sulfur vacancy, a molybdenum atom substituted by an iron atom, a sulfur atom substituted by a carbon, a nitrogen, and a boron atom. Each of these defects are associated with electronic states inside the band gap of MoS_2 (here expectedly close to the bulk value of 1.3 eV) or close to the band gap edges (see Figures 3.27a). The sample bias of -2.0 V corresponds to electrons tunneling from the sample to the tip, in an energy window of 2.0 eV below the MoS_2 Fermi level, which is presumably located close to the conduction band minimum. It is thus expected that the defect electronic state within the band gap have a significant contribution compared to the valence band, given that they correspond to a lower tunnel barrier.

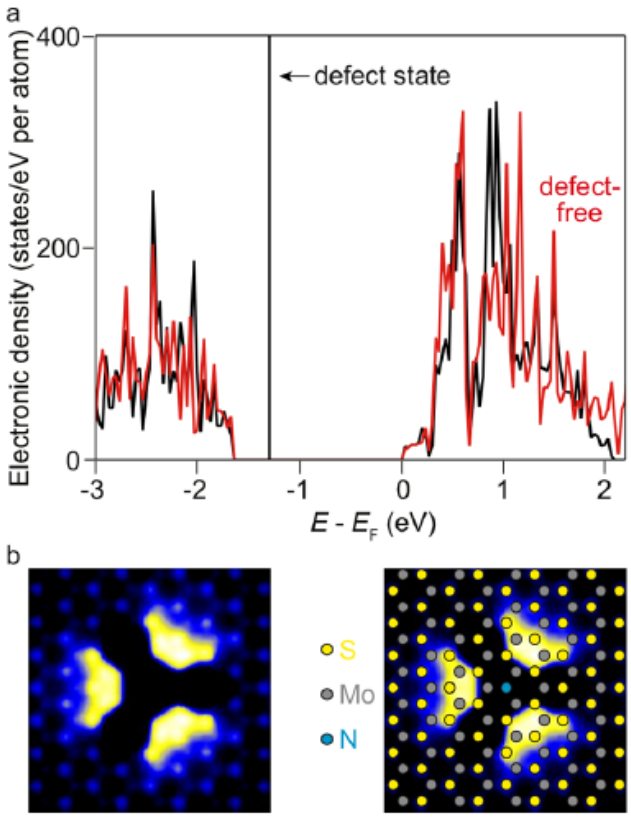

Figure 3.27 – (a) Electronic density of states as a function of electron energy with respect to the Fermi level for a nitrogen atom substituting a sulfur atom in single layer MoS_2 and for defect-free MoS_2 (red). The spectra have been shifted horizontally to match the bottoms of the conduction band. The arrow points to the position of a very sharp defect state. (b) Corresponding simulated STM image with the Fermi level located at the bottom of the conduction bond and a -2 V tip-sample bias, with the STM tip 4A from the surface with (right) and without (left) the atomic structure overlaid. (DFT calculations performed by Van-Dung Nguyen and Laurence Magaud, Institute NEEL)

We simulated STM images by taking into account the STM tip in the presence of the different defects. The DFT localized-orbital molecular-dynamics code as implemented in Fireball has been used for the structural relaxation of the different defects in MoS_2 considered for STM image calculations. The results are shown in Figure 3.29 and for one specific defect (nitrogen atom substituting a sulfur atom) in Figure 3.27b. For the latter defect, the simulated STM image is in rather good agreement with the experimental one, despite the significant difference in spatial resolution, which is higher in the simulations. Indeed in the experiment, an Angstrom-scale instability of the scanning tip is observed (as shown by the occurrence of horizontal stripes at the defect location in Figure 3.26c), and the tip's shape presumably deviates from the ideal pyramidal shape assumed in the calculations. STM simulation and calculations were supported by Yannick J Dappe of CEA, Saclay.

We consider this as the reason that the three brilliant lobes observed in the simulated image appear as a circle in the experimental image. Beyond this, the main features compare very well for the N substitutional defect: the sizes of the lower-intensity central feature match, and

the three pairs of legs appearing in the experimental image seem reminiscent of the three lobes found in the simulations. On the basis of this comparison we propose that the ring-shaped defects we observed correspond to nitrogen atoms having replaced sulfur ones during the HP/HT sample preparation (and originating,for example, from the h-BN capsule used in this process).

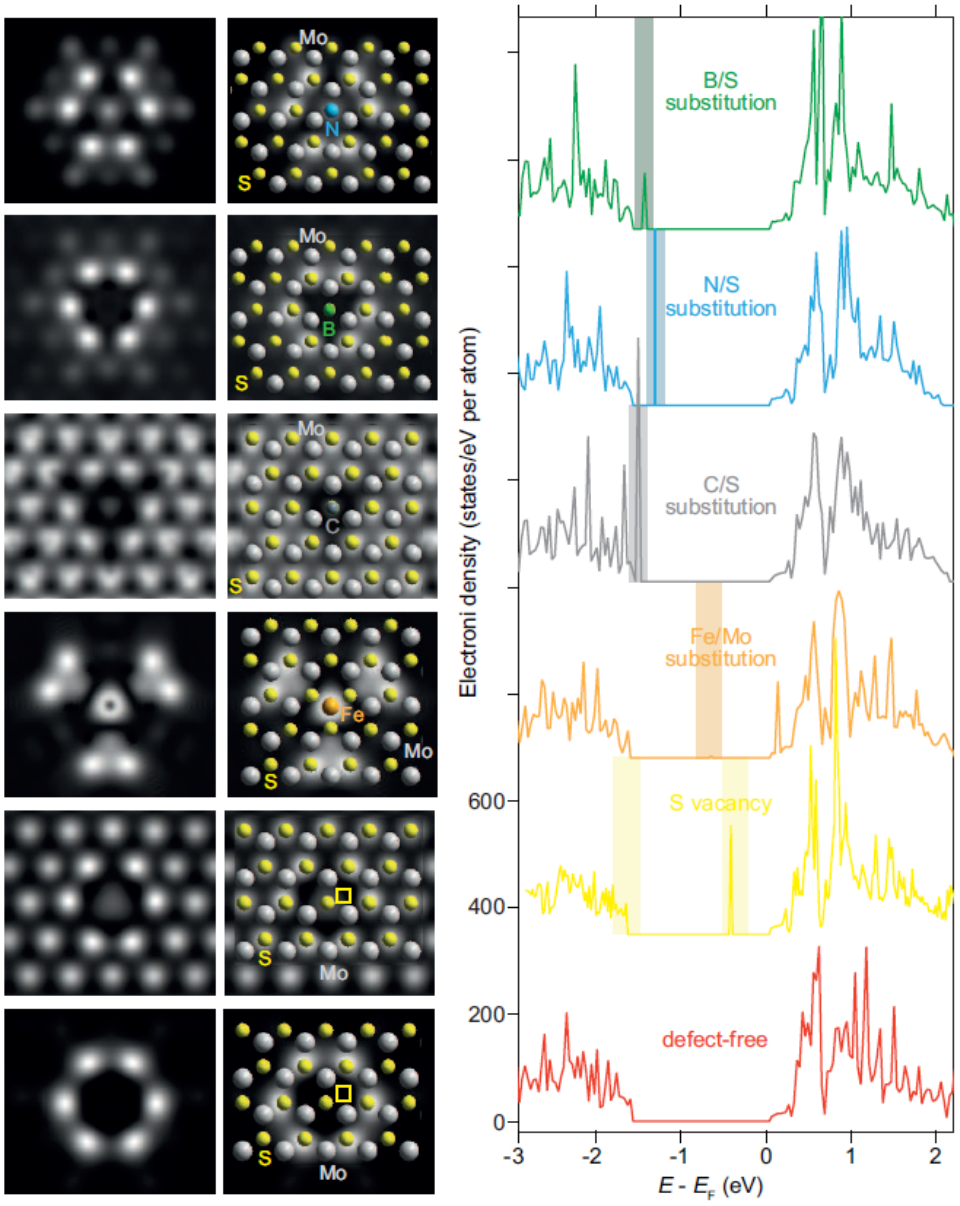

Figure 3.28 – Electronic density of states and constant-height cuts (1 Å) around the sulfur vacancy, the Mo/Fe, C/S N/S and B/S substituted atoms integrated in the energy range shaded in the electronic density of states spectra (the fifth and sixth rows correspond to the two lower- and higher-energy yellow-shaded ranges respectively). The electronic density of states for defect-free MoS_2 is shown as a reference. All spectra have been shifted horizontally to match the minima of the conduction band (at zero energy) and vertically for clarity. (Images from Yannick J Dappe, CEA, Saclay)

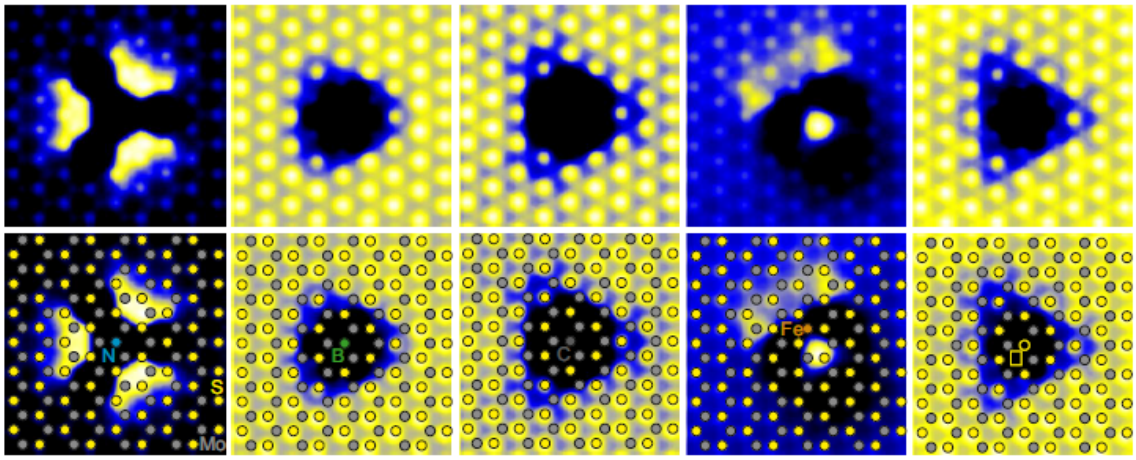

Figure 3.29 – Simulated STM images for the five kind of defects (from left to right): nitrogen/sulfur, boron/sulfur, carbon/sulfur, iron/molybdenum substitionals, and sulfur vacancy. (Images from Yannick J Dappe, CEA, Saclay)

3.6.3 Field Effect characterization of artificial HP/HT MoS_2

Single-layer MoS_2 prepared under HP/HT conditions was finally integrated into a field-effect transistor (FET) with electrostatic gating from the back side, in which direct contact with SiO_2 was avoided by a h-BN buffer layer (Figure 3.30). Accordingly, a low amount of charged impurities is expected in the vicinity of MoS_2. Consistent with previous reports, we find that the conduction properties are improved under vacuum (compared to ambient pressure), presumably due to the desorption of species acting as charged impurities.[138] We only observe the blocked state of the transistor and the regime of electron conduction (and not the hole conduction regime) in the source-drain current vs gate-voltage characteristic (Figure3.30).

The transport properties overall show very typical semi-conducting properties that match those found in similar devices based on natural MoS_2. We estimate the threshold voltage to be at a gate voltage of 10 V. The mobility from the gating curve is estimated to be 2 $cm^2/V.s$ (the device in the on-state has not reached saturation in the range of applied gate voltage, so this value is a lower estimate). These two values are similar to those found in devices using the same geometry based on natural MoS_2 and more recently in similar field-effect transistor architecture featuring single-layer MoS_2 synthesized by chemical vapor deposition transferred onto h-BN.[139], [140] In all these works and ours, we stress that the Schottky barriers at the Au/MoS_2 junctions under the source and drain electrodes play a dominant role in the low-value mobility obtained from the two-probe measurement; in other words, the defects that are present in the MoS_2 channel are not limiting transport in this configuration.

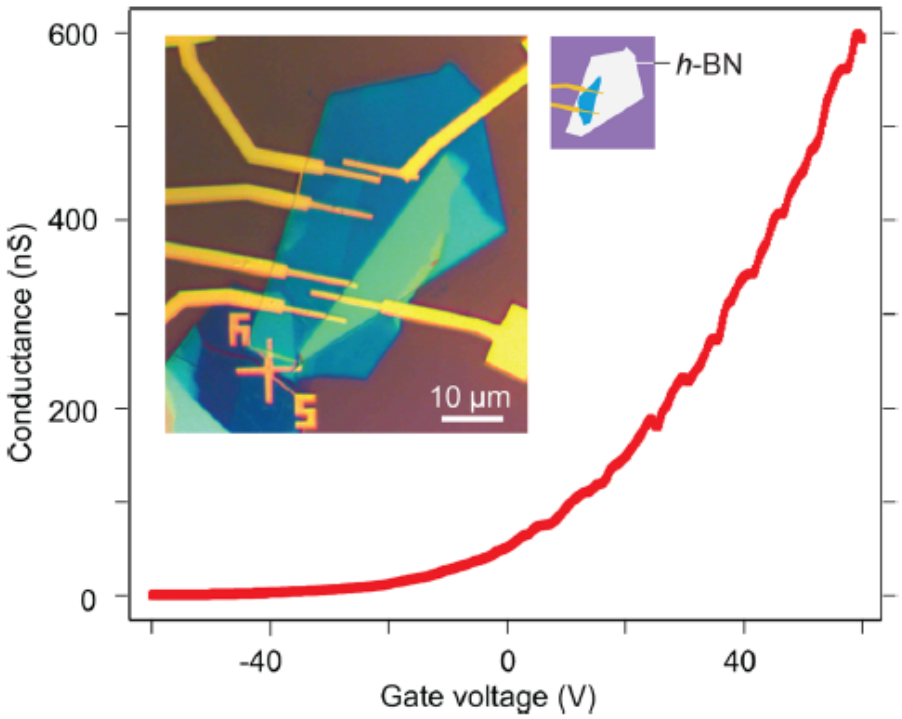

Figure 3.30 – Room temperature conductance measured under vacuum in a single-layer transistor based on HP/HT MoS_2, as a function of gate voltage, with a source-drain bias of 0.2 V. The inset shows an optical micrograph of a single layer device, which is transferred on hBN (exfoliated on SiO_2) and contacted with Au electrodes.The two contacts used for measuring the conductance are shown in the cartoon.

3.7 Chapter conclusions and perspectives

3.7.1 Conclusions

In this chapter, using Raman spectroscopy, photoluminescence spectroscopy,scanning tunneling microscopy, density functional theory, and electronic transport measurements, we addressed the optoelectronic properties of MoS_2 single layers prepared by exfoliation from two different sources of bulk material: a natural one and another one prepared under high-pressure and high-temperature conditions. The latter preparation process opens the route to the control of the structure of MoS_2, in terms of intentional generation of otherwise inaccessible defects and possibly in the future as well in terms of superior quality, namely, increased single-crystal size and lower defect (e.g., vacancies) concentration as was achieved with h-BN. This holds promise for close-to-ideal support for other two-dimensional materials and high-performance optoelectronic devices.

Natural and HP/HT both have a substantial electron-type doping, on the order of $10^{12} cm^{-2}$, which is stronger on SiO_2 substrates than on h-BN due to a lower amount of extrinsic charged impurity in the latter case. Additional defects are present in HP/HT MoS_2. We argue that they lead to defect-bound excitons, with a few 10 meV binding energy. We propose that these defects are nitrogen atoms substituting sulfur atoms. Exploring the nature of the localization potential associated with the defects and its effects on the coupling to the electromagnetic field will provide valuable insights to understand light-matter coupling in transition metal dichalcogenides.

In addition, the defect-bound exciton we discover, may couple coherently with the neutral exciton. Stronger coupling and larger coherent times than reported in $MoSe_2$ at low temperature between excitons and trions might result from the weak trapping of the defect-bound exciton. On a general note, our work also sheds light on the influence of defects on the optoelectronic properties of these two-dimensional materials and their interplay with internal and external (force, electric, optical) fields.

3.7.2 Perspectives

As explained in the introduction, the goal of the synthetic HP/HT production method was to improve the quality of the MoS_2 crystal. But during the first trial (explained in this thesis), we saw that a new kind of substitutional defect was identified along with the most common sulphur vacancy defects found in natural MoS_2. Hence the process has to be improved to avoid contamination from hBN capsule to get rid of these substitutional defects. Further the sulphur vacancy defects need to be taken care of by introducing sulphur rich atmosphere during the HP/HT process.

These process improvements have already been taken care of and as a result new kind of synthetic crystals MoS_2 and MoS_2+S have been produced using the same high pressure and high temperature approach. Similar detailed analysis using optical probes have been continued on these newly obtained samples and are still ongoing.

Chapter 4

hBN encapsulated MoS_2 Van der Waals heterostructures

Contents

4.1 Brief introduction to the chapter . . . 130
4.2 Cathodoluminescence set-up . . . 132
4.3 Fabrication of hBN/monolayer MoS_2/hBN heterostructures . . . 133
4.3.1 hBN/monolayer MoS_2/hBN stack by PDMS method . . . 133
4.3.2 hBN/monolayer MoS_2/hBN stack by PPC method . . . 134
4.4 hBN encapsulation as passive component for enhancement of optical properties . . . 135
4.4.1 Homogeneous and inhomogeneous broadening . . . 135
4.4.2 Line-width reduction/improvement . . . 136
4.4.3 Four-wave mixing spectroscopy in monolayer MoS_2 . . . 137
4.5 hBN encapsulation as active component for efficient light generation in MoS_2 . . . 141
4.5.1 Probing Interlayer coupling . . . 141
4.5.2 Type I band alignment in hBN/ monolayer MoS_2/ hBN heterostructure 143
4.5.3 Non uniform cathodoluminescence and quenching . . . 144
4.5.4 Importance of hBN . . . 146
4.5.5 Raman studies on defects created by ion bombardment . . . 147
4.5.6 Raman analysis before and after electron beam irradiation . . . 148
4.5.7 Origin of defects . . . 152
4.5.8 Heterostructure fabrication for better interlayer coupling . . . 153
4.6 Chapter conclusions and perspectives . . . 154
4.6.1 Conclusions . . . 154
4.6.2 Perspectives: $MoSe_2$ heterostructure in tailored electromagnetic environments . . . 155
4.7 APPENDIX . . . 156
4.7.1 Photoluminescence spectrum fitting procedure . . . 156
4.7.2 Raman spectrum fitting procedure . . . 156
4.7.3 Noisy spectra on large scale images . . . 162

4.1 Brief introduction to the chapter

Eventhough MoS_2 monolayers are thought to be stable under the ambient conditions, they are found to degrade over time when exposed to the environment which may affect their electrical or optical properties. Several solutions are proposed to enhance the physical properties of the monolayer MoS_2 material to get the best intrinsic property out of the 2D direct bandgap semiconductor. Similar to graphene, hBN has been proposed as an atomically flat substrate and along with encapsulation has been shown to improve the electronic and optical properties as discussed in the previous chapters.

In the first part of chapter, we discuss how the encapsulation strategy with intimate Van der Waals interaction in the heterostructures promotes the intrinsic optical property of the material. Again the heterostructures are based on inert hBN which plays an important role in keeping the monolayer MoS_2 in pristine form. It not only forms an ideal substrate (buffer layer) where charged impurities orginating from Si/SiO_2 are cut off but also protects the monolayer MoS_2 getting degraded by the environment.

Here we show that in such a kind of heterostructures, the monolayer MoS_2 could be maintained pristine where photoluminescence reveals a very sharp excitonic feature approaching the homogeneous limit. Further, we characterize samples using a non linear optical probe called as four wave mixing. Using this technique, we study about homogeneous broadening and inhomogeneous broadening which quantifies the purity of the material.

Further, in this chapter, yet again we revisit optical spectroscopy techniques used for characterization. In the previous chapter we discussed about Raman spectroscopy and the photoluminescence spectroscopy to probe the material. Though these techniques provide excellent and efficient information for large scale samples, the spatial resolution is poor. The spatial resolution estimated around 0.5 microns to 0.25 microns is limited by diffraction limit of laser light. Obviously to improve the spatial resolution beyond the diffraction limit of light, we need to use either near-field optics or electron-beam for probing the samples. In our case we use a standard electron microscope to obtain a electron beam that could be focused to a sub-nanometer diameter. The spatial resolution given by this technique is very high, determined by spatial and energy profile of the electrons.

In a scanning electron microscope (SEM), different diameters of the focused electron beam that could be tuned with different accelerating voltages are available. The electron beam impinges the material and interacts with its surface. The spatial resolution is strongly dependent on the interaction of the impinging electrons with the specimen. For example, a high energy electron could penetrate the specimen transferring energy through a series of inelastic scattering events. During this time, the sample can release the energy by various kind of emission as shown in the figure 4.1. The emission could be secondary or backscattered electrons detected and used as SEM image, could be x-rays or photons. Our area of interest are the photons emitted called as cathodoluminescence.

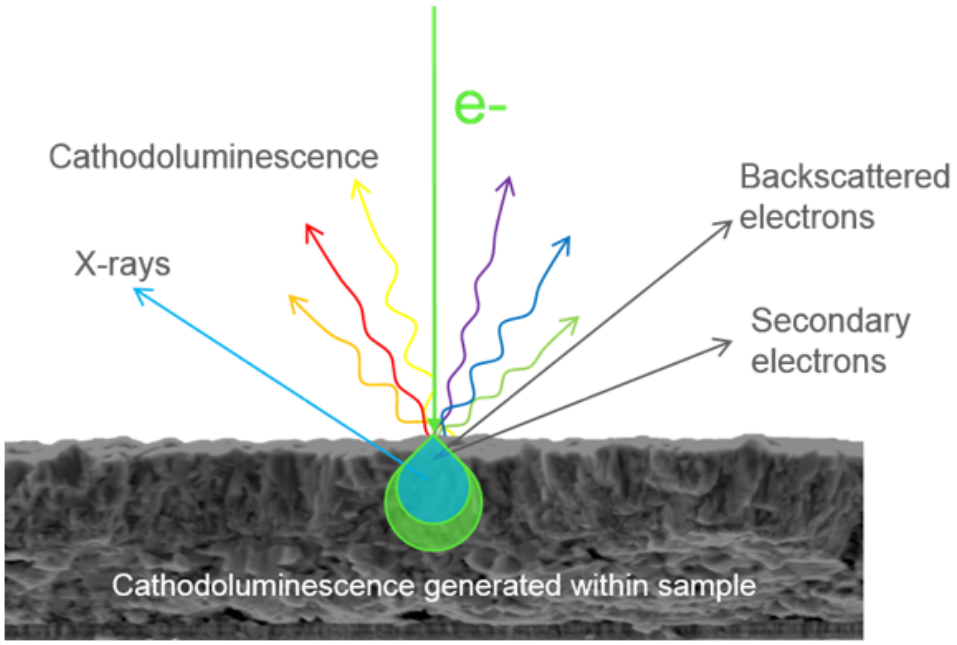

Figure 4.1 – An electron beam interacting with bulk of the sample generating different kind of secondary signals. The pear shows the cross-sectional area of interactions and green pear region in particular corresponding to the generation volume of cathodoluminescence photons. Figure adapted from Gatan, Inc.

Hence this cathodoluminescence technique provides the local spectroscopic information which could be typically as small as few nanometers. Generally since high energy electrons impinge the surface of the material, this technique could be destructive for the samples. This is the major disadvantage of this characterization technique. However, we could overcome this disadvantage again with the concept of Van der Waals heterostructures where the 2D material is encapsulated between the two thin (20nm) hBN flakes. Here the hBN flake acts not only as protector but also as initiator which we would discuss in detail in this chapter.

In the same context we explain the importance of interlayer coupling. We also compare the different polymer transfer techniques with regard to the quality of the monolayer MoS_2. Since the heterostructures are produced in conditions that are far from the ultrahigh vacuum systems, there are possibilities of impact of air bubbles, traps and residuals at the interface. Finally we show that cathodoluminescence technique can be used to spatially probe this poor contact and thus the electronic coupling at nanometric scale.

4.2 Cathodoluminescence set-up

Cathodoluminescence is a process where photons are generated due to recombination of an electron and hole pair in a semiconductor which were excited by an impinging electron beam. In this electron beam, the primary beam has very high energy to directly excite electrons, instead the secondary beam created due to inelastic scattering of these primary electrons excite the valence electrons into the conduction band. The main advantage of this spectroscopy is that one can obtain a high spatial resolution below the diffraction limit of light as they are excited by a beam of electrons.

In the Cathodoluminescence set up as shown in the figure 4.2, we utilize a FEI Inspect F50 FESEM for producing the beam of electron (30KeV to 1KeV) and imaging the samples (spatial resolution down to 1nm to 3nm). This SEM is equipped with a Gatan helium cooled stage using which we can perform low temperature measurements down to 4K. The emitted light is collected through a bare aluminium parabolic mirror and separated into its component wavelength with a 550mm focal length iHR550 monochromator equipped with diffraction grating with 600 grooves/mm. In the setup a Andor technology thermoelectric cooled silicon CCD detector is used to record the spectrum. A single channel detector R928 Hamamastu photomultiplier tube that is synchronized to electron beam scanning is used to obtain the cathodoluminescence mapping.

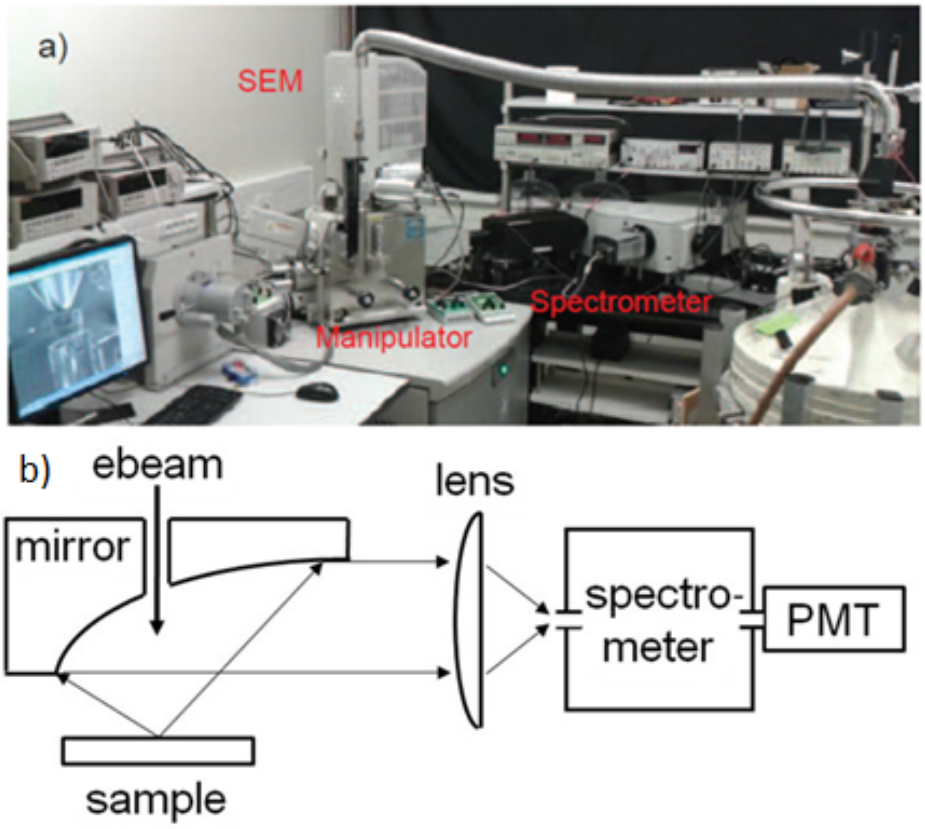

Figure 4.2 – a) Modified SEM into Cathodoluminescence set up in the lab. b) Block diagram of the cathodo set up. (figure adapted from Donatini et al. [141])

4.3 Fabrication of hBN/monolayer MoS_2/hBN heterostructures

As explained in the introduction, in case of monolayer MoS_2, we try to enhance its optical properties by encapsulating it into two h-BN layers to form a hBN/MoS_2/hBN heterostructure. As described in the chapter 2 and 3, we could make heterostructures either using pickup technique called as PPC method[17] or a deposit technique based named PDMS method [16]. Each method has their advantages along with a set of disadvantages. In this chapter, we make MoS_2 stacks using both the PPC and PDMS polymer techniques and we compare regarding which transfer method yields high quality samples.

4.3.1 hBN/monolayer MoS_2/hBN stack by PDMS method

In the case of PDMS method, first the h-BN crystal is placed on a scotch tape and is mechanically exfoliated onto a Si/SiO_2 substrate whereas the MoS_2 crystal is exfoliated onto a PDMS layer. A large SL MoS_2 is identified on PDMS based on optical contrast and is aligned and transferred onto the hBN on Si/SiO_2 by viscoelastic stamping method discussed in the PDMS transfer method in chapter 3. Likewise, another hBN is exfoliated on PDMS and again aligned and stamped over the monolayer MoS_2, hence to encapsulate it and to obtain a hBN/MoS_2/hBN Van der Walls heterostructure.

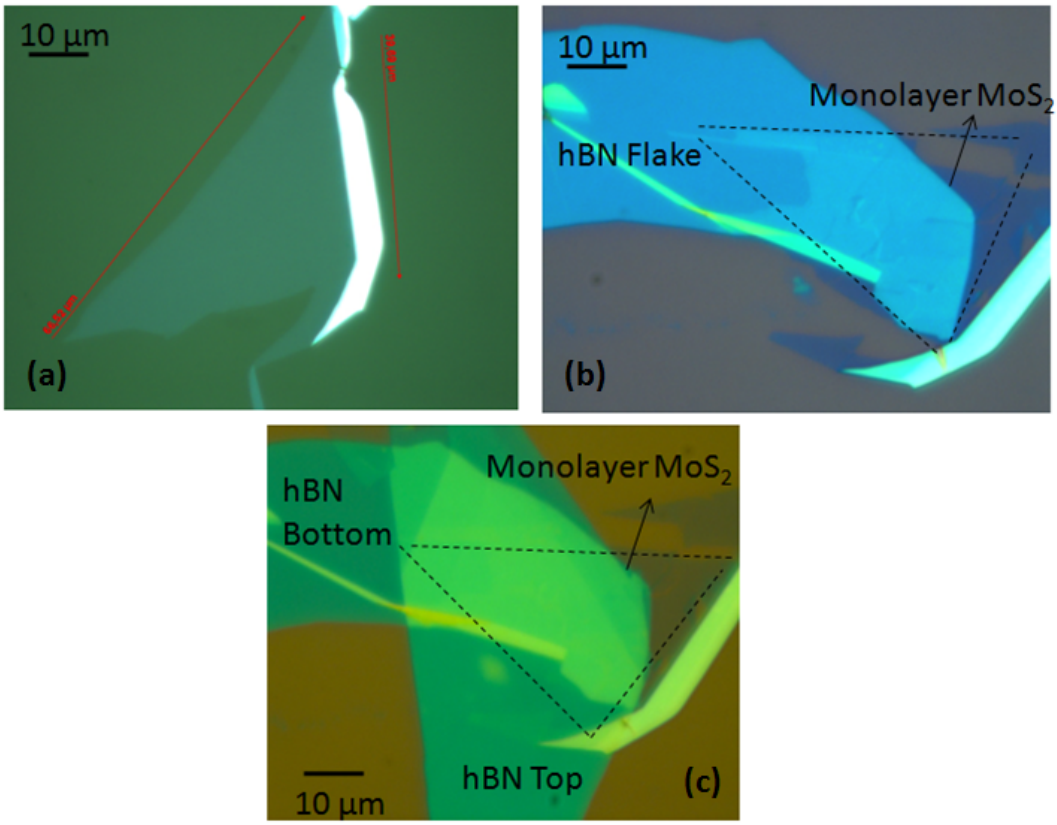

Figure 4.3 – hBN/MOS_2/hBN heterostructure prepared using PDMS technique of viscoeleastic stamping. a) Monolayer MoS_2 identified on PDMS b) Monolayer MoS_2 stamped on bottom hBN in the first step of stamping c) Top hBN stamped on MoS_2/hBN in the second step of stamping.

The main advantages of using this method is that we could make heterostructures at a faster

pace at room temperature and we obtain large scale heterostructures upon which many devices could be fabricated and characterized. While this process is known to yield clean MoS_2/h-BN interface at the bottom, the top interface with h-BN may encapsulate air blisters, puddles and cracks. These may form as a result of the exerted mechanical stress, but a negligible amount of contaminants is expected which could be verified by AFM or TEM. Hence the monolayer MoS_2 is not strictly pristine considering that it is in contact with PDMS.

4.3.2 hBN/monolayer MoS_2/hBN stack by PPC method

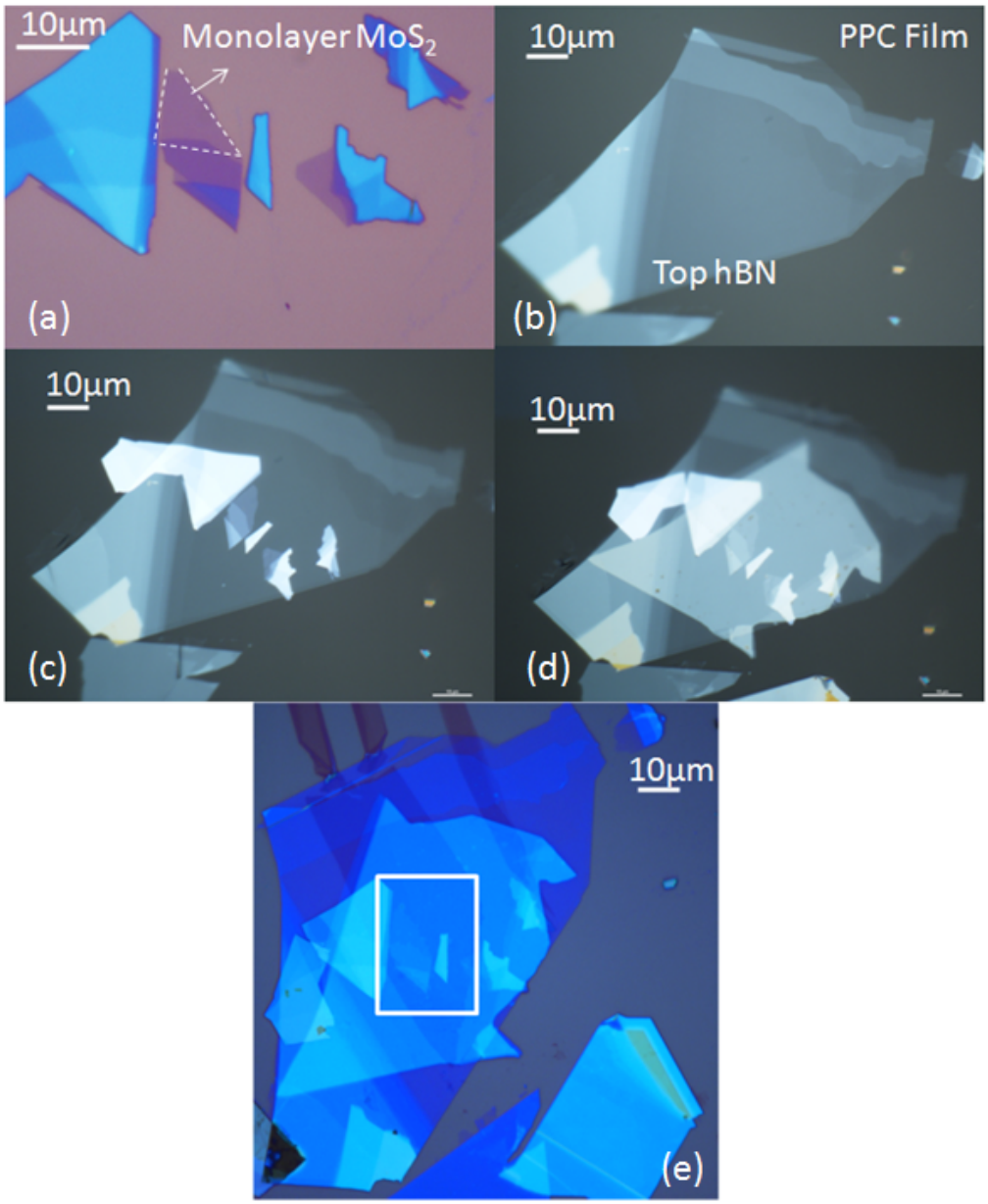

Figure 4.4 – hBN/MOS_2/hBN heterostructure prepared using PPC pickup technique. a) Monolayer MoS_2 exfoliated on Si/SiO_2 substrate. b) Top hBN already picked up on PPC film c) Monolayer MoS_2 picked up in the second step d) Third pickup of bottom hBN to encapsulate the monolayer MoS_2 e) Resulting heterostructure dropped on Si/SiO_2 substrate. The monolayer MoS_2 is encapsulated in the region of white square shown in the figure.

In the PPC method, the top, bottom hBN and also the MoS_2 are exfoliated onto Si/SiO_2 substrates respectively. Monolayer MoS_2 and 15-20nm thick hBN flakes are identified and selected using an optical microscope. Using a micron-thick, thin-film of PPC polymer, the top hBN, monolayer MoS_2 and the bottom hBN are picked up one after another by PPC method to form $hBN/MoS_2/hBN$ Van der Waals heterostructure. This stack is dropped onto the Si/SiO_2 substrate and the PPC is removed using annealing. Refer PPC technique in chapter 2 for details. The main advantage of this method is that the MoS_2 is pristine and is not touched by any polymer or solvents. However there are possibilities of air bubbles during the stacking process.

4.4 hBN encapsulation as passive component for enhancement of optical properties

Monolayer MoS_2 has been the most widely studied semiconducting 2D material due to its direct bandgap and superior stability in atmospheric conditions. Due to its efficient emission and absorption of light, where excitons are created with high binding energy and fast radiative recombination, it has been regarded as the next generation candidate for future optoelectronics along with other TMDCs. However its atmospheric stabilty has been in question as the measured exciton linewidth has been on the order of several tens of meV even at low temperatures.

In this section, by employing a method of Van der Waals heterostructures where monolayer MoS_2 is encapsulated between two flakes of hBN as explained in the sample fabrication section, we show that sharp excitonic features of few meV linewidth approaching the expected homogeneous limit could be observed. By using a technique called four wave mixing microsocopy and imaging, we correlate the homogeneous and inhomgeneous broadening of the exciton.

4.4.1 Homogeneous and inhomogeneous broadening

Homogeneous broadening (γ) refers to broadening of the optical linewidth of an electronic transition where the effect equally affects the different radiating or absorbing spatial area of the sample. Hence the spectral shape of the transistion cross section across the sample would be equal. The causes of the broadening include finite lifetimes of the energy levels involved called lifetime broadening. The homogeneously broadened emission would have a Lorentzian profile.

Inhomogeneous broadening (σ) refers to the case where there is an increase in the exciton linewidth of an electronic transition caused by different radiating or absorbing spatial area of the sample to interact with different wavelength components. Hence the spectral shape of the transistion cross section will be different across the sample. This broadening arises due to impurities or dopants where local electric would be different for each of the emitter. Inhomogeneously broadened emission exhibits a Gaussian profile.

Two fundamental parameters are used to characterize the exciton quantum dynamics as depicted in the figure 4.5. The two parameters are excited state population relaxation rate(Γ) which is inversely proportional to the population decay time T_1 arising from both radiative and nonradiative recombination. The second parameter is the dephasing rate (γ) arising due to the coherent superposition of the crystal ground state ($\mid 0\rangle$) and the exciton state ($\mid 1\rangle$) that defines the homogeneous linewidth of an exciton resonance.

The dephasing rate is inversely proportional to the coherence time T_2. The homogeneous linewidth that is related to population relaxation through $\gamma = \frac{\Gamma}{2} + \gamma^*$ where γ^* characterizes the

pure dephasing processes arising due to elastic exciton-exciton and exciton-phonon interactions.

The popultaion decay time T_1 and coherence time T_2 are the two fundamental time scales used in quantum optoelectronics. These time scales could be probed by employing either the frequency or the time domain using linear or non linear spectroscopic techniques. It is observed that the excitonic spectral line shape measured using linear transmission or reflection techniques is a convolution of γ and σ. The separation of these components by applying line-shape fits like Voigt profile requires prior knowledge of homogeneous and inhomogeneous line shapes.

For instance, in the ($\sigma \gg \gamma$) limit, the lineshape would be gaussian and γ cannot be reliably estimated. Interestingly the exciton emission measured using non resonantly excited PL could show narrower linewidths than those measured via resonant absorption. The reason being that the carrier and exciton relaxation selecting a local potential minima at low temperatures prior to recombination. Hence to separate the homogeneous component from the inhomogeneous broadening in the exciton line-shape, the most suited method is nonlinear spectroscopy and in particularly four wave mixing (FWM) spectroscopy which would be explained in the coming subsections.

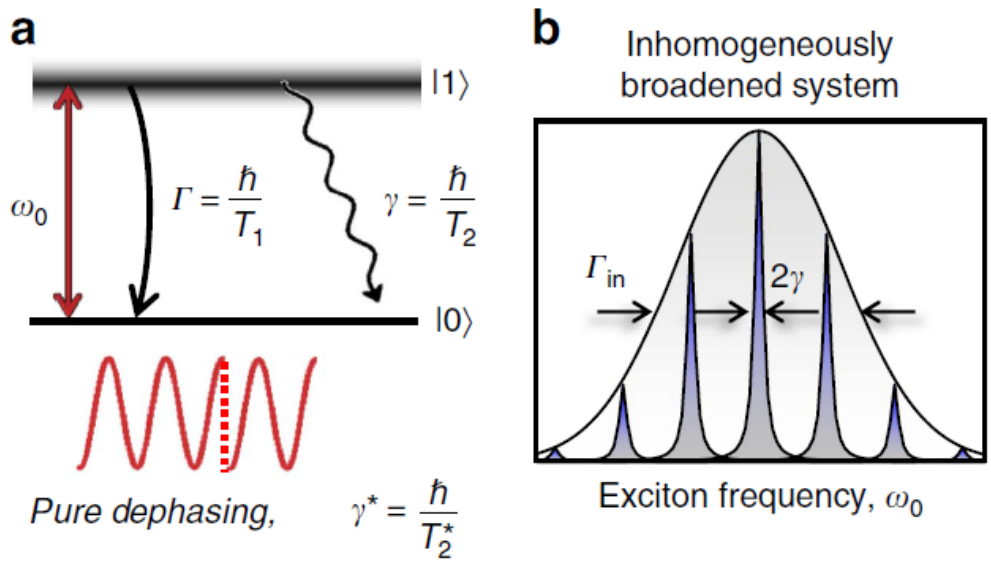

Figure 4.5 – Intrinsic exciton coherent dynamics and resonance broadening mechanisms. (a) The quantum dynamics of an exciton with resonance frequency ω_0 are characterized by two key parameters: the population decay rate Γ (population lifetime T_1), and the dephasing rate γ (coherence time T_2), which defines the exciton homogeneous linewidth. (b) An inhomogeneous distribution of exciton oscillator frequencies (Γ_{in}) due to a varying local potential landscape masks the intrinsic homogeneous linewidth in most optical spectroscopy experiments. Figure adapted from Galan Moody et al. [142]

4.4.2 Line-width reduction/improvement

As discussed before, at room and even at low temperature monolayer MoS_2 exhibits excitonic linewidth of several tens of meV range. The large value of this linewidth indicates the presence of inhomogeneous broadening (σ) of the exciton transition which would be more than an order of magnitude compared to the homogeneous broadening (γ). This dominating inhomogenities ($\sigma \gg \gamma$) in monolayer MoS_2 masks the intrinsic properties of excitons and its role in complex

band structure. These inhomogenities observed in the MoS_2 arise from the external defects such as adsorbed impurities,substrate effects and internal defects such as crystal defects with vacancies or substitutional atoms that were discussed in detail in the previous chapter. The most conventional substrate, Silicon with thin amorphous thermal oxide used to fabricate optoelectronic devices have rough and corrugated surface containing charged impurities that generate a disorder potential landscape for excitons.

The advancement in the transfer technology where two dimensional materials could be stacked one over another in the form of so called Van der Waals heterosturctures by polymer transfer methods have significantly improved the quality of the devices. In these kind of superlattice structures, MoS_2 is devoid of charge impurities arising from the SiO_2 or the possible adsorbed impurities from the environment due to its encapsulation between two atomically flat and inert hBN flakes.

These VdW heterostructures are thought to promote conformal, intimate and atomicall flat contact at the MoS_2/hBN interfaces rendering the MoS_2 close to its intrinsic quality. Other research groups have shown that these kind of samples reveal extremely sharp excitionic features of down to 2 meV linewidth approaching the homogeneous limit as shown in the figure 4.6.[143] The used encapsulation strategy here for monolayer MoS_2 has been extended to other TMD materials to reduce the inhomogeneous broadening.

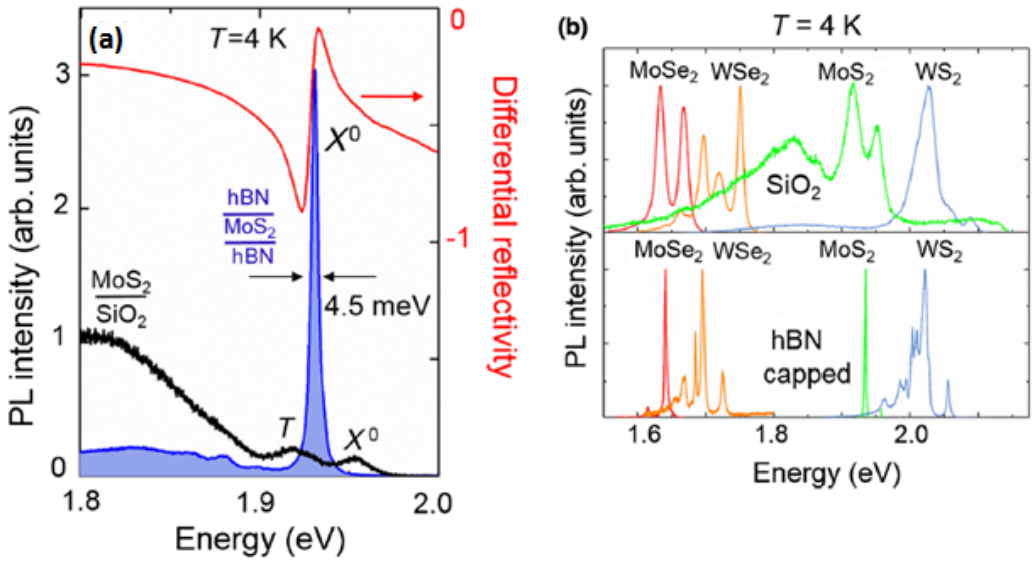

Figure 4.6 – (a) PL spectrum (filled curve) at 4 K for one capped ML when excited with a 2.33eV cw laser with a power density of 50 $\mu W/\mu m^2$. The neutral exciton transition, which is also the main feature of the differential reflectivity spectrum (red curve), exhibits a very narrow linewidth of 4.5 meV for this particular sample. Also shown is the PL spectrum of an uncapped MoS_2 ML deposited directly onto the SiO_2 substrate (black curve) measured under the same conditions. b) Typical PL spectra for different TMDC MLs at 4K when deposited directly onto SiO_2 (top) and when capped with hBN (bottom).Figure adapted from Cadiz et al. [143]

4.4.3 Four-wave mixing spectroscopy in monolayer MoS_2

As explained in the previous paragraphs, due to impurities and disorder in monolayer MoS_2, the excitonic linewidths exhibits inhomogeneous broadening along with the intinsic homogeneous

broadening. This inhomogeneous broadening is because of spatial variation of the exciton energy and it can vary spatially across the whole sample surface area. Hence to seperate the homogeneous from inhomogeneous braodening in the exciton line-shape, we use a non linear spectroscopy called four-wave mixing(FWM). In this technique, to measure the coherent and resonant FWM spectra, heterodyne spectral interferomerty(HSI) is used which would not be discussed in detail in this thesis.

In this FWM technique, three laser beams are pumped and corrected so that they arrive at sample close to their Fourier limit, with around 150fs duration. These three beams are labelled as $\varepsilon_{1,2,3}$ which are resonant with the exciton transition. They are focussed on the sample with a microscope of objective NA=0.6 down to diffraction limit. Enhanced spatial and temporal resolutions are required and hence FWM spectroscopy, resolving the signal on a 100 femto-second(fs) time and 300nano-meter(nm) spatial scale is implemented. While the signal is discerned via optical heterodyning, the exciting laser pulses propagate co-linearly in the same spatial mode. This technique allows us to spatially resolve σ and γ, and underlying correlations between exciton-dephasing and σ.

Eventhough the encapsulation strategy leads to monolayer MoS_2 being maintained close to pristine, there could be variations across the flake due to strain from the substrate or encapsulating layer, dielctric environment, intrinsic impurities and defects, and the free carrier concentration. These spatial variations give rise to disorder affecting the exciton radiating rates and thus the inhomogeneous broadening. FWM driven on such an inhomogeneously broadened optical transition created by a spatially varying exciton transition, forms a photon echo as shown in the figure 4.7. While its temporal width is determined by σ, assuming sufficiently short excitation pulses with respect to $\hbar/\sigma$, the amplitude decay with delay time between the first two exciting pulses (τ_{12}) is only due to microscopic exciton dephasing. During the simple exponential decay, it determines the full width half maximum (FWHM) of the $\gamma = 2\hbar/T_2$.

From the experiment, we find in general that the hBN encapsulation of monolayer MoS_2 leads to a global reduction of σ to a few meV, comparable to the homogeneous broadening. At some micron sized sample areas, a decrease of σ correlated with an enhanced FWM signal could be observed. In the regions of varying inhomogeneous broadening across the sample, we investigate the impact of exciton disorder and retrieve the correlations between σ,γ, μ and T_1.

The estimation of σ and γ is made by inspection of the time-resolved FWM amplitude as a function of τ_{12}. The recorded experimental details are as shown in the figure 4.7 c and d. From the graph c, it could be noted that FWM is observed for $\tau_{12} > 0$, and already for $\tau_{12} > 0.2ps$, the photon echo is formed where FWM takes the form of a Gaussian pulse centered close to $t = \tau_{12}$.

For two-level systems and for delta-pulses, ideally, the FWM signal for $\tau_{12} > 0, t > 0$ can be assessed by a product of an exponential decay and a Gaussian shifting its maximum in time, given as

$$\mid FWM(t,\tau_{12}) \mid \propto exp\left[-\tau_{12}/T_2\right].exp\left[-\nu^2(t-\tau_{12})^2/2\right] \tag{4.4.3.1}$$

The photon echo has a constant temporal width exhibiting a standard deviation of $1/\nu$ and FWHM $\sqrt{8ln2/\nu}$. The quantity ν could be linked to inhomogeneous broadening σ as $\sigma = \sqrt{8ln2\hbar\nu}$. On contrary to this, the amplitude decay of the echo with increasing τ_{12} at-

tributes the homogeneous dephasing time $T_2 = 2\hbar/\gamma$. Hence using the above theoretical analysis and fitting the experimental data, we could estimate σ and γ that provides information about the local character of the sample.

The two-dimensional fit to the experimental data is shown in the right panels in the figure 4.7(left panels are the experimentally observed data respectively). The fit 4.7d for figure 4.7c yields $(\gamma, \sigma) \approx (2.1, 12.5) meV$ indicating strong inhomogeneous broadening due to disorders. Similarly at another point of the flake, 4.7e we could obtain $(\gamma, \sigma) \approx (3.1, 5.5)$, reaching closer to homogeneous limit signifying less disorders at the position.

In the plot 4.7e, we can notice that photon echo is different from 4.7c in several aspects. First, it is broader in real time, exhibiting a smaller σ. Second, the amplitude decay along τ_{12} is faster revealing a shorter T_2 and hence a larger γ. These changes were quantified and included during the fit of the echo form. Further, we could identify that in 4.7e, the response starts to deviate from the echo form, where maximum of the signal is not aligned along the diagonal, indicating the transition to be close to the homogeneously broadened case. These two cases 4.7c and e demonstrate that the exciton optical response is affected by disorders on the scale above and below the resolution of the experiment (300nm).To probe the optical response, below this resolution limit, we define a new kind of characterization explained in the next section of the chapter.

All the above observations were made on the hBN/MoS_2/hBN sample prepared using PDMS method as explained in section 4.3.1 with optical image of the sample shown in 4.7a. Based on above discussion, it could be concluded that the sample has both cleaner part and parts with disorder. In addition to this, another sample was made using PPC method (section 4.3.2) and the FWM signatures are shown in the figure 4.7 g,h. In this sample, at micron-sized areas, we were able to record FWM amplitude as narrow as 4.4meV at T=4.5K as shown in the figure 4.7h. Strictly speaking, no signatures of the photon echo were noticed while inspecting FWM transients versus τ_{12}. Hence in this sample, σ is not detectable and the boradening reaches its homogeneous limit.

Along with above experiments, further in-depth studies regarding exciton's coherence dynamics and four-wave mixing mapping and statistical correlation were performed on the same samples in collaboration with Jacek Kasprzak team. This will not be part of this thesis but for more information one can refer to Jakubczyk et al.[144]

These experiments indicate that the samples produced using PPC method are pristine showing the optical properties close to their intrinsic limit than the ones made using PDMS stamping process. In the further experiments, we study the kind of disorders possible in these heterostructure and ways to probe them below the resolution limit of light.

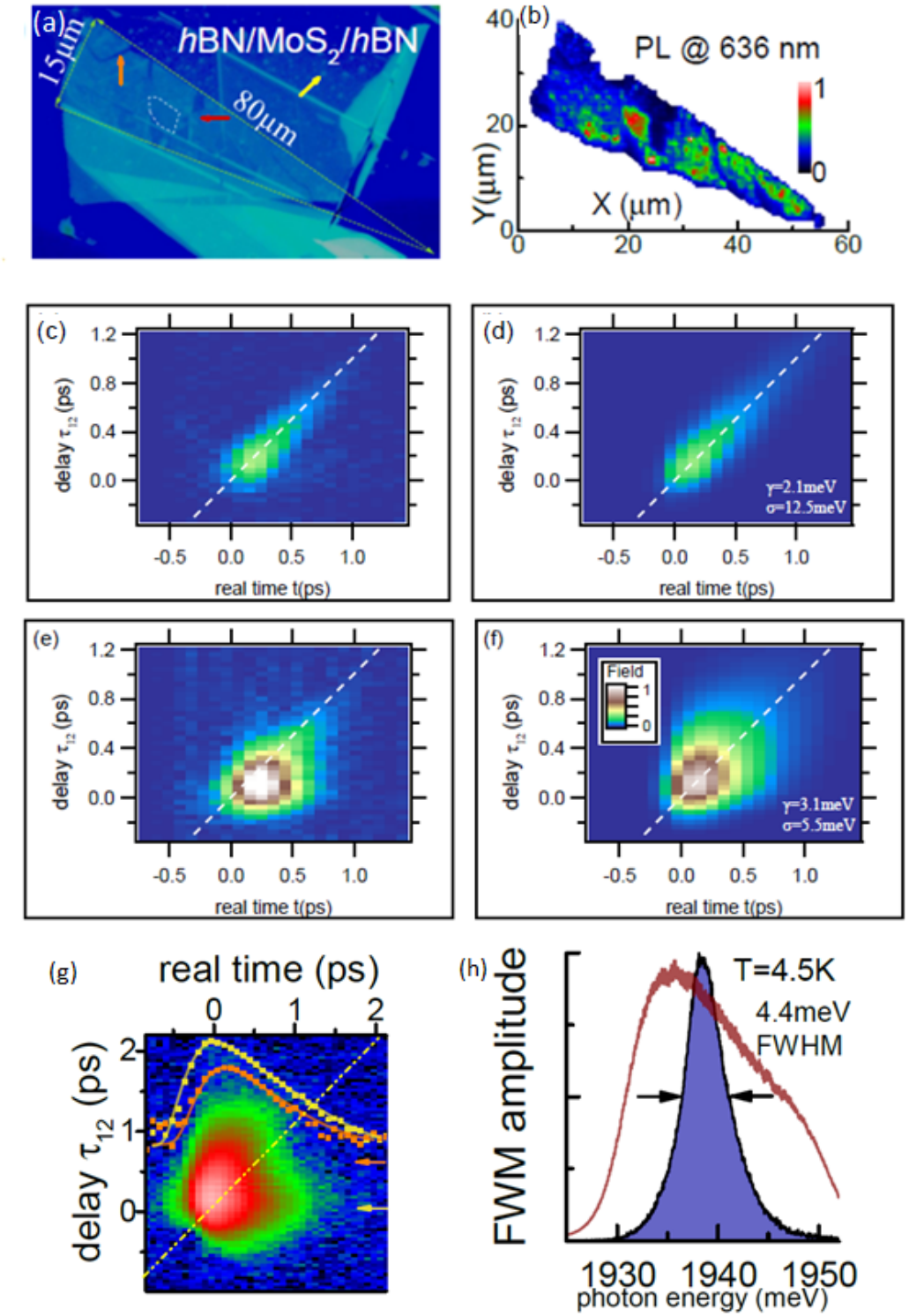

Figure 4.7 – (a) Optical microscopy image of the sample under the white light illumination (b) Spatial mapping of the confocal photoluminescence (PL) at (636±5)nm of the investigated heterostructure. (c,d,e,f) Time-resolved FWM amplitude for different delays τ_{12} at T=5 K, showing formation of the photon echo. The disorder is decreasing from top to bottom, quantifed by the increase of γ and decrease of σ and graphs beside are corresponding simulations. (g) FWM transients versus τ_{12} at T=4.5K FWM free induction decay, thus proving Exciton broadening in its homogeneous limit. (h) Corresponding FWM spectra measured for $\tau_{12} = 0.5$ ps. Red trace in the panel is the spectral shape of the reference pulse.

4.5 hBN encapsulation as active component for efficient light generation in MoS_2

In all the previous sections and other chapters, it has been shown that hBN could be used as a passive layer either as a buffer layer or as a protective layer to improve the physical properties of the relevent 2D material. In this section we devise a technique where hBN is used both as a passive component and as an active component to bring the best out of the monolayer MoS_2.

As explained in the fabrication section before, the MoS_2 is encapsulated in between two 20nm hBN flakes to obtain a heterostructure where hBN acts as a buffer and protection layer for the charge impurities originating from substrate or the environment. In this section, we explain the use of hBN as an active component that acts as exciton resevoir to provide the same to monolayer MoS_2 for light generation.

4.5.1 Probing Interlayer coupling

The development of deterministic stacking of individual or few layers from layered materials such as graphite, boron nitride, or transition metal dichalcogenides (TMDCs) in the last few years allows now to build van der Waals heterostructures at will.[145] Even though such structures are produced in conditions that are far from ultra high vacuum conditions usually required to obtain very high quality heterostructures, carefull preparation yields clean enough interfaces to observe phenomena requiring efficient electronic coupling between layers. For instance, long-lived interlayer excitons were observed,[146, 147] interlayer exciton-phonon coupling was reported in WSe_2/hexagonal boron nitride (h-BN), [148] interlayer phonon coupling was demonstrated in MoS_2/graphene [149] as well as in TMDC-based Van der Waals heterostructures [150].

Type II band alignment and charge transfer was already realized using monolayer two dimensional materials such as WSe_2 and MoS_2. The optical image in the figure 4.8 B) and D) shows the fabricated heterostructures by exfoliation/polymer transfer and CVD grown/PMMA transfer respectively. This was probed using photoluminescence technique with the spectrum from each part WSe_2, MoS_2 and the heterostructure WSe_2/MoS_2 as shown in the figure 4.8. Complete or efficient charge transfer is possible only if the two monolayers are coupled well within the Van der Waals gap limit.

It could be confirmed from the figure 4.8A,C, that the interlayer coupling was extremely good for the exfoliation-polymer transfer case than the CVD grown-PMMA transfer one. This is because, in the hetrostructure part, in the exfoliation-polymer transfer sample almost all the excitons combine radiatively and emit light pertaining to the expected type I band alignment compared to the CVD grown-PMMA transfer sample. In the CVD grown-PMMA transfer sample, the interlayer coupling might be disturbed by transfer residues in between, at the interface of the heterostructures.

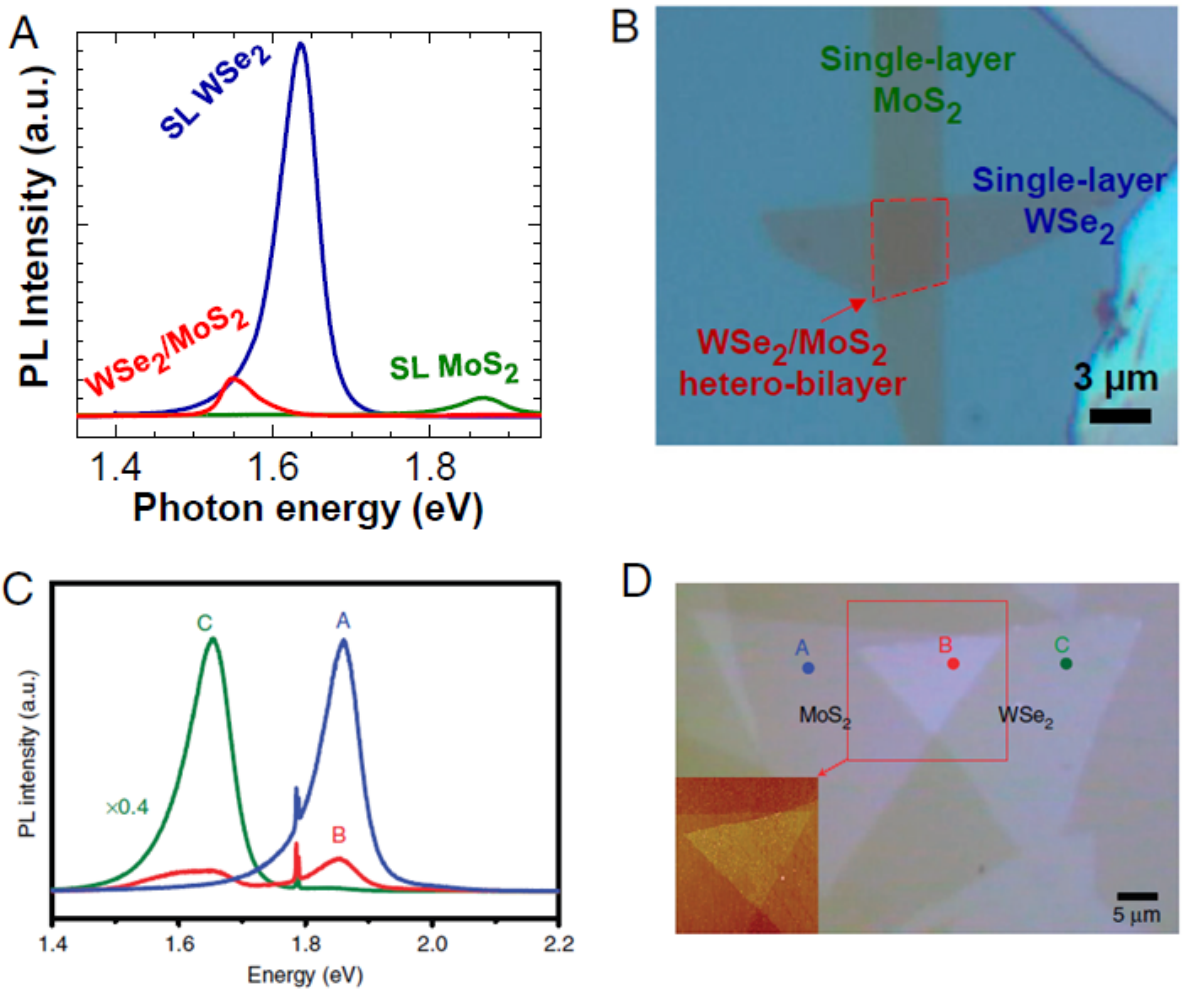

Figure 4.8 – A) Photoluminescence spectra of monolayer WSe_2, MoS_2, and the corresponding hetero-bilayer B) Optical image of WSe_2/MoS_2 hetero-bilayer prepared using polymer transfer method. C) Optical image and atomic force microscopy images(inset) for the WSe_2/MoS_2 heterostructure on a sapphire substrate. (D) Photoluminescence spectra for the selected sites including MoS_2 only (A), WSe_2 only (C) and WSe_2/MoS_2 (B) stacked areas. Figure adapted from [151], [152].

These achievements demonstrate that both inter-layer electronic and structural coupling can be obtained in such heterostructures. Moiré superlattices, which are the van der Waals (soft) counterpart of dislocation networks in heteroepitaxial three-dimensional semiconductors, enrich the electronic and optical properties. [153, 154, 155, 156, 157] Direct observations with high resolution transmission electron microscopy indeed revealed locally perfect crystalline interfaces between two-dimensional materials, with no apparent defects and only a van der Waals gap a few Ångström-thick, devoid of impurity species.[158]

Even though beam-induced damages can be reduced by lowering the energy of the electron beam to a few 10 keV in the transmission electron microscope column [159], such analysis is destructive (the samples need to be cut and thinned down to a few nanometer), and it is tedious to extend it at the scale of the entire heterostructure. On the contrary optical hyperspectral microscopies, mapping excitonic (photoluminescence) or vibrational (Raman) interlayer modes of the heterostructures, require no additional sample preparation, and provide indirect information on the quality of interfaces.[150, 160] Their downside is their limited spatial resolution, which conceals information on, *e.g.*, strain or electronic doping variations at scales below a few 100 nm.

4.5.2 Type I band alignment in hBN/ monolayer MoS_2/ hBN heterostructure

Cathodoluminescence (CL) is a powerful tool to study opto-electronic properties at the nanometer scale, when implemented in a scanning electron microscope. Here, an electron beam of adjustable energy in the keV range excites electrons and holes, that can form electron-hole pairs (excitons) and recombine radiatively, giving local spectroscopic information. In that case spatial resolution is linked to the size of the excitation source, *i.e.* the electron beam which is as small as a few nanometers, rather than limited by the optical diffraction limit.

In fact, spatial resolution in such experiment could ultimately be set by the diffusion of the excitons. It can reach several hundreds of nanometers at room temperature in monolayer TMDCS but is expected to be strongly quenched at low temperature due to the enhancement of the radiative recombination rate[161]. Due to the low interaction with the electron beam, atomically thin layers are expected to produce a small signal below the detection limit of most instruments. In fact, no CL could be measured so far on a free-standing TMDC single layer.

Van der Waals heterostructures can be used to artificially enhance the interaction by encapsulating the active layer into an electronic barrier, very much like semiconductor quantum wells are build: a small band gap material (well) is surrounded by a larger band gap material (barrier). Electron beam irradiation generates hot electrons and holes inside the barrier, which can be arbitrarily thick and hence produce a significant population of hot charge carriers that relax and can be transferred into the low band gap material. This approach has been recently demonstrated with h-BN as a barrier and a single layer TMDC (MoS_2,WS_2, WSe_2) as the active layer.[162]

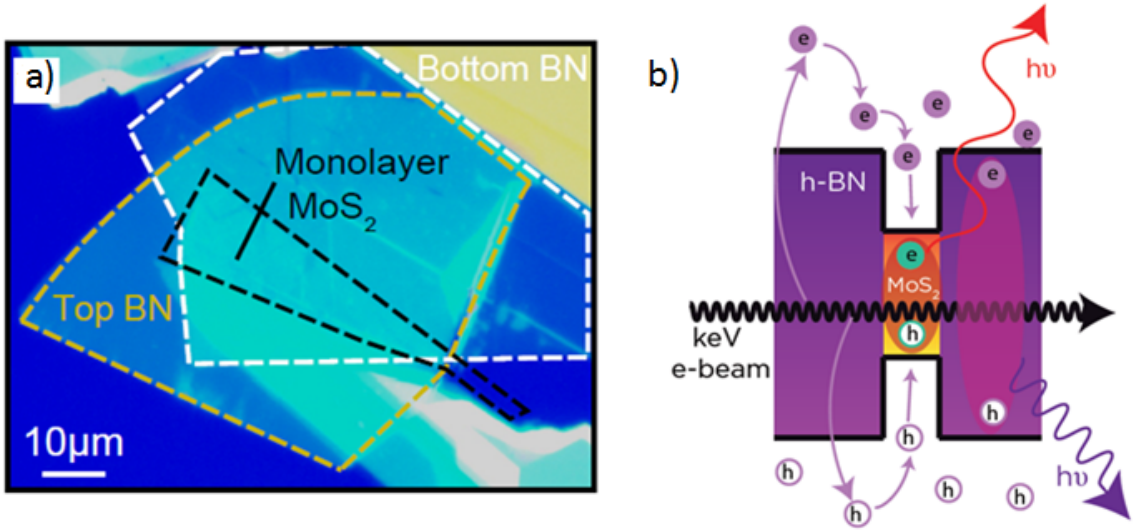

Figure 4.9 – a) Optical micrographs of the full stack prepared with PDMS stamping . b)The process of luminescence excitation in a van der Waals heterostructure with an electron beam.

So far cathodoluminescence was observed only in limited area of van der Waals heterostructures, and the absence of cathodoluminescence was ascribed to a locally poor contact between the h-BN and TMDC surfaces.[162] In this scenario, it is implied that charge carrier transfer between the barrier and active material is inefficient, so no excitons can be generated in the

latter material. Poor-contact-regions are indeed very common in heterostructures. They correspond to blisters trapped at the interfaces, where contaminants associated to the manipulation of the two-dimensional materials gather.[163]

Here we demonstrate that indeed an intimate contact between the materials is key to observe efficient cathodoluminescence. Conversely, we find that in presence of contaminants at the interfaces cathodoluminescence is quenched. This quenching is also observed in photoluminesence performed after the cathodoluminescence. It is hence not only the signature of an inefficient transfer of electrons and holes, but it proves the creation of crystal defects inside MoS_2 that presumably strongly promote non-radiative exciton recombination.

Such defects are detected in Raman spectroscopy. We trace back the origin of defects to a possible chemical reaction between trapped species and the pristine MoS_2, promoted by the electron beam. We show that the spatial uniformity of the cathodoluminescence response of the heterostructures can be greatly enhanced by reducing the amount of contaminants at interfaces (in particular, the amount of trapped blister), using polypropylene carbonate (PPC) to pick-up and release the different materials of the heterostructure.[163]

4.5.3 Non uniform cathodoluminescence and quenching

Figure 4.10a shows a typical CL spectrum of single-layer MoS_2 encapsulated between h-BN with the PDMS transfer technique. A strong emission is centered around 1950 meV corresponding to the energy of the recombination of the neutral A-exciton (EX) in MoS_2. The high energy of the electrons (1keV) compared to the h-BN band gap allows to excite electrons and holes directly in the h-BN, as witnessed by near band edge luminescence from h-BN (see figure 4.12). Due to its thickness (top: 18 nm, bottom: 22 nm) a significant number of electrons and holes can be generated in h-BN.

Using Monte-Carlo simulations, we have shown that at 1keV, the absorption length in h-BN is of the order of several tens of nm (see figure 4.11). When the contact with single-layer MoS_2 is intimate, electrons and holes can be transferred into the latter material which has a much smaller band gap than h-BN. They can then form an EX that will eventually contribute to luminescence when recombining radiatively (A-exciton emission in Figure 4.10a). Alternatively EX can be formed directly in h-BN and either recombine radiatively or relax into MoS_2. The full CL process is illustrated in Figure 4.10b.

For comparison with CL, a PL spectrum taken in the same area is presented in figure 4.10a. We see that the spectra are very similar proving their common origin, that is radiative recombination (photon emission) of the A exciton of single layer MoS_2. We also want to stress that linewidths are both of the order of 10 meV. It shows that no additional broadening is brought by using a high energy electron beam (in the CL experiment) as the excitation instead of light (PL experiment).

This is a very important point, and rather unexpected when referring to literature on CL. Large broadenings, associated to the large number of free charges generated, can indeed often be observed [164]. The lack of broadening demonstrated here is a strong asset for the potential application of CL in mapping properties of van der Waals heterostructures at the nanoscale. We note that the excitation used in our PL experiment is not sufficient (unlike in the CL experiment) to excite electrons and holes directly in h-BN, so we do not observe luminescence from this material in these conditions.

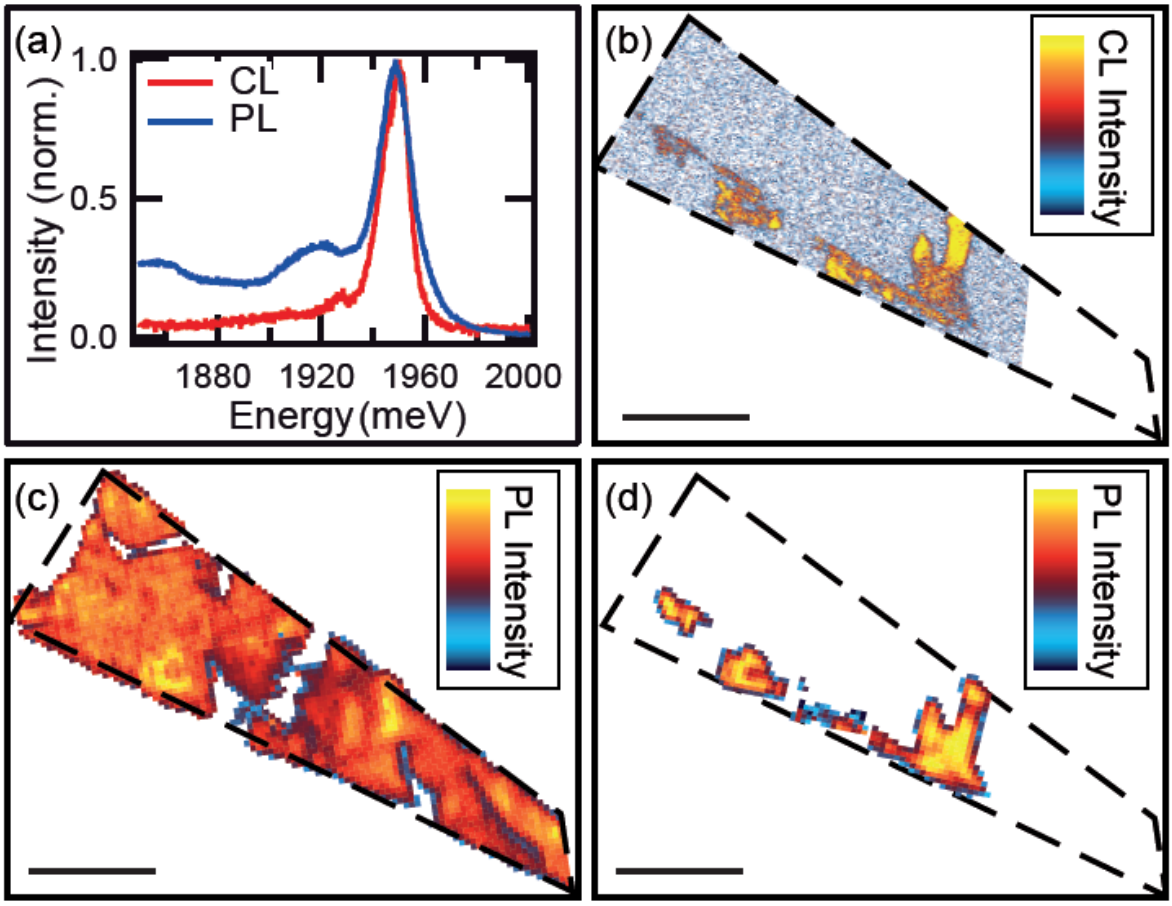

Figure 4.10 – Optical characterization using Photoluminescence (PL) and Cathodoluminescence (CL). A comparison of spatially-resolved spectra at 5K obtained in PL and CL is presented in (a). The spectra are acquired within less than 1 μm of each other, bearing in mind that the probed area differ in both techniques. In both cases, the signal is dominated by neutral exciton emission. The spatially-resolved integrated CL intensity of the exciton is shown in (b) showing some strong inhomogeneities. This is not the case for the integrated PL intensity measured before CL at room temperature (c). In contrast, integrated PL intensity performed after CL (d) shows a strong inhomogeneity presenting a spatial correlation with the CL mapping. Scale bar are 10 μm.

The spatial mapping of the CL intensity measured at 1937 meV (+/- 30 meV) is presented in figure 4.10b. Bright and dark regions are observed, in accordance with a previous report[162]. In the absence of the encapsulating h-BN, no CL is detected; CL is only detected in localized regions of the h-BN-encapsulated MoS_2 (see 4.12b). Encapsulation hence appears necessary, because h-BN is the source of electrons and holes that will eventually recombine in MoS_2, but not sufficient.

An absence of CL in presence of h-BN is in principle surprising, and this was proposed as an evidence of a poor contact between h-BN and MoS_2.[162] Atomic force microscopy (AFM) reveals that the corresponding regions show a significant roughness and bubble-like features at the surface (see figure 4.16). We relate these observations to the presence of blisters filled with species (airborne, contaminants from the polymer stamp) and trapped at the interface between h-BN and MoS_2. The regions exhibiting CL actually appear very flat in AFM (see 4.16), with a root minus square roughness in the range of 2 Å, typically several times lower than for other regions. This is indicative of very smooth and flat (buried) interfaces between the materials.

Prior to the measurement of CL maps, we measured PL maps. Figure 4.10c,d displays the integrated PL intensity of the EX (sum of neutral and charged excitons, which appear as a low energy shoulder, contributions). Unlike for CL, we here only observe bright regions, except at locations where the MoS_2 layer is physically cracked. There are variations of the PL intensity and position which are attributed to local changes (strain, doping, coupling to h-BN) but no quenching.

A straightforward interpretation for the only partial spatial correlations between CL and PL maps on one hand, and the clear correlation between dark regions as found with CL and rough regions as found in AFM on the other hand, relates to the effectiveness of electrons and holes transfer at the interface between MoS_2 and h-BN. [162] Indeed, it seems reasonable to expect that the presence of species intercalated in between the two materials, in the form of blisters or in other forms, hinders charge transfers. However, we will now see that other effects prevail.

4.5.4 Importance of hBN

As explained before hBN plays a crucial role as exciton reservoir. The intensity of CL would be dependent on thickness of the hBN. When the hBN is too thin, the CL intensity coming from monolayer MoS_2 reduces because of the limited interaction cross section. If the hBN is too thick, for instance above 50nm, then few layers form like a barrier and the excitons from hBN cannot reach the monolayer MoS_2. In our case the top hBN was around 20nm so that it could have sufficient interaction cross section and exciton proximity to the MoS_2.

To estimate the interaction length of the electron beam with the sample we have performed Monte-Carlo simulations using the Casino program. Simulations were performed using 1keV electrons and a density of 2.1 g/cm3 for h-BN and are presented in Figure 4.11. It shows that at this acceleration voltage, most of the energy is transferred within the top 20 nm.

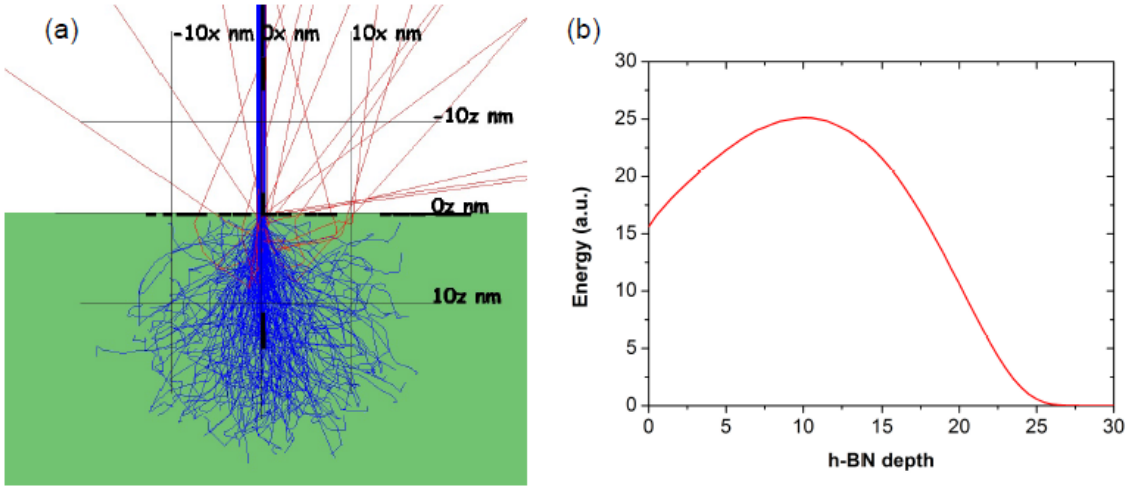

Figure 4.11 – Electron trajectory simulations (a). The in-plane integrated energy that is transferred to the material is illustrated in (b). The horizontal scale is in nm.

Due to the high energy of the electron beam compared to the h-BN band gap, it was possible to retrieve near band edge CL emission from the hBN as illustrated in Figure 4.12a. Observation

of near band edge emission around 215nm is also the signature of the high crystalline quality of hBN flakes. We note that recent studies have established that hBN is an indirect band gap semiconductor[6] and that the complex emission spectra should be interpreted with regards to the phonon band structure. In addition, in figure 4.12b, we show that in region where MoS_2 is not encapsulated in hBN, no measurable CL signal can be retrieved. This shows that hBN plays a very important role as exciton contributor.

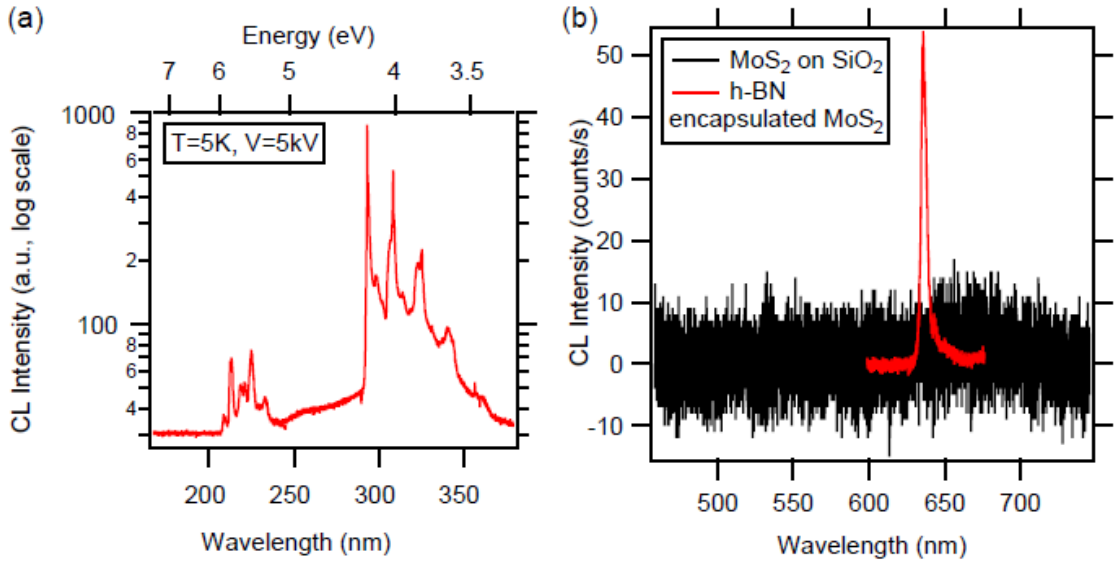

Figure 4.12 – (a) CL obtained at 5K and 5kV on a thick h-BN flake. (b) Comparaison of CL spectra measured on MoS_2 with (red) and without (black) hBN encapsulation.

4.5.5 Raman studies on defects created by ion bombardment

Structural defects created due to ion bombardment has already been studied by Mignuzzi et al [165]. In this report, they have made a detailed Raman spectroscopic analysis on change in the different Raman modes as a result of ion radiation. The density of defects were controlled during ion bombardment and they were able to quantify these defects with respect to vibrational spectroscopy. It could be seen from the figure 4.13a, that as the defects increased, the high frequency peaks A_1' and E' broadened along with significant appearance of LA(M) mode. They were also able to quantify the defects with respect to position of the high frequency modes and the full width half maximum of the modes as shown in the figure 4.13c and d respectively.

The introduced defects perturb the spatial translational invariance of the system resulting in breakdown of fundamental selection rules. Hence the defect causes a situation of moving away from Γ point to M point in the corresponding branches of phonon dispersion curve. As a result, the broadening of first order high frequency peaks A_1' and E' and appearance of several acoustic peaks occur in the Raman spectrum. These disorder activated peaks have been assigned to different phonon at M point as shown in the table.

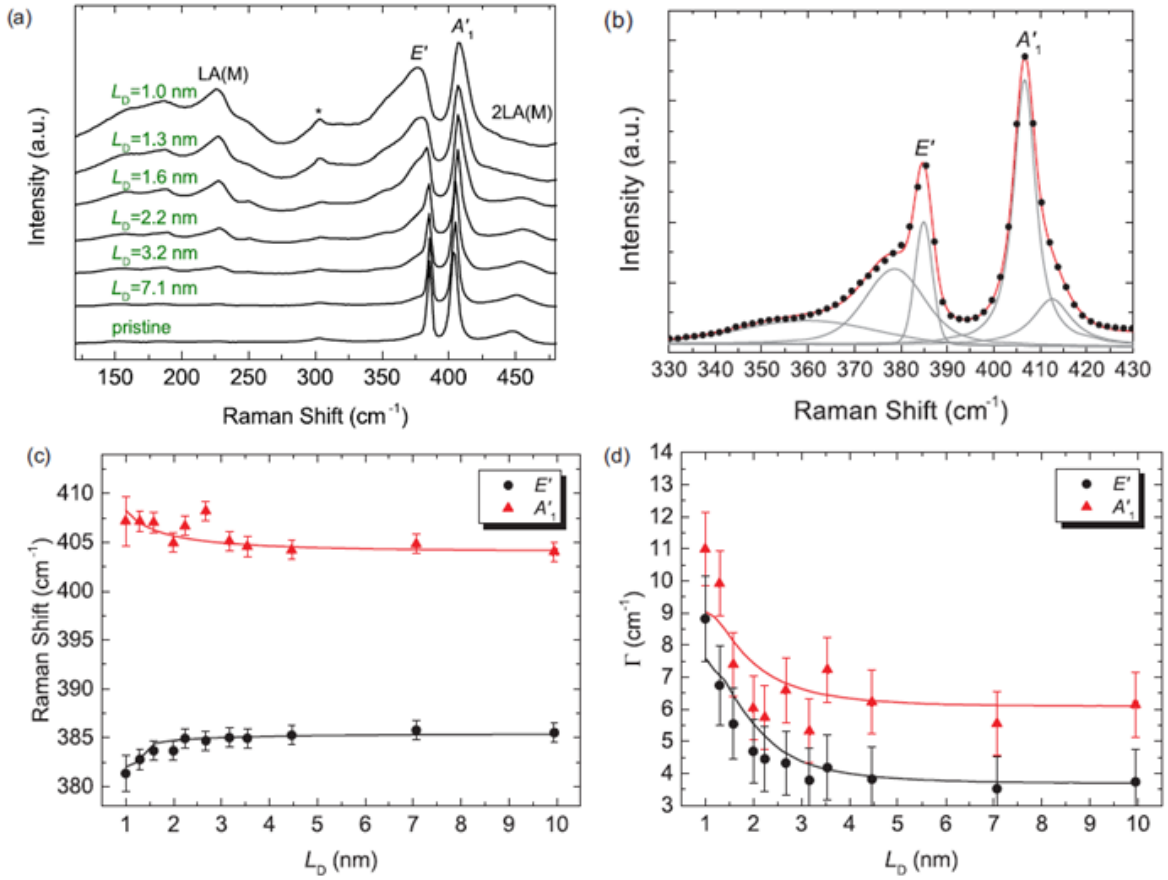

Figure 4.13 – (a) Raman spectra of monolayer MoS_2 flakes with varying inter-defect distances L_D. (b) High frequency first order Raman spectrum for sample with $L_D = 2.2$ nm. The gray lines are the fitted Voigt peaks, and the red line is the cumulative spectrum from the Voigt fitting process. The black dots represent the experimental spectrum. (c)Position of E' and A'_1 as a function of L_D (d) FWHM(Γ) of E' and A'_1 as a function of L_D.Figure adapted from [165].

Band (cm^{-1})	Assignment
154.5 ± 2.4	TA(M)
180.6 ± 1.9	ZA(M)
187.9 ± 0.8	TA(K)
227.6 ± 0.7	LA(M)
357.7 ± 2.8	TO(M)
377.0 ± 1.1	LO(M)
411.9 ± 1.2	ZO(M)

Table 4.1 – Assignment of the different Raman modes observed due to disorder in the monolayer MoS_2.

4.5.6 Raman analysis before and after electron beam irradiation

While before exposure to the electron beam (used for the CL measurement), PL revealed essentially bright regions, the PL map measured after CL strongly correlates with the CL maps, showing the same dark regions (compare Figures 4.10 c,e). Obviously the irradiation by the electron beam locally quenches luminescence, whatever the source of excitation used to observe

it. This observation questions the common conception that CL is quenched only by charge transfer hindrance at interfaces; instead it suggests a more invasive effect of the electron beam, damaging MoS_2.

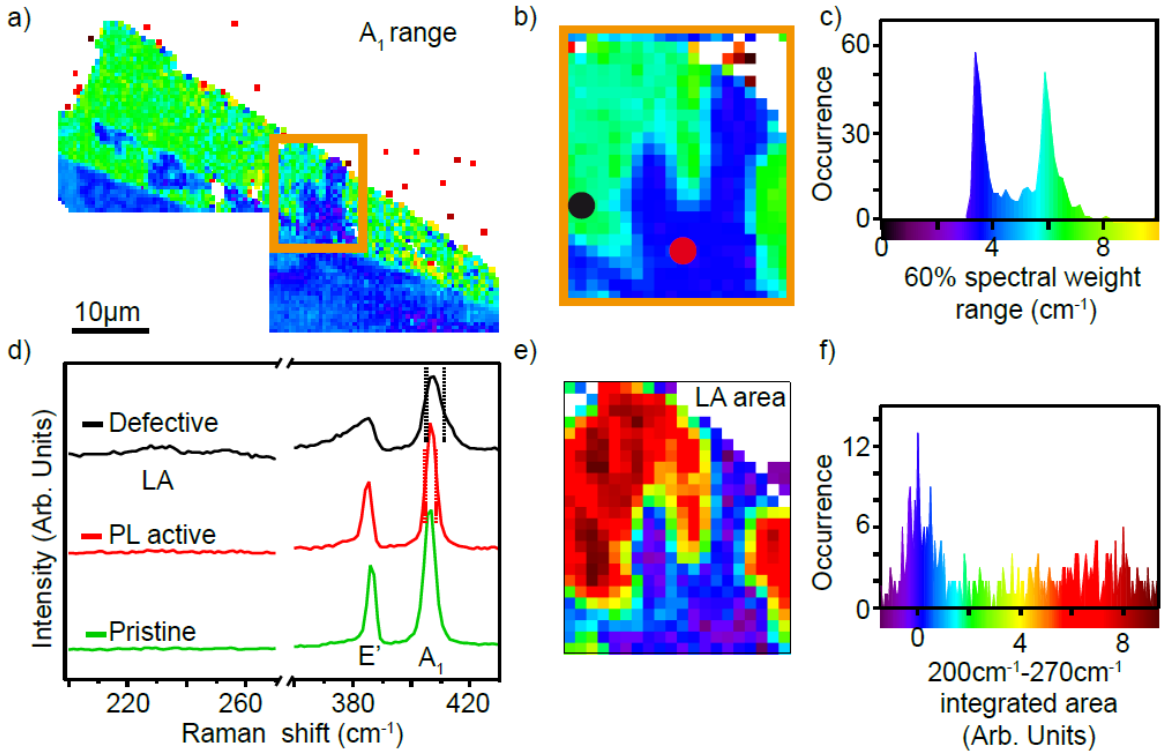

Figure 4.14 – Raman spectroscpopy and spatial mapping of defects. The spatially resolved width of the A_1' peak is used as a metric for the presence of defects created during the CL experiment, as discussed in the main text. The map shown in (a) presents a strong spatial correlation with both CL and PL mapping performed after CL (see Figures 2b,d). A_1' map with a better spatial resolution of a smaller area is presented in (b). The histogram of A_1' widths is presented in (c), in which two peaks attributed to the absence (blue, small width) or presence (green, large width) of defects appear. The color scale meaning in (a), (b) is provided in (c). In (d) representative spectra of the different regions are presented: pristine (i.e. before CL), PL active and PL inactive/defective. PL active and pristine are virtually indistinguishable. In addition to a broader A_1' peak, the defective regions show the emergence of Raman signal around 230 cm^{-1}, which we refer to as the LA area. Such signal in this area is also a signature of defects. (e) shows the spatially-resolved integrated intensity in this spectral region at the same position as in (b). As expected, defective/PL inactive regions shows more signal in this area (red) and correlate with a wider A_1' peak (b) providing a consistent picture. The color scale used in (e) is detailed in (f).

To address this possibility, we analyzed the vibrational properties of MoS_2, before and after electron beam irradiation. We performed Raman spectroscopy at room temperature using an excitation wavelength of 532 nm (see Methods). In the regions showing CL, we always observe Raman spectra with two prominent peaks (Figure 4.14a), corresponding to the intralayer in-plane $E^{'}$ and out-of-plane $A_1^{'}$ modes.[104],[166]. These modes correspond to first-order Raman processes and arise from single phonon at the center of the Brillouin zone.

Small deviations from single Lorentzian lineshapes, expected for such processes, can never-

theless be extracted from the experimental spectra of pristine monolayer MoS_2. Such deviations likely come from the additional contributions of doubly resonant Raman (DRR) processes. For the $E^{'}$ mode, a low energy shoulder was already reported in pristine monolayer MoS_2[167, 168]. As the $E^{'}$ mode is doubly degenerate, such shoulder could be attributed to a degeneracy lifting induced by strain or doping. [166]

Electron beam irradiation has no effect on the spectra in regions showing CL. In regions showing no CL, on the contrary, electron irradiation has strong effects. Prior to irradiation, we also exclusively observe signatures of the $E^{'}$ and $A_1^{'}$ modes. After irradiation, the corresponding peaks appear broader and show some structure, and new modes are found at lower frequency, around 230 cm^{-1} (Figure 4.14a). They form a band, that is referred to as LA(M) in the literature.[169, 167, 168]. While an exact fitting procedure would require a full theoretical description of Raman intensities including DRR contributions, such complex spectra have been fitted with a sum of Lorentzian in the literature [170, 167, 168].

Within this approximation, we can associate a peak to a given phonon in the band structure. The band around 230 cm^{-1} was shown to be defect-induced. A detailed, excitation energy dependent study, showed that this band arises from DRR processes involving one phonon; elastic scattering by a defect ensuring momentum conservation [168]. This band has three main contributions: a van Hove singularity in the phonon density of states between the K and M points, the LA band in vicinity of the M point (LA(M)) and the LA band in the vicinity of the K point (LA(K)) [168]. In addition we observe another defect-activated contribution near 250 cm^{-1} which was also reported by Mignuzzi et al. [167] but left unassigned.

We now discuss the evolution of the spectra in the vicinity of the $E^{'}$ and $A_1^{'}$ modes upon electron irradiation in regions showing no CL. Defect-induced contributions are visible close to both $E^{'}$ and $A_1^{'}$. They have been attributed to phonons in the vicinity of the M points on the TO, LO and ZO branches [167]. We have quantitatively analyzed the weight of those defect-induced contributions in order to spatially map the occurrence of defects. The details of the analysis are presented in the appendix section. In Figure 4.14b,c , we image the presence of defects in the sample using this approach.

We see that there is a remarkable spatial correlation between defect mapping using Raman spectroscopy and CL/PL mapping (Figure 4.10c,e). In addition, to strengthen the validity of our method, we perform a similar defect-mapping analysis based on the LA(M) band (Figure 4.14e). We see here that regions with a measurable contribution around 230 cm^{-1} are the ones that are defective and thus CL/PL inactive. The quenching of luminescence by electron beam irradiation is hence related to defect creation in MoS_2.

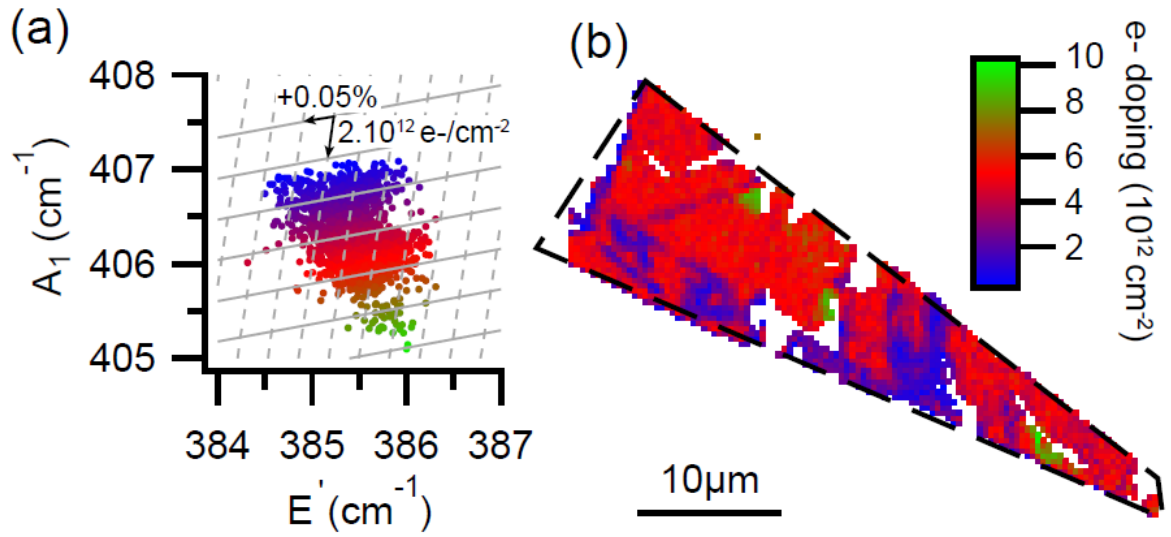

Figure 4.15 – Spatially resolved contact mapping through doping analysis before cathodoluminescence. In (a) the energy shifts of both the E' and $A_1^{'}$ Raman modes acquired on the whole sample are presented. Their positions are both dependent on strain and doping (strain and doping axis are represented by non-orthogonal vectors in this space). The spatially resolved doping (b) shows that region that are tightly coupled to hBN present less electron doping. The colorscale in (a) represents the electron doping as in (b).

We now turn our attention to the origin of defects creation and the possibility to locate regions with an intimate contact between h-BN and MoS_2 prior to CL and the creation of defects.

In Figure 4.15, we present a doping analysis of the sample realized prior to CL. We used Raman spectroscopy and tracked local shifts in the positions of the $E^{'}$ and $A_1^{'}$ modes (see the distribution in Figure 4.15a) to retrieve the spatial dependence of doping (Figure 4.15b). This is possible thanks to their different dependence on strain and doping. This kind of analysis was already outlined in the literature on monolayer MoS_2 in chapter 3. [112, 94] We observe that regions exhibiting CL have a smaller n doping, by typically several 10^{12} cm^{-2}, compared to regions presenting no CL. Noting that the analysis concerns measurements acquired before the CL measurements, *i.e.* prior to electron beam irradiation, we conclude that regions tightly coupled to h-BN are less electron doped than regions with a loose coupling.

While the presence of an h-BN susbtrate has been shown to reduce electron doping compared to SiO_2, [94] in which case doping is created by charge traps at the interface, [114] the exact mechanism at stake here to explain the coupling-dependent doping is more complex. Species trapped at the interface and gathered in the form of blisters are likely candidates to explain the observed n doping. But the effect of, for instance, oxygen, that was present during the sample preparation in ambient atmosphere is still debated and might depend on the substrate. [171] While the identification of the exact mechanism responsible for the observed reduction of n doping in tighly coupled h-BN/MoS_2 regions will require further investigations, it is nevertheless possible to identify those regions using Raman spectroscopy as shown in Figure 4.15b.

We note that we could not observe low-energy interlayer vibrational modes in Raman spectroscopy, that could be another signature, besides electronic doping level, of an intimate contact between MoS_2 and h-BN. Although such modes have indeed been observed in between TMDC layers,[172, 173, 174] we are not aware of any reports of such modes between h-BN and MoS_2.

4.5.7 Origin of defects

Having established that defects are induced by irradiation by the electron-beam used during the cathodoluminescence measurements, and that these defects yield prominently non-radiative recombination of EXs, we now discuss their possible origin. The energy of the electron beam is well below the threshold for knock-on displacement of individual S or Mo atoms in MoS_2, which is several 10 keV and few 100 keV respectively.[175, 176, 177] This effect can hence be ruled out as a source of defects in MoS_2 here. The dose in a typical CL experiment is estimated to be of the order of tens of mC/cm^2 (tens of electrons/nm^2) which is several orders of magnitude below the dose for typical transmission electron microscopy experiments [109].

Another possible origin, also related to the electron beam, is a chemical reaction rather than a scattering effect. MoS_2 has indeed been shown to act as an active catalyst for hydrogen evolution reactions (HER). Following a Volmer-Heyrovsky type of mechanism, the electron beam used in our experiment might thus promote a multi-step chemical processes proceeding for instance through the formation of MoH adducts.[178, 179] In our case, it is reasonable to assume that the blisters located at the MoS_2/h-BN interface contain airborne species such as water and/or oxygen that naturally adsorb on surfaces in ambient pressure conditions and will be trapped during the assembly of the heterostructure.

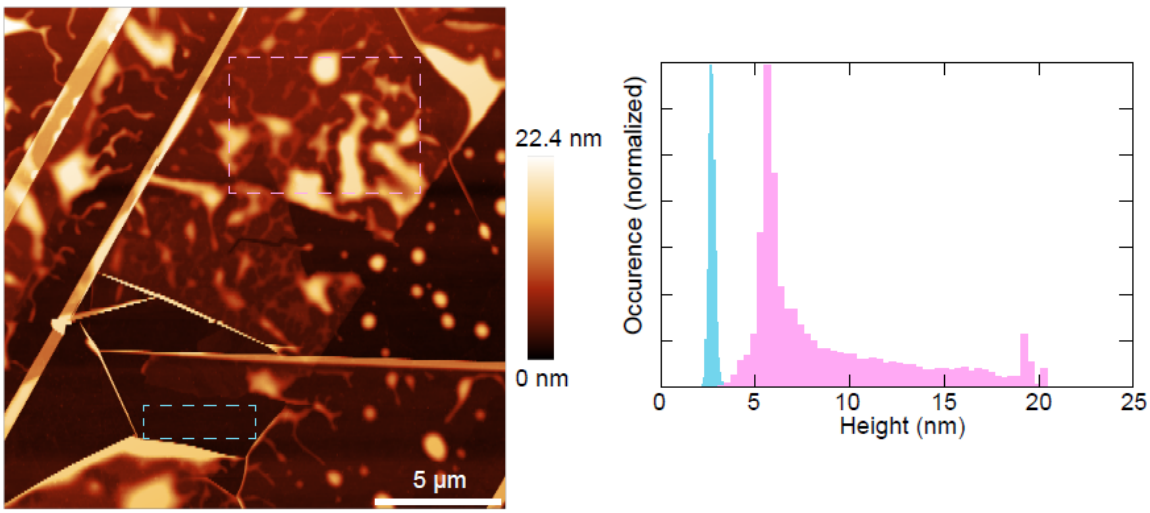

Figure 4.16 – Atomic force microscopy image of the sample made using the PDMS technique. Regions with very different roughness can be observed. The left histograms are obtained in the blue and pink area on the right image. The blue region, that presents a much smaller roughness (root minus square roughness in the range of 2 Å) is the one which shows the best coupling between h-BN and MoS_2.

It has been shown that the presence of oxygen can enhance catalytic reactions in MoS_2.[180] The trapped blisters may hence behave as aqueous solution micro- or nano-reactors. The chemical environment of the MoS_2 atoms bonded to hydrogen is different from that of the pristine material, which may authorize the electron scattering processes needed to activate the above-discussed defect-induced Raman signatures.

4.5.8 Heterostructure fabrication for better interlayer coupling

The nanometer-scale spatial resolution of cathodoluminesence, as implemented in a scanning electron microscope, together with the tendency for defect formation under electron-beam irradiation of the blisters, represents a high resolution probe of the quality of the MoS_2/h-BN contact. Employing this probe allowed us to conclude that the PDMS transfer technique does not allow to achieve extended clean contacts beyond a few μm.

We then used an alternative transfer technique based on pick-up and drop-down with a PPC stamp. This technique allows to reduce the amount of blisters trapped at the interface.[163] Figure 4.17a shows an optical micrograph of a h-BN/MoS_2/h-BN heterostructure. The CL map of this sample is much more uniform than that of heterostructures prepared with a PDMS stamping as expected from the more uniform contact (compare Figures 4.17c and 4.4). Also the PL taken before and after CL are very similar (see Figures 4.17) in contrast to the sample prepared using PDMS (see Figures 4.3). It shows that electron beam irradiation in CL has not created extended defective regions because of the uniform coupling in that sample. The complete suppression of bubbles should allow further optimization of the process. [163]

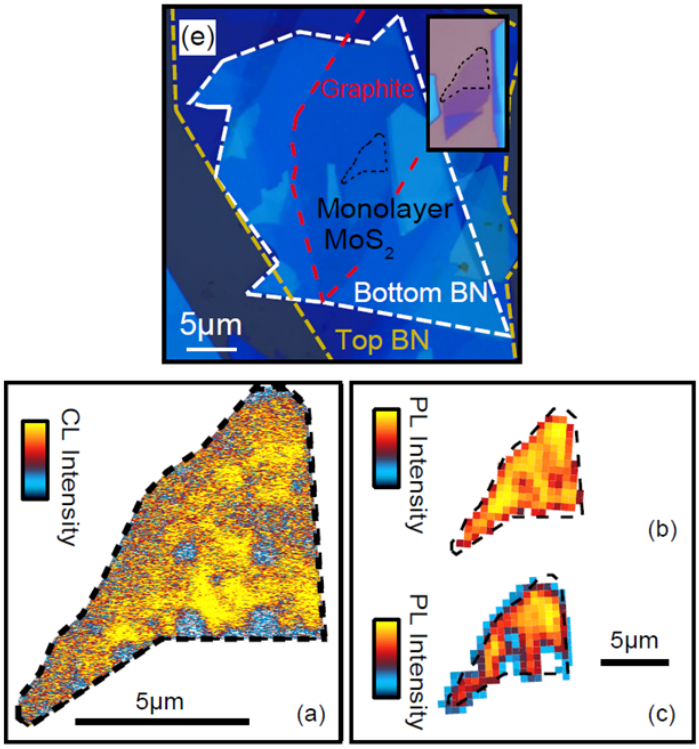

Figure 4.17 – Uniform coupling and properties using PPC preparation technique.The sample prepared using the pick-up technique is shown in (e). The inset presents the region of interest of MoS_2 prior pick-up, i.e. on SiO_2, in which case the optical contrast is higher.The CL signal measured at 5K in the sample prepared by the pick-up drop-down technique is uniform across the flake. We observe sub-micrometric regions with reduced CL signal (blue) that are (air) bubbles. The integrated PL intensity measured at room temperature before (b) and after (c) CL shows a limited evolution compared to the sample made using PDMS. The absence of signal is limited to sub-micrometer size regions that are caused by (air) bubbles created in the fabrication process.

4.6 Chapter conclusions and perspectives

4.6.1 Conclusions

In this chapter, we have shown that encapsulating MoS_2 SLs in between h-BN layers drastically improves the optical quality in this material and permits to recover its intrinsic optical properties .We have performed three-beam FWM which reveals the formation of the photon echos, extracting homogeneous and inhomogeneous contributions to the EX spectral line-shape. Interestingly, at some positions the echo formation is suppressed. The FWM transient approaches the form of interaction dominated free-induction decay, implying that locally the EX broadening is dominantly homogeneous.

FWM microscopy reveals the impact of the local disorder onto the EX's oscillator strength and its line-shape. The latter is shown to be affected also by the temperature. This methodology is well suited to accurately assess the impact of disorder on the EX responses in forthcoming experiments with novel TMD heterostructures.

Finally we show that clean interfaces between TMDCs (here MoS_2) and h-BN are required to allow efficient charge transfer between the barrier and active material. Assembly techniques that are commonly employed to prepare heterostructures often trap blisters of contaminants at the interface between the TMDC and h-BN surfaces. Contrary to what may have been thought, the detrimental effect of such blisters is a hindrance of charge transfers at interface. Cathodoluminescence is there quenched due also to electron-beam-induced damage of the TMDC crystal. Defects are generated, and induce non-radiative charge carrier combination.

We ascribe the formation of defects to an electron-promoted chemical reaction. We find that the cleanliness of the interface is of superior spatial uniformity, and the generation of defects is greatly avoided, when a pick-up/drop-down assembly technique with PPC is employed. The narrow emission linewidth observed in CL and the localized electron beam should allow to spatially map strain and doping profiles with nanometer resolution by analyzing the exciton peak position and the presence of trion emission. CL could also be used to study with unprecedented spatial resolution single photon emitters that were reported in several TMDCs.

4.6.2 Perspectives: $MoSe_2$ heterostructure in tailored electromagnetic environments

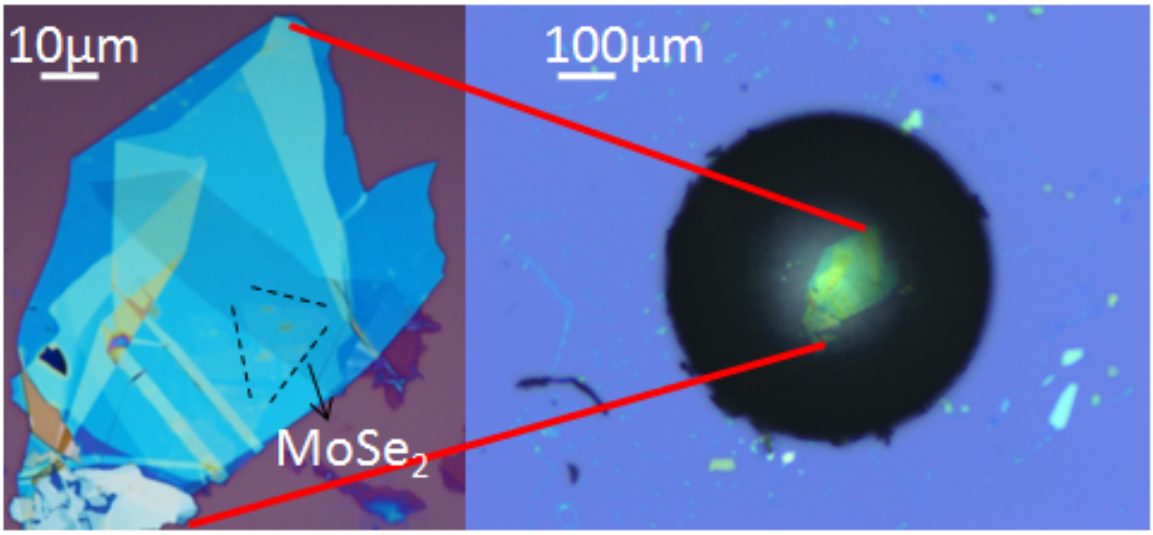

Figure 4.18 – (left) Monolayer $MoSe_2$ encapuslated in hBN. (right) A 500 micron diameter zirconium lens covering the heterostructure.

The monolayer $MoSe_2$ was encapuslated inside two hBN flakes by using the PPC technique as explained in the sample fabrication section. Similar to monolayer MoS_2, it has direct bandgap at the single-layer limit. A 500 micron diameter zirconium lens is transferred on the hBN/ $MoSe_2$/hBN heterostructure using micromanipulator techniques. Here the goal is to study the exciton dispersion further in k-space. It has been predicted theoritically that the exciton dispersion has several branches, one of them being linear near k.[181] Therefore, using the zirconium lens and anti-reflective coating on top of it, we want to probe the dispersion relation experimentally. We chose $MoSe_2$ heterostructure as its spectral range is adapted to the use of a tunable Ti-Sa laser.

Further, in the team there is now an ongoing effort to measure such heterostructures in microcavities in the regime of strong light matter coupling, in order to study the role of interactions. TMDC are especially suitable to reach the strong coupling regime due to their high oscillator strength.[182]

4.7 APPENDIX

I would like to thank the post doc of the group Dr. Simone Lisi for the specific complex IGOR codes developed for the analysis of Photoluminescence and the Raman spectra and maps. His fitting procedures were used in all of our published papers and in the present thesis and a brief description is given in this appendix.

4.7.1 Photoluminescence spectrum fitting procedure

Photoluminescence spectra were acquired with a 532 nm Nd:YAG laser using a commercial confocal WITEC spectrometer at room temperature under ambient conditions. The laser spot size was around 1 μm. The signal was collected through a 50x objective with a numerical aperture of 0.75. A low power of 8 μ W was used to avoid any possible photodoping along with a grating of 600 lines/mm. The photoluminescence spectra were taken with an integration time of 30s to improve signal-to-noise ratio, and the spatially resolved photoluminescence maps were taken with an integration time of 3-5s.

Photoluminescence spectra at room temperature have been fitted with purely Lorentzian lineshape, as intrinsic effect dominate the character of the spectral distribution in such material. Indeed, gaussian broadening due to extrinsic effect are hardly detectable, and a satisfactory fit is achieved with a purely Lorentzian curves. The two contributions comprised in the spectral range $1.75eV - 1.95eV$ can be straightforwardly ascribed to the A exciton and and its charged counterpart, the A- trion, at higher and lower photon energies respectively.

4.7.2 Raman spectrum fitting procedure

All the Raman spectras were acquired with a 532 nm Nd:YAG laser using a commercial confocal WITEC spectrometer at room temperature under ambient conditions. The laser spot size was around 1 μm. The signal was collected through a 50x objective with a numerical aperture of 0.75. For the Raman spectra, the power was kept at 300 μW to avoid damage due to laser-induced heating in MoS_2 flakes. The signal was integrated for 2s after being dispersed by a 1800 lines/mm grating.

This spectral region is fitted with a single Voigt line profile together with a linear background. The simplicity of the spectral shape allows for an unambiguous fit.For a pristine, poorly defected sample, two Raman signatures can be identified in the spectral region ranging from $320 - 420cm^{-1}$. Increasing the defect density qualitatively results in a broadening of these spectral features and a the concomitant rise of additional spectral weight in their proximity.The first step of our strategy consists in approximating these additional spectral weight with the combination of series of Voigt line profiles. It is important to remark that the aim of these first step is not to extract physically relevant information from the fit parameters, but rather to obtain a smoothing spline to be later used in our fits to separate purely defective signatures from spurious ones. With spurious features we refer to the spectral features due to the both purely Raman Eg and Ag peaks and their broadening due to defect scattering. The deconvolution of pristine and defect related features for these peaks is beyond the scope of this analysis.

4.7.2.1 Residuals for quantitative fit analysis

Fitting spectral distributions is a common practice in spectroscopy for extracting valuable physical information, when an 'a priori' known model is available to describe the observed spectra.The

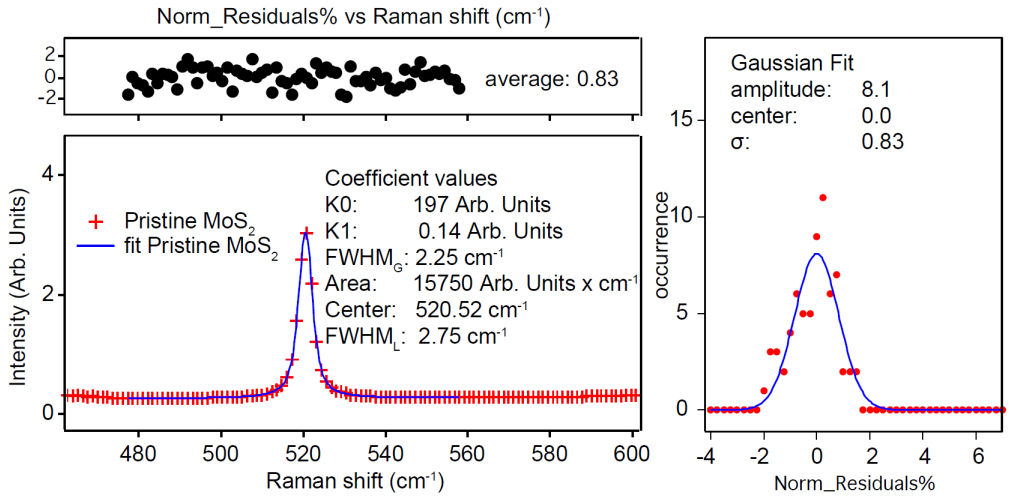

Figure 4.19 – Details of residual analysis for error bars estimation. The subscript G (resp. L) stems to the Gaussian (resp. Lorentzian) contribution to the Voigt lineshape.

reliability of the fit and in particular the standard deviation associated to each fit parameter fundamentally relies on error-bars associated to each point in the spectral distribution, that are normally not readily available experimental outputs. In the following, a strategy is defined to evaluate the standard deviation associated to our experimental curves. The spectrum of the pristine MoS_2 will be used as a model.

For each spectrum, a region comprising a single Raman peak together with a smoothly varying background is found. In our case the spectral range 477-558 cm^{-1} is chosen (as shown in the bottom-left panel of Figure 4.19), where only signal from the SiO_2/Si substrate is found, on an almost flat background. It is worth noting that a peak-less region would be a fair choice as well, but for the sake of accumulating statistics on a wide experimental range, a region comprising a single peak was chosen for our analysis.

This spectral region is fitted with a single Voigt line profile together with a linear background (bottom-left panel of Figure 4.19). The simplicity of the spectral shape allows for an unambiguous fit. The fit function takes the form of a linear component plus a Voigt function:

$$fit(x) = K0 + K1 \times x + Voigt(x)$$

The % of fit residuals (%Norm_Residuals(x)) are calculated point by point, computing the difference between the fit value (Fit(x)) and the spectral intensity (Iexp(x)), normalized by the latter and multiplying by 100 (top-left panel of Figure 4.19).

$$\%Norm\_Residuals(x) = 100 * (Fit(x) - Iexp(x))/(Iexp(x))$$

Then the standard deviation is computed and double checked fitting with a gaussian function the distribution of the residuals (right panel of Figure 4.19):

$$st\_dev\% = \sqrt{(\sum_x (\%Norm\_Residuals(x)^2)/(N-1))}$$

with N number of points.

Finally, this st_dev% is used to compute the error-bars for each point in the spectrum by

rescaling as:

$$error\_bars(x) = st\_dev\% \times Iexp(x)/100$$

4.7.2.2 The spectral function

The aim of this study is to exploit spatially resolved Raman spectroscopy to readily ascertain, and to quantify to some extent, the presence of defects in large area flakes (several tens of μm^2). Raman spectroscopy is an efficient tool for identifying defect related spectral features, as recently shown by Mignuzzi et al. [167]. To this end, the possibility to densely sample Raman spectra on large areas is explored.

The main downside of a dense spatial sampling is the consequent lowering of spectral quality (i.e. signal to noise ratio) that is needed for scanning the whole sample surface in a time compatible with drift in position and focus in the setup (typically on the hour scale).

Such a loss of spectral quality hinders refined fit analysis, where multiple unresolved peaks are found, (as shown in the literature [167]). Therefore the aim of our analysis is to devise a simple strategy for extracting defect related quantities out of noisy data.

For a pristine sample, two Raman signatures can be identified in the spectral region ranging from 320-420 cm^{-1}. Increasing the defect density qualitatively results in a broadening of these spectral features and a concomitant rise of additional spectral weight in their proximity.

The first step of our strategy consists in approximating these additional spectral weight with the combination of series of Voigt line profiles. It is important to remark that the aim of these first step is not to extract physically relevant information from the fit parameters, but rather to obtain a smoothing spline to be later used in our fits to separate purely defective signatures from the remaining features, (peak3 and peak 5 in the following discussion) in the spectra. Such features arise primarily from $E^{'}$ and $A_1^{'}$, but with additional contribution, mainly in the form of broadening, due to defects. The deconvolution of pristine and defect related features for these peaks is beyond the scope of this analysis.

A good fit of a defect rich area has been achieved with a series of 7 peaks (Figure 4.20). Peaks 3 and 5 refer to the features just described, peaks 0-2 describe the smoothing spline of defect signatures around the $E^{'}$ peak (bunch1), while peak 4 an 6 describe defect signatures near the $A_1^{'}$ peak (bunch2).

$$bunch1(x) = peak0(x) + peak1(x) + peak2(x)$$

$$bunch2(x) = peak4(x) + peak6(x)$$

	G_FWHM [cm^{-1}]	Rel. Area [Arb. Units]	Center [cm^{-1}]	L_FWHM [cm^{-1}]
peak0	28.693	0.334479	361.86	0.06775
peak1	14.237	0.370025	375.42	0.012103
peak2	7.7384	0.295496	381.8	0.0083741
peak4	1.5332	0.314408	403.15	3.9348
peak6	3.4388	0.685592	412.81	4.416

Table 4.2 – Fit parameters for the spectrum presented in Figure 4.20.

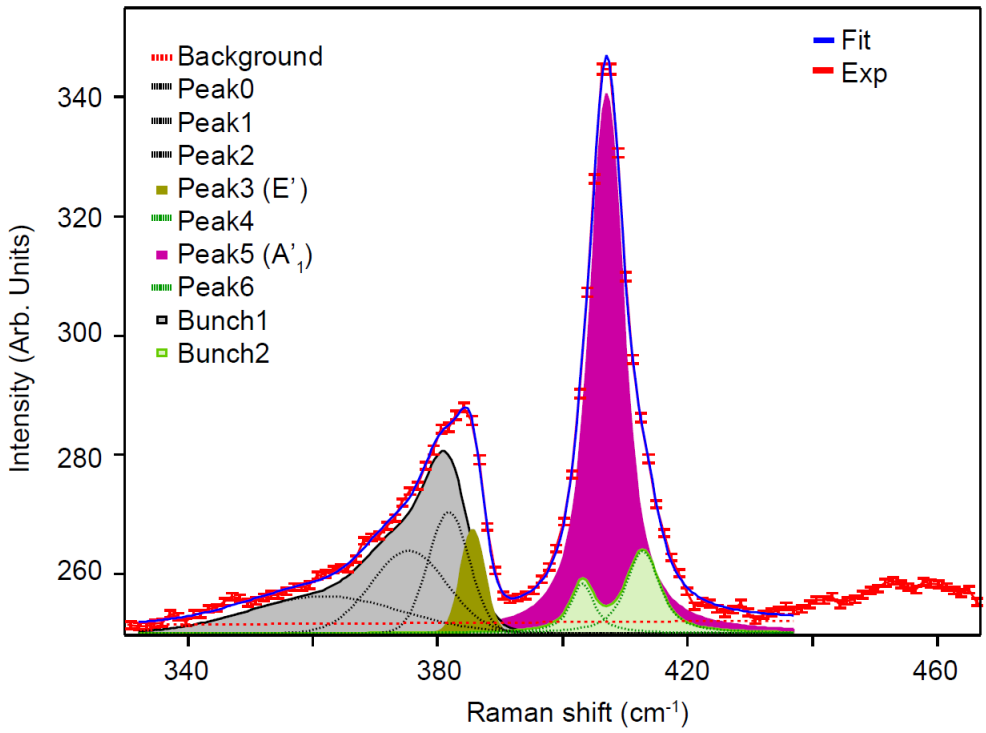

Figure 4.20 – Fit of a Raman spectrum from MoS_2 in a defective area.

We then proceeded to fit good quality spectra (Figure 4.21) with various defect densities by fixing the shape of these smoothing splines and allowing for small relative position adjustment (offset_bunch_i, i=1,2) and area rescaling (area_bunch_i, i=1,2), plus two Voigt peaks representing the $E^{'}$ and $A_1^{'}$ peaks (peak3 and peak5 respectively) and a linear background ($K0+K1\times x$):

$$F(x) = K0 + K1 \times x + Area\_bunch\_1 \times bunch1(x - offset\_bunch\_1) + Area\_bunch\_2 \times bunch2(x - offset\_bunch\_2) + peak3(x) + peak5(x)$$

The spectra acquired at different locations show a varying amount of defect related spectral weight, with higher levels of defects being correlated to broader $E^{'}$ and $A_1^{'}$ spectral features. The tables below report the fit results for the spectra in Figure 4.21.

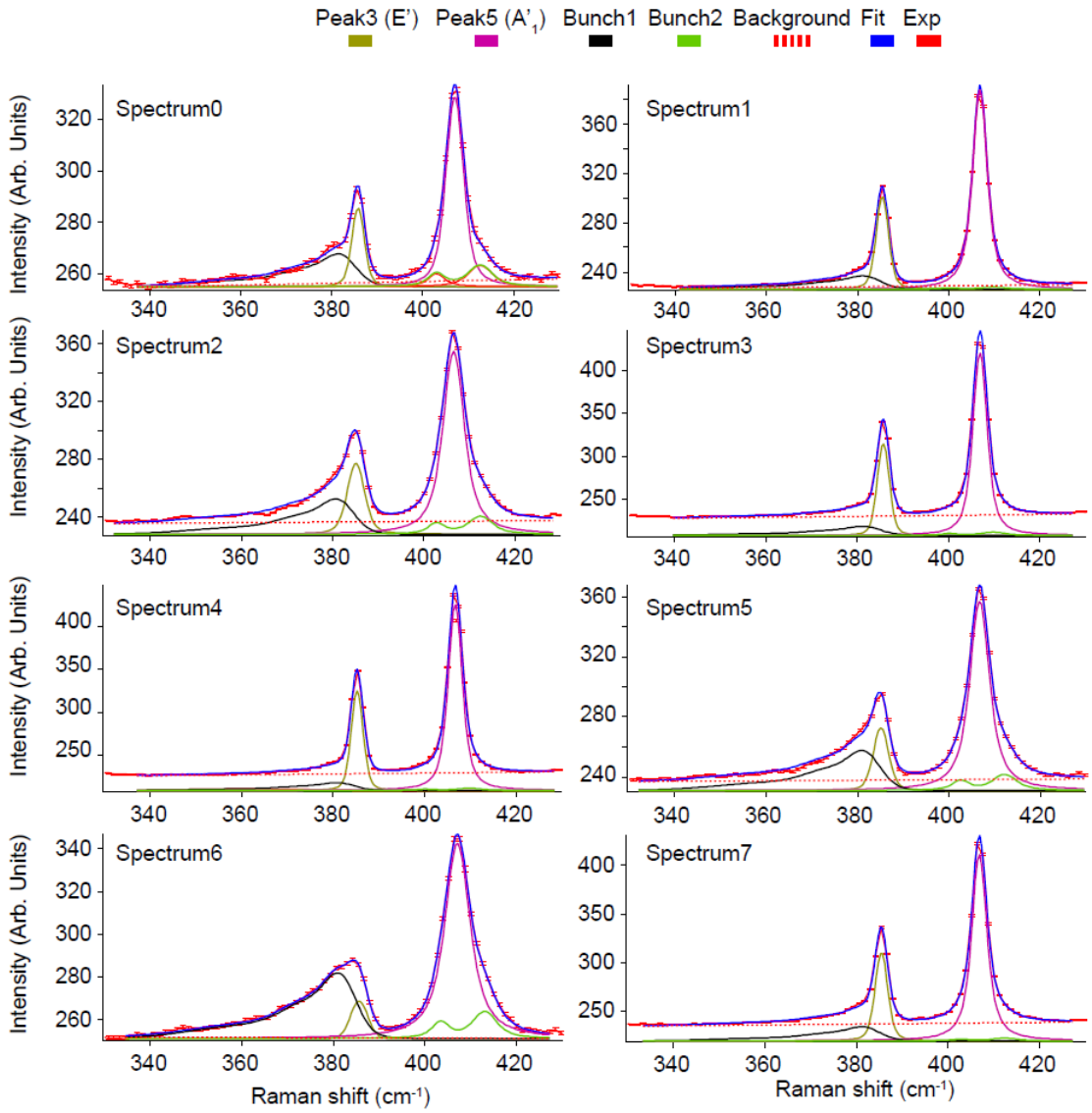

Figure 4.21 – Examples of fits in regions presenting a wide range of defect densities.

	Spectrum0	Spectrum1	Spectrum2	Spectrum3
K0	243.1 (1.7)	215.7 (1.1)	228 (3)	208.8 (1.4)
K1	0.035 (0.005)	0.0331 (0.003)	0.022 (0.008)	0.056 (0.004)
Area_bunch_1	236 (19)	202 (12)	450 (40)	196 (14)
Offset_bunch_1	0.4 (0.9)	0.1 (0.6)	0.0 (1.0)	0.2 (0.8)
$E^{'}$_G_FWHM	2.6 (0.3)	2.60 (0.09)	3.6 (0.5)	2.65 (0.08)
$E^{'}$_Area	120 (20)	295 (13)	270 (40)	393 (16)
$E^{'}$_Center	385.80 (0.05)	385.380 (0.015)	385.18 (0.09)	385.680 (0.014)
$E^{'}$_L_FWHM	1.1 (0.6)	1.06 (0.15)	1.6 (0.6)	0.81 (0.14)
Area_bunch_1	110 (20)	22 (11)	160 (0.6)	48 (14)
Offset_bunch_1	-0.1 (0.4)	-3.0 (0.8)	-0.3 (0.4)	-3 (0.5)
$A_1^{'}$_G_FWHM	3.3 (0.4)	1.91 (0.12)	2.9 (0.4)	2.36 (0.10)
$A_1^{'}$_Area	440 (30)	893 (14)	1000 (60)	1065 (16)
$A_1^{'}$_Center	407.07 (0.03)	406.810 (0.009)	406.63 (0.03)	406.910 (0.009)
$A_1^{'}$_L_FWHM	2.2 (0.6)	2.85 (0.12)	4.0 (0.5)	2.18 (0.12)

	Spectrum4	Spectrum5	Spectrum6	Spectrum7
K0	209.3 (1.4)	231.1 (1.4)	254 (2)	220.5 (1.4)
K1	0.050 (0.004)	0.017 (0.004)	-0.006 (0.006)	0.044 (0.004)
Area_bunch_1	171 (14)	494 (20)	570 (20)	270 (17)
Offset_bunch_1	-0.26 (1.0)	0.0 (0.5)	0.0 (0.5)	0.2 (0.7)
$E^{'}$_G_FWHM	2.61 (0.08)	3.3 (0.2)	4.4 (0.6)	2.60 (0.11)
$E^{'}$_Area	427 (16)	200 (20)	84 (20)	365 (19)
$E^{'}$_Cent	385.310 (0.014)	385.11 (0.04)	385.60 (0.16)	385.445 (0.017)
$E^{'}$_L_FWHM	0.84 (0.14)	1.2 (0.3)	0.01 (1.01)	1.14 (0.17)
Area_bunch_1	35 (15)	140 (20)	162 (17)	37 (15)
Offset_bunch_1	-3.0 (0.7)	-0.6 (0.2)	0.2 (0.2)	-0.5 (0.7)
$A_1^{'}$_G_FWHM	2.36 (0.10)	2.4 (0.2)	2.9 (0.3)	2.00 (0.16)
$A_1^{'}$_Area	1087 (19)	950 (30)	880 (30)	1079 (19)
$A_1^{'}$_Center	406.780 (0.009)	406.720 (0.018)	407.06 (0.03)	406.845 (0.011)
$A_1^{'}$_L_FWHM	2.17 (0.12)	4.0 (0.3)	5.3 (0.3)	2.89 (0.16)

Table 4.3 – Fit parameters for the spectra presented in Figure 4.20.

By fitting, with the above model, Raman maps with a small field of view and good quality spectra, a correlation can be established between low defect related intensity and strong PL activity (Figure 4.22). In Figure 4.22 we report the FWHM of the $E^{'}$ and $A_1^{'}$ Voigt curves (Figure 4.22a and Figure 4.22b respectively) and we compare them with the area of the two defect-related bunches (1 and 2 in Figure 4.22c and Figure 4.22d respectively). The histogram representing the distributions of values on the 2D plots are also reported for clarity.

The outputs of such analysis clearly shows that a correlation exists between regions where the PL emission is still prominent, after the CL experiments and regions where the spectral contribution from defect related peaks are the smallest (confront with main text Figure 2). Moreover, these PL active regions also show the sharpest $E^{'}$ and A'_1 spectral features, i.e. a spectral distribution very close to a pristine sample. In conclusion, extracting the spectral weight of the purely defect related feature is an efficient way to identify potentially PL active regions.

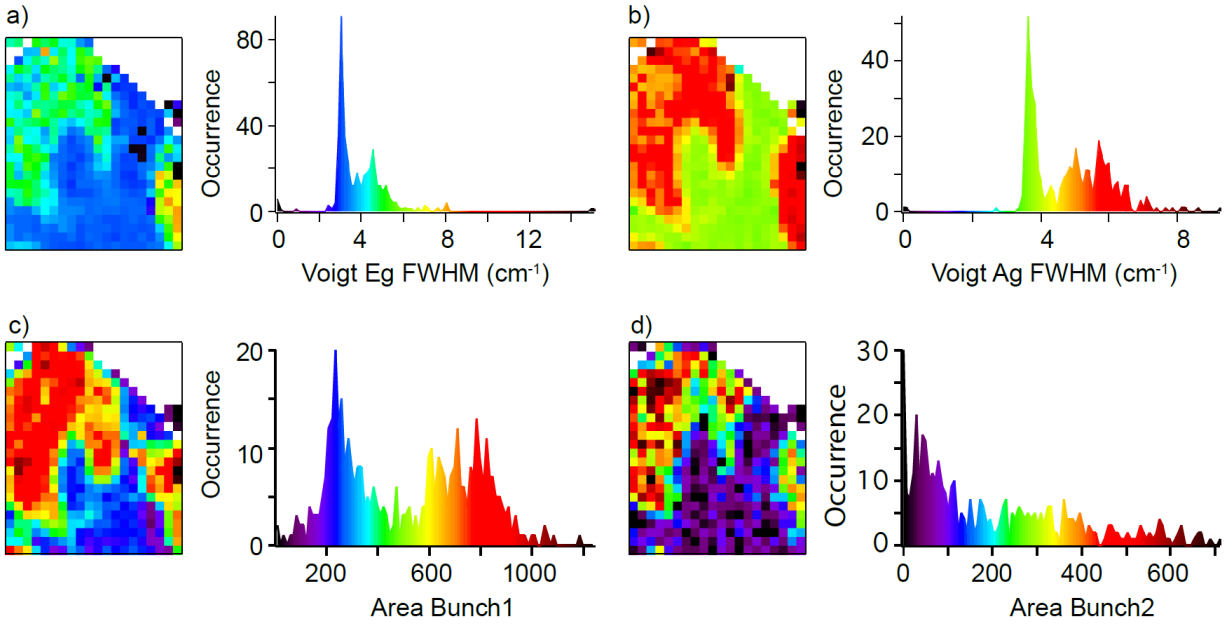

Figure 4.22 – Example of small scale Raman mapping. FWHM of the $E^{'}$ (a) and $A_1^{'}$ (b) peaks. (c) and (d) represent the area of two defect related features.

4.7.3 Noisy spectra on large scale images

However, performing highly resolved, spatially extended Raman mapping while preserving a signal to noise ratio low enough to perform curve fitting with many degrees of freedom may be extremely time consuming, if not completely unfeasible. Therefore, we investigated the possibility of identifying the PL active regions from noisier spectra, acquired with a faster rate. The concomitant occurrence of sharp $E^{'}$ and $A_1^{'}$ spectral features, together with reduced defect ones , and vice versa, naturally suggests the following approach:

I) we define a spectral range around the $A_1^{'}$ features comprising both the A'_1 peak an the defect spectral contributions (395-420 cm^{-1}).
II) For each spectrum, we compute the total area comprised in this region, after the subtraction of a background to set the minimum of the spectrum around zero.
III) Afterward, we shrink the spectral range from each side (low and high energy) until a 20% of the spectral weight is lost on each side and we record the width of such spectral window.

In Figure 4.23a two spectra extracted from a PL active region (red) and a PL mute one (black) are shown. The vertical bars define the range where 60% of the spectra weight is found, after cutting 20% of it from the left and 20% from the right. In Figure 4.23b we report a small 2D plot of such spectral width mapped around a region with PL active and mute regions (check Figure 2 in the main text for comparison), together with its histogram (Figure 4.23c). The result of the above analysis clearly shows how the narrowest spectral windows are found around PL active regions, while larger windows are associated to defective regions, due to the broader spectral distributions. This method, due to the integral nature of the areas, reduces the effect of the noise (at the expenses of more quantitative analysis).

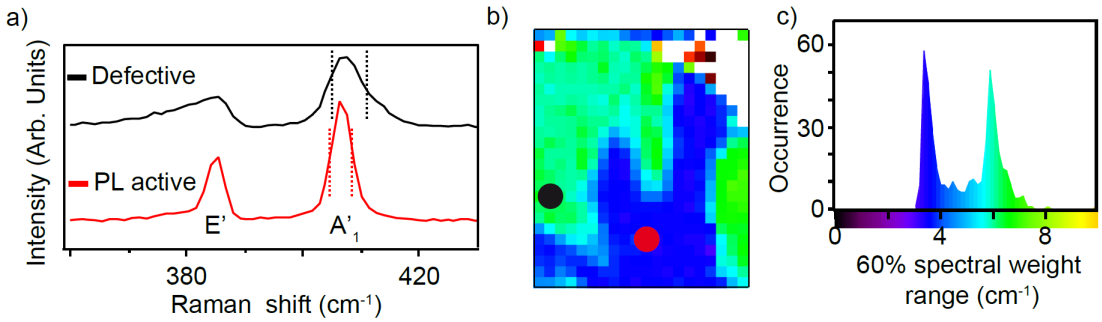

Figure 4.23 – Optimizing the metric used for mapping allows to improve the signal to noise ratio. Spectra on defective and pristine area (a). (b) shows a map of the 60% spectral weight width of the A'_1 area. (c) details the colorscale. This figure is the same as Figure 3 (c,d) in the main text.

Chapter 5

Enhanced composite silk nano-biomaterial by systemic intake of low dimensional materials

Contents

5.1 Introduction: Nanomaterials integrated into composite silk fibers 165
5.2 Single Walled Carbon Nanotubes (SWCNT) 167
5.2.1 Mechanical properties of SWCNTs 167
5.2.2 Growth of SWCNT by HipCO process 169
5.2.3 SWCNT fibers 170
5.3 Bombyx Mori Silk as high mechanical strength fibers 171
5.3.1 Bombyx mori silk 171
5.3.2 Mechanical properties of Bombyx Mori silk 172
5.3.3 Recent developments in silk fibers 173
5.4 Systemic process of SWCNT silk production 174
5.4.1 Mulberry leaves and Bombyx Mori eggs 175
5.4.2 Spin coating Nopo SWNTs on leaves 176
5.4.3 Cocoon growth 177
5.4.4 Reeling of silk fibers 178
5.4.5 Key observations during the rearing and reeling of SWCNT silk fibers . 179
5.5 Characterization of SWCNT silk 180
5.5.1 Raman spectroscopy on SWCNT silk 180
5.5.2 Scanning electron microscopy of SWCNT silk 182
5.5.3 Transmission electron microscopy on SWCNT silk 184
5.6 Mechanical experiments of SWCNT silk 186
5.6.1 Measurement setup for mechanical strength characterization 186
5.6.2 Critical radius and Youngs modulus 187
5.6.3 Breaking strength versus SWCNT concentration 189
5.6.4 X- ray nano diffraction studies on SWCNT silk 190
5.7 Conclusions and perspectives 196

5.1 Introduction: Nanomaterials integrated into composite silk fibers

Silk is a natural protein fiber produced by arthropods which has been used from the very ancient period to manufacture textiles in the form of sericulture industry by rearing the cocoons of the larvae of several types of worms. Silk produced by Bombyx Mori silkworms is mainly composed of protein fiber, fibroin, that give the material excellent physical and mechanical properties[183] which are held together by an adhesive protein called sericin.

Upon softening of the sericin are obtained the silk fibers of about 10 to 20 micrometers in diameter and are one of the strongest natural fibers found in nature just after the spider silk[184], however the latter is not compatible with industrial production. Owing to this strength and durability, silk has been used from long time as high-end textile fibers for clothing that protects the body from many insect bites that would easily pierce through the normal clothing and is still used today for bulletproof garments.[185]

Enormous amount of research has already led to rapid improvement of silk production and diversifying its uses from biological or technical processing into foams and gels[186], artificial composite fibers[187] or epoxy matrices, silk-based chimaeric hybrid proteins[188], technical applications like novel woven Bombyx Mori natural silk reinforced epoxy composite face sheet/skin for impact testing[189], to wide range of biomedical applications. Along with its impressive mechanical strength, silk is biocompatible and biodegradable which makes it an excellent biomaterial to be used as substrate in a wide range of biomedical applications.[190]

Different ways can be undertaken to functionalize silk with a nanomaterial. The fast and simplest method in post processing is either by mixing after cocoon threading (post treatment of silk fiber) or by feeding the silk worm with specific enhanced food (systemic intake). Systemic intake of chemicals to enhance silk quality or to add new functionalities (color, strength, diameter) has been already used in the past. For example, the silk has been hybridized by feeding the silkworms with dye-containing diet to produce a new class of functional luminescent silk that could possibly find an useful application in biology.[191, 192]

With recent developments in nanotechnology, carbon nanomaterials like 1D carbon nanotubes(CNT) would be the natural choice with impressive mechanical and electrical properties which could nicely integrate into the silk without any structural changes. These SWCNTs(single-walled) have been amalgamated with the silk to form composite scaffolds that has found to promote human stem cell neuronal differentiation.[193] Artificial composite fibers of more than 100 meters in length were already being processed using SWCNT for promising electronic textiles.[194] Regenerated silk fibroin dissolved and mixed with a dispersion of SWCNTs[195] and MWCNTs(multi-walled) [196] are then drawn into fibers by electro-spinning process that show significant increase in Young's modulus and breaking strength.

In recent studies, SWCNTs have been already incorporated with the spider silk by nurturing the spiders with CNT dispersed in water and thus obtained spider silk has been found to be strongest till date with the mechanical strength matching the material like Kevlar used in bulletproof applications[20]. Though the spider silk has slightly better mechanical properties than Bombyx Mori silk, the obvious disadvantage of this process is the industrial scale production whereas the sericulture is one of the oldest and evolving industry related to the mass production of the silk.

In the first attempt with Bombyx Mori, the MWNTs were sprayed on the food of the

silkworms to get the CNT integrated silk fibers by a natural process which shows enhanced mechanical, thermal and electrical properties.[124] More recently the silk has also been reinforced similarly with the SWNTs that exhibits superior mechanical properties in terms of fracture strength and elongation at the break.[197]

Although silk has been also touted to be made electrically conductive by heavily doping it with SWCNTs using methods discussed before, a step of carbonization is necessary to obtain such conductance, which strikingly affect the mechanical resistance of the fiber[197]. Even though all these studies indicate that the mechanical strength of the CNT enriched silk is enhanced, we present here for the first time the influence of the dose intake of CNTs on the silk mechanical properties directly produced by the silk worms.

In the present experiment, we use small diameter, HiPCO -type Single-Walled Carbon nanotubes which are mass-produced in Nopo nanotechnologies, Bangalore. They are incorporated into silk by tuning the dose concentrations and we are then measure the enhancement of their properties such as Young modulus, breaking strength, and finally could make them electrical conductive.

5.2 Single Walled Carbon Nanotubes (SWCNT)

Carbon nanotubes are cylindrical nanostructures made of sp^2 hybridized carbon atoms belonging to the structural family of fullerenes and graphene. These nanotubes of carbon can be single-walled or multi-walled, with a large dispersion of possible structure caused by the infinite way of wraping a sheet of graphene leading to armchair, zigzag or chiral structures. From the wraping symmetry, emerge the electronic properties, which can be metallic or semiconducting. It has extraordinary thermal, mechanical and electrical properties which has led to boom in its usage in research areas such as the nanotechnology, electronics, optics and material science fields. It is possible to grow carbon nanotubes by many processes namely arc discharge, laser ablation , chemical vapor deposition and by high-pressure carbon monoxide disproportionation (HipCo).

HipCo SWCNTs used in our following work are high purity single walled CNTs grown using a reactor that operates at high temperature 900-1100 °C and high pressure of 30-50 bars using carbon monoxide (CO) as carbon source and nickel carbonyl as catalyst. HipCo is a continuous growth process and the SWCNTs thus obtained have been studied for different applications.

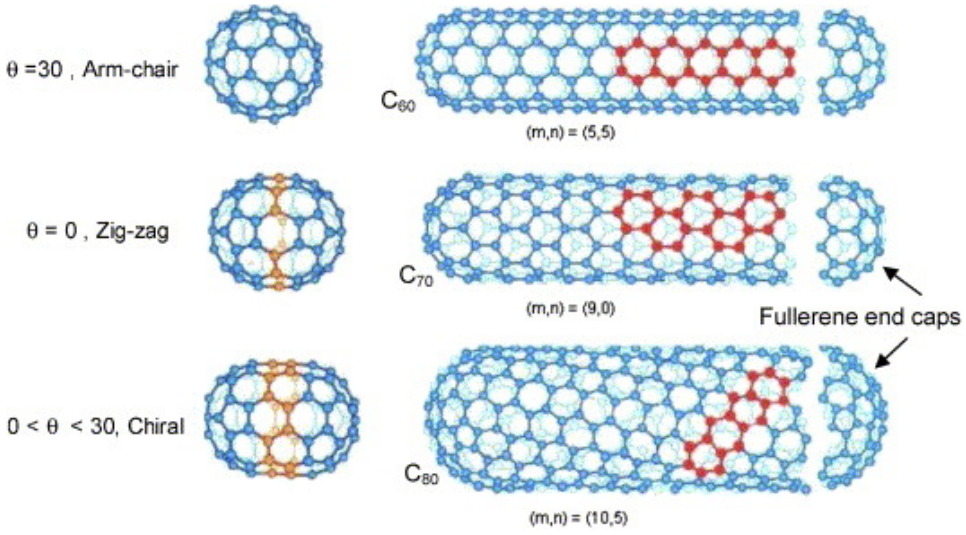

Figure 5.1 – Varieties of single walled carbon nanotubes from top to bottom, armchair, Zigzag and chiral. Figure adapted from [198],[199]

5.2.1 Mechanical properties of SWCNTs

Single walled carbon nanotubes are the strongest material in the world in terms of Young's modulus and tensile strength. Theoretically it was predicted that the Young's modulus to be in the range from 1-5 TPa whereas the tensile strength from 15-50 GPa based on its analogy with mechanical properties of graphite. Surely, the outstanding mechanical properties were derived from covalent bonds of sp^2 hybridization.

While SWCNTs are brittle at low temperature, they are flexible at room temperature. This flexibility is not because of any plastic deformation but due to their high strength and capability to form hexagonal network to relax and release the stress. Hence high breaking strengths were predicted for SWCNTs where they could be used for high strength cum light weight material applications.[200]

Multiple range of papers forecasted that the Youngs modulus for nanotubes were close to 1TPa independent of its type and diameter. It was also envisioned that very large strain could be sustained mainly in the axial direction due to preferred strain-releasing mechanisms. It was also found out that strained SWCNT easily releases the strain energy by nucleation of defects and dislocations beyond a critical tensile strain of about 5%. Studies were also conducted to analyze the kind of dislocations involved. In these strained SWCNTs, defects such as spontaneous formation of double pentagon–heptagon pairs were formed. These single pentagon–heptagon pair defects were found to act as nucleation centres for further possible dislocations.

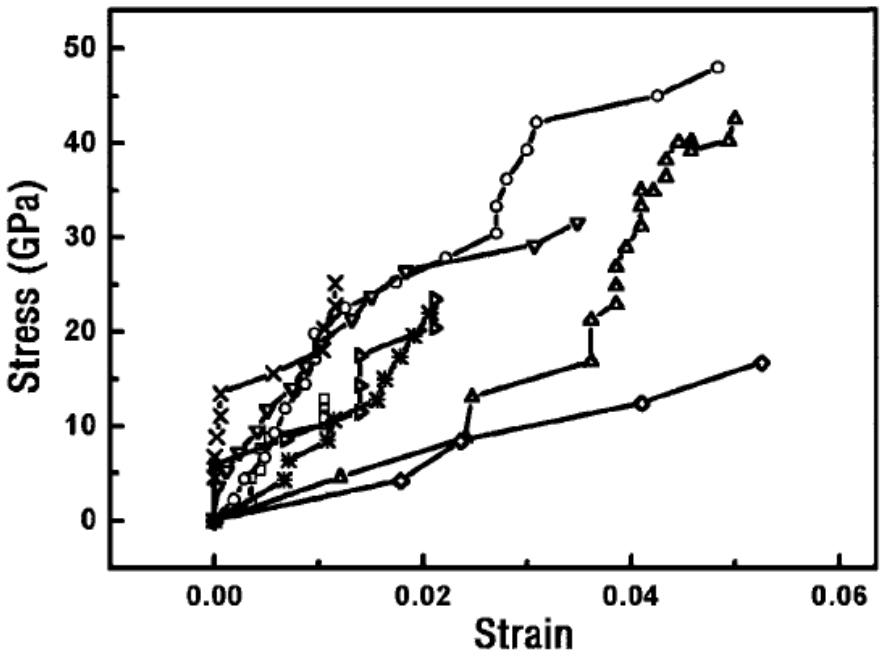

Figure 5.2 – Eight stress versus strain curves obtained from the tensile-loading experiments on individual SWCNT ropes. Each rope diameter is measured at high magnification in the SEM, accuracy a few nm. Figure adapted from [201]

The major mechanical experiments were executed by Yu et al.[201] in 2000 where they performed stress-strain measurements on individual arc-MWNTs inside a electron microscope. In this scanning electron microscope, SWCNT ropes were tensile loaded to a nanostressing stage which is incorporated with an AFM probe that can provide a deflection of upto 150μm and a force of around 0.1N. They executed experiments on 8 of these ropes where δL as a function of applied load was measured and hence the strain was obtained as δL/L. Based on this experiment, they caluclated the average Youngs modulus to be in the range of 320 to 1470 GPa and average breaking strength of about 13 to 52GPa. At the breaking point, the maximum breaking strain values for these SWCNTs were around 5.3% or lower.

5.2.2 Growth of SWCNT by HipCO process

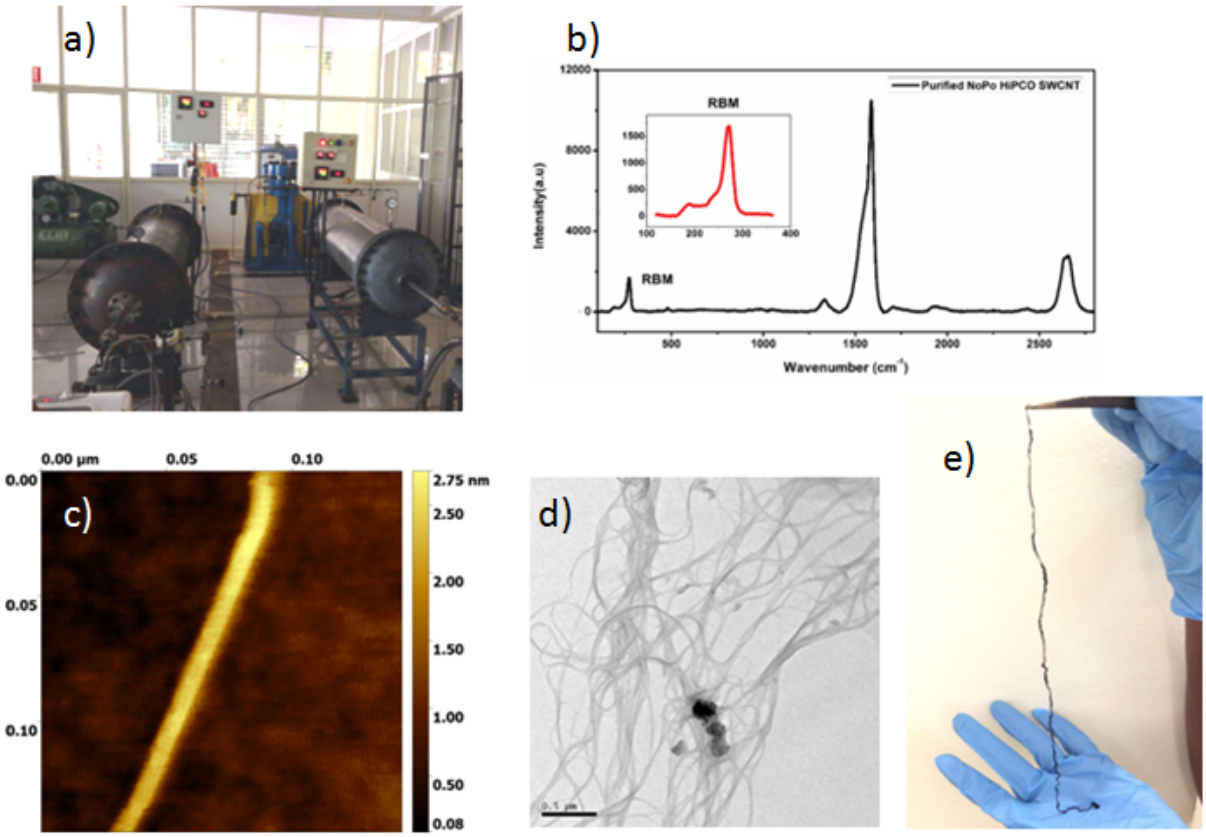

Figure 5.3 – a) Growth of SWCNTs by HipCO process in Nopo nanotechnologies, Bangalore. b,c,d) Raman, AFM and SEM characterization of the as grown SWCNTs.e) Macroscopic fiber resulting from the as-grown product.

The High Pressure Carbon Monoxide (HiPCO) process developed under the guidance of Dr. Richard Smalley was very promising development for the growth of SWCNTs [202]. The material is very well studied[203], its properties and chemistry are well known making it a perfect starting material for generating composites. HiPCO-type SWNT are characterized by their well-defined and interesting features, such as their narrow diameter (0.6-1.2nm) homogeneity and low density of metal impurities. The main difficulty is to ramp up the production and quality control in order to reach industrial grade.

Nopo have developed a new HiPCO technology that is rugged, scalable, safe, reliable, capable of producing 200g/month of SWNTs with defect and catalyst content less than 0.1% material. The production has been doubling every 2 months. They first developed a continuous Iron Carbonyl and Nickel Carbonyl Generator that uses Monds process with feedback from a chemiluminescence detector to produce small amounts of catalyst on the fly. This eliminates the need to store toxic metal carbonyls as they are produced in-situ.[204]

Nopo eliminated quartz and ceramics as structural materials as they were deemed unsuitable for scaling. After evaluation of several high temperature alloys, they have zeroed in on a nickel based alloy as the structural material of the reactor. It exhibits excellent resistance to metal dusting attack. The reactor has been operated at pressure between 20-30 Bar and temperature between 900-950 $^{\circ}$C. To ensure rapid mixing of gases, they have developed a new injector that mimics a turbine like gas flow without the need of a physical turbine.

Material is collected using a dual 1-micron microglass cellulose filter supplied by 3B filters. The NoPo HiPCO reactor has consistently produced material with G/D Raman Peaks ratio above 50 as measured on a25 532nm Raman Spectrometer from EnWave Optronics. G/D ratios of 90 and above have been observed in a few instances. Catalyst content as measured by TGA is between 4-10 wt%. SWCNT content by weight is over 75% for as produced raw material. An interesting observation is the high reactivity of the material. Significant increase in defects during brief periods, 30s of ultrasonication and in the presence of dilute acids has been noticed. The enhanced reactivity could be useful in fabricating devices and dispersing the material. The as-prepared SWCNT is mechanically sieved through micro porous sieve to remove the amorphous carbon that are produced because of carburization on the metal with 99% carbon content.

5.2.3 SWCNT fibers

As explained in the section before, SWCNTs have high strength and high Young's modulus where these properties would be advantageous to enhance the mechanical properties of other materials like polymers. They are the highly desirable and potential candidates to improve the properties of the conventional reinforcement fibers. The production of these nanoscale composites leads to special challenges. There are many important requirements when it comes to the preparation of these enhanced effective reinforcement fibers. These parameters include high aspect ratio, excellent dispersion, interfacial load transfer and alignment of the nanotubes. To improve the mechanical property of the SWNT reinforced fiber, possesing a high aspect ratio of SWCNTs is very important. This allows the effective load transfer from the polymer to the nanotube.

Intrinsically nanotube should remain stable without any defects or dislocations and also not creating further any defects during the functionalization. The surface area of the SWCNTs are very efficient when it comes to interface stress transfer but there might be a problem if it induces undesirable attractive forces among SWCNTs themselves forming agglomorates. The adhesion between the matrix and the SWCNT plays a key role for effective load transfer. When adhesion is not good enough, it cannot sustain high load and the advantage of high tensile strength property added by SWCNTs could be lowered or worsened.

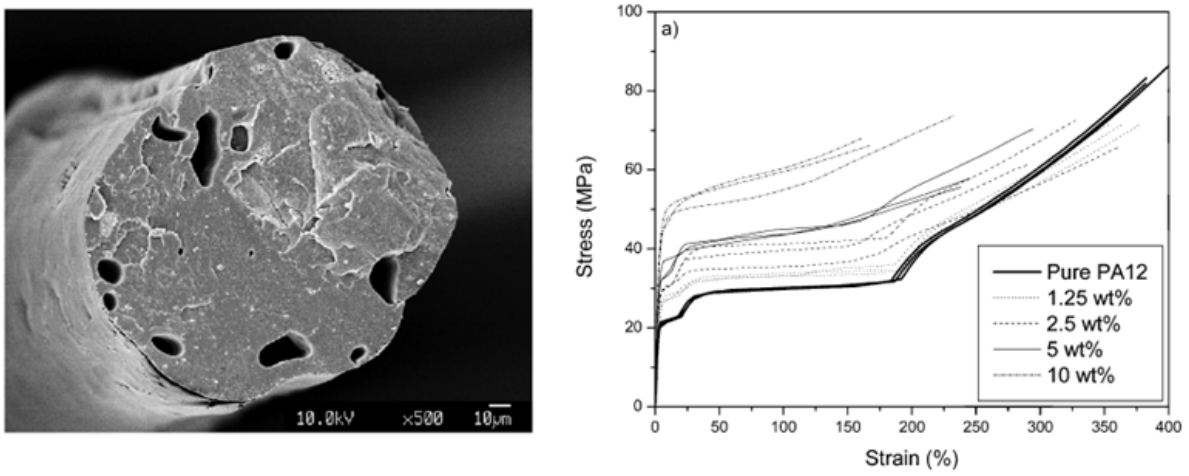

Figure 5.4 – (left) SEM image of nanocomposite fiber with carbon nanotubes. (right) Nominal stress–strain curves with increasing filler weight content obtained under stress control at 30 °C for nanocomposite fibres containing nanotubes. figure adapted from [205].

To increase the mechanical properties and also conductivity in some cases, SWCNTs were used as filler in the polymer composite fibers[206]. Composite fibers have potential in wide range of applications. SWCNTs have been dispersed into solution or melt of the polymer and have been drawn into fibers. SWCNTs have been sucessfully dispersed in polymers such a PMMA, polyamide-12, polypropylene, polyvinyl alcohol (PVA) to name a few[205]. In one of the reported experiment, the arc-grown carbon nanotubes were dispersed in polymer matrix of polyamide-12 at different concentrations and were spun into fibers. The SEM image of one such fiber is shown in the figure 5.4. The stress-strain plot of performed tensile load test is also shown in the figure 5.4. It could be seen that the composite-nanotube fibers with higher concentration of nanotube have superior mechanical properties compared to the composite fibers without nanotubes.

5.3 Bombyx Mori Silk as high mechanical strength fibers

Bombyx Mori silk is a natural protien fiber obtained from the cocoons of the Bombyx Mori silk worms. Its a very common fiber used in textiles and hence produced in abundant quantities. The structure, mechanical properties have been well studies over the years. Due to its strong mechanical strength, it has been used in many different industrial applications such as textiles, fabrics, parachutes etc. Its is an excellent biomaterial where it is both biocompatiable and biodegradable. Therefore its used in medical applications such as non-absorbable surgical sutures, tenson tissue enginnering and drug delivery systems. In this section, we explain in detail about the structure of the silk, mechanical properties and recent developments in silk that have taken place to improve its properties.

5.3.1 Bombyx mori silk

Bombyx Mori silk is the most common silk that is used for different suitable applications. It is one of the strongest natural fibers available. In the raw form, a pair of primary fibroin filaments called brin are held together by gluing agent sericin. The whole structure is callled as bave. This fiber when produced by the silk worms would be in form a cocoon composed of 700-1500 m in length and 10-15 μm in diameter. Each fibroin is built from twisted bunches of nanofibrils which are of 20-30 nm in diameter. Further a fibroin is made up of heavy (H) chain of 390 kDa and a light (L) chain of 26 kDa connected by a disulfide bond, along with a glycoprotein named P25 (30 kDa).

Nevertheless, structural analysis studies point out that silk fibers are composed of crystalline units of β- sheet protien embedded in a less ordered semi amorphus matrix along with the random coils.[207] XRD and NMR studies indicate that these β crystallites are aligned with the peptide chain along the axis of the fiber.[208] These β sheets along with the hydrogen bonds, Van der Waals and hydrophobic components between their intersheets give a stong stability to the fiber structure.

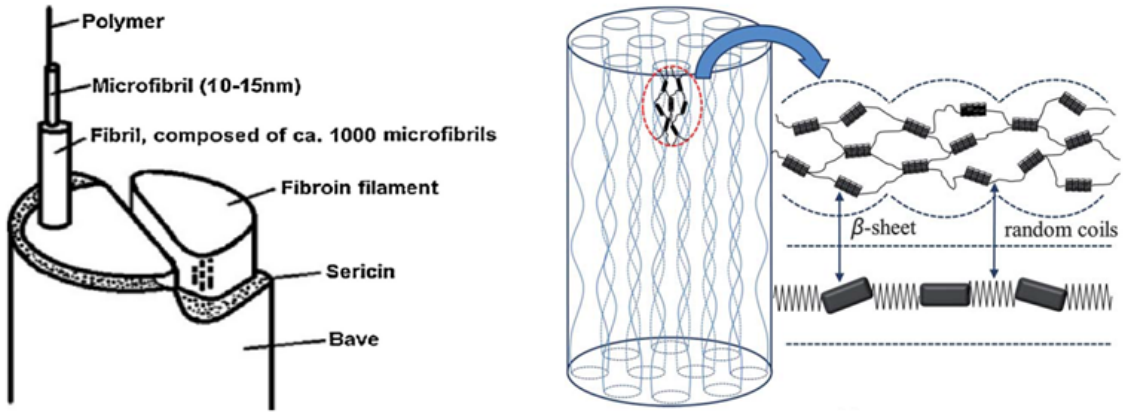

Figure 5.5 – Structure of the Bombyx Mori silk fibers. Figure adapted from [189],[209]

5.3.2 Mechanical properties of Bombyx Mori silk

Bombyx Mori silk has astounding mechanical properties like high tensile strength, large breaking strain and high toughness exceeding the different available synthetic fibers. These superior mechanical properties are due to the main structral component β sheet crystallites. Several experimental studies were conducted on Bombyx Mori silk to study the mechanical properties such as Young's modulus, shear modulus, yield stress and tensile breaking strain under different conditions.

Load extension test performed on the silk fibers usually provides the tensile properties in the form of a stress-strain plot. A typical stress-strain plot is as shown in the figure 5.6. From this stress-strain curve, for one such experiment conducted, we could obtain different parameters from the curve.[189] The parameter such as Elastic region, Plastic region, Elastic modulus/ Youngs modulus, Yield point and breaking point/strength could be invesitgated from the obtained curve.

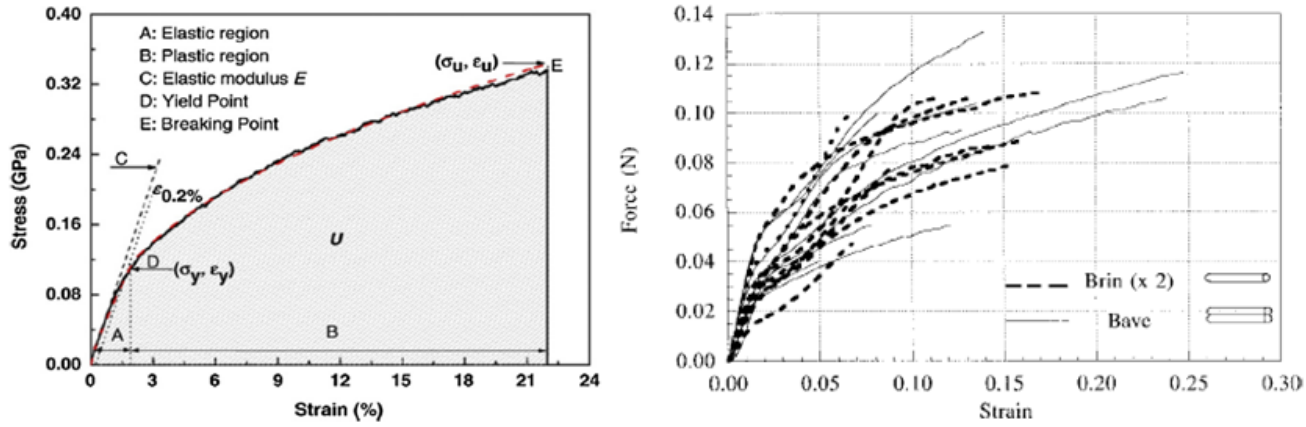

Figure 5.6 – (left) Typical stress-strain plot obtained in the tensile load experiment[189].(right) Stress-strain curves for Bombyx Mori silk bave and brin.[183]

The comparison of mechanical properties along with other natural and synthectic fibers are listed in the table below.

Material	Youngs modulus (GPa)	Tensile Strength (MPa)	Breaking strain (%)	Toughness (MJ/m3)
Bombyx Mori silk	10-17	300-740	4-26	70-78
Spider silk	10	1100	16-38	200
Wool	0.5	200	50	60
Nylon	1.8-5	430-950	18	80
Kevlar	130	3600	2.7	50
Polypropylene	4.6	490	23	-

During these tensile load experiments, usually average diameter of bave or brin is taken into account to obtain the stress-strain curves. This is not desirable as the diameter is highly varying across the length of the fiber. Scanning electron microscopy confirms that the diameter of the fibers are varying with more than a factor of two. Another problem is the presence of patches of sericin even in the degummed fibers. These are the two important points to be considered during the characterization of the tensile loading.

In our tensile load test (explained in the mechanical characterization section), we have considered another parameter called minimal radius where the highest amount of stress would be accumulated. The same minimal radius is used during the calculations of the stress-strain curves. The second problem of the sericin residues remain, as the silk is produced from conventional textile yarn industry. Better methods and processes to obtain sericin free silk needs to be investigated. Further mechanical properties depend on several factors such as feeding, rearing conditions and spinning or reeling process.

5.3.3 Recent developments in silk fibers

Several methods have been utilized to enhance the mechanical properties of the silk. The silk worms have been genetically transformed where a gene sequence from spider silk has been incorporated in silkworms to improve the tensile performance. Degummed silk have been dissolved into a fibroin solution and artificially drawn into reconstructed and regenerated silk fibers for different applications. But it has been found that natural silk fibers have superior properties than the artificially reconstructed ones. Further other polymers have been cross linked to form a composite fiber for mechanical enhancements.

A wide range of regenerated silk scaffolds such as fibroin sponges, fibroin hydrogels, fibroin films, fibroin mats etc have been demonstrated for different applications. Similarly silk has been functionalized with drugs, peptides, fluorescent protiens, antibodies, enzymes, conductive polymers, and nanoparticles to improve one of their functionalities. Fluorescent colored silk has been constructed by genetic modifications where fluorescent color gene was inserted into the silkworm genome. In this method, fluorescent colored silk cocoons have been produced with more or less the same mechanical properties.[192]

To take a step further, to enhance the mechanical properties of the silk, in-vivo upload of the components into silk have been demonstrated by natural methods. Silkworms haven been fed directly with nanoparticles, molecules etc where these components reach the silk within the glands so that it can interact with the silk protein in the gland itself. In particular, citric acid (CA) molecules were mixed with mulberry leaves at 0.05 wt% and were fed to the silkworms directly. Thus obtained CA-silk has been recorded to have significantly enhanced mechanical properties. Tensile load testing have shown that CA-silk features remarkably short crystallites rendering the silk mechanically strong and tough.[210]

Very recently, with the advent of nanomaterials, such as carbon nanotubes, have been incorporrated into Bombyx Mori silk[197] and spider silk [20] by similar natural methods. Carbon nanotubes being the strongest and toughest material was expected to enhance the mechanical properties of the silk significantly. These experiments indeed reported that there is remarkable enhancement in the tensile properties of the silk. The same approach has been extended in this thesis where single walled carbon nanotubes (SWCNT) with different concentration have been incorporated in the silk by a systemic approach explained in detail in the next section.

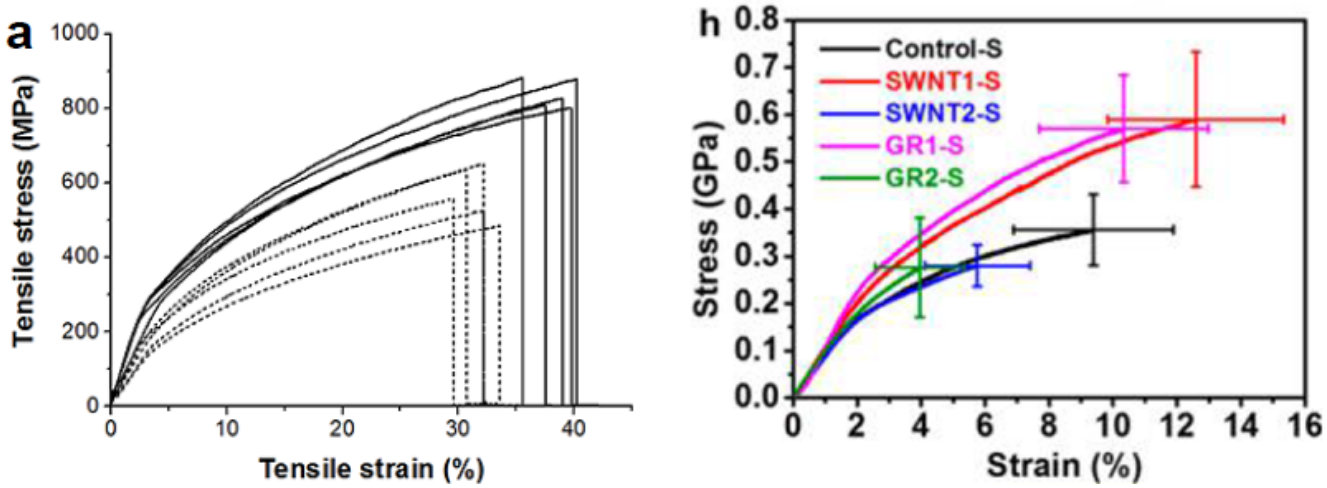

Figure 5.7 – Stress-strain plots for CA-Silk(left) and SWCNT-silk(right) showing superior mechanical properties when incorporated with SWCNT.Figure adapted from [210],[197]

5.4 Systemic process of SWCNT silk production

In this thesis, the SWCNT Silk fibers are produced in a natural systemic process. In this process, we use the purified SWCNTs grown using HipCO process. These SWCNTs are sprayed on the mulberry leaves and fed to the Bombyx Mori silkworms. The silkworms eat the SWCNT doped mulberry leaves for about 2 to 3 days. After the leaf consumption stage stops, they start producing the silk fibers around them in the form of the cocoons. These cocoons after certain matrurity level are reeled into silk where the SWCNTs are embeded into the fiber matrix of the silk. The hence obtained silk is called as SWCNT silk.

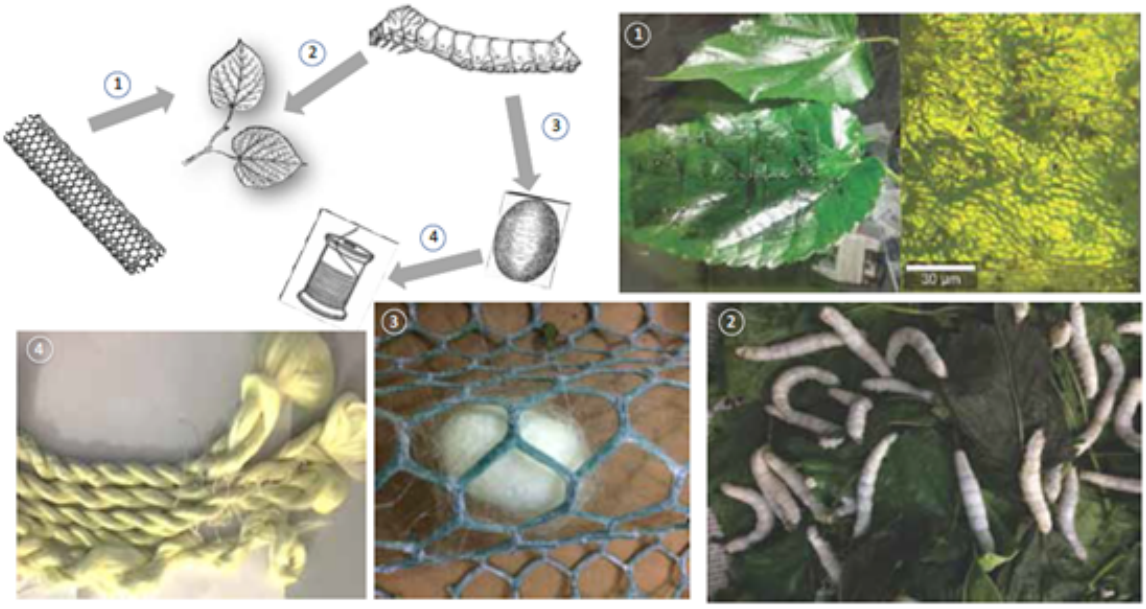

Figure 5.8 – Schematics of the principle for the production of Single Walled Carbon Nanotube(SWCNT) enriched silk. The numbers refer to each steps of the process with picture of the setup used 1) SWCNTs dispersed in Iso-Propyl-Alcohol solution is sprayed on mulberry leaves and blow dried before given as food as feed. Optical image of a mulberry leaf coated with SWCNTs. 2) Bombyx Mori Silkworms feeding on SWCNT coated mulberry leaves. 3) Formation of cocoons by silk worms kept in a mesh kind of structure 4) SWCNT enriched silk fibers obtained after the reeling process.

5.4.1 Mulberry leaves and Bombyx Mori eggs

Mulberry leaves were freshly plucked from mulberry plants and stored in a thread-sack by spreading water on the sack. The leaves were wiped properly with tissue paper to remove all trace of water before feeding them to silk worms since silkworms are allergic to water. The worms were separated into different batches in different trays having 70 worms in each. One of the batch of wiped mulberry leaves were fed directly to the control worms without further treatment.

Figure 5.9 – Mulberry leaves arranged in different batches as the feed.

5.4.2 Spin coating Nopo SWNTs on leaves

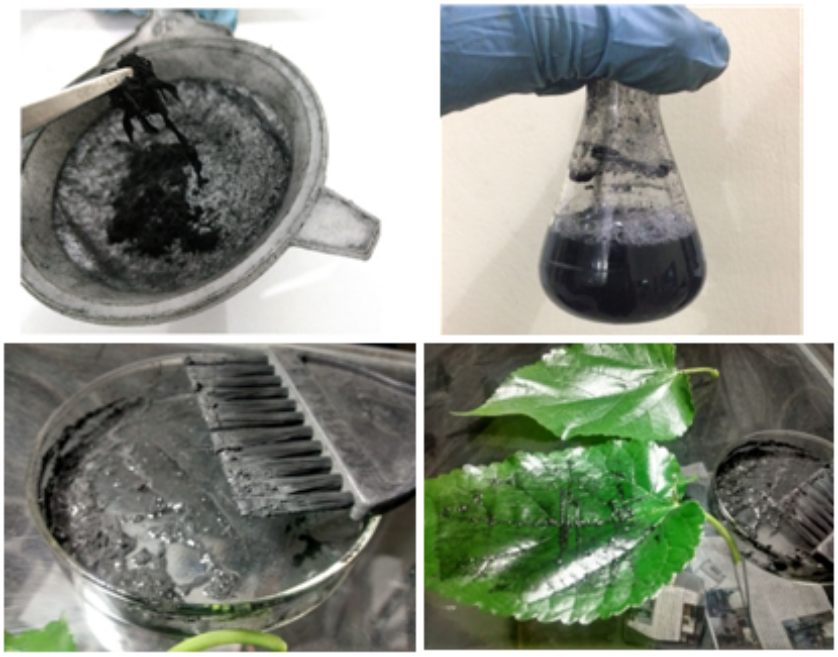

Figure 5.10 – Mulberry leaves coated with purified SWCNT.

The as-prepared SWCNT is mechanically sieved through micro porous sieve to remove the amorphous carbon that are produced because of carburization on metal. Different concentration of nanotubes pastes (0.001, 0.01, 0.05, 0.1, 0.5, 1 wt. %) were prepared. To prepare them, in detail, 0.001g, 0.01g, 0.05g, 0.1g, 0.5g and 1 g of single walled carbon nanotubes (SWCNT) were weighed and taken in a 100 ml flask. 20ml of isopropyl alcohol (IPA) was added to each of

them. The SWCNT and IPA mixture was sonicated for 5-10 min keeping the sonication bath at room temperature. Once the SWCNTs were dispersed well, the resulting solution were coated over thoroughly wiped mulberry leaves using a hair dye brush and were allowed to dry.

5.4.3 Cocoon growth

Once the IPA evaporates from the leaves, the control and obtained SWCNT coated leaves were fed to silk worms. The silk worms were fed thrice a day with the leaves. The silkworms do not tolerate high temperature, high humidity and poor ventilation. The temperature of the room was maintained at 23 ˚C using wall mounted A/C.

Figure 5.11 – Mulberry leaves coated with different concentration of SWCNTs fed to the silk worms in different batches.

Once the silk worm reaches its final stage the color of the worm turns yellowish. The behavior of the worms also differ. They stop eating the mulberry leaves. Once this behavior is noticed, they are transferred to another tray which is prepared for formation of cocoons. Once the moth is transferred to the tray, they start to make web network with the near walls. In the course of 4 days they make the complete form of cocoon. The weight of cocoon varies from one another. The average weight of a single cocoon is approximately 2g in the case of normal (control batch in this case) silk worm. If we leave the cocoon for long time such as 10 days or more after the mature state, it forms a kind of liquid and brakes the shell and comes out.

Figure 5.12 – Process of formation of coccoon.

5.4.4 Reeling of silk fibers

The cocoons reared by NoPo technologies, Bangalore were prepared and reeled at at CSTRI, Bangalore. The cocoons were dried in hot air drier at 100 ˚C for one hour. Then the cocoons were conditioned for one day. Later the cocoons were cooked using two pan cooking system following low-high low method to soften the sericin and then brushed at 85 ˚C to find the true ends from the cocoons. The cooked cocoons were shifted to reeling basin to conduct the reeling.

CSTRI Multiend reeling technology: The cooked cocoons were transferred to reeling basin. About 7 cocoons were accumulated and passed through Jetteboute, porcelain button, croissure pulleys, traverse guide on to small reels. During the passage the raw silk is taken on croissure pulleys to form tavallette type of croissure to remove excess water from raw silk, harden the sericin and to impart circular cross section in raw silk. The raw silk is continuously reeled by maintaining required number of cocoons through out the process of reeling by the reeler. During the process of reeling in CSTRI multiend reeling machine the following parameters were maintained.

1. Reel speed : 100 - 120 meters/min.
2. Croissure length : 8 - 10 Cm
3. Reeling basin water temperature : 40 ˚C
4. Good quality reeling button with appropriate hole size developed by CSTRI.

The raw silk thus reeled on small reels are converted into standard size skeins in CSTRI closed type re-reeling machine after reel permeation. The silk skeins thus produced are removed from re-reeling machine and skeinned and weighed.

Figure 5.13 – Silk obtained after reeling.

5.4.5 Key observations during the rearing and reeling of SWCNT silk fibers

The first observation during the growth of the silk worms was that for the lower concentrations (0.001, 0.01 and 0.05 wt. %) of SWNT the death rate of the silk worms were very similar to that of control but as we increase the concentration (0.1, 0.5, 1 wt. %) of SWNT the death rate of the silk worms significntly decreased. This was thought to be due to the non-toxic effect of single walled carbon nanotubes. While the worms grew up, the worms that were fed with SWCNT appeared thinner than the control.

Adding to this, control worms consumed the mulberry leaves completely whereas the SWNT coated leaves were not completely consumed by the worms almost leaving 1/8th of leaf unconsumed. One reason could be that the leaves dry faster. We keep the leaf for drying, so as to evaporate all the alcohol that is used during the coating process. These dried part of leaves are not eaten by the worms. Also, it could be due to the nanotoxicity of the SWNTs that were added on the leaves.

SWCNT wt% coated	**No. of worms expired**
Control	12-15
0.001	12-15
0.01	13
0.05	12
0.1	7
0.5	3
1	0

Further, it was noticed that the average weight of cocoon varies and that the average weight of a single cocoon was 1.5g in case of 1 wt. % SWNT silk and 2g in the case of control silk which also points toward the nanotoxicity of the SWCNTs. A statistics was made by measuring the diameters of the fibers, both control and SWCNT doped fibers. It indicates that both the average diameter and the minimum diameter of the control silk fiber were larger than the SWCNT doped silk fibers.

A table is shown regarding the average diameter and the minimum diameter with respect to the different concentration of SWCNT. It is interesting to note that, while average diameter decreased with the increased concentration of SWCNT, the minimum diameter initially decreased and then had a more stabilized value. These parameters were taken into account in our mechanical measurement analysis.

Silk Type	Average radius (μm)	Minimum radius(μm)	Single cocoon wt (gm)
Control	33	25	1.6
0.001 wt%	xx	xx	1.717
0.01 wt%	31	22	1.858
0.05 wt%	29	21	xx
0.1 wt%	26	18	1.76
0.5 wt%	29	20	1.574
1 wt%	28	21	1.613

5.5 Characterization of SWCNT silk

Once the SWCNT silk with different concentration of SWCNTs is obtained by natural systemic process explained in the previous section, the first and foremost study would be to confirm the presence of SWCNTs in it. Different characterization techniques could be used such as Raman spectroscopy, scanning electron microscopy(SEM), transmission electron spectrscopy(TEM) and also X-ray diffraction(XRD) techniques. These characterization techniques are complementary. While Raman spectroscopy indicates the presence of SWCNT, SEM could give us the texture and surface properties of the fiber. TEM was used to check the possible orientation of the SWCNTs in the fiber. Finally the XRD provides the overall crystallinity and material properties of the fibers which will be discussed seperately in the next section.

5.5.1 Raman spectroscopy on SWCNT silk

Raman spectroscopy was used to confirm the SWCNT presence on the mulberry leaves (see figure 5.14) , in as obtained SWCNT silk fibers and in the excreta of the silkworms compared to that of the control. Raman spectra were registered at the room temperature using a 1mW power 532nm green laser. The G-band SWCNT signature was readily observable on the leaf as shown in the figure 5.14 but was majorly shifted due to doping by possible alcohol used in the solution. Raman was performed on the SWCNT silk at the edges and on the bulk to verify the existence of SWCNTs either protruding out or being embedded into the silk.

We could slightly observe SWNT signature using green laser on the cross section of the fiber at 1615 cm^{-1} along with many other peaks from 1000 cm^{-1} to 2500cm^{-1}. The peaks at around 1085 cm^{-1} is characteristic of the n(C-C) skeletal band of polypeptide chains. Two peaks were also observed at around 1230 cm^{-1} which maybe of amide III groups in π-sheets structured proteins and at around 1444 cm^{-1} as signature of CH_2 bending modes. The peak 1665 cm^{-1} are signature of n(CO) amide I bands characteristic of the π-sheets configuration for the polypeptide backbone. Raman spectroscopy carried out at the cut edges of the fibers clearly pointed the presence of SWNTs. We could observe G+ and G- peak at 1615 cm^{-1} and 2D peak at 2600 cm^{-1} as shown in the figure 5.16 which indicates the presence of SWCNT bundle. Raman spectra on droppings also show the SWCNT signatures but majorly shifted due to doping by many constituent materials and breaking down of SWCNT into smaller parts.

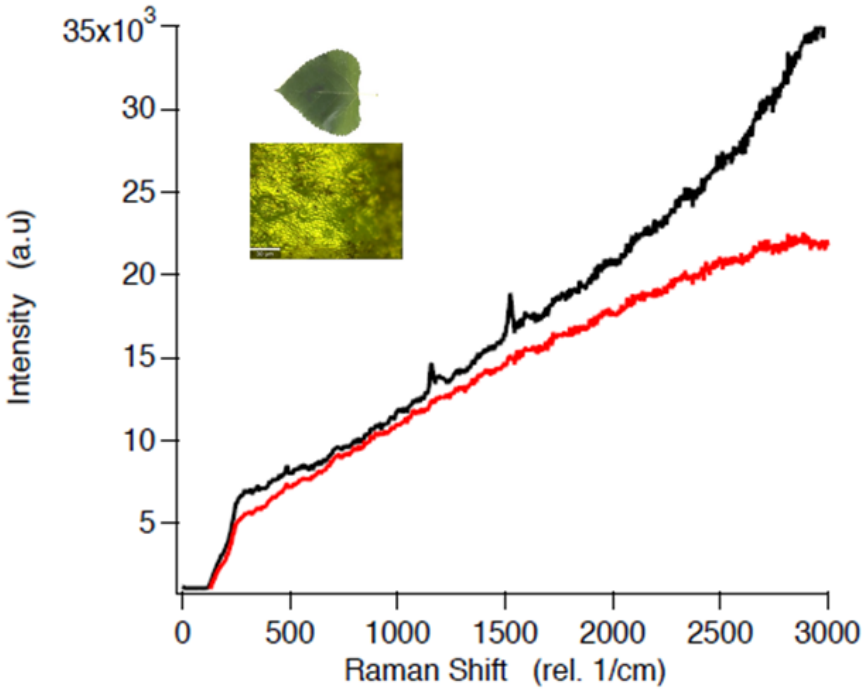

Figure 5.14 – Raman spectra of normal/control mulberry leaf in red and SWCNT coated mulberry leaf in black. (inset) Picture of a mulberry leaf sprayed with SWCNT solution. Optical image of SWCNT sprayed mulberry leaf.

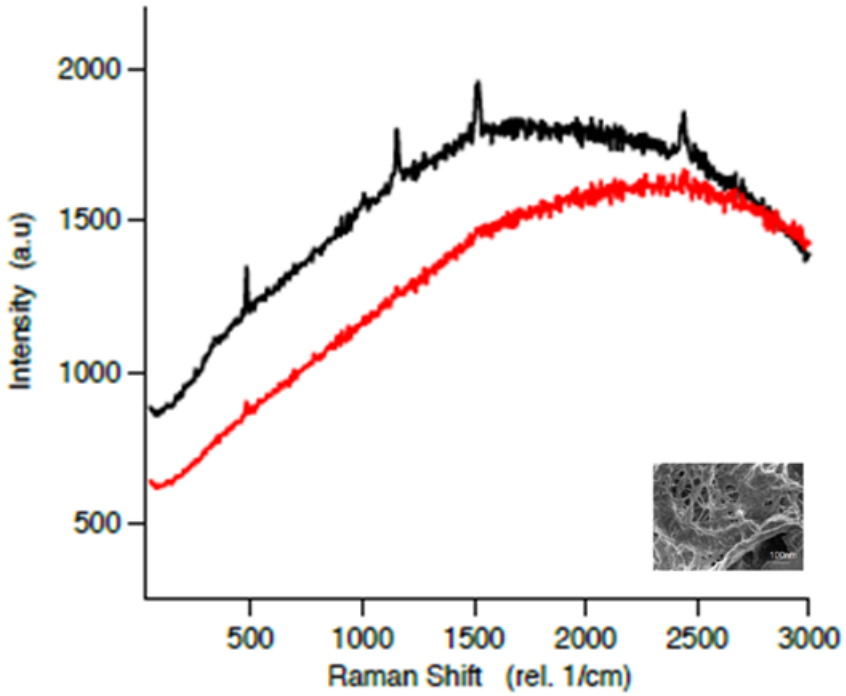

Figure 5.15 – Raman Spectra of the droppings of the worms, enriched with SWCNT (black) vs control (red curve)

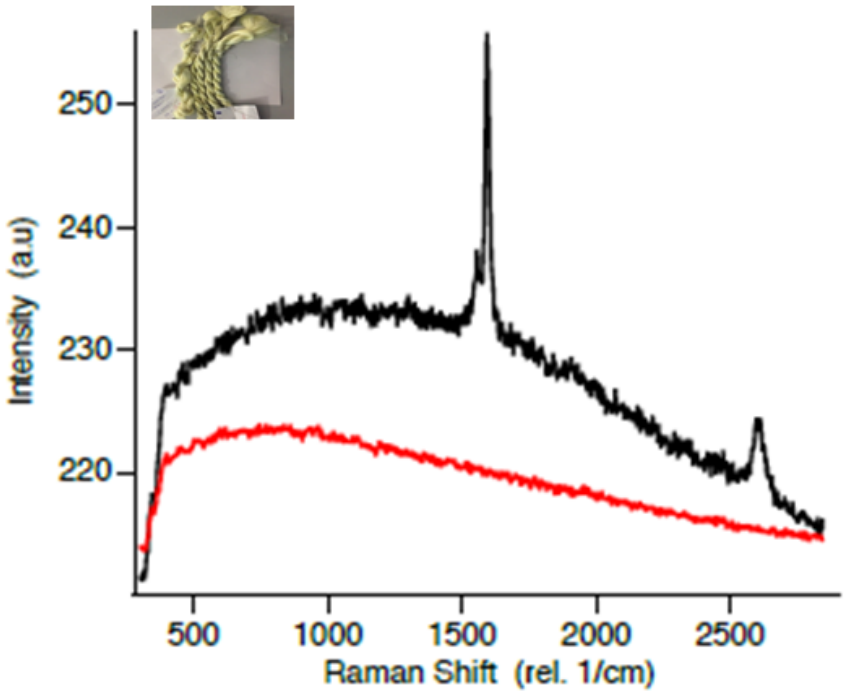

Figure 5.16 – Raman spectroscopy at the cut edges of a silk brin produced by SWCNT-fed worms (in black) compared to control sample (in red) of silk produced at the same time with similar worms but fed with pristine (no-SWCNT enriched) mulberry leaves.

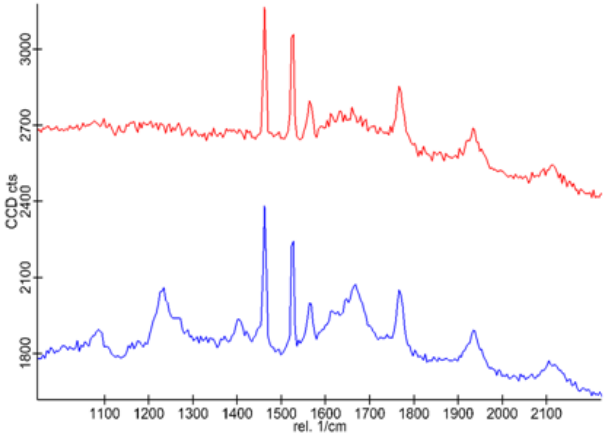

Figure 5.17 – Raman spectroscopy on the surface of a Silk brin produced by SWCNT-fed worms (in blue) compared to control sample (in red) of silk produced at the same time with similar worms but fed with pristine (no-SWCNT enriched) mulberry leaves.

5.5.2 Scanning electron microscopy of SWCNT silk

SEM was performed on silk fibers and droppings with an aim to confirm the SWCNTs and to measure the average diameters of the fibers with various SWCNT concentration. SEM was performed at very low operating voltage of 1.5kV. It was cumbersome to visualize the SWCNTs in the fibers because of the charging effects, but on the droppings a Bucky ball (bundle of CNTs) kind of structure were seen as shown in figures 5.20.

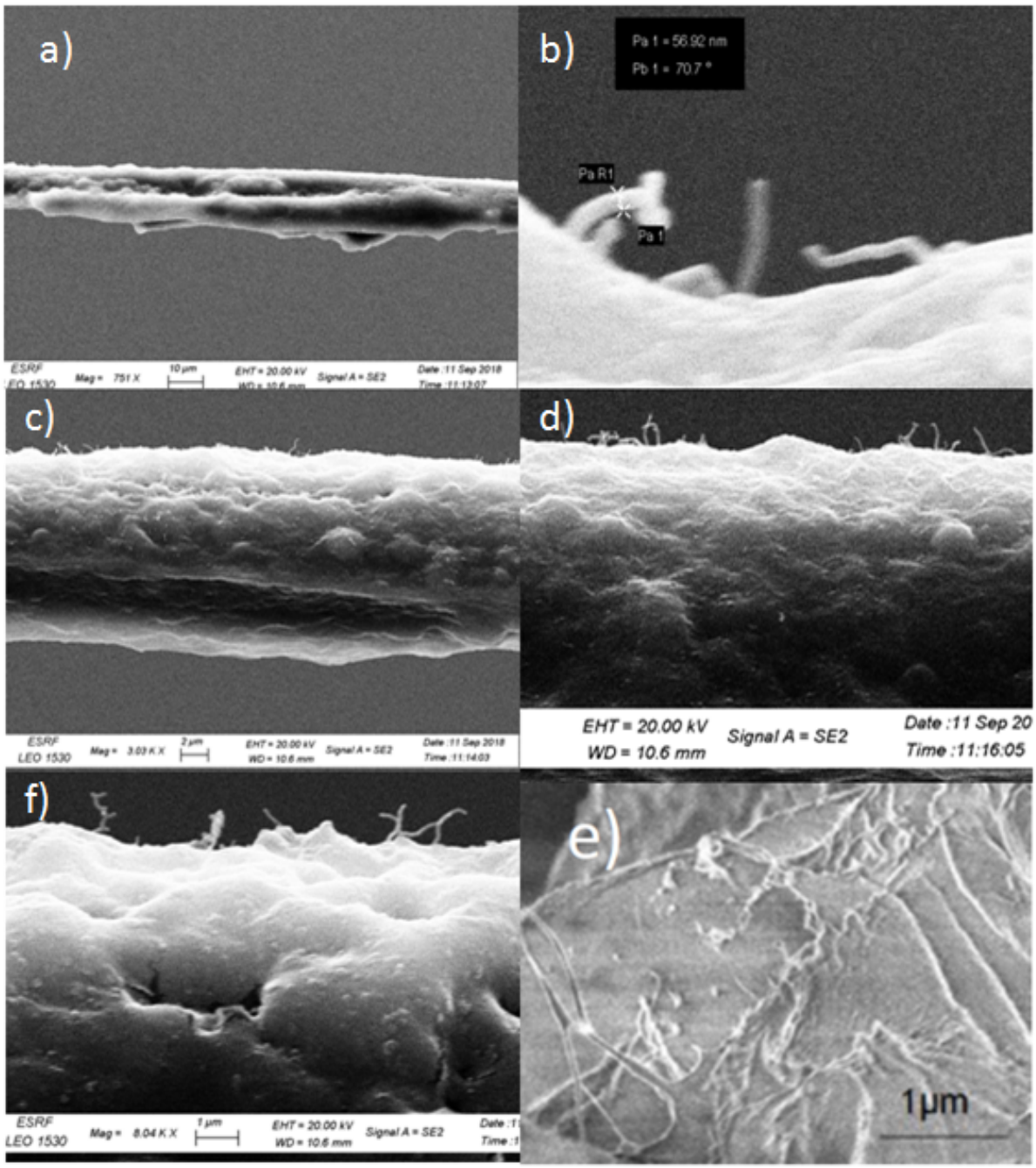

Figure 5.18 – Scanning Electron Microscopy images of SWCNT silk brin surface and sidewalls a) principle of the observation at the surface of a brin shown in SEM image b) zoomed view at the surface c,d,f) large view of the surface e) principle of the observation at the cut edge of a brin shown in SEM image.

In SWCNT silk, as indicated by Raman spectroscopy, the SWCNT bundles were observed at the edges of the silk brin and also on the surface of the silk brin. These features were not observed in the control silk where the SWCNT doping was absent as shown in the figure 5.19. This gives a clear confirmation that SWCNT are present in the silk fibers. The surface of the silk fibers doped with SWCNT were corrugated and non uuniform when compared to the control silk fibers where the fiber surface was smooth and uniform.

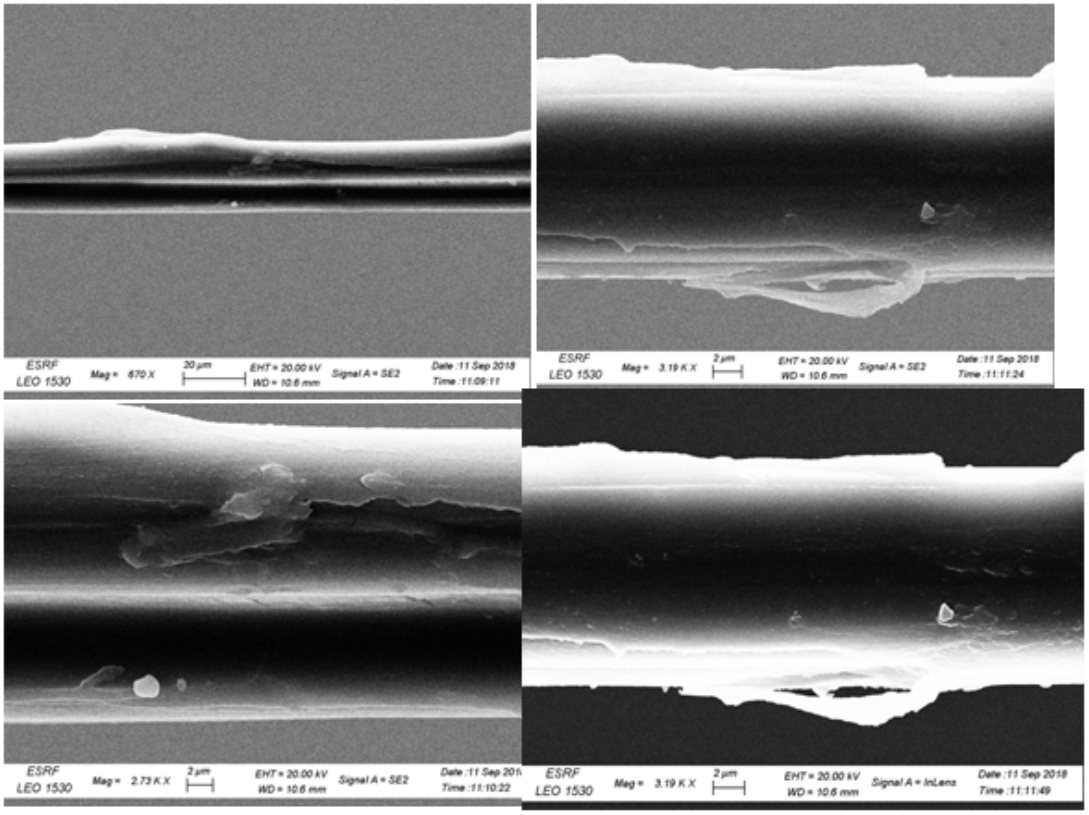

Figure 5.19 – a) Scanning Electron Microscopy image of control silk brin surface and sidewalls

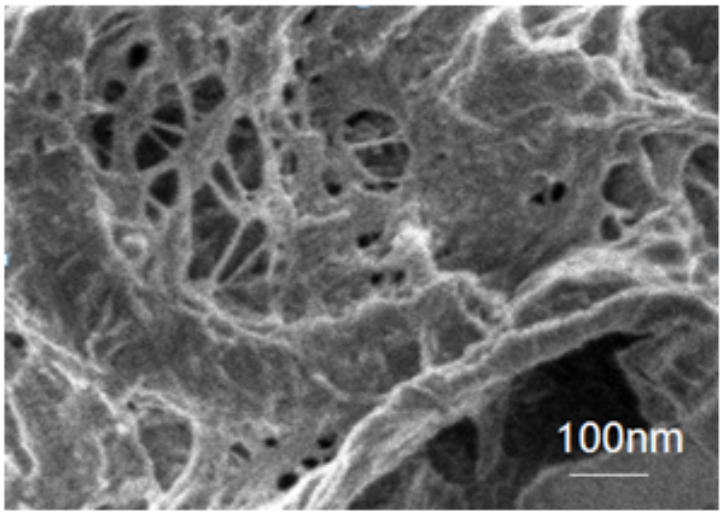

Figure 5.20 – SEM micrograph showing the mesh (bucky paperlike) of carbon nanotubes embedded in the dropping/excreta of worms fed with SWCNT enriched food.

5.5.3 Transmission electron microscopy on SWCNT silk

Transmission electron microscopy was used to observe fine structure of silk with and without SWCNTs. The acceleration voltage of electron beam was 200 kVolt in the FEI Technai microscope. A strand of sample was coiled and stuck with glue onto the TEM grid. A scalpel was used to make cuts on the sample as shown in the SEM image in figure 5.18f. The TEM images in figure 5.21 (a) show that the nanotube-like structures are protruding out of the edges of the silk. The large diameter variation of these structures could be either due to SWCNT bundles

or silk wrapping around some of the SWCNTs. It is difficult to differentiate between silk and SWCNT since both are made of carbon.

It was also observed that these SWCNT structures were also embedded into the silk as shown in the figure 5.21 (b) and (c). We note here that not all tube-like-structures found in the figures could be SWCNTs as many of them could be ripples created due to folding of the silk. However, we found no tube-like-structure either protruding or embedded in the control samples. This is clearly visible in the TEM image of the silk without SWCNTs in the figure 5.22.This indicates that the tube-like structures in figure 5.21 are indeed CNTs.

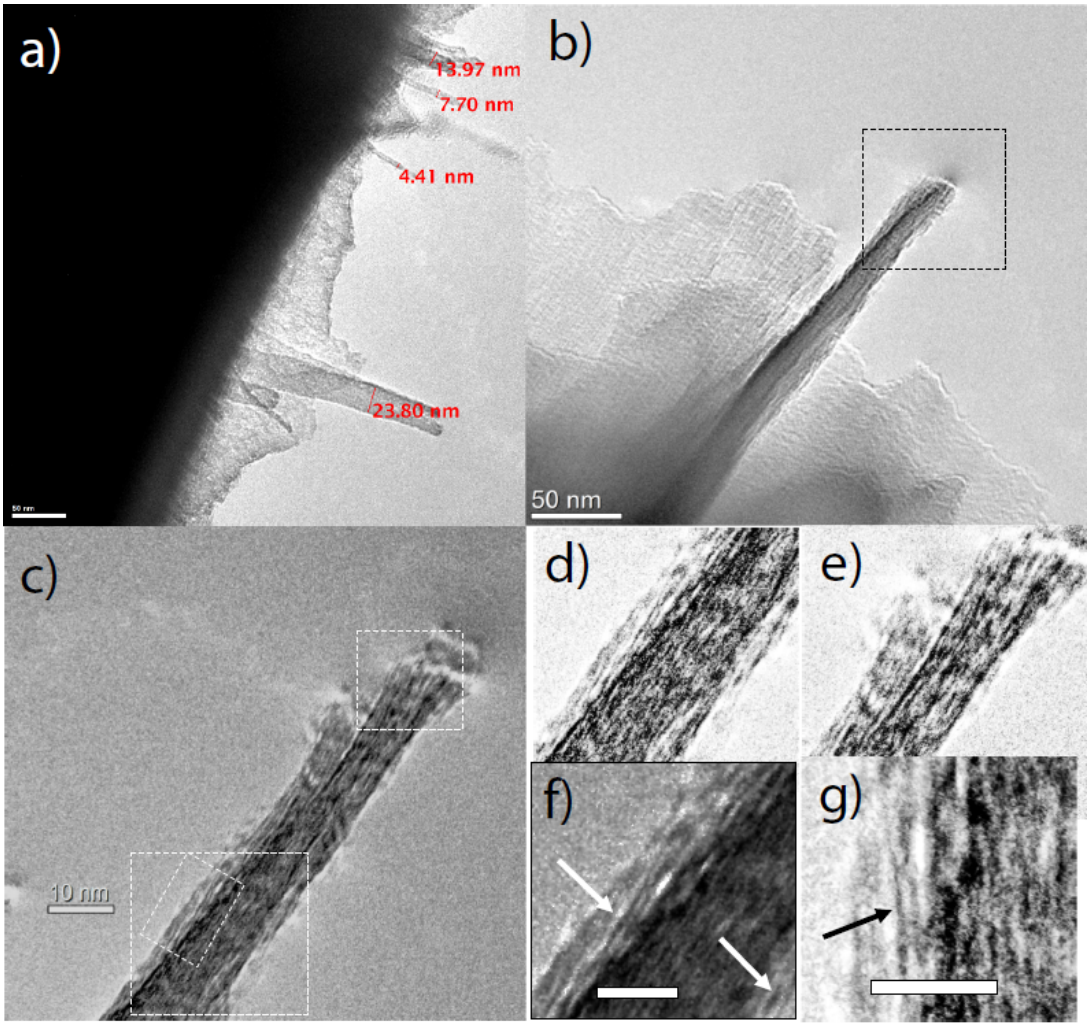

Figure 5.21 – Transmission electron microscopy images of the SWCNT-enriched silk at the cut edges showing the SWNT bundles protruding out the brin cross section.

Figure 5.22 – Transmission electron microscopy images of on control silk samples probed at the edges and cross-section of silk brins.

5.6 Mechanical experiments of SWCNT silk

In this section, we discuss about the tensile loading tests (stress-strain experiments) performed on the fibers obtained corresponding to various concentration of SWCNT fed to silkworms.

5.6.1 Measurement setup for mechanical strength characterization

100cms of length of fibers (7 threads) were obtained by gently pulling with the help of a pair of tweezers from the raw silk with maximal care to avoid the stretching of fibers plastically. One side of each sample was tied to a U-shaped support attached to a wall. The support was held 10 cm from the wall so that the hanging fiber doesn't touch or rest on the wall. The fiber was held vertically so that all the load was imparted through the fiber. The other end of the fiber was tied to a balance with a resolution of 100mg. A black mark was made on the fiber with a graph paper glued to the wall. Gradually the weight was increased in the balance and the corresponding change in the length was immediately recorded. The process of registering the weight vs length change was continued until the fiber elongates and finally breaks. The weight at the fiber breaking instant was also recorded which serves as an important parameter in the study. The experiment was repeated under same circumstances and conditions so as to minimize any possible errors in our calculations and statistics. The schematic representation of the experimental setup used for the mechanical experiment is illustrated in the figure 5.23.

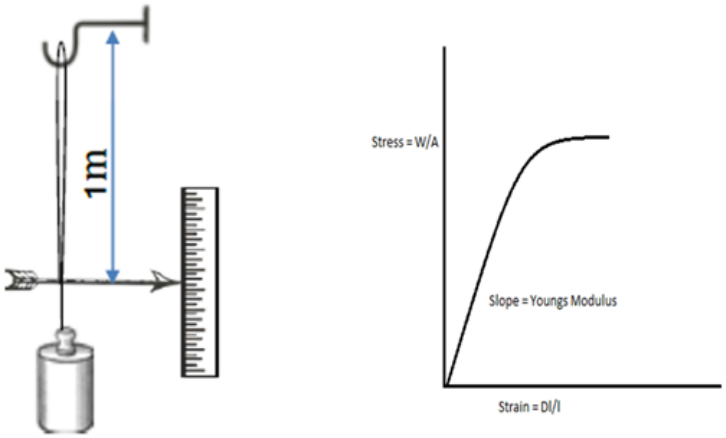

Figure 5.23 – Schematic of the stress versus strain mechanical experimental set up.

5.6.2 Critical radius and Youngs modulus

The obtained silk fibers doped with SWCNTs showed significant improvement in mechanical properties with respect to the fracture strength, elongation at the break and in terms of roughness modulus compared to that of the control silk with no doping. The mechanical properties clearly depend on the concentration of the SWCNTs fed to the silkworms. The plots of mechanical measurements are shown in the figure 5.245.25. While 0.1 wt% SWCNT silk showed fracture strength of 0.6GPa and 14% elongation at the break which is 3 times higher than that of the control silk, the 0.01 wt% SWCNT silk showed fracture strength of 0.35GPa an 12% elongation at the break showing that even slight incorporation of SWCNTs improves the mechanical strength considerably.

These values match with the recent publication made by Wang et al [197] on SWCNT silk, but there is significant improvement in fracture strength, percentage elongation and the toughness modulus in our case considering the concentration of SWCNT used. A table indicating the fracture strength, elongation at break and toughness modulus is shown for the comparison. Further we have assessed the dependence of mechanical properties with respect to doping concentration of SWCNTs in the silk(fed to the silkworms).

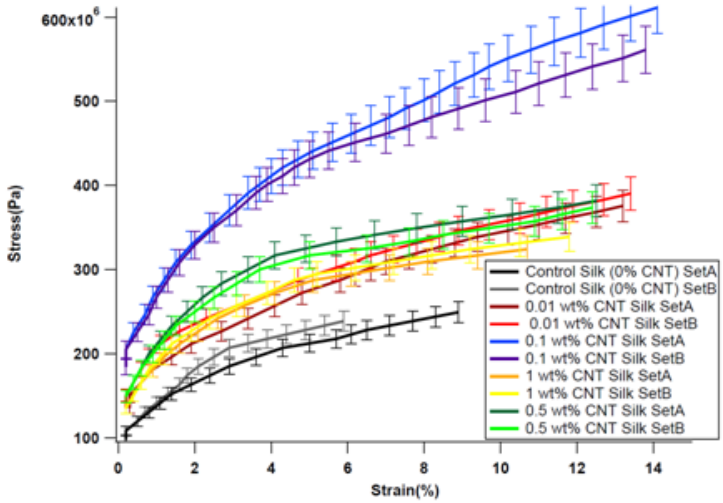

Figure 5.24 – Stress versus strain graph for control and SWNT silk with different concentration of SWNTs fed.

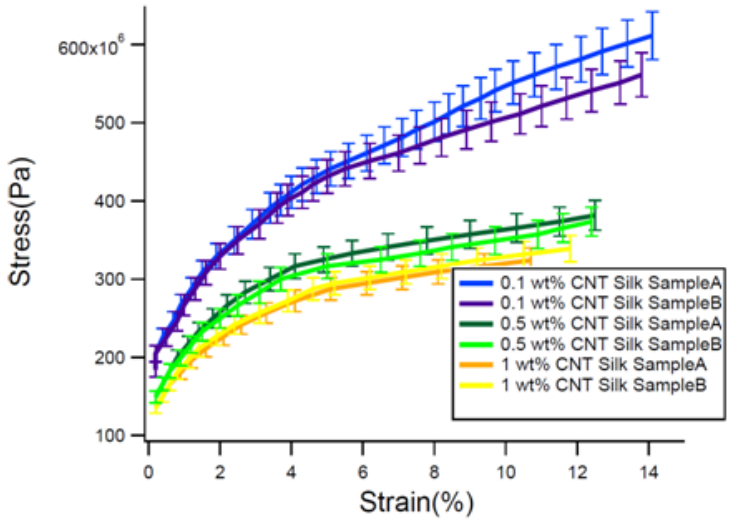

Figure 5.25 – Stress versus strain graph for control and SWNT silk with different concentration of SWNTs fed.

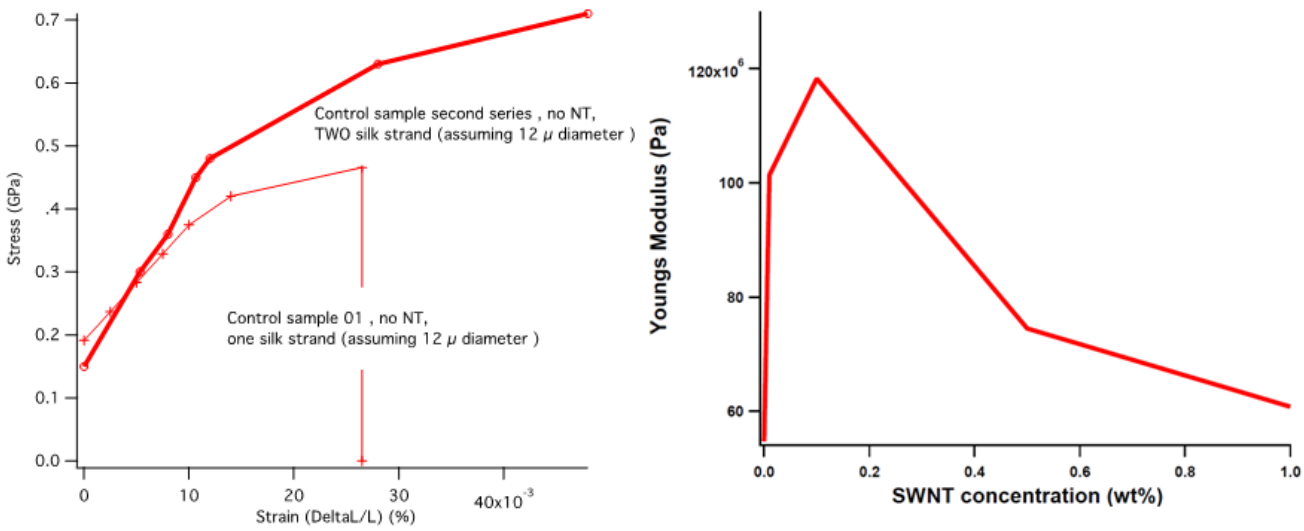

Figure 5.26 – (left) Stress-strain curves for single silk-strand control fiber and double silk-strand control fiber. (right) Plot of Youngs modulus for different concentration of SWCNT.

5.6.3 Breaking strength versus SWCNT concentration

To keep the mechanical experiment simple and minimise the errors we have measured only the breaking strength of the 2 fibers (7 threads in each) stuck together. Figure 5.275.28 is a plot of breaking strength/fracture strength at different concentration of SWCNTs doped into the silk via feeding. The results indicate that the fracture strength increases as we increase the amount of doping up to a certain optimum doping level, later the it decreases and reaches a saturation which is still higher than the control sample. In this particular example, we see that the breaking strength linearly increases and peaks at 0.1 wt% at 1.8 GPa and further above this concentration namely at 0.5 wt% and 1.0 wt%, it tends to decrease and saturate. If we take an average for a single fibre the 0.1 wt% breaking strength value comes around 0.9 GPa which is considerably higher than previous single string experiment where it was 0.6 GPa showing that sticking fibers together minimises the errors or the possible defects/fractures in the fiber.

It is not clearly known to us whether this decrease in the mechanical properties at the higher concentration of SWCNTs is due to nanotoxicity of the SWCNTs exerted on the worms to produce a lower quality fibre or if the higher amount of SWCNTs in the fiber changes the composition and the structure of the silk to degrade its mechanical properties. Nevertheless, the mechanical properties of the SWCNT silk fiber are superior than the control silk at any SWCNT concentrations that we have used.

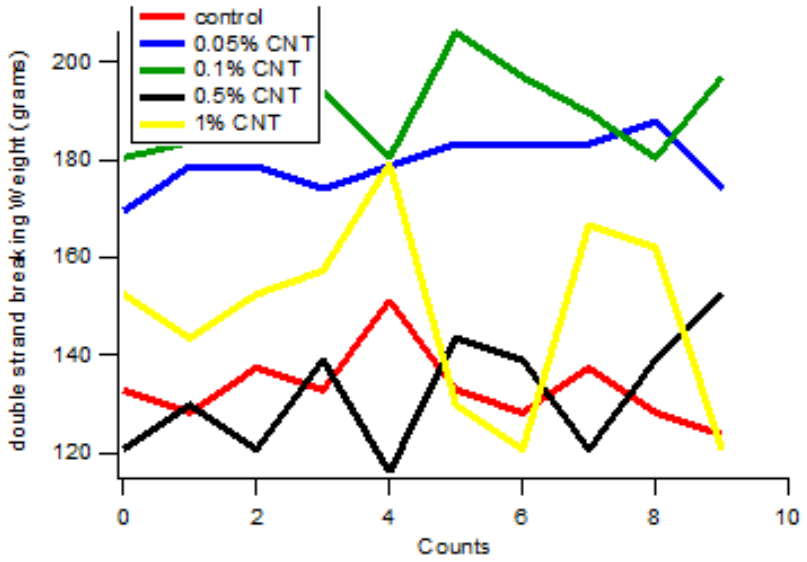

Figure 5.27 – Breaking strength measurement where the maximum weight the silk can withstand is plotted for various SWNT silk corresponding to different concentration of SWNTs sprayed.

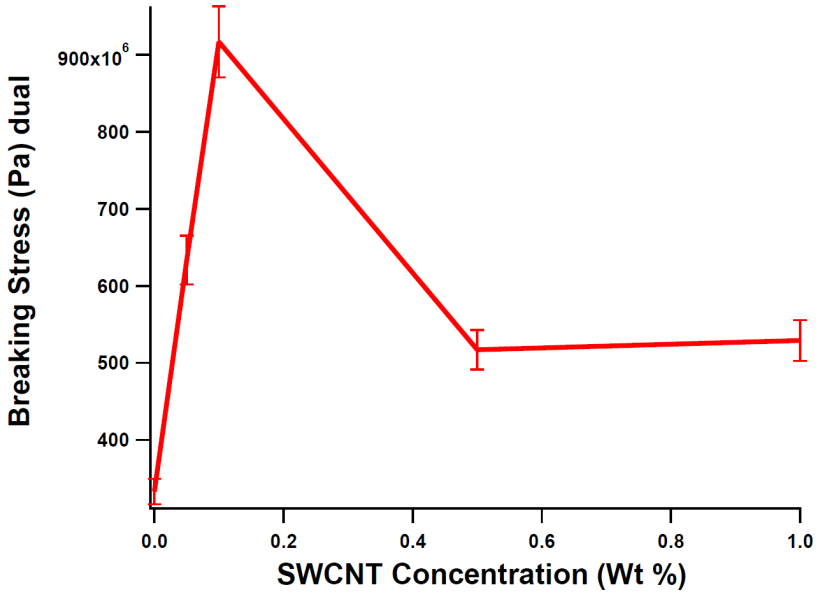

Figure 5.28 – Breaking Strength measurement where the maximum weight the silk can withstand is plotted for various SWNT silk corresponding to different concentration of SWNTs sprayed.

5.6.4 X- ray nano diffraction studies on SWCNT silk

Further to understand the mechanical characterization, scanning X-ray nanodiffraction (nanoXRD) was performed for probing the Bombyx mori single brin-thread control and also the ones loaded with carbon nanotubes. The measurements and analysis were conducted at ESRF, Grenoble using ID13 beamline by Christian Riekel. Using this technique, we could obtain information about structure of the silk fibers and crystallinity in particular. Further, we could verify the homogeneity of the SWCNTs contained in the silk fibers.

The approach followed is described for spider silk in the reference, Riekel et al [211]. It consisted of scanning a fiber through an X-ray nanobeam and recording at each position, a

diffraction pattern by a 2D detector. For the experiments we used a monochromatic beam of 0.008157 nm wavelength and a focal spot size of about 200nm x 200nm ([211]) at the sample position. The threads were imaged and positioned in the focal spot by an on-axis Olympus microscope. Optical microscopy images of the samples attached to the Si_3N_4 sample support are shown in figure 5.29a,b. For the samples, short pieces of single-brin-threads (control, 0.1wt% and 1wt%) were attached by fast glue to Silson Si_3N_4 membranes.

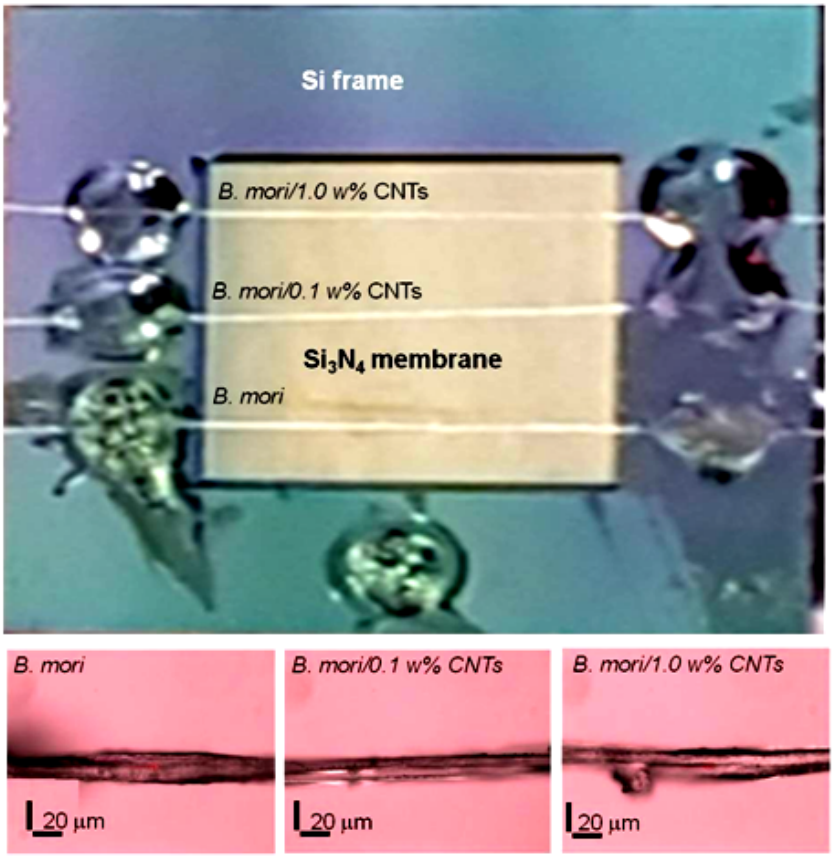

Figure 5.29 – (Top) Optical microscopy of single-threads attached to the Si-frame of a highly X-ray transparent, 1 μm thick Si_3N_4 membrane of 5x5 mm^2 area (Silson). Below: Optical microscopy of selected parts of the single-threads recorded by an on-axis Olympus microscope at the ESRF-ID13 beamline prior to the experiments[211]. The images were recorded while aligning the scanning area of each fiber (e.g. centre: red circle in left image) in the about 200nm x 200nm focal spot of the X-ray beam.

Scanning nanoXRD was performed in transmission geometry along the vertical (z) and horizontal (y) axis, in a plane normal to the beam direction with the fiber axis along the y-axis. The scanning approach is schematically shown for a B. mori control thread in the figure 5.30a. In this particular case we used step-increment of 1.0μm x 1.0μm to reveal overall structural features. The sequence of patterns recorded is transformed by software to a composite diffraction image which corresponds to the projection of the fiber (electron density) is shown in the 5.30(inset). We used only a fraction of the full patterns containing the strongest Bragg reflections for each pixel of the composite image, providing information on the projection of the local electron density (e.g. crystallinity, phases) variation. The projection shown in figure 5.30b corresponds closely to the optical image of the B. mori fibre.

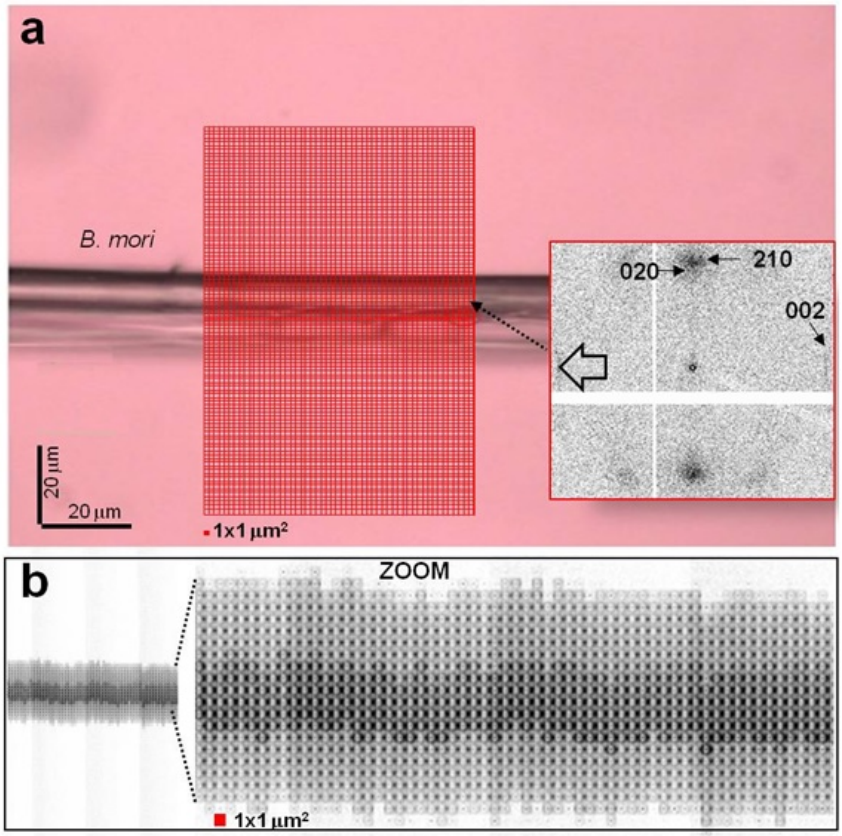

Figure 5.30 – (a) Schematic design of mesh-scan of B. mori thread by 1.0μm x 1.0μm step-increments. At each position of the mesh a 2D X-ray nanodiffraction pattern was recorded. (b) Composite X-ray nanodiffraction image[211] and zoom derived from the mesh-scan. The pattern-pixels of the image are composed of a selected area of the full pattern. Indeed, the pattern-pixel shown as inset to (a) is limited to the strongest Bragg reflections. The black open arrow corresponds to the fiber axis

To obtain an information on the overall structural feature, we have averaged about 100 of the patterns from each fiber and subtracted a corresponding background recorded outside of the fibre. The averaged patterns, shown in figure 5.31 corresponds all to the fibroin crystal structure [212],[213],[214],[215] and show only qualitatively an increase in diffuse scattering attributed to short-range order (SRO). One can show this more quantitatively by calculating the azimuthal average of about 20 degrees around the equatorial axis containing the (hk0) reflections. For a more detailed approach see reference [211]. One obtains in this way an 1D scattering profile. The scattering profiles were individually scaled to the scattering volume by a reference scattering volume outside the Bragg and SRO scattering on the meridional axis.

The 1D scattering profile of B. mori can be simulated by a sequence of Gaussians (Figure 5.32a) corresponding to the Bragg peaks of the fibroin structure and the SRO scattering [214]. The comparison of the B. mori sample with the SWCNTs containing samples shows a systematic intensity reduction as evidence by a decrease of the β-sheet (210) and neighbouring (020) Bragg reflections (Figure 5.32b).

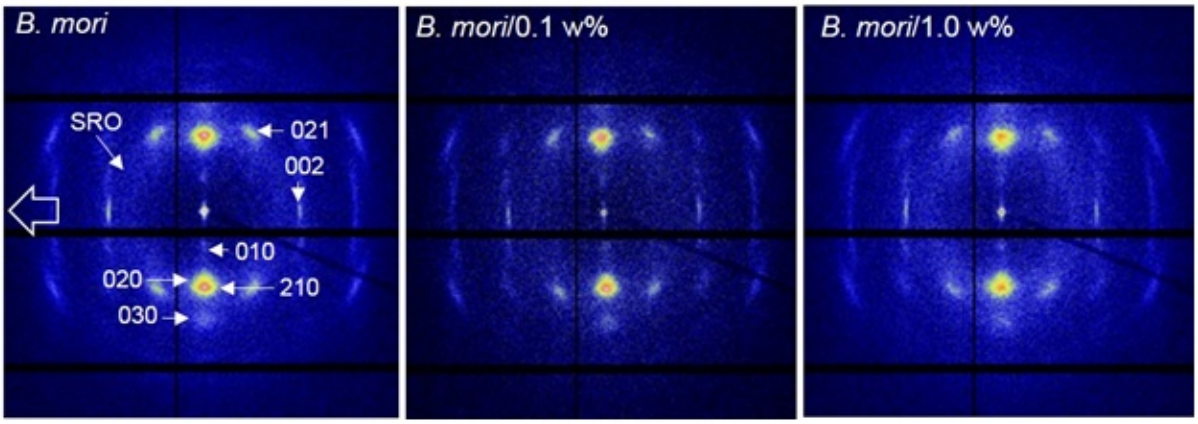

Figure 5.31 – Color-scale X-ray nanodiffraction patterns of B. mori fiber without and with SWCNTs. About 100 diffraction patterns recorded during a mesh-scan were averaged for each pattern. The patterns show fiber texture and can be indexed for the antipolar, antiparallel β-sheet structure[212],[213],[214],[215]. The limitation of the indexation to the (010), (020), (210), and (030) equatorial peaks is based on results from doubly oriented samples[216]. The open arrow corresponds to the meridional (fiber-axis) direction assumed by definition to be along the c-axis. The orthogonal equatorial axis contains the (hk0) reflections. The scattering from the three samples is very similar but shows an increase of short-range-order (SRO) scattering visible as a broad, diffuse powder ring.

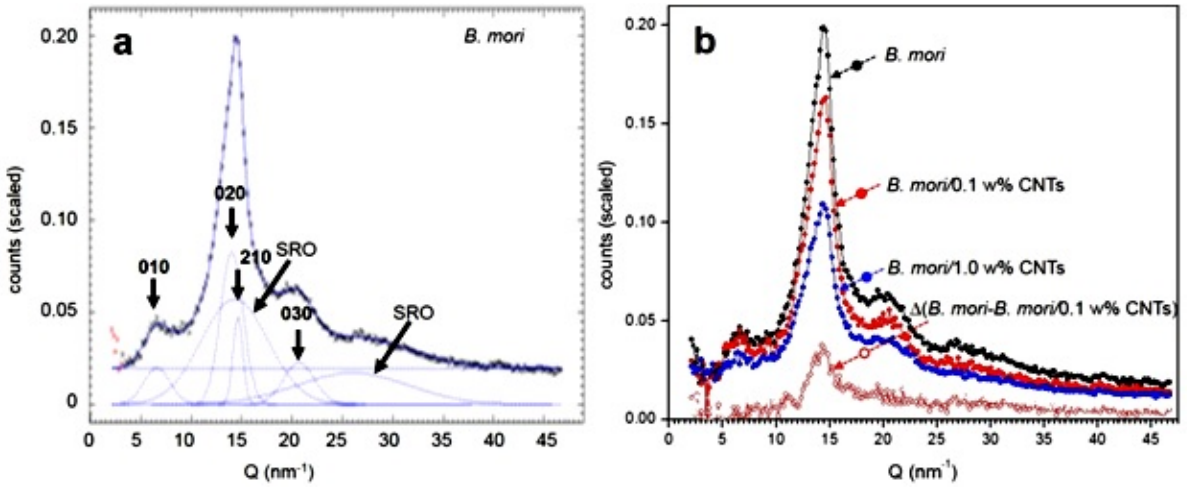

Figure 5.32 – 1D scattering profile of B. mori fiber obtained by azimuthal integration of the averaged pattern in figure 5.31 for appx. 20˚around the equator containing the (hk0) reflections. The experimental curve was simulated by Gaussians (in blue) using the FIT2D program [217]. Miller's indices of the Bragg peaks correspond to the the antipolar, antiparallel β-sheet structure[212],[213],[214],[215]. (b) Analysis of 1D scattering profiles from the averaged patterns. The profiles are scaled to equivalent scattering volumes. To show the decrease in crystallinity with increasing SWCNTs content, the difference of the B. mori control minus B. mori/0.1 wt% SWCNTs profile is shown.

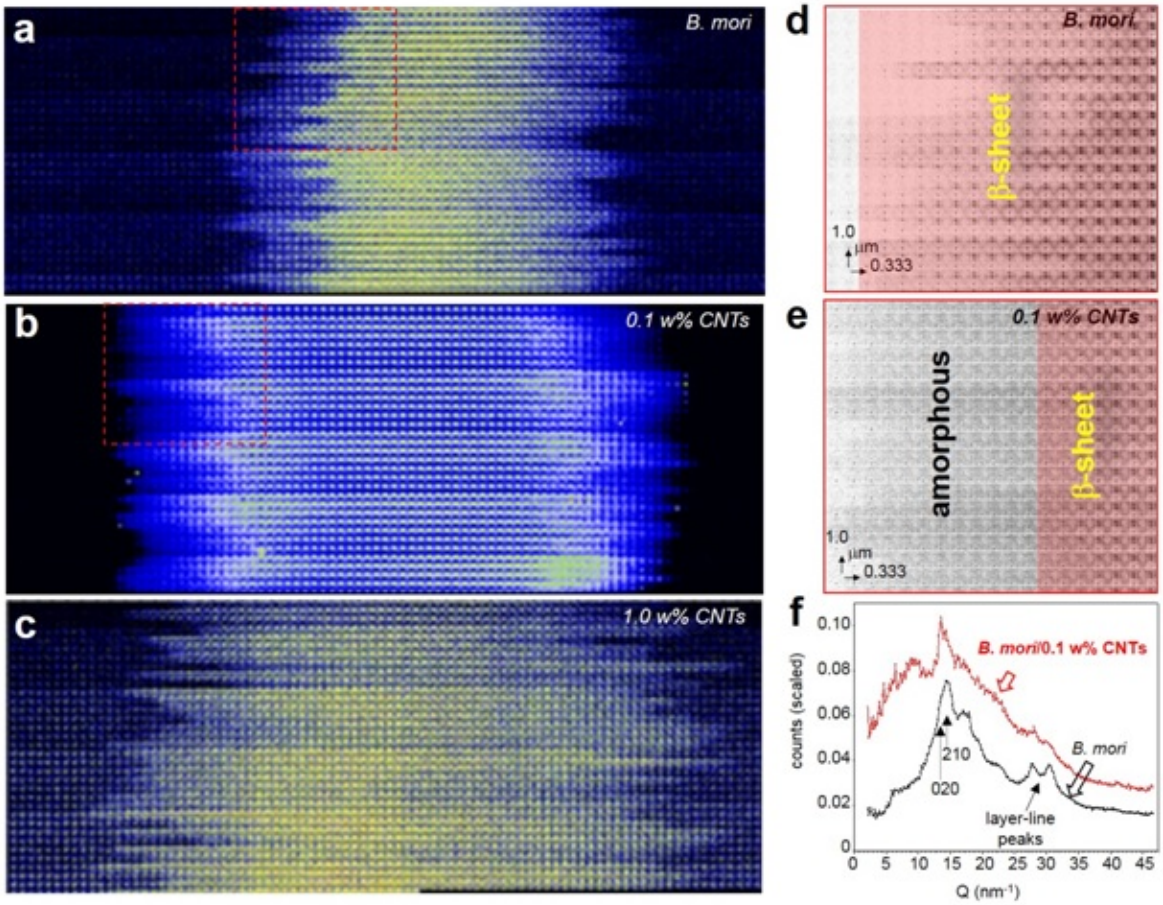

Figure 5.33 – (a-c) Comparison of the evolution of the composite X-ray nanodiffraction images with increasing SWCNTs content based on mesh-scans with 1.0x0.333 μm^2 step-increments. Zoom of equivalent areas of the left, outer edges is shown to the right for B. mori and B. mori/0.1 wt% SWCNTs (red, dashed rectangles). (d,e) The range of fibroin Bragg reflections in the zooms is shown approximately by a reddish rectangle. The comparison of the zooms corresponding to equivalent areas shows an amorphous skin layer for the B. mori/0.1 wt% SWCNTs which is not present for the B. mori sample. (f) Comparison of scattering from amorphous zone in the skin of B. mori/0.1 wt% SWCNTs fiber to the B. mori fibre profile. In both cases the azimuthal integration of the patterns was performed for the full (3600) angular range. The B. mori/0.1 wt% SWCNTs profile shows mostly diffuse scattering (called here "amorphous") as compared to the B. mori curve.

We now checked the variation of the crystallinity across the radius of the fibers by a higher resolution mesh-scan of 1.0μm(along fiber)x0.333 μm (across fiber). We observe for the B. mori thread that the crystallinity as evidenced by the presence of the (020)/(210) reflections extends until the edge of the fibre (Figure 2.39a,d) as already observed for the lower resolution scan (Figure 5.30b). The 0.1wt% SWCNTs containing fiber shows, however, an amorphous skin of about 3 μm diameter (Figure 2.39b,e). For the higher SWCNTs concentration, we also observe that the Bragg peaks extend to the edge of the fibre (Figure 2.39c). The comparison of the semicrystalline B. mori fiber with the amorphous skin of 0.1 wt% SWCNTs is also shown for the azimuthally averaged patterns in figure 2.39f.

One can postulate that the skin/core structure is at the origin of the increase of Young's modulus and breaking strength, although a detailed discussion will not be attempted here. It should, however, be noted that the high-performance dragline silk fibre also has an amorphous

skin and a crystalline core ([211], [218]). The decrease of mechanical properties for the 1 wt% SWCNT-silk concentration with higher amorphisation could be discussed in the context of the network model developed for spider silk. Indeed, a network of random peptidic chains reinforced by nanodomains has been proposed to be at the origin of the exceptional spider dragline silk mechanical features [219]. Although the crystallinity of B. mori (about 52% [214]) is higher than that of Nephila dragline silk (about 12% [220]), one can also assume a network with reinforcing nanodomains. Reducing the fraction of crystalline nanodomains could explain a loss in mechanical properties. This does not exclude other factors such as a change in nanodomains size.

5.7 Conclusions and perspectives

In conclusion, in this work we have shown a natural method where silk fibers of higher mechanical properties can be produced in mass scale by integrating the home-grown SWCNTs which were also produced in large quantities. Raman, SEM and TEM measurements show the proofs that the SWCNTs are well incorporated into the silk fibers. The detailed tensile load measurements indicate that there exist an optimum of concentration of SWCNT either in the food given to the worms or integrated into the fibers which gives a maximum increase of the breaking strength of the produced silk.

In addition, detailed scanning X-ray nanodiffraction (nanoXRD) probing of Bombyx mori threads loaded with carbon nanotubes (SWCNTs) reveals a reduction in crystallinity with increasing SWCNT content. A disordered skin layer is observed at the lowest examined SWCNT concentration of 0.1wt%, while the disordered fraction appears to be distributed throughout the fibre for 1.0 wt% SWCNT. We note that 0.1wt% SWCNTs containing fiber has an amorphous skin of about 3 μm diameter. This skin/core structure could be the origin of the increase of Young's modulus and breaking strength. Further, increased amorphisation for 1 wt% SWCNT silk, may alter the structure by reducing the fraction of crystalline nanodomains leading to loss of mechanical properties.

Further, though it is extremely difficult to make silk conduction by doping it with SWCNTs by above shown natural method, instead it would be interesting to weave the SWCNT silk fibers into a fabric and perform the mechanical stress tests to validate its future use in many engineering and technological applications.

General conclusions and future perspectives

In this thesis, we have emphasized on novel experimental methods to better control the environment and the interfacing of low-dimensional materials. The goal of this nano-engineering project was to unleash the full potential of the novel intrinsic physical properties of 2D and 1D materials and to study potential novel effects originating from novel couplings. By utilizing shielding and synergistic strategies, it has been proved that the properties of low dimensional materials could be enhanced significantly in very different fields such as electron transport, nano-optics and mechanics.

In the second chapter, where the discussion was dealing with graphene, we showed that, by encapsulating graphene in between two hBN flakes, we could obtain high quality devices especially when combined with the edge-contacted fabrication method. Graphene could then reach quasi-ideal properties. Indeed these graphene devices exhibited mobility up to million cm^2/Vs and displayed fractional quantum Hall effect. These regimes show that indeed devices are of very high quality. Again, we introduce a novel 1/f noise technique to study the charge dynamics in the edge state and the bulk state in quantum Hall regimes. In this regard, we confirm that the 1/f noise is at its minimum at the plateaus of quantum Hall regime and increases almost by 4 orders during the transition between plateaus.

In the third chapter, we presented the distinctive signature of intrinsic and extrinsic defects in MoS_2 2D crystals. We studied in details the behavior of these defects with respect to material and environment. In particular, we compared two different sources of crystals namely natural MoS_2 crystal and HP/HT MoS_2 crystal and were able to discriminate the origin of defect and effect on optoelectronics properties. Distinction between intrinsic and extrinsic defects was indeed achieved using complementary characterization techniques such as Raman spectroscopy, photoluminescence and scanning tunneling microscopy. We discovered a new kind of substitutional defect in synthetic MoS_2 whose signature could be traced both by STM and by room-temperature photoluminescence.

Following a similar strategy, in the fourth chapter, we fabricated VdW heterostructures based on monolayer MoS_2 embedded in hBN. Once more, the VdW transfer technique allowed controlled deposition of flakes that protected the monolayer MoS_2 from any possible degradation due to environment. The encapsulation strategy was found to improve the excitonic features of monolayer MoS_2. Narrow photoluminescence peak linewidths approaching to intrinsic limit of 4 meV have been observed. In these new type of heterostructures, we have studied the correlations in homogeneous and inhomogeneous broadening. Further, we characterized theses devices using cathodoluminescence and found that this technique provided a useful instrument to probe the interlayer coupling and interfacial defects in VdW heterostructures. We also found that it allowed the effective generation of light with spatial resolution below the diffraction limit paving the way to further nano optoelectronic studies in Van der Waals heterostructures.

Finally in chapter five, we reported the fabrication of novel composite fibers based on the incorporation of controlled fraction of single-walled carbon nanotubes inside industrial-grade silk. For that purpose, we used a natural systemic process to embed the single walled carbon nanotubes into silk fibers by feeding Bombyx Mori silkworms with controlled doses of CNT-enriched mulburry leaves. This is performed in order to further enhance the mechanical properties of the silk. Surprisingly, it has been observed that there exists an optimum carbon nanotube concentration upto which both the Youngs modulus and the breaking strength could be enhanced. Beyond a certain concentration, the mechanical properties lowers due to the appearance of structural changes in the way the silk is produced by the silkworms.

Perspectives

By now it is well known fact that hexagonal boron nitride beyond its own intrinsic properties, (such as large bandgap semiconducting properties) is the most suitable and ideal substrate for interfacing other 2D materials. Hence we either need to transfer or directly grow the 2D materials on hBN. Presently the technologies, either the transfer techniques or the growth methods such as Atomic layer deposition(ALD), epitaxial methods(MBE) and, in a lesser extent, chemical vapour deposition are still in young and immature stage, and therefore can only accomodate the realization of prototypes and proof-of-concept devices. Both synthesis and assembly techniques needs to be rationalized and enhanced before reaching semi-industrial grade. Indeed, it is still very difficult to grow the 2D materials directly on hBN by ALD, MBE or CVD techniques. Additionaly, one must note that transfer methods used for building the heterostructures are also far from an ideally clean limit (i.e. pristine crystal non interacting in 'vacuum'), as some impurities may get embedded into it and creating strain or doping of the material.

Figure 5.34 – Picture of microtransfer machine built inside the glove box with Argon atmosphere.

To further conclude in a simple way, both intrinsic and extrinsic defects further need to be reduced and requires different but combined strategies. To reduce intrisic defects, work has to be done on synthesis techniques (combined synthesis with interfacial control) while to reduce extrinsic defects, work has to be done in controlled encapsulation and in-situ contacts in inert environment (i.e. vacuum and/or gloveboxes filled with inert gases). A glove box filled with Argon as shown in the figure 5.34 which was developed in-house in our lab. The control of interfacial stress and crystal tilt orientation are other issues that need to be better adressed.

Bibliography

[1] A. K. Geim and I V Grigorieva. Van der Waals Heterostructures. *Nature*, 499:419, 2013.

[2] A. K. GEIM AND K. S.NOVOSELOV. The rise of graphene. *Nature Materials*, 6(3):183–191, 2007.

[3] W.Y. Huc a D. Caoa, H.B. Shub, T.Q. Wua, Z.T. Jianga, Z.W. Jiaoa, M.Q. Caic and Ping Wu. First-principles study of the origin of magnetism induced by intrinsic defects in monolayer MoS2. *Computational Materials Science*, 126:52–58, 2017.

[4] N. Sule, K. J. Willis, S. C. Hagness, and I. Knezevic. EMC/FDTD/MD simulation of carrier transport and electrodynamics in two-dimensional electron systems. *Journal of Computational Electronics*, 12(4):563–571, 2013.

[5] A. V. Kretinin, Y. Cao, J. S. Tu, G. L. Yu, R. Jalil, K. S. Novoselov, S. J. Haigh, A. Gholinia, A. Mishchenko, M. Lozada, T. Georgiou, C. R. Woods, F. Withers, P. Blake, G. Eda, A. Wirsig, C. Hucho, K. Watanabe, T. Taniguchi, A. K. Geim, and R. V. Gorbachev. Electronic properties of graphene encapsulated with different two-dimensional atomic crystals. *Nano Letters*, 14(6):3270–3276, 2014.

[6] G. Cassabois, P. Valvin, and B. Gil. Hexagonal boron nitride is an indirect bandgap semiconductor. *Nature Photonics*, 10(4):262–266, 2016.

[7] Dimitri Kopeliovich. Boron nitride as solid lubricant, 2012.

[8] Keun Soo Kim, Yue Zhao, Houk Jang, Sang Yoon Lee, Jong Min Kim, Kwang S. Kim, Jong Hyun Ahn, Philip Kim, Jae Young Choi, and Byung Hee Hong. Large-scale pattern growth of graphene films for stretchable transparent electrodes. *Nature*, 457(7230):706–710, 2009.

[9] Zheng Han. electronique : de la croissance CVD jusqua la suparconductivite de proximite a deux dimensions Macroscopic CVD Graphene for Nano- electronics : from growth to proximity-induced Graphene macroscopique pour la nanoelectronique : de la croissanc. 2013.

[10] Hadi Arjmandi-Tash, Dipankar Kalita, Zheng Han, Riadh Othmen, Goutham Nayak, Cecile Berne, John Landers, Kenji Watanabe, Takashi Taniguchi, Laëtitia Marty, Johann Coraux, Nedjma Bendiab, and Vincent Bouchiat. Large scale graphene/h-BN heterostructures obtained by direct CVD growth of graphene using high-yield proximity-catalytic process. *Journal of Physics: Materials*, 1(1):015003, sep 2018.

[11] C. R. Dean, A. F. Young, I. Meric, C. Lee, L. Wang, S. Sorgenfrei, K. Watanabe, T. Taniguchi, P. Kim, K. L. Shepard, and J. Hone. Boron nitride substrates for high-quality graphene electronics. *Nature Nanotechnology*, 5:722 EP –, Aug 2010.

[12] Jiamin Xue, Javier Sanchez-Yamagishi, Danny Bulmash, Philippe Jacquod, Aparna Deshpande, K. Watanabe, T. Taniguchi, Pablo Jarillo-Herrero, and Brian J. Leroy. Scanning tunnelling microscopy and spectroscopy of ultra-flat graphene on hexagonal boron nitride. *Nature Materials*, 10(4):282–285, 2011.

[13] C. R. Dean, A. F. Young, P. Cadden-Zimansky, L. Wang, H. Ren, K. Watanabe, T. Taniguchi, P. Kim, J. Hone, and K. L. Shepard. Multicomponent fractional quantum Hall effect inÂ graphene. *Nature Physics*, 7(9):693–696, 2011.

[14] B. Hunt, T Taniguchi, P Moon, M Koshino, and R C Ashoori. Massive Dirac Fermions and. *Science*, 340(June):1427–1431, 2013.

[15] P. J. Zomer, M. H. D. Guimarães, J. C. Brant, N. Tombros, and B. J. van Wees. Fast pick up technique for high quality heterostructures of bilayer graphene and hexagonal boron nitride. 2014.

[16] Andres Castellanos-Gomez, Michele Buscema, Rianda Molenaar, Vibhor Singh, Laurens Janssen, Herre S.J. Van Der Zant, and Gary A. Steele. Deterministic transfer of two-dimensional materials by all-dry viscoelastic stamping. *2D Materials*, 1(1):1–34, 2014.

[17] L. Wang, I. Meric, P. Y. Huang, Q. Gao, Y. Gao, H. Tran, T. Taniguchi, K. Watanabe, L. M. Campos, D. A. Muller, J. Guo, P. Kim, J. Hone, K. L. Shepard, and C. R. Dean. One-dimensional electrical contact to a two-dimensional material. *Science*, 342(6158):614–617, 2013.

[18] Leng Duei Koh. BOMBYX MORI SILK: FROM MECHANICAL PROPERTIES TO FUNCTIONALITIES.

[19] Sunghyun Nam, Brian D. Condon, Christopher D. Delhom, and Krystal R. Fontenot. Silver-cotton nanocomposites: Nano-design of microfibrillar structure causes morphological changes and increased tenacity. *Scientific Reports*, 6(September):1–10, 2016.

[20] Emiliano Lepore, Francesco Bonaccorso, Matteo Bruna, Frederico Bosia, Simone Taiolo, Giovanni Garberoglio, Andrea Ferrari, and Nicola Maria Pugno. Silk reinforced with graphene or carbon nanotube spun by spiders. *Physiological Research*, 64(6):897–905, 2015.

[21] K. S. Novoselov, D. Jiang, F. Schedin, T. J. Booth, V. V. Khotkevich, S. V. Morozov, and A. K. Geim. Two-dimensional atomic crystals. *Proceedings of the National Academy of Sciences*, 102(30):10451–10453, 2005.

[22] E. H. Hwang, S. Adam, and S. Das Sarma. Carrier transport in two-dimensional graphene layers. *Physical Review Letters*, 98(18):2–5, 2007.

[23] Jian-Hao Chen, Chaun Jang, Shudong Xiao, Masa Ishigami, and Michael S Fuhrer. Intrinsic and extrinsic performance limits of graphene devices on SiO 2. *Nature Publishing Group*, 2008.

[24] K. I. Bolotin, K. J. Sikes, Z. Jiang, M. Klima, G. Fudenberg, J. Hone, P. Kim, and H. L. Stormer. Ultrahigh electron mobility in suspended graphene. *Solid State Communications*, 146(9-10):351–355, 2008.

[25] Shaowen Chen, Zheng Han, Mirza M. Elahi, K. M.Masum Habib, Lei Wang, Bo Wen, Yuanda Gao, Takashi Taniguchi, Kenji Watanabe, James Hone, Avik W. Ghosh, and Cory R. Dean. Electron optics with p-n junctions in ballistic graphene. *Science*, 353(6307):1522–1525, 2016.

[26] A. H. Castro Neto, F. Guinea, N. M. R. Peres, K. S. Novoselov, and A. K. Geim. The electronic properties of graphene. 81(March), 2007.

[27] JN Fuchs and MO Goerbig. Introduction to the physical properties of graphene. *Lecture Notes*, 2008.

[28] G. Bannon. sp2 orbital hybridization. pages 129–134.

[29] Y.-W. Tan, Y. Zhang, H. L. Stormer, and P. Kim. Temperature dependent electron transport in graphene. *The European Physical Journal Special Topics*, 148(1):15–18, 2007.

[30] P. Blake, E. W. Hill, A. H. Castro Neto, K. S. Novoselov, D. Jiang, R. Yang, T. J. Booth, and A. K. Geim. Making graphene visible. *Applied Physics Letters*, 91(6), 2007.

[31] G. Batey, A. J. Matthews, and M. Patton. A new ultra-low-temperature cryogen-free experimental platform. *Journal of Physics: Conference Series*, 568, 2014.

[32] M. O. Goerbig. Quantum Hall Effects. 2009.

[33] David Tong. The quantum Hall effect. *American Journal of Physics*, 61(2):179–183, 1993.

[34] B. Frieß. Spin and Charge Ordering in the Quantum Hall Regime. 2014.

[35] Kazi Rafsanjani Amin. Conductance Fluctuations in High-mobility Graphene Field Effect Transistors. (April), 2018.

[36] Katrin Zimmermann. Quantum point contact in high mobility graphene. 2017.

[37] K. V. Klitzing, G. Dorda, and M. Pepper. New method for high-accuracy determination of the fine-structure constant based on quantized hall resistance. *Physical Review Letters*, 45(6):494–497, 1980.

[38] K. S. Novoselov, A. K. Geim, S. V. Morozov, D. Jiang, M. I. Katsnelson, I. V. Grigorieva, S. V. Dubonos, and A. A. Firsov. Two-dimensional gas of massless Dirac fermions in graphene. *Nature*, 438(7065):197–200, 2005.

[39] Y. Zhang, Z. Jiang, J. P. Small, M. S. Purewal, Y. W. Tan, M. Fazlollahi, J. D. Chudow, J. A. Jaszczak, H. L. Stormer, and P. Kim. Landau-level splitting in graphene in high magnetic fields. *Physical Review Letters*, 96(13):1–4, 2006.

[40] M. Büttiker. Absence of backscattering in the quantum Hall effect in multiprobe conductors. *Physical Review B*, 38(14):9375–9389, 1988.

[41] H. L. Stormer, A. Chang, D. C. Tsui, J. C.M. Hwang, A. C. Gossard, and W. Wiegmann. Fractional quantization of the hall effect. *Physical Review Letters*, 50(24):1953–1956, 1983.

[42] R. B. Laughlin. Anomalous quantum Hall effect: An incompressible quantum fluid with fractionally charged excitations. *Physical Review Letters*, 50(18):1395–1398, 1983.

[43] W. Pan, H. L. Stormer, D. C. Tsui, L. N. Pfeiffer, K. W. Baldwin, and K. W. West. Fractional Quantum Hall Effect of Composite Fermions. *Physical Review Letters*, 90(1):4, 2003.

[44] J. K. Jain. Composite-fermion approach for the fractional quantum Hall effect. *Physical Review Letters*, 63(2):199–202, 1989.

[45] H. L. Störmer. The fractional quantum Hall effect, 2003.

[46] F. D.M. Haldane. Fractional quantization of the hall effect: A hierarchy of incompressible quantum fluid states. *Physical Review Letters*, 51(7):605–608, 1983.

[47] B. I. Halperin, P. A. Lee and N. Read. Theory of the half-filled Landau level. *Semiconductor Science and Technology*, 9(11 S):1859–1864, 1994.

[48] B. I. Halperin. Statistics of quasiparticles and the hierarchy of fractional quantized hall states. *Physical Review Letters*, 52(18):1583–1586, 1984.

[49] J. K. Jain. Theory of the fractional quantum Hall effect. *Physical Review B*, 41(11):7653–7665, 1990.

[50] Aveek Bid, N. Ofek, M. Heiblum, V. Umansky, and D. Mahalu. Shot noise and charge at the 2/3 composite ffractional qquantum hall state. *Physical Review Letters*, 103(23):3–6, 2009.

[51] R. Willett, J. P. Eisenstein, H. L. Störmer, D. C. Tsui, A. C. Gossard, and J. H. English. Observation of an even-denominator quantum number in the fractional quantum Hall effect. *Physical Review Letters*, 59(15):1776–1779, 1987.

[52] J. P. Eisenstein, K. B. Cooper, L. N. Pfeiffer, and K. W. West. Insulating and fractional quantum hall states in the first excited Landau level. *Physical Review Letters*, 88(7):768011–768014, 2002.

[53] D. R. Luhman, W. Pan, D. C. Tsui, L. N. Pfeiffer, K. W. Baldwin, and K. W. West. Observation of a fractional quantum hall state at ν=1/4 in a wide GaAs quantum well. *Physical Review Letters*, 101(26):2–5, 2008.

[54] Martin Greiter, Xiao Gang Wen, and Frank Wilczek. Paired Hall state at half filling. *Physical Review Letters*, 66(24):3205–3208, 1991.

[55] Gregory Moore and Nicholas Read. Nonabelions in the fractional quantum hall effect. *Nuclear Physics B*, 360(2-3):362–396, 1991.

[56] G. S. Canright and S. M. Girvin. Fractional statistics: Quantum possibilities in two dimensions. *Science*, 247(4947):1197–1205, 1990.

[57] W Pan, J S Xia, V Shvarts, D E Adams, H L Stormer, D C Tsui, L N Pfeiffer, K W Baldwin, and K W West. Exact quantization of the even-denominator fractional quantum Hall state at v=5/2 Landau level filling factor. *Physical Review Letters*, 83:3530–3533, 1999.

[58] Xu Du, Ivan Skachko, Fabian Duerr, Adina Luican, and Eva Y. Andrei. Fractional quantum Hall effect and insulating phase of Dirac electrons in graphene. *Nature*, 462(7270):192–195, 2009.

[59] Kirill I. Bolotin, Fereshte Ghahari, Michael D. Shulman, Horst L. Stormer, and Philip Kim. Observation of the fractional quantum Hall effect in graphene. *Nature*, 462(7270):196–199, 2009.

[60] F. Amet, A. J. Bestwick, J. R. Williams, L. Balicas, K. Watanabe, T. Taniguchi, and D. Goldhaber-Gordon. Composite fermions and broken symmetries in graphene. *Nature Communications*, 6:1–30, 2015.

[61] Benjamin E. Feldman, Andrei J. Levin, Benjamin Krauss, Dmitry A. Abanin, Bertrand I. Halperin, Jurgen H. Smet, and Amir Yacoby. Fractional quantum hall phase transitions and four-flux states in graphene. *Physical Review Letters*, 111(7):1–5, 2013.

[62] Benjamin E Feldman, Benjamin Krauss, J. H. Smet, and Amir Yacoby. Unconventional Sequence of Fractional Quantum Hall States in Suspended Graphene. *Science*, 337(6099):1196–1199, 2012.

[63] Mark O. Goerbig and Nicolas Regnault. The Fractional Quantum Hall Effect in Graphene – a Theoretician ' s Perspective Graphene in a Magnetic Field. pages 28–30, 2010.

[64] Hemanta Kumar Kundu, Sujay Ray, Kapildeb Dolui, Vivas Bagwe, Palash Roy Choudhury, S. B. Krupanidhi, Tanmoy Das, Pratap Raychaudhuri, and Aveek Bid. Quantum Phase Transition in Few-Layer NbSe2 Probed through Quantized Conductance Fluctuations. *Physical Review Letters*, 119(22):1–6, 2017.

[65] R. Koushik, Siddhartha Kumar, Kazi Rafsanjani Amin, Mintu Mondal, John Jesudasan, Aveek Bid, Pratap Raychaudhuri, and Arindam Ghosh. Correlated conductance fluctuations close to the Berezinskii-Kosterlitz- Thouless transition in ultrathin NbN films. *Physical Review Letters*, 111(19):1–5, 2013.

[66] F. K. Du Pré. A suggestion regarding the spectral density of flicker noise. *Physical Review*, 78(5):615, 1950.

[67] A. H. McWhorter. McWorther Proc Physics of Semiconductor Surface p 207 1957.pdf, 1957.

[68] P. Dutta and P. M. Horn. Low-frequency fluctuations in solids: 1f noise. *Reviews of Modern Physics*, 53(3):497–516, 1981.

[69] A. P. Dmitriev, M. E. Levinshtein, and S. L. Rumyantsev. On the Hooge relation in semiconductors and metals. *Journal of Applied Physics*, 106(2), 2009.

[70] F. N. Hooge. 1/f Noise Sources. *IEEE Transactions on Electron Devices*, 41(11):1926–1935, 1994.

[71] F N Hooge, T G M Kleinpenning, and L K J Vandamme. Experimental studies on 1/f noise. *Rep. PRog. Phys.*, 44(December 1980):31, 1981.

[72] Aveek Bid. Resistance fluctuations and instability in metal nanowires. (August), 2006.

[73] R Koushik. Study of Phase Transitions in Two Dimensions using Electrical Noise. (January), 2014.

[74] John H. Scofield. Ac Method for Measuring Low-Frequency Resistance Fluctuation Spectra. *Review of Scientific Instruments*, 58(6):985–993, 1987.

[75] Peter D. Welch. The Use of Fast Fourier Transform for the Estimation of Power Spectra: A Method Based on Time Averaging Over Short, Modified Periodograms. *IEEE Transactions on Audio and Electroacoustics*, 15(2):70–73, 1967.

[76] Gold Lawrence, R Rabiner, Bernard. Theory and application of digital signal processing. *Englewood Cliffs, NJ, Prentice-Hall, Inc.,*, (2):777, 1975.

[77] Alexander A. Balandin. Low-frequency 1/f noise in graphene devices. *Nature Nanotechnology*, 8(8):549–555, 2013.

[78] S L Rumyantsev and Balandin Shur, M S, G., Liu, A.A. Low frequency noise in 2D materials:graphene and MoS2. *Noise and Fluctuations (ICNF), 2017 International Conference on*, pages 31–34, 2017.

[79] A. A. Kaverzin, A. S. Mayorov, A. Shytov, and D. W. Horsell. Impurities as a source of 1/f noise in graphene. *Physical Review B - Condensed Matter and Materials Physics*, 85(7):1–5, 2012.

[80] S. L. Rumyantsev, D. Coquillat, R. Ribeiro, M.a Goiran, W. Knap, M. S. Shur, Alexander A. Balandin, and M. E. Levinshtein. The effect of a transverse magnetic field on 1 /f noise in graphene. *Applied Physics Letters*, 103(17):173114, 2013.

[81] Atindra Nath Pal, Subhamoy Ghatak, Vidya Kochat, Arjun Sampathkumar, Srinivasan Raghavan, and Arindam Ghosh. Microscopic Mechanism of 1 / f Noise in Graphene : Role of Energy. *ACS Nano*, (3):2075–2081, 2011.

[82] Maxim A. Stolyarov, Guanxiong Liu, Sergey L. Rumyantsev, Michael Shur, and Alexander A. Balandin. Suppression of 1/ f noise in near-ballistic h -BN-graphene- h- BN heterostructure field-effect transistors. *Applied Physics Letters*, 107(2):28–33, 2015.

[83] C. C. Kalmbach, F. J. Ahlers, J. Schurr, A. Müller, J. Feilhauer, M. Kruskopf, K. Pierz, F. Hohls, and R. J. Haug. Nonequilibrium mesoscopic conductance fluctuations as the origin of 1/f noise in epitaxial graphene. *Physical Review B*, 94(20):1–11, 2016.

[84] S. Kumar, A. Kaczmarczyk, and B. D. Gerardot. Strain-induced spatial and spectral isolation of quantum emitters in mono- and bilayer wse2. *Nano Letters*, 15(11):7567–7573, 2015. PMID: 26480237.

[85] Paritosh Karnatak, T. Phanindra Sai, Srijit Goswami, Subhamoy Ghatak, Sanjeev Kaushal, and Arindam Ghosh. Current crowding mediated large contact noise in graphene field-effect transistors. *Nature Communications*, 7:1–8, 2016.

[86] Atikur Rahman, Janice Wynn Guikema, and Nina Marković. Quantum interference noise near the Dirac point in graphene. *Physical Review B - Condensed Matter and Materials Physics*, 89(23):1–5, 2014.

[87] F Liefrink and A J Scholten. ballistic and quantum Hall regime. 175:213–216, 1991.

[88] Kensaku Chida, Tomonori Arakawa, Sadashige Matsuo, Yoshitaka Nishihara, Takahiro Tanaka, Daichi Chiba, Teruo Ono, Tokuro Hata, Kensuke Kobayashi, and Tomoki Machida. Observation of finite excess noise in the voltage-biased quantum Hall regime as a precursor for breakdown. *Physical Review B - Condensed Matter and Materials Physics*, 87(15):3–9, 2013.

[89] B. W. Ricketts. Low frequency noise and the quantised Hall effect. *J. Phys. D: Appl. Phys.*, 18:885–892, 1985.

[90] Katrin Zimmermann, Anna Jordan, Frédéric Gay, Kenji Watanabe, Takashi Taniguchi, Zheng Han, Vincent Bouchiat, Hermann Sellier, and Benjamin Sacépé. Tunable transmission of quantum Hall edge channels with full degeneracy lifting in split-gated graphene devices. *Nature Communications*, 8:1–7, 2017.

[91] Aveek Bid, N. Ofek, H. Inoue, M. Heiblum, C. L. Kane, V. Umansky, and D. Mahalu. Observation of neutral modes in the fractional quantum Hall effect regime. *AIP Conference Proceedings*, 1399(7306):633–634, 2011.

[92] T. Taniguchi and K. Watanabe. Synthesis of high-purity boron nitride single crystals under high pressure by using Ba-BN solvent. *Journal of Crystal Growth*, 303(2):525–529, 2007.

[93] Wu Zhou, Xiaolong Zou, Sina Najmaei, Zheng Liu, Yumeng Shi, Jing Kong, Jun Lou, Pulickel M. Ajayan, Boris I. Yakobson, and Juan Carlos Idrobo. Intrinsic structural defects in monolayer molybdenum disulfide. *Nano Letters*, 13(6):2615–2622, 2013.

[94] Sudipta Dubey, Simone Lisi, Goutham Nayak, Felix Herziger, Van-Dung Nguyen, Toai Le Quang, Vladimir Cherkez, César González, Yannick J. Dappe, Kenji Watanabe, Takashi Taniguchi, Laurence Magaud, Pierre Mallet, Jean-Yves Veuillen, Raul Arenal, Laëtitia Marty, Julien Renard, Nedjma Bendiab, Johann Coraux, and Vincent Bouchiat. Weakly trapped, charged, and free excitons in single-layer mos2 in the presence of defects, strain, and charged impurities. *ACS Nano*, 11(11):11206–11216, 2017. PMID: 28992415.

[95] Andor Kormányos, Guido Burkard, Martin Gmitra, Jaroslav Fabian, Viktor Zólyomi, Neil D. Drummond, Vladimir Fal'ko, Vladimir Fal'ko, and Vladimir Fal'ko. K.P Theory for Two-Dimensional Transition Metal Dichalcogenide Semiconductors. *2D Materials*, 2(2):022001, 2014.

[96] Jun Xiao, Mervin Zhao, Yuan Wang, and Xiang Zhang. Excitons in atomically thin 2D semiconductors and their applications. *Nanophotonics*, 6(6):1309–1328, 2017.

[97] Andrea Splendiani, Liang Sun, Yuanbo Zhang, Tianshu Li, Jonghwan Kim, Chi Yung Chim, Giulia Galli, and Feng Wang. Emerging photoluminescence in monolayer MoS2. *Nano Letters*, 10(4):1271–1275, 2010.

[98] Ting Cao, Gang Wang, Wenpeng Han, Huiqi Ye, Chuanrui Zhu, Junren Shi, Qian Niu, Pingheng Tan, Enge Wang, Baoli Liu, and Ji Feng. Valley-selective circular dichroism of monolayer molybdenum disulphide. *Nature Communications*, 3(May):885–887, 2012.

[99] Gang Wang, Alexey Chernikov, Mikhail M. Glazov, Tony F. Heinz, Xavier Marie, Thierry Amand, and Bernhard Urbaszek. Colloquium: Excitons in atomically thin transition metal dichalcogenides. *Reviews of Modern Physics*, 90(2):21001, 2018.

[100] Misra. *Physics of Condensed Matter Physics of Condensed Matter*, volume 1. 2017.

[101] Alejandro Molina-Sánchez, Kerstin Hummer, and Ludger Wirtz. Vibrational and optical properties of MoS2: From monolayer to bulk. *Surface Science Reports*, 70(4):554–586, 2015.

[102] Nedjma Bendiab. Optical phonons in 1D and 2D carbon systems :. 2017.

[103] Martina Ballerio. Hybrid Carbon Based Devices for Optoelectronics. 2015.

[104] Changgu Lee, Hugen Yan, Louis E. Brus, Tony F. Heinz, James Hone, and Sunmin Ryu. Anomalous lattice vibrations of single- and few-layer mos2. *ACS Nano*, 4(5):2695–2700, 2010. PMID: 20392077.

[105] G. Plechinger, S. Heydrich, J. Eroms, D. Weiss, C. Schüller, and T. Korn. Raman spectroscopy of the interlayer shear mode in few-layer MoS 2 flakes. *Applied Physics Letters*, 101(10), 2012.

[106] Yanyuan Zhao, Xin Luo, Hai Li, Jun Zhang, Paulo T Araujo, Chee Kwan Gan, Jumiati Wu, Hua Zhang, Su Ying Quek, Mildred S Dresselhaus, and Qihua Xiong. Inter layer Breathing and Shear Modes in Few-Trilayer MoS$_2$ and WSe$_2$. *Nano Lett.*, 13(3):1007–1015, 2013.

[107] Krishna P. Dhakal, Dinh Loc Duong, Jubok Lee, Honggi Nam, Minsu Kim, Min Kan, Young Hee Lee, and Jeongyong Kim. Confocal absorption spectral imaging of MoS2: Optical transitions depending on the atomic thickness of intrinsic and chemically doped MoS2. *Nanoscale*, 6(21):13028–13035, 2014.

[108] Hiram J. Conley, Bin Wang, Jed I. Ziegler, Richard F. Haglund, Sokrates T. Pantelides, and Kirill I. Bolotin. Bandgap engineering of strained monolayer and bilayer MoS2. *Nano Letters*, 13(8):3626–3630, 2013.

[109] William M. Parkin, Adrian Balan, Liangbo Liang, Paul Masih Das, Michael Lamparski, Carl H. Naylor, Julio A. Rodríguez-Manzo, A. T. Charlie Johnson, Vincent Meunier, and Marija Drndić. Raman shifts in electron-irradiated monolayer mos2. *ACS Nano*, 10(4):4134–4142, 2016. PMID: 26998814.

[110] Andres Castellanos-Gomez, Rafael Roldán, Emmanuele Cappelluti, Michele Buscema, Francisco Guinea, Herre S. J. van der Zant, and Gary A. Steele. Local Strain Engineering in Atomically Thin MoS 2. *Nano Letters*, 13(11):5361–5366, 2013.

[111] Biswanath Chakraborty, Achintya Bera, D. V S Muthu, Somnath Bhowmick, U. V. Waghmare, and A. K. Sood. Symmetry-dependent phonon renormalization in monolayer MoS 2 transistor. *Physical Review B - Condensed Matter and Materials Physics*, 85(16):2–5, 2012.

[112] A. Michail, N. Delikoukos, J. Parthenios, C. Galiotis, and K. Papagelis. Optical detection of strain and doping inhomogeneities in single layer mos2. *Applied Physics Letters*, 108(17):173102, 2016.

[113] N. L. Vočadlo and Geoffrey D. Price. The Grüneisen parameter - computer calculations via lattice dynamics. *Physics of the Earth and Planetary Interiors*, 82(3-4):261–270, 1994.

[114] Chih-Pin Lu, Guohong Li, Jinhai Mao, Li-Min Wang, and Eva Y. Andrei. Bandgap, mid-gap states, and gating effects in mos2. *Nano Letters*, 14(8):4628–4633, 2014. PMID: 25004377.

[115] Wenzhong Bao, Xinghan Cai, Dohun Kim, Karthik Sridhara, and Michael S. Fuhrer. High mobility ambipolar MoS2field-effect transistors: Substrate and dielectric effects. *Applied Physics Letters*, 102(4), 2013.

[116] M Buscema, G A Steele, Herre S J van der Zant, and A Castellanos-Gomez. The effect of the substrate on the Raman and photoluminescence emission of single layer MoS2. *Nano Research*, 7(4):561–571, 2014.

[117] Jiajie Pei, Jiong Yang, Renjing Xu, Yong Hui Zeng, Ye Win Myint, Shuang Zhang, Jin Cheng Zheng, Qinghua Qin, Xibin Wang, Wugui Jiang, and Yuerui Lu. Exciton and Trion Dynamics in Bilayer MoS2. *Small*, 11(48):6384–6390, 2015.

[118] Haiyan Nan, Zilu Wang, Wenhui Wang, Zheng Liang, Yan Lu, Qian Chen, Daowei He, Pingheng Tan, Feng Miao, Xinran Wang, Jinlan Wang, and Zhenhua Ni. Strong photoluminescence enhancement of MoS2 through defect engineering and oxygen bonding. *ACS Nano*, 8(6):5738–5745, 2014.

[119] Shinichiro Mouri, Yuhei Miyauchi, and Kazunari Matsuda. Tunable photoluminescence of monolayer MoS₂ via chemical doping. *Nano Letters*, 13(12):5944–5948, 2013.

[120] Kin Fai Mak, Keliang He, Changgu Lee, Gwan Hyoung Lee, James Hone, Tony F. Heinz, and Jie Shan. Tightly bound trions in monolayer MoS 2. *Nature Materials*, 12(3):207–211, 2013.

[121] A. Steinhoff, J. H. Kim, F. Jahnke, M. Rösner, D. S. Kim, C. Lee, G. H. Han, M. S. Jeong, T. O. Wehling, and C. Gies. Efficient Excitonic Photoluminescence in Direct and Indirect Band Gap Monolayer MoS2. *Nano Letters*, 15(10):6841–6847, 2015.

[122] P. Dey, J. Paul, Z. Wang, C. E. Stevens, C. Liu, A. H. Romero, J. Shan, D. J. Hilton, and D. Karaiskaj. Optical Coherence in Atomic-Monolayer Transition-Metal Dichalcogenides Limited by Electron-Phonon Interactions. *Physical Review Letters*, 116(12):1–6, 2016.

[123] D. Sercombe, S. Schwarz, O. Del Pozo-Zamudio, F. Liu, B. J. Robinson, E. A. Chekhovich, I. I. Tartakovskii, O. Kolosov, and A. I. Tartakovskii. Optical investigation of the natural electron doping in thin MoS2films deposited on dielectric substrates. *Scientific Reports*, 3:1–15, 2013.

[124] Jun Ting Wang, Lu Lu Li, Meng Yuan Zhang, Si Lu Liu, Lin Hai Jiang, and Qing Shen. Directly obtaining high strength silk fiber from silkworm by feeding carbon nanotubes. *Materials Science and Engineering C*, 34(1):417–421, 2014.

[125] Sefaattin Tongay, Joonki Suh, Can Ataca, Wen Fan, Alexander Luce, Jeong Seuk Kang, Jonathan Liu, Changhyun Ko, Rajamani Raghunathanan, Jian Zhou, Frank Ogletree, Jingbo Li, Jeffrey C. Grossman, and Junqiao Wu. Defects activated photoluminescence in two-dimensional semiconductors: Interplay between bound, charged, and free excitons. *Scientific Reports*, 3:1–5, 2013.

[126] P K Chow, R B Jacobs-Gedrim, J Gao, T M Lu, B Yu, H Terrones, and N Koratkar. Defect-Induced Photoluminescence in Mono layer Semiconducting Transition Metal Dichalcogenides. *Acs Nano*, 9(2):1520–1527, 2015.

[127] Byung Hoon Kim, Min Park, Minoh Lee, Seung Jae Baek, Hu Young Jeong, Min Choi, Sung Jin Chang, Won G. Hong, Tae Kyung Kim, Hoi Ri Moon, Yung Woo Park, Noejung Park, and Yongseok Jun. Effect of sulphur vacancy on geometric and electronic structure of MoS2 induced by molecular hydrogen treatment at room temperature. *RSC Advances*, 3(40):18424, 2013.

[128] Diana Y. Qiu, Felipe H. da Jornada, and Steven G. Louie. Optical Spectrum of MoS${}_2$: Many-body Effects and Diversity of Exciton States. 2013.

[129] Hannu Pekka Komsa and Arkady V. Krasheninnikov. Native defects in bulk and monolayer MoS2 from first principles. *Physical Review B - Condensed Matter and Materials Physics*, 91(12):1–17, 2015.

[130] Kapildeb Dolui, Ivan Rungger, Chaitanya Das Pemmaraju, and Stefano Sanvito. Possible doping strategies for MoS2 monolayers: An ab initio study. *Physical Review B - Condensed Matter and Materials Physics*, 88(7):1–9, 2013.

[131] Ji Young Noh, Hanchul Kim, Minkyu Park, and Yong Sung Kim. Deep-to-shallow level transition of Re and Nb dopants in monolayer MoS2 with dielectric environments. *Physical Review B - Condensed Matter and Materials Physics*, 92(11):6–9, 2015.

[132] Rafik Addou, Stephen McDonnell, Diego Barrera, Zaibing Guo, Angelica Azcatl, Jian Wang, Hui Zhu, Christopher L. Hinkle, Manuel Quevedo-Lopez, Husam N. Alshareef, Luigi Colombo, Julia W.P. Hsu, and Robert M. Wallace. Impurities and Electronic Property Variations of Natural MoS<inf>2</inf> Crystal Surfaces. *ACS Nano*, 9(9):9124–9133, 2015.

[133] Stephen McDonnell, Rafik Addou, Creighton Buie, Robert M Wallace, and Christopher L Hinkle. Defect-Dominated Doping and Contact Resistance in MoS 2. *ACS Nano*, 8(3):2880–2888, 2014.

[134] Hideki Abe, Kotaro Kataoka, Keiji Ueno, and Atsushi Koma. Scanning tunneling microscope observation of the metal-adsorbed layered semiconductor surfaces, 1995.

[135] Yu Li Huang, Yifeng Chen, Wenjing Zhang, Su Ying Quek, Chang Hsiao Chen, Lain Jong Li, Wei Ting Hsu, Wen Hao Chang, Yu Jie Zheng, Wei Chen, and Andrew T.S. Wee. Bandgap tunability at single-layer molybdenum disulphide grain boundaries. *Nature Communications*, 6:1–8, 2015.

[136] Xiaodong Zhou, Kibum Kang, Saien Xie, Ali Dadgar, Nicholas R. Monahan, X. Y. Zhu, Jiwoong Park, and Abhay N. Pasupathy. Atomic-Scale Spectroscopy of Gated Monolayer MoS2. *Nano Letters*, 16(5):3148–3154, 2016.

[137] Gábor Zsolt Magda, János Petõ, Gergely Dobrik, Chanyong Hwang, László P. Biró, and Levente Tapasztó. Exfoliation of large-area transition metal chalcogenide single layers. *Scientific Reports*, 5:3–7, 2015.

[138] Dominik Lembke, Adrien Allain, and Andras Kis. Thickness-dependent mobility in two-dimensional MoS2 transistors. *Nanoscale*, 7(14):6255–6260, 2015.

[139] Min Kyu Joo, Byoung Hee Moon, Hyunjin Ji, Gang Hee Han, Hyun Kim, Gwanmu Lee, Seong Chu Lim, Dongseok Suh, and Young Hee Lee. Electron Excess Doping and Effective Schottky Barrier Reduction on the MoS2/h-BN Heterostructure. *Nano Letters*, 16(10):6383–6389, 2016.

[140] Min-Kyu Joo, Byoung Hee Moon, Hyunjin Ji, Gang Hee Han, Hyun Kim, Gwanmu Lee, Seong Chu Lim, Dongseok Suh, and Young Hee Lee. Understanding Coulomb Scattering Mechanism in Monolayer MoS ₂ Channel in the Presence of h -BN Buffer Layer. *ACS Applied Materials & Interfaces*, 9(5):5006–5013, 2017.

[141] Fabrice Donatini and Le Si Dang. A single-step electron beam lithography of buried nanostructures using cathodoluminescence imaging and low temperature. *Nanotechnology*, 21(37), 2010.

[142] Galan Moody, Chandriker Kavir Dass, Kai Hao, Chang Hsiao Chen, Lain Jong Li, Akshay Singh, Kha Tran, Genevieve Clark, Xiaodong Xu, Gunnar Berghäuser, Ermin Malic, Andreas Knorr, and Xiaoqin Li. Intrinsic homogeneous linewidth and broadening mechanisms of excitons in monolayer transition metal dichalcogenides. *Nature Communications*, 6(May):1–6, 2015.

[143] F. Cadiz, E. Courtade, C. Robert, G. Wang, Y. Shen, H. Cai, T. Taniguchi, K. Watanabe, H. Carrere, D. Lagarde, M. Manca, T. Amand, P. Renucci, S. Tongay, X. Marie, and B. Urbaszek. Excitonic linewidth approaching the homogeneous limit in mos_2-based van der waals heterostructures. *Phys. Rev. X*, 7:021026, May 2017.

[144] Tomasz Jakubczyk, Goutham Nayak, Lorenzo Scarpelli, Francesco Masia, Wei-Lai Liu, Sudipta Dubey, Nedjma Bendiab, Laëtitia Marty, Takashi Taniguchi, Kenji Watanabe, Gilles Nogues, Johann Coraux, Vincent Bouchiat, Wolfgang Langbein, Julien Renard, and Jacek Kasprzak. Coherence and density dynamics of excitons in a single-layer MoS$_2$ reaching the homogeneous limit. 2018.

[145] K. S. Novoselov, A. Mishchenko, A. Carvalho, and A. H. Castro Neto. 2d materials and van der waals heterostructures. *Science*, 353(6298), 2016.

[146] Pasqual Rivera, John R. Schaibley, Aaron M. Jones, Jason S. Ross, Sanfeng Wu, Grant Aivazian, Philip Klement, Kyle Seyler, Genevieve Clark, Nirmal J. Ghimire, Jiaqiang Yan, D. G. Mandrus, Wang Yao, and Xiaodong Xu. Observation of long-lived interlayer excitons in monolayer mose2-wse2 heterostructures. *Nature Communications*, 6:6242 EP –, Feb 2015. Article.

[147] Pasqual Rivera, Kyle L. Seyler, Hongyi Yu, John R. Schaibley, Jiaqiang Yan, David G. Mandrus, Wang Yao, and Xiaodong Xu. Valley-polarized exciton dynamics in a 2d semiconductor heterostructure. *Science*, 351(6274):688–691, 2016.

[148] Chenhao Jin, Jonghwan Kim, Joonki Suh, Zhiwen Shi, Bin Chen, Xi Fan, Matthew Kam, Kenji Watanabe, Takashi Taniguchi, Sefaattin Tongay, Alex Zettl, Junqiao Wu, and Feng Wang. Interlayer electron-phonon coupling in wse2/hbn heterostructures. *Nature Physics*, 13:127 EP –, Oct 2016.

[149] Hai Li, Jiang-Bin Wu, Feirong Ran, Miao-Ling Lin, Xue-Lu Liu, Yanyuan Zhao, Xin Lu, Qihua Xiong, Jun Zhang, Wei Huang, Hua Zhang, and Ping-Heng Tan. Interfacial interactions in van der waals heterostructures of mos2 and graphene. *ACS Nano*, 11(11):11714–11723, 2017. PMID: 29068659.

[150] C. H. Lui, Zhipeng Ye, Chao Ji, Kuan-Chang Chiu, Cheng-Tse Chou, Trond I. Andersen, Casie Means-Shively, Heidi Anderson, Jenn-Ming Wu, Tim Kidd, Yi-Hsien Lee, and Rui He. Observation of interlayer phonon modes in van der waals heterostructures. *Phys. Rev. B*, 91:165403, Apr 2015.

[151] Ming-Hui Chiu, Chendong Zhang, Hung-Wei Shiu, Chih-Piao Chuu, Chang-Hsiao Chen, Chih-Yuan S. Chang, Chia-Hao Chen, Mei-Yin Chou, Chih-Kang Shih, and Lain-Jong Li. Determination of band alignment in the single-layer MoS2/WSe2 heterojunction. *Nature Communications*, 6(May):7666, 2015.

[152] H. Fang, C. Battaglia, C. Carraro, S. Nemsak, B. Ozdol, J. S. Kang, H. A. Bechtel, S. B. Desai, F. Kronast, A. A. Unal, G. Conti, C. Conlon, G. K. Palsson, M. C. Martin, A. M. Minor, C. S. Fadley, E. Yablonovitch, R. Maboudian, and A. Javey. Strong interlayer coupling in van der Waals heterostructures built from single-layer chalcogenides. *Proceedings of the National Academy of Sciences*, 111(17):6198–6202, 2014.

[153] Jun Kang, Jingbo Li, Shu-Shen Li, Jian-Bai Xia, and Lin-Wang Wang. Electronic structural moiré pattern effects on mos2/mose2 2d heterostructures. *Nano Letters*, 13(11):5485–5490, 2013. PMID: 24079953.

[154] Fengcheng Wu, Timothy Lovorn, and A. H. MacDonald. Topological exciton bands in moiré heterojunctions. *Phys. Rev. Lett.*, 118:147401, Apr 2017.

[155] Yi Pan, Stefan Fölsch, Yifan Nie, Dacen Waters, Yu-Chuan Lin, Bhakti Jariwala, Kehao Zhang, Kyeongjae Cho, Joshua A. Robinson, and Randall M. Feenstra. Quantum-confined electronic states arising from the moiré pattern of mos2–wse2 heterobilayers. *Nano Letters*, 18(3):1849–1855, 2018. PMID: 29415536.

[156] Shengxi Huang, Liangbo Liang, Xi Ling, Alexander A. Puretzky, David B. Geohegan, Bobby G. Sumpter, Jing Kong, Vincent Meunier, and Mildred S. Dresselhaus. Low-frequency interlayer raman modes to probe interface of twisted bilayer mos2. *Nano Letters*, 16(2):1435–1444, 2016. PMID: 26797083.

[157] Kha Tran, Galan Moody, Fengcheng Wu, Xiaobo Lu, Junho Choi, Akshay Singh, Jacob Embley, André Zepeda, Marshall Campbell, Kyounghwan Kim, Amritesh Rai, Travis Autry, Daniel A. Sanchez, Takashi Taniguchi, Kenji Watanabe, Nanshu Lu, Sanjay K. Banerjee, Emanuel Tutuc, Li Yang, Allan H. MacDonald, Kevin L. Silverman, and Xiaoqin Li. Moiré excitons in van der waals heterostructures. *arxiv.1807.03771*.

[158] Aidan. P. Rooney, Aleksey Kozikov, Alexander N. Rudenko, Eric Prestat, Matthew J. Hamer, Freddie Withers, Yang Cao, Kostya S. Novoselov, Mikhail I. Katsnelson, Roman

Gorbachev, and Sarah J. Haigh. Observing imperfection in atomic interfaces for van der waals heterostructures. *Nano Letters*, 17(9):5222–5228, 2017. PMID: 28741958.

[159] Hannu-Pekka Komsa, Jani Kotakoski, Simon Kurasch, Ossi Lehtinen, Ute Kaiser, and Arkady V. Krasheninnikov. Two-dimensional transition metal dichalcogenides under electron irradiation: Defect production and doping. *Phys. Rev. Lett.*, 109:035503, Jul 2012.

[160] Evgeny M. Alexeev, Alessandro Catanzaro, Oleksandr V. Skrypka, Pramoda K. Nayak, Seongjoon Ahn, Sangyeon Pak, Juwon Lee, Jung Inn Sohn, Kostya S. Novoselov, Hyeon Suk Shin, and Alexander I. Tartakovskii. Imaging of interlayer coupling in van der waals heterostructures using a bright-field optical microscope. *Nano Letters*, 17(9):5342–5349, 2017. PMID: 28753319.

[161] Marvin Kulig, Jonas Zipfel, Philipp Nagler, Sofia Blanter, Christian Schüller, Tobias Korn, Nicola Paradiso, Mikhail M. Glazov, and Alexey Chernikov. Exciton diffusion and halo effects in monolayer semiconductors. *Phys. Rev. Lett.*, 120:207401, May 2018.

[162] Shoujun Zheng, Jin-Kyu So, Fucai Liu, Zheng Liu, Nikolay Zheludev, and Hong Jin Fan. Giant enhancement of cathodoluminescence of monolayer transitional metal dichalcogenides semiconductors. *Nano Letters*, 17(10):6475–6480, 2017. PMID: 28933857.

[163] Filippo Pizzocchero, Lene Gammelgaard, Bjarke S Jessen, José M Caridad, Lei Wang, James Hone, Peter Bøggild, and Timothy J Booth. The hot pick-up technique for batch assembly of van der waals heterostructures. *Nat. Commun.*, 7:11894, 2016.

[164] J. Rodriguez-Viejo, K. F. Jensen, H. Mattoussi, J. Michel, B. O. Dabbousi, and M. G. Bawendi. Cathodoluminescence and photoluminescence of highly luminescent cdse/zns quantum dot composites. *Applied Physics Letters*, 70(16):2132–2134, 1997.

[165] Sandro Mignuzzi, Andrew J. Pollard, Nicola Bonini, Barry Brennan, Ian S. Gilmore, Marcos A. Pimenta, David Richards, and Debdulal Roy. Effect of disorder on Raman scattering of single-layer Mo S2. *Physical Review B - Condensed Matter and Materials Physics*, 91(19):1–7, 2015.

[166] A. Molina-Sánchez and L. Wirtz. Phonons in single-layer and few-layer mos_2 and ws_2. *Phys. Rev. B*, 84:155413, Oct 2011.

[167] Sandro Mignuzzi, Andrew J. Pollard, Nicola Bonini, Barry Brennan, Ian S. Gilmore, Marcos A. Pimenta, David Richards, and Debdulal Roy. Effect of disorder on raman scattering of single-layer Mos_2. *Phys. Rev. B*, 91:195411, May 2015.

[168] Bruno R. Carvalho, Yuanxi Wang, Sandro Mignuzzi, Debdulal Roy, Mauricio Terrones, Cristiano Fantini, Vincent H. Crespi, Malard Leandro M., and Marcos A. Pimenta. Intervalley scattering by acoustic phonons in two-dimensional mos_2 revealed by double-resonance raman rpectroscopy. *Nat. Commun.*, 8:14670, 2017.

[169] Gitti L. Frey, Reshef Tenne, Manyalibo J. Matthews, M. S. Dresselhaus, and G. Dresselhaus. Raman and resonance raman investigation of mos_2 nanoparticles. *Phys. Rev. B*, 60:2883–2892, Jul 1999.

[170] Tsachi Livneh and Jonathan E Spanier. A comprehensive multiphonon spectral analysis in mos 2. *2D Materials*, 2(3):035003, 2015.

[171] Long Qi, Ying Wang, Lei Shen, and Yihong Wu. Chemisorption-induced n-doping of mos2 by oxygen. *Applied Physics Letters*, 108(6):063103, 2016.

[172] X. Zhang, W. P. Han, J. B. Wu, S. Milana, Y. Lu, Q. Q. Li, A. C. Ferrari, and P. H. Tan. Raman spectroscopy of shear and layer breathing modes in multilayer mos_2. *Phys. Rev. B*, 87:115413, Mar 2013.

[173] Maria O'Brien, Niall McEvoy, Damien Hanlon, Toby Hallam, Jonathan N. Coleman, and Georg S. Duesberg. Mapping of low-frequency raman modes in cvd-grown transition metal dichalcogenides: Layer number, stacking orientation and resonant effects. *Scientific Reports*, 6:19476 EP –, Jan 2016. Article.

[174] Liangbo Liang, Jun Zhang, Bobby G. Sumpter, Qing-Hai Tan, Ping-Heng Tan, and Vincent Meunier. Low-frequency shear and layer-breathing modes in raman scattering of two-dimensional materials. *ACS Nano*, 11(12):11777–11802, 2017. PMID: 29099577.

[175] Recep Zan, Quentin M Ramasse, Rashid Jalil, Thanasis Georgiou, Ursel Bangert, and Konstantin S Novoselov. Control of radiation damage in mos_2 by graphene encapsulation. *ACS Nano*, 7(11):10167–10174, 2013.

[176] Gerardo Algara-Siller, Simon Kurasch, Mona Sedighi, Ossi Lehtinen, and Ute Kaiser. The pristine atomic structure of mos_2 monolayer protected from electron radiation damage by graphene. *Appl. Phys. Lett.*, 103(20):203107, 2013.

[177] Alejandra Garcia, Andres M Raya, Marcelo M Mariscal, Rodrigo Esparza, Miriam Herrera, Sergio I Molina, Giovanni Scavello, Pedro L Galindo, Miguel Jose-Yacaman, and Arturo Ponce. Analysis of electron beam damage of exfoliated mos_2 sheets and quantitative haadf-stem imaging. *Ultramicroscopy*, 146:33–38, 2014.

[178] Lei Liao, Jie Zhu, Xiaojun Bian, Lina Zhu, Micheál D Scanlon, Hubert H Girault, and Baohong Liu. Mos_2 formed on mesoporous graphene as a highly active catalyst for hydrogen evolution. *Adv. Func. Mater.*, 23(42):5326–5333, 2013.

[179] Junfeng Xie, Hao Zhang, Shuang Li, Ruoxing Wang, Xu Sun, Min Zhou, Jingfang Zhou, Xiong Wen David Lou, and Yi Xie. Defect-rich mos_2 ultrathin nanosheets with additional active edge sites for enhanced electrocatalytic hydrogen evolution. *Adv. Mater.*, 25(40):5807–5813, 2013.

[180] Eric Parzinger, Bastian Miller, Benno Blaschke, Jose A. Garrido, Joel W. Ager, Alexander Holleitner, and Ursula Wurstbauer. Photocatalytic stability of single- and few-layer mos_2. *ACS Nano*, 9(11):11302–11309, 2015.

[181] Diana Y. Qiu, Ting Cao, and Steven G. Louie. Nonanalyticity, valley quantum phases, and lightlike exciton dispersion in monolayer transition metal dichalcogenides: Theory and first-principles calculations. *Physical Review Letters*, 115(17):1–5, 2015.

[182] Xiaoze Liu, Tal Galfsky, Zheng Sun, Fengnian Xia, Erh Chen Lin, Yi Hsien Lee, Stéphane Kéna-Cohen, and Vinod M. Menon. Strong light-matter coupling in two-dimensional atomic crystals. *Nature Photonics*, 9(1):30–34, 2014.

[183] J. Pérez-Rigueiro, C. Viney, J. Llorca, and M. Elices. Mechanical properties of single-brin silkworm silk. *Journal of Applied Polymer Science*, 75(10):1270–1277, 2000.

[184] Vollrath & David P. Knight. Other spinning arthropods(Liquid crystalline spinning of spider silk). *Nature*, 410(March):541–548, 2001.

[185] Stephen Willingham. Scientists weave spider silk into new bulletproof vests. *National Defense*, pages 26–27, 2000.

[186] Danielle N. Rockwood, Rucsanda C. Preda, Tuna Yücel, Xiaoqin Wang, Michael L. Lovett, and David L. Kaplan. Materials fabrication from Bombyx mori silk fibroin. *Nature Protocols*, 6(10):1612–1631, 2011.

[187] E. Muñoz, A.B. Dalton, S. Collins, M. Kozlov, J. Razal, J.N. Coleman, B.G. Kim, V.H. Ebron, M. Selvidge, J.P. Ferraris, and R.H. Baughman. Multifunctional Carbon Nanotube Composite Fibers. *Advanced Engineering Materials*, 6(10):801–804, 2004.

[188] John G. Hardy and Thomas R. Scheibel. Silk-inspired polymers and proteins. *Biochemical Society Transactions*, 37(4):677–681, 2009.

[189] A. U. Ude, R. A. Eshkoor, R. Zulkifili, A. K. Ariffin, A. W. Dzuraidah, and C. H. Azhari. Bombyx mori silk fibre and its composite: A review of contemporary developments. *Materials and Design*, 57:298–305, 2014.

[190] Dae-hyeong Kim, Jonathan Viventi, Jason J Amsden, Jianliang Xiao, Yun-soung Kim, Justin a Blanco, Bruce Panilaitis, Eric S Frechette, Diego Contreras, David L Kaplan, Fiorenzo G Omenetto, Yonggang Huang, Mitchell R Zakin, Brian Litt, and John a Rogers. Dissolvable Films of Silk Fibroin for Ultrathin, Conformal Bio- Integrated Electronics. *Electronics*, 9(6):511–517, 2011.

[191] Natalia C. Tansil, Yang Li, Choon Peng Teng, Shuangyuan Zhang, Khin Yin Win, Xing Chen, Xiang Yang Liu, and Ming Yong Han. Intrinsically colored and luminescent silk. *Advanced Materials*, 23(12):1463–1466, 2011.

[192] Natalia C. Tansil, Leng Duei Koh, and Ming Yong Han. Functional silk: Colored and luminescent. *Advanced Materials*, 24(11):1388–1397, 2012.

[193] Chi-Shuo Chen, Sushant Soni, Catherine Le, Matthew Biasca, Erik Farr, Eric Y-T Chen, and Wei-Chun Chin. Human stem cell neuronal differentiation on silk-carbon nanotube composite. *Nanoscale Res Lett*, 7(E2/2.726/625/2011):126, 2012.

[194] Alan B Dalton, Steve Collins, Edgar Muñoz, Joselito M Razal, Von Howard Ebron, John P Ferraris, Jonathan N Coleman, Bog G Kim, and Ray H Baughman. Super-tough carbon-nanotube fibres. *Nature*, 423:703, 2003.

[195] Jonathan Ayutsede, Milind Gandhi, Sachiko Sukigara, Haihui Ye, Chen-ming Hsu, Yury Gogotsi, and Frank Ko. Carbon nanotube reinforced Bombyx mori silk nanofibers by the electrospinning process. *Biomacromolecules*, 7(1):208–214, 2006.

[196] Hui Pan, Yaopeng Zhang, Yichun Hang, Huili Shao, Xuechao Hu, Yuemin Xu, and Chao Feng. Significantly reinforced composite fibers electrospun from silk fibroin/carbon nanotube aqueous solutions. *Biomacromolecules*, 13(9):2859–2867, 2012.

[197] Qi Wang, Chunya Wang, Mingchao Zhang, Muqiang Jian, and Yingying Zhang. Feeding Single-Walled Carbon Nanotubes or Graphene to Silkworms for Reinforced Silk Fibers. *Nano Letters*, 16(10):6695–6700, 2016.

[198] M. S. DRESSELHAUS, G. DRESSELHAUS, SAITO, and R. PHYSICS OF CARBON NANOTUBES. 33(7):1–9, 2003.

[199] A. L. Kalamkarov, A. V. Georgiades, S. K. Rokkam, V. P. Veedu, and M. N. Ghasemi-Nejhad. Analytical and numerical techniques to predict carbon nanotubes properties. *International Journal of Solids and Structures*, 43(22-23):6832–6854, 2006.

[200] L. Zuppiroli J.-P. Salvetat, J.-M. Bonard, N.H.Thomson, A.J.Kulik, L. Forro, W. Benoit. Mechanical properties of carbon nanotubes composites. *Journal of Computational and Theoretical Nanoscience*, 1(2):204–215, 2004.

[201] Min-Feng Yu, Bradley S. Files, Sivaram Arepalli, and Rodney S. Ruoff. Tensile Loading of Ropes of Single Wall Carbon Nanotubes and their Mechanical Properties. *Physical Review Letters*, 84(24):5552–5555, 2000.

[202] Michael J. Bronikowski, Peter A. Willis, Daniel T. Colbert, K. A. Smith, and Richard E. Smalley. Gas-phase production of carbon single-walled nanotubes from carbon monoxide via the HiPco process: A parametric study. *Journal of Vacuum Science & Technology A: Vacuum, Surfaces, and Films*, 19(4):1800–1805, 2001.

[203] I. W. Chiang, B. E. Brinson, A. Y. Huang, P. A. Willis, M. J. Bronikowski, J. L. Margrave, R. E. Smalley, and R. H. Hauge. Purification and characterization of single-wall carbon nanotubes (SWNTs) obtained from the gas-phase decomposition of CO (HiPco process). *Journal of Physical Chemistry B*, 105(35):8297–8301, 2001.

[204] Richard E. Smalley, Yubao Li, Valerie C. Moore, B. Katherine Price, Ramon Colorado, Howard K. Schmidt, Robert H. Hauge, Andrew R. Barron, and James M. Tour. Single wall carbon nanotube amplification: En route to a type-specific growth mechanism. *Journal of the American Chemical Society*, 128(49):15824–15829, 2006.

[205] J. K.W. Sandler, S. Pegel, M. Cadek, F. Gojny, M. Van Es, J. Lohmar, W. J. Blau, K. Schulte, A. H. Windle, and M. S.P. Shaffer. A comparative study of melt spun polyamide-12 fibres reinforced with carbon nanotubes and nanofibres. *Polymer*, 45(6):2001–2015, 2004.

[206] Jonathan N. Coleman, Umar Khan, Werner J. Blau, and Yurii K. Gun'ko. Small but strong: A review of the mechanical properties of carbon nanotube-polymer composites. *Carbon*, 44(9):1624–1652, 2006.

[207] Yuan Cheng, L.-D. Koh, Dechang Li, Baohua Ji, M.-Y. Han, and Y.-W. Zhang. On the strength of B-sheet crystallites of Bombyx mori silk fibroin. *Journal of The Royal Society Interface*, 11(96):20140305–20140305, 2014.

[208] Tetsuo Asakura, Keiko Okushita, and Mike P. Williamson. Analysis of the structure of Bombyx mori silk fibroin by NMR. *Macromolecules*, 48(8):2345–2357, 2015.

[209] Guoqing Liu, Xiaopeng Huang, Yuanjing Wang, Yu Qing Zhang, and Xinwei Wang. Thermal transport in single silkworm silks and the behavior under stretching. *Soft Matter*, 8(38):9792–9799, 2012.

[210] Leng Duei Koh. BOMBYX MORI SILK: FROM MECHANICAL PROPERTIES TO FUNCTIONALITIES, 2015.

[211] Christian Riekel, Manfred Burghammer, Thomas G. Dane, Claudio Ferrero, and Martin Rosenthal. Nanoscale Structural Features in Major Ampullate Spider Silk. *Biomacromolecules*, 18(1):231–241, 2017.

[212] Richard E Marsh, Robert B Corey, and Linus Pauling. An investigation of the structure of silk fibroin. *Biochimica et Biophysica acta*, 16:1–34, 1955.

[213] RDB Fraser and TP Macrae. Conformations of fibrous proteins. 1973. *Academic Press, New York. Biemann, KMartin, S. Mass Spec. Rev*, 1987:1–76, 1987.

[214] A Martel, M Burghammer, RJ Davies, and C Riekel. Thermal behavior of bombyx mori silk: Evolution of crystalline parameters, molecular structure, and mechanical properties. *Biomacromolecules*, 8(11):3548–3556, 2007.

[215] Yu Shen, Michael A Johnson, and David C Martin. Microstructural characterization of bombyx mori silk fibers. *Macromolecules*, 31(25):8857–8864, 1998.

[216] Yasuhiro Takahashi, Mikio Gehoh, and Kimio Yuzuriha. Structure refinement and diffuse streak scattering of silk (bombyx mori). *International journal of biological macromolecules*, 24(2-3):127–138, 1999.

[217] A Hammersley. Fit2d program, in www. esrf. fr/computing/scientific, 2009.

[218] Alexander Sponner, Wolfram Vater, Shamci Monajembashi, Eberhard Unger, Frank Grosse, and Klaus Weisshart. Composition and hierarchical organisation of a spider silk. *PloS one*, 2(10):e998, 2007.

[219] Yves Termonia. Molecular modeling of spider silk elasticity. *Macromolecules*, 27(25):7378–7381, 1994.

[220] David T. Grubb and Lynn W. Jelinski. Fiber morphology of spider silk: The effects of tensile deformation. *Macromolecules*, 30(10):2860–2867, 1997.